Design, Development and Characterization of High Current Electron Cyclotron Resonance Ion Source

By

PRADIP ROYCHOWDHURY

PHYS01200704005

BHABHA ATOMIC RESEARCH CENTRE, MUMBAI

A thesis submitted to the

Board of studies in Physical Sciences

In partial fulfillment of requirements

For the Degree of

DOCTOR OF PHILOSOPHY

of

HOMI BHABHA NATIONAL INSTITUTE

July, 2014

HOMI BHABHA NATIONAL INSTITUTE

Recommendations of the viva voce committee

As members of the Viva Voce Board, we recommend that the dissertation prepared by **Pradip Roychowdhury** entitled **"Design, Development and Characterization of High Current Electron Cyclotron Resonance Ion Source"** may be accepted as fulfilling the dissertation requirement for the Degree of Doctor of Philosophy.

Chairman:	**Prof. B. N. Jagtap**	Date: 27. 11. 2014
Guide / Convenor:	**Prof. D. S. Patil**	Date: 27.11. 2014
Member 1:	**Prof. Lokesh Trivedi/ Prof. A.K. Mohanty**	Date: 27.11. 2014
Member 2:	**Prof. S. C. Gadkari**	Date: 27. 11. 2014
External Examiner:	**Prof. G. Mohan Rao**	Date: 27. 11. 2014

Final approval and acceptance of this dissertation is contingent upon the candidate's submission of the final copies of the dissertation to HBNI.

I hereby certify that I have read this dissertation prepared under my direction and recommend that it may be accepted as fulfilling the dissertation requirement.

Date: 27. 11. 2014

Place: Mumbai

Guide: Prof. D. S. Patil

STATEMENT BY AUTHOR

This dissertation has been submitted in partial fulfillment of requirements for an advanced degree at Homi Bhabha National Institute (HBNI) and is deposited in the Library to be made available to borrowers under rules of the HBNI.

Brief quotations from this dissertation are allowable without special permission, provided that accurate acknowledgement of source is made. Requests for permission for extended quotation from or reproduction of this manuscript in whole or in part may be granted by the Competent Authority of HBNI when in his or her judgment the proposed use of the material is in the interests of scholarship. In all other instances, however, permission must be obtained from the author.

Pradip Roychowdhury

DECLARATION

I hereby declare that the investigation presented in the thesis has been carried out by me. The work is original and has not been submitted earlier as a whole or in part for a degree/diploma at this or any other Institution / University.

Pradip Roychowdhury

List of Publications

I. INTERNATIONAL REFFERED JOURNALS

a. Published

1. ‘Beam Extraction and High Stability Operation of High Current Electron Cyclotron Resonance Proton Ion Source’, **P. Roychowdhury**, L. Mishra, H. Kewlani, D. S. Patil and K. C. Mittal, Review of Scientific Instruments **85**, (2014), p. 033303-1 to 033303-10.

2. ‘Langmuir Probe Diagnostics of Plasma in High Current Electron Cyclotron Resonance Proton Ion Source’, **P. Roychowdhury**, H. Kewlani, L. Mishra, D. S. Patil and K. C. Mittal, Review of Scientific Instruments **84**, (2013), p. 073303-1 to 073303-12.

3. ‘High Intensity Electron Cyclotron Resonance Proton Ion Source for Low Energy High Intensity Proton Accelerator’, **P. Roychowdhury** and D. P. Chakravarthy, Review of Scientific Instruments, **80**, (2009), p. 123305-1 to 123305-8.

b. To be communicated

4. ‘Emittance and Proton Fraction Measurement in High Current Electron Cyclotron Resonance Proton Ion source’ **P. Roychowdhury** and coworkers, under preparation.

II. Books/Report/ General Articles

5. 'Design and Development of High Intensity ECR Proton Source for LEHIPA', **P. Roychowdhury**, BARC NEWSLETTER FOUNDER'S DAY Special Issue, October 2010, Paper No. 10.

III. CONFERENCE PROCEEDINGS

6. 'Development and Characterization of High Current Electron Cyclotron Resonance Proton Ion Source', **P. Roychowdhury**, L. Mishra, H. Kewlani, S. Grarat, D. S. Patil and K. C. Mittal, (Invited talk) Proceedings of Indian Particle Accelerator Conference, InPAC-2013, 19-21 November, 2013 VECC, Kolkata. p. 130, Paper No.: ITS-10.

7. 'Design and Development of Langmuir Probe Circuit for online measurement of Plasma Parameters in ECR Ion Source', H. Kewlani, **P. Roychowdhury**, L. Mishra, S. Gharat and K. C. Mittal, Proceedings of Indian Particle Accelerator Conference, InPAC-2013, 19-21 November, 2013 VECC, Kolkata. p. 308, Paper No.: ID-095.

8. 'Design and Development of Instrumentation of Two Slit Emittance Meter for High Current ECR Ion Source', H. Kewlani, **P. Roychowdhury**, L. Mishra, S. Gharat, S. Ghodke and K. C. Mittal, Proceedings of Indian Particle Accelerator Conference, InPAC-2013, 19-21 November, 2013 VECC, Kolkata. p. 564, Paper No.: ID-224.

9. 'Electron Cyclotron Resonance Ion Source Control System', H. Kewlani, **P. Roychowdhury,** S. Grarat, L. Mishra, D. P. Chakravarthy and K. C. Mittal, Proceedings

of Ninth International Workshop on Personal Computers held at VECC Kolkata December 4-7, 2012, p. 217, Paper No.: THPD43 (www.jacow.org).

10. ‘Plasma Parameter Measurement in High Current ECR Ion Source’, **P. Roychowdhury**, H. Kewlani, L. Mishra, S. Grarat, D.S. Patil and D. P. Chakravarthy, Proceedings of 2nd International Workshop on Accelerator Driven Sub-Critical Systems & Thorium Utilization, BARC Mumbai, December 11-14, 2011, p. 50.

11. ‘Ion Source for ADS Applications’ **P. Roychowdhury**, H. Kewlani, L. Mishra, S. Grarat, and D. P. Chakravarthy, Proceedings of 2nd International Workshop on Accelerator Driven Sub-Critical Systems & Thorium Utilization, BARC Mumbai, December 11-14, 2011, p. 68.

12. ‘Five Electrode ECR Proton Source for LEHIPA’, **P. Roychowdhury**, S. R. Ghodke, D. P. Chakravarthy, Abhay Kumar, J. J. Roy and S. Guha, , Proceedings of Indian Particle Accelerator Conference InPAC 2011, February 15-18, 2011, IUAC, Delhi, Paper No. 141.

13. ‘Beam Line for Emittance and Specie Measurement in ECR Proton Source’, **P. Roychowdhury**, S. R. Ghodke, S. Gharat and D.P. Chakravarthy, Proceedings of Indian Particle Accelerator Conference InPAC 2011, 15-18 February 2011, IUAC, Delhi, Paper No. 149.

14. ‘Optically Isolated Remote Operation and Data Acquisition System for ECR Ion Source Developed for LEHIPA’, V. Yadav, R. B. Chavan, K. P. Dixit, **P. Roychowdhury**, K. C. Mittal and D. P. Chakravarthy, Proceedings of Indian Particle Accelerator Conference InPAC 2011, 15-18 Feb. 2011, IUAC, Delhi, Paper No. 134.

15. ‘High intensity electron cyclotron resonance proton source development for LEHIPA’, **P. Roychowdhury**, An Invited talk in Indo-Russian Meeting on linear Accelerators, IUAC, Delhi, 15 – 17 February 2010.

16. ‘Simulation of ion beam extraction from single aperture triode extraction column’, **P. Roychowdhury** and D. P. Chakravarthy, Proceedings of the International Symposium on Nuclear Physics, December 8-12, 2009, BARC, Mumbai, p.714.

17. ‘High Intensity ECR Ion Source Development for LEHIPA-ADS-commissioning and operational experience’, **P. Roychowdhury**, K. P. Dixit, S. R. Ghodke, P. C. Saroj, S. Chandan, S. Gharat, V. Yadav, R. B. Chavan and D. P. Chakravarthy, Proceedings of Indian Particle Accelerator Conference InPAC 2009, February 10-13, 2009, RRCAT, Indore, Paper No.226.

Pradip Roychowdhury

Dedicated to

My Parents and

My Family

ACKNOWLEDGEMENTS

First and foremost, I would like to express my deep sense gratitude to my research guide Prof. D. S. Patil, Head, Plasma Processing Section, LPTD, BARC for his valuable guidance, constant encouragement and support that he provided during the course of this dissertation. I take the pleasure to thank Dr. L. M. Gantayet, Director, BTDG, BARC, Dr. K. C. Mittal, Former Head, APPD, BARC and Dr. P. Singh, Head, IADD, BARC, for constant encouragement and support throughout this work.

I greatly acknowledge the contributions of my doctoral committee members Prof. B. N. Jagtap, Prof. Lokesh Trivedi and Prof. S. C. Gadkari who spent their valuable time for periodical critical assessment of my work. Incorporation of their constructive suggestions has greatly enhanced the technical level of my research work. I would like to thank Sh. D. P. Chakravarthy, Former Head, APPD, BARC and Dr. A. K. Ray, Former Director, BTDG for their support and encouragement.

I would like to thank my younger colleagues Sh. H. Kewlani, Sh. Love Mishra and Sh. S. Gharat of ECR Ion Source Section, APPD for useful discussions and participation in the experiments. I would also like to thank Smt. K. P. Dixit, Sh. S. R. Ghodke, Sh. P. C. Saroj, Sh. V. Yadav, Sh. S. Chandan, Sh. S. Chavan, Sh. Manjunath, Sh. N. K. Lawangre, Sh. G. L. Patil and other members of APPD, who were associated with the project.

My special thanks to Sh. V. T. Nimje and Dr. S. Das for providing their valuable friendship, encouragement and support.

Finally I express gratitude to my family for their heartful support without that I could not have done this work.

P. Roychowdhury

TABLE OF CONTENTS

SYNOPSIS

The high beam power (Megawatt) proton accelerators of Giga electron volt (GeV) energy are built in several countries for Accelerator Driven Subcritical System (ADSS) Applications. The possibility of generating a high neutron flux with a broad energy spectrum by means of a high current proton beam (1GeV) impinging on a spallation target open new perspectives in the use of high energy (high current) proton accelerators. A continuously working (cw) proton beam power in excess of a few tens of megawatt (MW) could produce the neutron flux to a subcritical nuclear reactor. Moreover, the high neutrons flux also allows the incineration of nuclear waste (actinides and long lived fission fragment) produced by conventional critical reactors, leaving no substantial amount of radioactive waste at the end of the cycle. Realizing the potential of ADSS for the transmutation of long lived nuclear waste and sustenance of subcritical reactors, it is decided to define research and development program for ADSS, promoted by Carlo Rubbia idea of Energy Amplifier.

The front end accelerator for ADSS is the 20 MeV, 30 mA, Low Energy High Intensity Proton Accelerator (LEHIPA) that is under development at our institute (Bhabha Atomic Research Center, Trombay, Mumbai, India). LEHIPA consists of high current H^+ ion source at 50 keV to be accelerated to 3 MeV by radio frequency quadrupole (RFQ) and to 20 MeV by Alvarez type drift tube linac accelerating structure.

High current cw electron cyclotron resonance (ECR) proton ion source with good beam quality and high reliability is the essential requirement of LEHIPA. A desirable property of the source is that the proton fraction be as high as possible so as to avoid need for selection of desired ion, i.e., to enable direct injection into RFQ.

In high current ECR proton sources, microwaves are directly introduced into the plasma volume through a dielectric window. This source has advantage of operating in wide range of pressures inside discharge chamber and produce homogeneous high density plasma with large cross-section. Due to high absorption efficiency in these sources, microwaves are able to generate plasma with relatively large electron temperature and density. The proton fraction is ~ 80% or more. Since microwaves preferentially heat electrons through ECR mechanism and keep ions cold, the emittance of the source is less compared to other sources. These sources are power and gas efficient, stable and reproducible and are demonstrably durable over long period of continuous operations.

In ECR ion source, the plasma is generated from neutral gas using RF electric fields. The ion beam is extracted from plasma by applying potential on electrodes. The ion beam is then transported to next accelerating structures or used for applications.

The most important aspect of ion source design is the methods of energy transfer to the plasma load from the impressed electromagnetic fields. ECR is a very efficient method of power transfer, and takes advantage of the cyclotron resonance of electrons to selectively transfer power from the impressed electric fields and into the electron gas. From this heated electron gas, the energy is transferred to the other constituents of the plasma through collisions.

The ECR ion source consists of a discharge confinement structure known as plasma chamber that may be made of quartz, alumina, boron nitride, stainless steel or copper. The plasma chamber is surrounded by electromagnetic coils or permanent magnets that generate the static magnetic field topology for ECR, and also to control (or restrict) the flow of charge species within, and outside the source. The discharge vessel is sealed to a vacuum system which ensures sufficiently low base pressures (usually of the order of 10^{-7} mbar). These low pressures are created with one or a combination of several types of pumps. Discharge gas (or a mixture of several gases) is fed into the plasma vessel through a controlled leak. Electromagnetic energy at the appropriate frequency is impressed on the neutral gas, generally through an applicator that ensures maximum power transfer to the gas.

Somewhere inside the plasma chamber, the static magnetic field is designed such that it has correct orientation and strength (with respect to the impressed electric field). ECR zones are thereby formed where the power absorbed by electron gas is enhanced. Subsequent ionizing collisions between the hot electrons and atoms (or molecules) create and sustain the discharge. In general, some sort of cooling (either air or water) is necessary for the ion source due to the heat generated from the wall losses of the electromagnetic fields, and also from the energy dissipated by collisions and recombination on the plasma containment vessel walls. Once the discharge is in steady state, a specific subspecies from the quasi-neutral plasma may be selectively extracted using an extraction apparatus.

The extraction process basically consists of applying a high voltage between an ion reservoir and a perforated acceleration electrode. The trajectories of the accelerated ions, which determine the beam quality, are influenced by several factors, such as the applied field strength, the shape of the emitting surface, and also on the space charge density of the resulting beam itself. In the case of plasma sources, the shape of the emitting surface (meniscus) depends on the electrical field distribution and the local densities of plasma ions, electrons, and accelerated ions. The meniscus is convex, when the plasma density is relatively high. It is plane under intermediate conditions and concave when the plasma density is low or, if the extraction field is higher.

In the extraction gap, there are three region formed. The first is the discharge plasma region, the second is the un-neutralized beam region and the third is the beam- plasma region. The beam of neutralized ions constitutes the beam-plasma region. It is generated by ionization of residual gases that are present within the beam line. This ionization process can generate sufficient number of compensating electrons. But these electrons must be kept from being accelerated back from the beam-plasma region in the direction of ion source, both to encourage the neutralization of ions of the beam and to protect the source against damage. For this reason a third electrode is introduced in the main extraction gap. The gap is biased to a sufficiently low potential so as to create a negative potential well, which prevents back-streaming electrons towards the source region.

ECR technology has several outstanding advantages over previously established ion source technologies (e.g., penning, duoplasmatron etc. that typically has cathodes or filaments that generates hot electrons and has short lifetime). ECR sources have long lifetimes i.e., they can operate hundreds of hours without problems, which ultimately leads to lower operational costs.

Another advantage of ECR technology is that the plasma electrons are preferentially heated by the impressed electric field. This contains the thermal ion energy to extremely low levels. Low thermal energy of ions is extremely good for several reasons. For ion beam sources, one of the factors that lead to beam divergence is high thermal energy of ions, which generates radially directed space charge fields and increases the repulsive force between the ions constituting the beam, ultimately prohibitive beam divergence.

The key components of ECR proton ion source are microwave generator and transmission system, plasma chamber, vacuum system, solenoid coils and power supplies, beam extraction electrodes and power supplies, gas injection system, plasma diagnostics devices and beam measuring device. The plasma chamber is coupled to microwave circuitry through DC waveguide break, ridge waveguide and microwave quartz window. ECR plasma is ignited with 400 -1100 W of microwave power at 2.45 GHz, in the presence of hydrogen gas. The solenoid coils are used for confinement of plasma and to satisfy ECR condition at the plasma chamber extremities.

The objective of the thesis was to design, develop and characterize the high current ECR proton ion source to meet the requirement of LEHIPA. The source is not available commercially with the required beam parameters. As the ion source is the critical component of LEHIPA, our effort is towards in house development of the ion source that can produce stable beam and operate reliably for long durations in cw and pulsed mode. There are many technological challenges and bottle necks that are encountered and overcome successfully while developing the source. The source is fully operational with the specified beam parameters and the long time operation of the source (several hours) has been tested. The source will be integrated to LEHIPA shortly.

The most important parameters of the ion source are the maximum beam current, emittance and proton fraction. The total beam current and the proton beam current are studied as a function of different experimental parameters. In order to characterize the source, further measurement are made, regarding the quality of the ion beam, i.e., emittance and proton fraction, by keeping the emittance as low as possible. In order to understand the plasma processes in the ion source and to improve its performance, a number of experiments have been carried out to characterize the plasma in terms of experimentally controlled parameters. Particular attention was paid to increase the electron density for a more efficient ionization, getting more intense currents.

The thesis is organized in the eight chapters and the content of each chapters are described briefly.

Chapter 1. Introduction

This chapter gives a literature review about the high power proton accelerators that are developed for ADSS applications.

Chapter 2. Plasma Physics applied to ion sources

This chapter discusses about the basic plasma physics applicable to the sources. This includes discussion about basic plasma parameters (e.g., plasma density, fractional ionization, and particle temperature), various types of collisions (Spitzer collisions, elastic electron-neutral collisions, binary inelastic electron collision etc.), ionization processes (electron impact ionization, photoionization, field ionization, surface ionization, and laser ionization), magnetic field effect (gyro orbits, gyro frequencies and magnetic confinement), and waves in the plasma.

Chapter 3. Ion sources

In this chapter discussion about the method of plasma generation using ECR mechanism, ion beam formation, low energy beam transport and ion beam emittance and brightness is presented. A review of various ion sources developed for various applications is presented.

Chapter 4. Design and construction of ECR proton ion source

In this chapter, the design, assembly and testing of three and five electrode ion source is presented. The design of microwave heating system, plasma chamber, magnetic system, extraction system, vacuum system, gas injection system and Low Conductivity Process Water system (LCW) is described in detail. The microwave generator section consists of magnetron, circulator, dual directional coupler, four stub auto tuner, waveguide break and ridge waveguide. It also discusses about the waveguide break, ridge waveguide and H-plane bend waveguide that are designed and fabricated in housed. The ridge waveguide and H-plane bend waveguide is operating under low pressure so it is designed to withstand vacuum pressure of 10^{-7} mbar. The ECR magnetic field of 875 G is generated using two solenoid coils and power supplies. A discussion about the design of the solenoid coils and fabrication details are given here. The coils are tested and field mapping is performed using Hall probe. The water-cooled plasma chamber is designed and fabricated. For three- electrode ion source the plasma chamber is made of SS 304L and a water jacket is provided for cooling. For five-electrode ion source the plasma chamber is made from OFHC copper and the cooling circuit is provided by cavity on the outer walls. The vacuum system of the ion source is designed to with stand a base pressure of 10^{-7} mbar and with gas load to maintain a differential pressure of 10^{-3} mbar in plasma chamber and 10^{-5} mbar in extractor region. The gas dosing system is designed to allow controlled working gas in the plasma chamber using precision leak valve and shut off valve that is floated at 50 kV and the gas reservoir and gas regulator that is at ground potential and isolated using polypropylene tube. The LCW system is designed to provide the cooling de-mineralized water to various subsystems of the ion source with the required flow rates. The beam extractor system is designed to provide total beam current of 50 mA at beam energy 50 keV. The beam extraction system is optimized via electrode apertures, electrode gaps and electrode shapes to minimize beam size and divergence. The three and five electrode extraction is designed and fabricated for ion extraction. In three electrode ion source the electrodes are made of SS304L and for five electrodes from

OFHC copper. The three and five electrode ion source are assembled in the test stand and vacuum tested. The high voltage test is performed under vacuum. Further tests and characterization are carried out with three electrode ion source only.

Chapter 5. Plasma characterization of ECR proton ion Source

In this chapter the discussion about ECR plasma generation, stabilization and characterization is presented. The three electrode ion source is put on the test stand. All the subsystems i.e., microwave generator and transmission components, solenoid coils and power supplies, vacuum pumps and gauges and gas injection system are connected. Plasma discharge is initiated by first evacuating the plasma and extractor chamber to a base pressure 10^{-7} mbar. The hydrogen gas is introduced in the plasma chamber and maintained at pressure ~10^{-3} mbar. The magnetic field profile of 875 G at the entrance and exit of plasma chamber is established by energizing two solenoid coils. Microwave at 2.45 GHz and 400-1100 W power is fed in the plasma chamber. The discharge is stabilized by minimizing the reflected microwave power using four stub auto tuner and magnetic field. The reflected microwave power is found to be 1 to 2 % of forward microwave power for the pressure range studied. Plasma characterization is performed once the discharge is stabilized. An automated Langmuir probe and associated circuits are developed in housed to characterize ECR plasma. The current – voltage (I – V) characteristics of the probe are taken by sweeping the voltage on the probe from – 115 V to + 53 V. These data are recorded on the digital storage oscilloscope (DSO) and are transferred to the personal computer. The probe is inserted radially into the plasma so that the probe tip is located at the center of the plasma and at different radius to the outer edge of the plasma.

The pulsed plasma characterization is performed by operating the magnetron in a pulsed mode. The magnetron is operated at frequency of 2.45 GHz with 400 - 1000 W output power for μs to ms pulse duration and 1% to 99 % duty cycle.

The characterization results of ECR plasma ion source are also presented. These results include measurements of ion density, electron temperature, plasma potential and electron energy distribution function. The measured value of plasma parameters are in the range, ion density: 5.6 x 10^{10} cm^{-3} to 3.8 x 10^{11} cm^{-3}, electron temperature: 4 eV- 14 eV and plasma potential: 20 V - 45 V. The following studies are performed on ECR plasma: 1) Dependence of reflected microwave power on forward microwave power for different neutral gas pressures, 2) Dependence of plasma electron density, plasma electron temperature and plasma potential on neutral gas pressure 3) Dependence of plasma electron density, plasma electron temperature and plasma potential on microwave power, and 4) Dependence of plasma electron density, plasma electron temperature and plasma potential on microwave power.

Chapter 6. Beam characterization of ECR Proton ion source

This chapter discusses about the ion beam extraction and characterization. A low energy beam transport line is designed and developed for ion beam characterization. For ion beam extraction two high voltage power supplies are used first 0 to +60 kV for plasma electrode and second 0 to -6 kV for suppressor electrode. The plasma chamber is floated at extractor voltage. The solenoid coils are isolated from extractor voltage and kept at ground potential using Perspex insulator. The microwave section is also isolated from extractor voltage and kept at ground potential using DC waveguide break. The total ion beam current measured using an electron suppressed Faraday cup developed in our laboratory. The total ion beam current of 42 mA (all species) is extracted at beam energy of 40 keV. But the long time operation of the ion source is hampered by (i) damage of microwave quartz window by bombardment of back streaming electrons and (ii) rise in cooling water temperature. These two problems are resolved by relocating the microwave window from the line of sight of back streaming electrons and by increasing the chill water flow in the heat exchanger. The ion beam is extracted when the plasma is stabilized and by applying bias of +10 to +50 kV on plasma electrode and -2 to -4 kV on suppressor electrode. The ion beam current is found stable for several hours of source operation. The following studies are performed when the beam is stable: 1) Dependence of beam current on extraction voltage 2) Dependence of beam current on microwave power and 3) Dependence of beam current on residual gas pressure.

The ion source is operated in a pulsed mode by generating pulsed plasma and extracting the ion beam. The magnetron is operated in a pulsed mode by the internal pulse generator or by external pulse from function generator. The pulse repetition rate is varied from 1 Hz, 10 Hz and 100 Hz to cw. The ion beam current is not stable for pulse duration below 1 ms.

A low energy beam transport line (LEBT) is designed and developed for measuring two important beam parameters i.e., beam emittance and proton fraction. The purpose of LEBT is to transport and focus the ion beam from ion source to the next accelerating structure. The low energy beam transport line consists of two solenoid magnets and power supplies, two x-y steering magnets and power supplies, an analyzing magnet and power supply, turbo-molecular pump and controller, dry roughing pump, vacuum gauge heads and controllers and beam diagnostics i.e., emittance meter, Direct Current Transformer, Alternative Current Transformer, CCD cameras and Faraday cups. The emittance meter and Faraday cups are designed and developed in our laboratory. The beam optics of the transport line is studied using standard software.

For measuring transverse beam emittance, an Emittance Measurement Unit (EMU) is designed and developed in housed. It consists of two slits and a Faraday cup. The slits are separated by distance 300 mm. Both the slits are made of tantalum 0.2 mm wide aperture and 80 mm length and installed on a water-cooled copper block. The second slit is having a Faraday cup attached to it. The movements of the slits are remotely controlled using stepper motors and controllers. The positions of the slits are recorded using linear encoders. The Faraday cup current on the second slit is recorded on a current meter.

The ion beam emittance is measured at three locations (i) at the ion source end after beam extraction, (ii) after focusing the beam using one solenoid magnet. In this case before emittance measurement, the focusing of the hydrogen ion beam consisting of H^+, H_2^+ and H_3^+ is studied by simulation and in experiment by measuring the beam profile, and (iii) after focusing and separating H^+ using a solenoid magnet and an analyzing magnet. In these three cases variation of beam emittance with microwave power is studied. The value of beam rms normalized emittance ε_n measured for the above three cases falls is in range (i) 0.07-0.19 π mm-mrad (ii) 0.15-0.25 π mm-mrad and (iii) 0.02-0.11π mm-mrad respectively.

After ion beam emittance measurement, the proton fraction in the hydrogen ion beam is measured. The proton fraction of the beam is measured by varying the magnetic field of the analyzing magnet and recording the current signal on Faraday cup. A 0.2 mm width slit is incorporated in front of the Faraday cup for spatial resolution of three species H^+, H_2^+ and H_3^+. The proton fraction measured is > 90%. The variation of proton fraction with microwave power and residual gas pressure is studied.

Chapter 7. Control and Automation of ECR proton ion source

In this chapter remote control and operation of the ion source is described. For reliable, stable and long-time operations of the ion source it is mandatory to monitor the forward and the reflected microwave power, vacuum pressure, solenoid coil power supply status, high voltage power supply status and the beam parameters. The control system of the ion source is a computer based control system where all the power supplies are operated remotely from computer. Graphic user interface (GUI) of the ion source is developed in LABVIEW. The control and automation of the ion source is developed in housed.

Chapter 8. Conclusions

The conclusions from the results of the systematic investigations that are carried out during the course of this thesis work are given in this chapter along with the scope for the future work.

List of Figures

List of Tables

CHAPTER 1

Introduction

The particle accelerator development started from the four-inch cyclotron built by E. Lawrence in Berkeley, California in the 1930s to the present day CERN's twenty-seven kilometer-circumference Large Hadron Collider (LHC) that has resulted discoveries in nuclear and particle physics and more investigations are underway in the field of neutron and photon sciences. Future energy production methods such as inertial and magnetic confinement fusion and accelerator driven system for fission, rely heavily on accelerator technology. Also in industrial and medical field i.e. semiconductor device manufacturing, hadron therapy cancer treatment and medical isotope production are based on ion accelerators. Currently, there are tens of thousands particle accelerators operating with ions in the world and in every case, the first and the most critical part of the accelerator system, is the ion source.

The high current ion sources find special applications in energy research. They can be employed to characterize the structure of the atoms or the molecular structure of the materials. It is possible to use them as probes X-rays and neutrons. Neutron beam can be produced through fission in nuclear reactors, or by spallation processes induced by accelerated proton beams, (a CW proton beam of a few tens of MW) produce a neutron flux that is able to sustain subcritical nuclear reactors. The same principle can be used for incineration of nuclear wastes (actinides and long lived fission fragments) produced by conventional critical reactors leaving no substantial amounts of radiotoxic waste at the end of the cycle. The concept has more recently been referred to as an Accelerator Driven System (ADS).

India being a developing country there is always demand for increasing energy production to sustain growth. This energy need can be fulfilled by utilizing nuclear power. Due to limited reserve of uranium, the large scale growth of nuclear power can be realized by efficient utilization of thorium as nuclear fuel and that has been a long term goal of Indian Nuclear Programme. Three stage programme for gradual switch over from Uranium to Plutonium-fueled fast breeders and finally to thorium fuel system has been in place. Since 2003, India initiated a program to pursue a roadmap on physics studies and stage wise technology development for ADS. Under this programme, activities related to the reactor concept and design, spallation target system and technology for high power proton accelerator have progressed. The most challenging aspect of the ADS is the development of high power accelerator that can produce a CW proton beam (> 30 mA) of energy ~ 1 GeV. It is required that the proton accelerator be reliable, rugged and stable in order to provide uninterrupted beam power to the spallation target, over long period of time. The most critical component of the high power proton accelerator is the high current proton ion source.

Bhabha Atomic Research Centre (BARC), Mumbai has initiated a Research & Development program to study various aspects of the ADS [1, 2]. The required 1 GeV proton beam will be produced by linear accelerator (linac) in three different phases viz, 20 MeV, 100 MeV and 1 GeV. The first phase is the 20 MeV accelerator that is named as Low Energy High Intensity Proton Accelerator (LEHIPA) where proton beam will be generated by 50 keV Electron Cyclotron Resonance (ECR) ion source that is accelerated further by 3 MeV Radio Frequency Quadrupole (RFQ) and 20 MeV Drift Tube Linac (DTL) [3 - 5]. Accelerator and Pulse Power Division (APPD), BARC is involved in the design, development and characterization of ECR proton ion source for LEHIPA. The 50 keV ion source has been designed, fabricated, installed and commissioned for LEHIPA accelerator at the basement of Common Facility Building (CFB) in BARC.

There are different types of ion sources. The variation in these sources arises from the ways in which the ions are generated from solid, liquid and gases and also the variation due to the generating plasma such as DC discharge, arc discharge, RF discharge, microwave discharge and laser driven discharge.

The ion sources consist of plasma generating system, ion extraction systems, electronic units that are used to generate plasma and supply extraction voltages. There are also devices used for guiding the ion beam.

The high current electron cyclotron resonance ion sources are the best among the ion sources available to feed ions for high energy and high power accelerators. The plasma is excited by microwaves (typically 2.45 GHz) that are coupled to the cylindrical chamber working as resonant cavity, where the plasma is produced, by a suitable system of waveguides, and are absorbed therein during the interaction with gases or vapors at low pressure ($\sim 10^{-3} – 10^{-5}$ mbar). In the presence of magnetostatic field, the electromagnetic wave absorption is particularly efficient at the so called 'Electron Cyclotron Resonance'. From the high density and low temperature plasma ($n_e \sim 10^{10} – 10^{12}$ cm^{-3}, $T_e \sim 1$ - 20 eV) part of the ion content is extracted, which constitutes the ion beam to be sent to the accelerators. Most of the parameters of the extracted beam, such as beam current, the emittance and the shape in the real space depend in a decisive way on the characteristics of the plasma from which the beam is extracted.

Two major advantages of an ECR ion source over conventional ion sources are large beam intensities and excellent reliability over long periods of operation. The reliability of these sources arises from the absence of cathode or plasma arcs in the ion source.

Realizing the vast potential of high-intensity proton accelerators for ADS and other equally important applications, a programme has been evolved for stage-wise development of systems and technologies in India [1]. The accelerator for ADS is required to deliver proton beam up to several tens of MW power and operate in CW mode with high current beams. This is based on proton linear accelerator development in the first stage. The programme of the accelerator development is shown in Figure 1.1 and consists of high current proton ion source at beam energy of 50 keV is accelerated to 3 MeV by Radio Frequency Quadrupole Linac (RFQ) to 40 MeV by Drift Tube Linac (DTL) and to 100 MeV by Couple Cavity Linac (CCDTL) and finally to 1 GeV by elliptical Super Conducting (SC) Cavity. The whole scheme is divided into three distinct technology modules involving: (i) a low energy, high intensity proton accelerator (LEHIPA) up to 20 MeV that is being built at BARC as the front end injector to the linac for

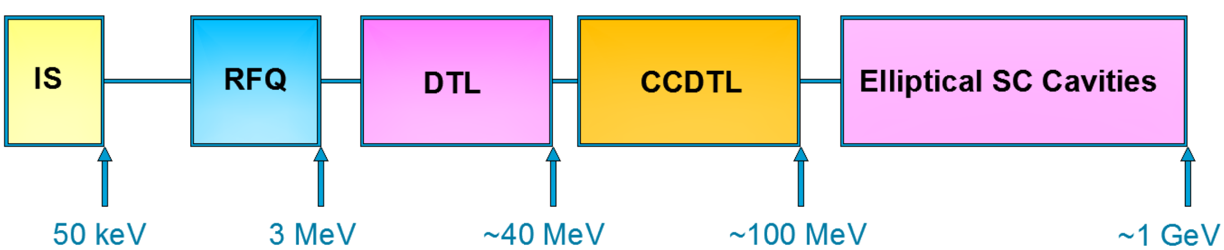

Figure 1.1 *Schematic layout of 1GeV linac [1].*

ADS, (ii) an intermediate energy linac up to 100 MeV; most likely superconducting cavities for savings operating energy costs, (iii) high energy, superconducting type linac for 100 to 1000 MeV section.

The front end injector of ADS accelerator is LEHIPA as shown in Figure 1.2 [2].

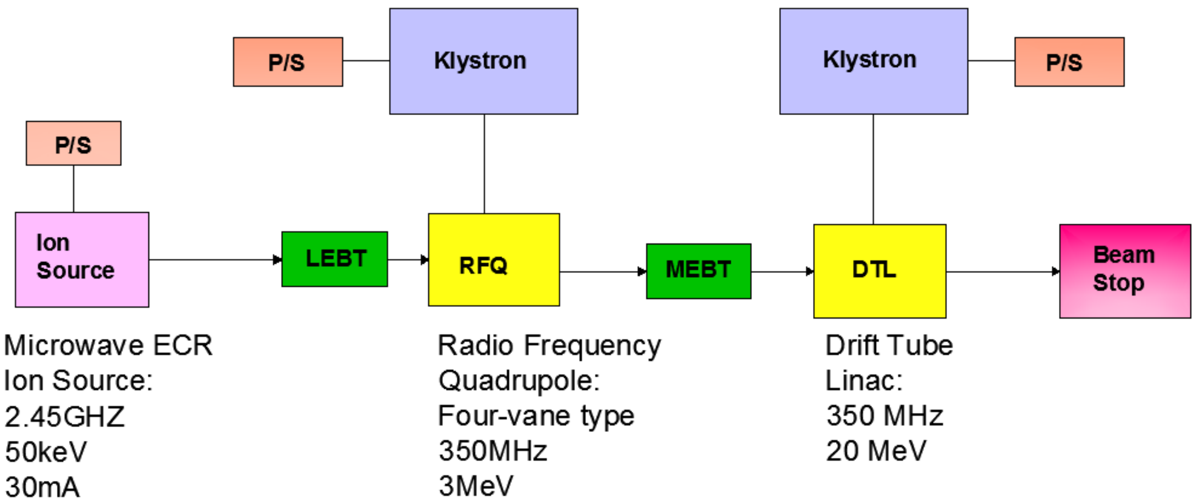

Figure 1.2 *Schematic layout of LEHIPA [2]*.

The major components of LEHIPA are 50 keV ECR ion source [3], a 3 MeV radio frequency quadrupole (RFQ) [4] and a 20 MeV drift tube linac (DTL) [5]. The Low Energy Beam Transport (LEBT) and Medium Energy Beam Transport (MEBT) line will match the beam from the ion source to RFQ and from RFQ to DTL respectively.

The ion source of LEHIPA is an ECR ion source that can deliver the required 30 mA of proton beam at 50 keV. A low energy beam transport (LEBT) line is used to match the transport of this beam into RFQ. The matching is done using two solenoids. The 4-vane CW RFQ operating at 352.21 MHz will accelerate the beam from 50 keV to 3 MeV. The RFQ is designed for a constant vane voltage of 76.7 kV. The transmission at the end of the RFQ is 3.52 m and the total power requirement is 385 kW which includes 88.5 kW of beam power.

The 3 MeV beam from the RFQ is then matched in to the DTL using a matching line (MEBT), which consists of four quadrupoles for transverse matching and two RF buncher for longitudinal matching. The beam from the RFQ is accelerated to 40 MeV using a 352.21 MHz DTL. A Focusing Defocussing (FFDD) lattice is used in the DTL for transverse focusing. The total length of DTL is 28 m and the RF power required is 3 MW. The axial electric field is kept constant at 2.5 MV/m in all DTL tanks.

1.1 Scope of the present thesis

The scope of the present thesis is to design, develop and characterized the high current ECR proton ion source to meet the requirement of LEHIPA. The source is not available commercially with the required beam parameters. As the ion source is the critical component of LEHIPA, our effort is towards in house development of the ion source that can produce stable beam and operate reliably for long durations in CW and pulsed mode. The components of the ion source are to be designed, fabricated, assembled and tested on the ion source test bench. The high current ECR ion source is characterized in terms of plasma parameters and beam parameters. The major aspects that are investigated as regard to this source are:

- Magnetic field: The detailed design of the coils to meet the necessary magnetic field distribution for the correct operation of ECR ion source.

- Microwave system: To generate 2.45 GHz, 2 kW microwave and transport it to plasma chamber for ECR plasma production.

- Gas injection system: To inject working gas in the plasma chamber at specified flow rate.

- Vacuum system: Design and installation of vacuum system for obtaining ultimate vacuum pressure of 10^{-7} mbar in the ion source. With gas load the vacuum pressure to be maintained is ~10^{-3} mbar in plasma chamber and ~10^{-5} mbar extractor chamber.

- Beam extraction: The simulation, optimization and design of the electrode system that will serve as the beam extraction component to accomplished the expected beam specifications.

- High voltage: The correct electrical isolation of the different subsystems in the assembly for proper function of the ion source.

- Cooling: Design and installation of low conductivity process water system to take out the heat dissipated in the ion source components during normal operation of the ECR ion source.

- Plasma characterization: Measurement of plasma parameters to understand the main physics principles that determined the behavior of the plasma and its dependence on some critical parameters in the ion source. Development of automatic Langmuir probe to measure the plasma parameters.

- Beam characterization: Design and development of low energy beam transport line (LEBT) to measure important beam parameters i.e., beam current, emittance and proton fraction and its dependence on some critical parameters. Design and development of beam line magnets and high current beam diagnostics to measure these parameters.

Apart from all the complex scientific procedures needed to be studied, analyzed and properly designed; it is also necessary to provide the mechanical design of all the parts and assemblies that will allow all these subsystems to be put together and properly function.

1.2 Thesis Organization

The thesis is organized in the following manner. Chapter I provide a brief introduction of high power proton accelerator and high current ion source. Chapter II discusses about plasma physics applied to the ion sources, waves in plasma and ECR plasma production mechanism. Chapter III describes ion beam formation, ion beam quality and the literature survey on High Power Proton Accelerators (HPPA) and high current ion sources. Chapter IV discusses the design, construction, assembly and testing of ECR proton ion source developed for LEHIPA. Chapter V discusses about the ECR plasma characterization using automated Langmuir probe and its dependence on some critical parameters. Chapter VI gives the details regarding the design and development of Low Energy Beam Transport Line (LEBT), design and fabrication of beam line magnets, design and fabrication of beam line diagnostics and characterization of proton beam in terms of beam current, emittance, and proton fraction and its dependence on some critical parameters. Chapter VII discusses about the control and automation of ECR ion source. Important conclusion and scope of future work on ECR ion sources is given in chapter VIII.

CHAPTER 2

Plasma Physics applied to ECR ion sources

The plasma is generated in all ion sources so the plasma physics plays a very important role in designing the ion sources. The plasma is defined as a quasineutral gas of charge and neutral particles which exhibit collective behavior.

Quasineutrality is the term used to imply that the density of the positive charges is approximately equal to that of the negative charges. Since both type charges coexist in the plasma, columbic forces exist between the particles. Elements of force exerted on particle will affect not only the intermediate particles in the immediate field but other particle further away. This is the condition of collective behavior, where motion depends not only on the local region but also on the regions further away.

In this chapter, some aspect of plasma directly linked with ECR ion sources is treated in some details. More details are available in standard textbooks [6-10].

2.1 Basic Plasma Parameters

The plasma parameters are attributes, which allow a specific discharge to be characterized and compared with other discharges. The most important plasma parameters, which define the discharge state in ECR ion source are electron and ion density n_e and n_i, and for quasi-neutral plasma $n_e \approx n_i$ (measured in cm^{-3}or m^{-3}), the temperature T of each species (usually measured in eV, where 1 eV = 11,600 ^{0}K) and the steady state static magnetic field B (measured in Tesla). All the main characteristics of the plasma and the extracted ion beam depend on these parameters. Several other parameters can be derived from these parameters e.g., Debye length λ_D, Larmor radius r_L, plasma frequency ω_p, cyclotron frequency ω_c, and thermal velocities of electrons v_e and ions v_i.

2.1.1 Debye length

A fundamental characteristic of the behavior of plasma is its ability to shield out electric potentials that are applied to it. When a charged conductor is placed inside plasma, it exerts an attractive or repulsive force depending on the type of charge on the conductor. The oppositely charged particles generate a region around the conductor, preventing the conductor field penetrating the quasi-neutral plasma. This shielding is known as Debye shielding and is the distance over which the free charges redistribute themselves to screen out the electric field of the charged conductor defined as:

$$\lambda_D = [\varepsilon_0 kT_e/e^2 n_e]^{1/2} \tag{2.1}$$

From the above Eq. (2.1) it can be seen that as the density is increased, λ_D decreases. As kT_e increases, then λ_D also increases. The electrons being lighter than ions are more mobile and it is the electrons that generally do the shielding by moving to create a surplus or deficit of negative charge. The plasma condition demands that the number of charged particles within the Debye sphere must be substantially greater than one i.e. $N_D >> 1$. Also, to perverse the quasi-neutrality property of the plasma, the plasma size must be much greater than the Debye sphere $L >> \lambda_D$.

2.1.2 Plasma Frequency

If plasma is perturbed, the separation of positive ions and electrons will generate an electric field, E. This electric field will give rise to restoring force which works at returning the particles to their equilibrium position. When the electron reaches its original position it has a finite velocity and continues past its position. The frequency of this oscillation is known as electron-plasma frequency and is defined as:

$$\omega_p = (n_e e^2/\varepsilon_0 m_e)^{1/2} \tag{2.2}$$

Substituting ion density and mass, generates a similar equation for ion-plasma frequency. As the ion mass is much greater than electron mass, the electron-plasma frequency is greater than the ion-plasma frequency for the particular plasma.

2.1.3 Cyclotron frequency

The frequencies with which ions and electrons gyrate around the magnetic field lines is known as cyclotron frequency or gyro-frequency and is given as

$$\omega_c = qB/m = 28\ B\ \text{(GHz)} \tag{2.3}$$

The radius of circular orbit with which the particle gyrate around the magnetic field B is known as cyclotron radius or gyro radius and given as

$$\rho = m\mathrm{v}_\perp/(eZB) \tag{2.4}$$

where $\mathrm{v}_\perp$ is the perpendicular velocity in circular motion.

2.2 Collisions in Plasmas

The collisions are of primary importance to determine the ionization rates in ion sources. They also regulate the electron and ions lifetime inside magnetically confined plasmas. The number and nature of the collisions is mainly determined by the electron temperature, the electron density and the background pressure of neutrals. Hence, ion source performance is determined by the number of collisions per unit time.

Collisions of charged particles can be divided into two categories: collision with neutral particles and collisions with other charge particles. From the ratio of these collision types, collisional plasmas are divided into two types: (1) fully ionized plasmas, where the charge-charge collisions dominate and (2) weakly ionized plasmas, where charge-neutral collisions are dominant. Because of the long range of the coulomb interaction the charge-charge collision tends to dominate when the ionization degree is only few percent. Above this limit the plasma is considered to be highly ionized or fully ionized, even though the ionization degree is often not 100%.

2.2.1 Fully ionized plasmas

The collisions in highly ionized plasmas differ from the weakly ionized case. The small-angle deflections happening at relatively long distances are so much more frequent than the large-angle collisions that the cumulative effect of such deflections turns out to be more significant than the effect of the fewer large-angle interactions.

The long range coulomb collision or Spitzer collisions [6] play an important role in ECR plasmas to determine the energy exchange processes. In this case, the thermalization via collisions is much easier among the electrons than among electrons and ions. In addition, as the ion life time in ECR ion source is shorter than the time required for the ion heating the collisions, the ions remains cold, whereas the electrons increase their energy because of the external electromagnetic field. This result is of primary importance for the ECR ion source, as one of the important quality parameters, the emittance, increases with ion temperature.

2.2.2 Weakly ionized plasmas

In weakly ionized plasmas most of the interactions are direct neutral-neutral collisions and direct charge-neutral collisions. The interactions may be elastic, in which the total kinetic energy of the particle is conserved and the processes drive the particles towards thermodynamic equilibrium. On the other, if the kinetic energy of the particles is high enough, the interaction may be inelastic leading to excitation and ionization of particles.

The binary collisions play a main role in plasma ionization. If the electron energy is not enough (it must overcome the ionizing potential), the effect of collision becomes the excitation of the atom. Hence there are two main inelastic ionization processes: a) total ionization from ground state b) total excitation from ground state.

The electron-neutral elastic and inelastic collisions play an important role in the case of high pressure plasmas with a low degree of ionization and low electron temperature ($T_e \leq 15$ eV). In microwave discharge plasmas the electron temperature is usually ~ 10 eV, but nevertheless the atom can be easily ionized because of the tail electron component, whose energy is high enough to provide effective ionizing collisions. The cross-sections for H_2^+ and H^+ are comparable when the atomic H^+ ion is formed from electron impact on the atomic H neutral, but this event requires the prior dissociation of neutral H_2 to neutral atomic species. The high atomic ion fraction is the characteristic of ECR plasma.

2.3 Drift effects in magnetized plasmas

The motion of charged particles in magnetized plasma can be affected by internal or external forces. Such forces can be superimposed from outside or self-generated from inside the plasma.

Their effect is to modify the original cyclotron motion of the particle, adding a drifting component to the velocity.

As in ECR ion source, ions are unmagnetized, so they cannot be affected by drift motions, depending on the interaction between the Lorentz force and the effective magnetic field. However if the ion lifetime is long enough to allow momentum transfer among ions and electrons, the drifting electrons can accelerate ions via *e-i* collisions. In many practical cases, the force generating the electron drift is due to the action of uniform or a non-uniform electric field on plasma electrons.

a) Drift generated by uniform electric field:

The drift velocity $\mathbf{v}_d$ in uniform electric field is given as [6]

$$\mathbf{v}_d = \boldsymbol{E} \times \boldsymbol{B}/B^2 \tag{2.5}$$

The drift velocity $\mathbf{v}_d$ is independent of q, m and $\mathbf{v}_\perp$ and both ions and electrons are drifted in the same direction with the same drift velocity whose magnitude is $|\mathrm{v}_d| = E / B$.

a) Drift generated by non-uniform electric field:

The drift velocity $\mathbf{v}_d$ in non-uniform electric field is given as [6]:

$$\mathbf{v}_d = \boldsymbol{E} \times \boldsymbol{B}/ B^2 + (1/4)\, r_L^2\, k^2\, (\boldsymbol{E} \times \boldsymbol{B}/ \mathrm{B}^2) \pm (1/\omega_c B)\, d\boldsymbol{E}/dt \tag{2.6}$$

where the self-generated electric fields vary both in space and time as $\boldsymbol{E} = \boldsymbol{E_0}\, e^{i(\boldsymbol{k}\cdot\boldsymbol{r}-\omega t)}$. The sign $\pm$ stands for sign of the particle charge. The first term of equation (2.6) corresponds to drift velocity in case of electric field. The second term is called the *finite-Larmor-radius effect*. Since r_L is much larger for ions than for electrons, $\mathbf{v}_d$ is no longer independent of species. However the effects due to this term are important only for relatively large k (small wavelength) or small scale length of inhomogeneity. The third term is called the polarization drift and it also depends on the charge state of the particle. It is directed along the direction of the electric field and it tends to separate ions from electrons.

2.4 Plasma diffusion in magnetic field

The plasma diffusivity plays a very important role because it strongly influences the lifetime, the charge state distribution and hence the performance of the ion source. This implies that the knowledge of the particle loss mechanisms in plasmas may play a fundamental role for the enhancement of the performance of such devices.

The ECR ion sources are characterized by strong magnetic fields (0.1 T) hence it is important to study the effects of magnetic fields on the diffusion mechanisms. The plasma particles in a magnetic field are forced to move along their gyration orbits and in absence of collisions, they cannot diffuse across magnetic field. Only by means of collision the particle can move to a different force line. The Lorentz force does not act along the magnetic field, therefore, along z, the diffusion mechanism occurs as in the case of unmagnetised plasmas. In presence of magnetic field, the diffusion is no longer isotropic, but it is necessary to distinguish the diffusion along and across the magnetic field, characterized respectively by the diffusion coefficient $D_{\parallel}$ and $D_{\perp}$.

In high current ECR ion sources, the ions are unmagnetized because of strong collisionality, while electrons can be considered collisionless or quasi-collisionless. This means that in these devices ion diffuse isotropically and only the electron diffusion is affected by the external magnetic field. The effect of strong magnetic field is indeed to reduce the coefficient of diffusion for electrons to value [6]:

$$D_{\perp} = D/(1 + \omega_c^2 \tau^2) \tag{2.7}$$

where ω and τ are respectively the cyclotron frequency and the mean time between collisions. In the limit $\omega_c^2\tau^2>>1$ we have:

$$D_\perp = kT\nu/m\omega_c^2 \tag{2.8}$$

In Eq. (2.8), the diffusion perpendicular to ***B***, $D_\perp$ is proportional to ν, since collisions are needed for cross field migration. On the contrary, the ions, being unmagnetized, diffuse faster. It might be supposed that, in such a case, an ambipolar diffusion would arise, in order to reduce the ion losses and accelerate electron diffusion across ***B***.

2.5 Plasma confinement

The plasma in the ion source is contained by magnetic field. In order to confine particle in bounded volume, the magnetic field must be curved and inhomogeneous. The particles are confined as Lorentz forces act on them and forced them to move in circular and helical orbit around the magnetic field lines.

The high current proton source, the object of this thesis, produces low charge ion beams, so it does not require a magnetic trap by mirror and multi-pole field that confines the electrons for times higher than 10^{-5} s. The presence of external magnetic field is for not aimed to the production of high-energy electron and multi-charge ions, so simple magnetic field configuration provided by two solenoid coils with coinciding axes, separated by finite distance from each other is used for plasma confinement. The function of the magnetic field is to make anisotropic plasma where the electromagnetic wave can transfer their energy to electrons.

2.6 Waves in plasmas

The study of wave propagation in plasma is an important topic to understand the properties of ion sources. The ECR plasmas are in fact generated and sustained by means of the interaction with electromagnetic (E.M.) waves. Plasma waves are associated with the time and space varying electric field, and the propagation properties of such fields are determined by the dielectric properties of the medium, which in turn depends on applied magneto-static or electro-static fields. Plasma may be inhomogeneous and anisotropic, and this affects its dielectric properties. The anisotropy can be easily introduced by the application of magneto-static field. ECR plasmas, for example, are anisotropic medium by the point of view of electromagnetic wave propagation and in this plasma the electromagnetic wave can couple to electrostatic wave by mode conversion.

2.6.1 Propagation of E.M. waves in plasmas

The wave propagation in plasma takes into account how the wave interacts with different plasma particles. If the thermal velocity of particle is low with respect to wave's phase velocity, i.e. $v_{th} << v_{\phi}$, then v_{th} can be neglected. This approximation is called "cold plasma approximation", is equivalent to set $T_e = T_i = 0$. Waves that depend on finite temperature effect, such as ion acoustic waves or Bernstein waves cannot be deduced by this treatment. Accordingly, for waves with very small phase velocities, warm plasma approximation must be used. The E.M. wave propagate in the plasma with phase velocity of $10^7 – 10^8$ *m/s*, values much higher than the particles thermal velocity $10^3 – 10^5$ *m/s*, except for the restricted regions where the waves exhibit resonances; therefore the cold plasma model is a useful approximation to determine the dispersion relation of the E.M. wave in magnetized plasma. The magnetic force due to the influence of the magnetic field of the wave is [11]:

$$F_m = (\mathrm{v}/c)\,(\varepsilon_r)^{1/2}\,qE \tag{2.9}$$

Thus, for particle velocity v << c the magnetic field of the wave can be neglected. This approximation is totally valid for high current ECR ion sources. The operative frequency of high current ECR ion sources is 2.45 GHz, so at high frequency, the ions are insensitive to electric field because of their high inertia, and their contribution in wave propagation can be neglected.

2.6.2 E.M. waves in cold un-magnetized plasma

In the absence of magnetic field, the plasma is an isotropic medium. The dielectric constant is given as [11]:

$$\varepsilon = \varepsilon_0\,(1 - \omega_p^2/\omega^2) \tag{2.10}$$

where ω_p is the plasma frequency and represents the natural oscillation frequency of an electron in a plasma. The plasma frequency is defined as:

$$\omega_p = (ne^2/\varepsilon_0 m_e)^{1/2} \tag{2.11}$$

As ε is defined positive, it follows that:

$$(1 - \omega_p^2/\omega^2) \geq 0, \text{ or } \omega^2 > \omega_p^2 \tag{2.12}$$

This means that the electromagnetic waves with frequency lower than ω_p cannot propagate into the plasma. As a consequence inhomogeneous and non-magnetized plasmas the density cannot exceed the so called cutoff density given as:

$$n_{cutoff} = 4\pi^2 (m\varepsilon_0/e^2)\, f_p^2 \tag{2.13}$$

An overdense (i.e. above cutoff) plasma would totally reflect the incoming (feeding) wave. The cutoff density is consequently the main limitation of the plasmas generated by means of E.M.

waves. Plasmas having a density larger than the cut-off density, i.e. $n_e > n_{cutoff}$, are usually named overdense. When this condition is not satisfied, i.e. $n_e < n_{cutoff}$, the plasma is named underdense. The dispersion relation for waves in un-magnetized plasma is [8].

$$\omega^2 - \omega_p^2 = k^2c^2 \tag{2.14}$$

For the dispersion relation $\boldsymbol{k}$ is imaginary whenever $\omega < \omega_p$, implying total reflection of incident wave, as it has been deduced from Eq. (2.10). In this case assuming propagation along x axis, the electric field in overdense region varies as:

$$\boldsymbol{E} = \boldsymbol{E_0}\, e^{i(\boldsymbol{k}\cdot\boldsymbol{r}-\omega t)} = \boldsymbol{E_0}\, e^{i(kx-\omega t)} = e^{x/\delta}\, e^{-i\omega t} \tag{2.15}$$

representing an evanescent oscillation whose amplitude in the medium decays exponentially with a characteristic distance δ called skin depth:

$$\delta = c\,/(\omega^2 - \omega_p^2)^{1/2} \tag{2.16}$$

Except for values close to ω_p, the penetration depth δ is of the order of 1 cm, i.e. small compared to most ECR plasmas.

2.6.3 E.M. waves in cold magnetized plasma

In the presence of magneto-static field, the plasma will become anisotropic medium for the electromagnetic wave propagation. The dielectric constant will transform in a tensor, as the field propagation will depend on the direction of propagation of the wave with respect to the external magnetic field. The dispersion relation of E.M. wave in magnetized plasma is given as [12, 13]:

$$(S\,sin^2\theta + Pcos^2\theta)\, N^4 + (RL\,sin^2\theta + SP\,(1 + cos^2\theta))\, N^2 + PRL = 0 \tag{2.17}$$

Where $R = S + D$ and $L = S - D$, $S = 1 - (\omega_p^2/\omega^2) / (1 - \omega_c)$, $D = - \omega_p^2\omega_c/ [(\omega^2\omega)(1 - \omega_c)]$ and $P = 1 - \omega_p^2/\omega^2$. Eq. (2.17) contains all the information about the propagation of the waves in magnetized plasma. It has two solutions:

$$N_{o,x}^2(\theta) = 1 - [2X(1-X)/(2(1-X) - Y^2\sin^2\theta \pm (Y^4\sin^4\theta + 4Y^2(1-X)^2\cos^2\theta)^{1/2}] \qquad (2.18)$$

Hence for a given arbitrary direction of propagation, defined by θ, we have two waves characterized by different index of refraction, $N_o(\theta)$ and $N_x(\theta)$ called ordinary wave and extraordinary wave. Here, we have introduced two important parameters, X and Y, given as:

$$X = \omega_p^2/\omega^2 \propto n_e, \; Y = \omega_c/\omega \propto B_0 \qquad (2.19)$$

where X is the parametric electron density, proportional to n_e, whereas Y is the parametric magnetic field, proportional to B_0.

By means of Eq. (2.19) it is possible to determine the wave's propagation properties as a function of angle θ, of the electron density n_e and magnetic field B_0. The wave can propagate in a medium only if $N > 0$. In general there are four different cases: a) $N > 0$, the propagation region, the wave propagates in the medium with phase velocity c / N, b) $N < 0$, stop band region, the wave cannot propagate, c) $N = 0$, cutoff, the wave is reflected, d) $N \rightarrow \infty$, resonance, the wave is absorbed by the medium.

According to Eq. (2.19), cutoff can be found by setting $N = 0$. So they occur only when $PRL = 0$, i.e. when:

$$P = 0 \text{ or } R = 0 \text{ or } L = 0 \qquad (2.20)$$

It is important to note that the condition (2.20) does not depend on θ i.e. the cutoff is independent on the angle of propagation θ. From (2.20) we get three cutoffs of E.M. waves in magnetized plasmas expressed as: 1) $P = 0 \rightarrow \omega = \omega_p$ or $X = 1$: as in unmagnetized plasmas, $\omega = \omega_p$ is a cutoff condition also for magnetized plasmas. This cutoff is known as *O cutoff*; 2) $R = 0 \rightarrow \omega = \omega_R = (1/2)[(\omega_c^2 + 4\omega_p^2)^{1/2} + \omega_c]$ or $Y = 1 - X$; this cutoff frequency is known as upper cutoff frequency or *R cutoff*, occurring at frequency above ω_p and ω_c; 3) $L = 0 \rightarrow \omega = \omega_L = (1/2)[(\omega_c^2$

$+ 4\omega_p^2)^{1/2}$ - ω_c] or $Y = X - 1$; this cutoff frequency is known as lower cutoff frequency or *L cutoff*, placed below ω_p.

Ordinary waves are reflected when $\omega_{RF} = \omega_p$ i.e. at *O* cutoff. Extraordinary waves are unaffected by this cutoff and at *R* and *L* cutoffs (they are not reflected at *O* cutoff). Resonances can be found by imposing the condition $N \rightarrow \infty$ in Eq. (2.17) that gives:

$$S\, sin^4\theta + P\, cos^2\theta = 0 \rightarrow tan^2\theta_r = - P/S \tag{2.21}$$

The resonance angle θ_r can be written as a function of the plasma parameters as follows:

$$cos^2\theta_r = (X + Y^2 - 1)/XY^2 \tag{2.22}$$

If the electron density and the applied magnetic field are almost constant, the resonance can occur only on the surface of the cone, named resonance cone, whose axis is aligned to the external magnetic field $B_0\hat{\boldsymbol{z}}$ and aperture angle θ_r. This cone corresponds to conical surface in real space.

The condition of establishing the resonances, thus depend on the direction of wave propagation. For the special case $\theta = 0^0$ the resonance takes place at each value of X when $Y = 1$, i.e. $\omega = \omega_{RF} = \omega_c$. In this case the microwave frequency is equal to the Larmor frequency; hence the wave is in resonance with the cyclotron motion of the electrons. This resonance is of primary importance for ECR ion sources and takes the name *Electron Cyclotron Resonance*. In plasma physics, the extraordinary wave propagating with $\theta = 0$ is named as R wave.

For the special angle $\theta = 90^0$ the resonance occurs when $X + Y^2 - 1 = 0$ i.e.:

$$\omega_{RF} = \omega_{UHR} = (\omega_c^2 + \omega_p^2)^{1/2} \tag{2.23}$$

This resonance is known as Upper Hybrid Resonance (UHR), and the wave propagating exactly across $\boldsymbol{B_0}$ ($\theta = 90^0$) is named X wave. When $\omega_{RF} = \omega_{UHR}$ the energy of the microwave can be transferred to the plasma wave.

It is useful to study the polarization of the waves in magnetized plasma. The relation between E_x and E_y that is polarization in the plane perpendicular to $\boldsymbol{B_0}$ is given as:

$$iE_x/E_y = (N^2 - S)/D \tag{2.24}$$

From this relation it follows that the waves are linearly polarized at resonance ($N^2 = \infty \rightarrow E_y = 0$) and circularly polarized at cutoff ($N^2 = 0$, $R = 0$ or $L = 0 \rightarrow E_x \pm E_y = 0$). Furthermore, following [8], it comes out that the ordinary waves are left-hand polarized whereas extraordinary waves are right hand polarized. Because of their polarization, electric field of the R wave rotates in the same direction as the gyrating electrons in a magnetic field.

2.7 ECR plasma production and heating

To create and sustain ECR plasma, microwaves at a specific frequency are injected into a region containing magnetic field. If the frequency of microwave matches the electron cyclotron frequency at that magnetic flux density, high power absorption is achieved as the microwaves accelerates the electrons, causing them to spiral around the magnetic field lines at higher velocities and larger radii. This usually occurs in a small region where the exact resonance condition is met, and it is termed as an ECR layer. Electrons receiving energy in this layer eventually drift downstream and proceed to collide with ions, neutral particles and other electrons.

The motion of charged particles under the influence of both electric and magnetic field is given as:

$$\frac{d}{dt} m_e \mathbf{v} = e\,(\mathbf{E} + \mathbf{v} \times \boldsymbol{B}) - m_e \mathbf{v}\, v_n \tag{2.25}$$

where $\mathbf{v}$ is the velocity of electron, m_e and e are the charge and mass of the electron. $\boldsymbol{E}$ and $\boldsymbol{B}$ are the external electric and magnetic field and v_n is the electron-neutral collision frequency.

The external electric field from the injected microwaves is given as:

$$\boldsymbol{E} = \boldsymbol{E_0}\, e^{i\omega t} \tag{2.26}$$

If the magnetic field has magnitude B and is in z direction of an x-y-z Cartesian coordinate system, the equations of motion in the x and y directions for the electron are:

$$(v_n + i\omega)\, m_e \mathrm{v}_{x,y} = e(E + \mathrm{v}_{x,y} B) \tag{2.27}$$

The electron velocity is related to current density through

$$\boldsymbol{J} = e\, n_e \mathbf{v} \tag{2.28}$$

where n_e is the electron density. Equations (2.26) and (2.27) and the Ohm's law,

$$\boldsymbol{J} = \overleftrightarrow{\sigma}\boldsymbol{.}\, \boldsymbol{E} \tag{2.29}$$

can be combined to solve for σ, the conductivity tensor. Since the oscillating electric field only pumps energy into the electron's gyration perpendicular to the magnetic field, the most interesting part of the conductivity tensor is [14]:

$$\sigma_\perp = (n_e e^2/m_e)\,[(\, v_n + i\omega\, /((\, v_n + i\omega)^2 + \omega_c^{\,2})] \tag{2.30}$$

where $\omega_c = eB/m_e$ is the electron cyclotron frequency, and ω is the frequency of the electric field. Since the power absorbed is equal to

$$\boldsymbol{P}_{abs} = Re\,(\boldsymbol{E}\boldsymbol{.}\, \overleftrightarrow{\sigma}\boldsymbol{.}\, \boldsymbol{E}), \tag{2.31}$$

then from Eqs. (2.30) and (2.31), the absorbed microwave power is given as [7, 14]:

$$P_{abs} = (4\pi n_e e^2 v_n/2m_e)\,[\{1/(\, v_n^{\,2} + (\omega - \omega_c^{\,2})\} + \{1/(\, v_n^{\,2} + (\omega + \omega_c)^2\}]\, |E|^2 \tag{2.32}$$

If the collision frequency is reasonably small, resonant power absorption is achieved at the microwave frequency of $\omega = \omega_c$. The electrons see a constant field leading to resonant energy absorption and therefore will become extremely energetic in the region where the microwave frequency and the magnetic field match the resonance condition and known as *ECR heating*.

The ECR ion source has cylindrically symmetric magnetic field, pointing along the cylindrical axis. This is achieved with circular electromagnets, whose position can be varied relative to each other to create any magnetic field profile. Resonant power absorption occurs where the magnetic field makes the electron cyclotron frequency match the microwave frequency. This generally happens somewhere along the cylindrical axis in a short region of space. In this region there is a visible brightening of the plasma in a very thin layer, known as the ECR layer. Electrons in the ECR layer are accelerated by the microwave's electric field to extremely high velocities and large Larmor radii. In the first quarter cycle, while the electric field is increasing the electron will accelerate perpendicular to the magnetic field and in the next quarter cycle, the electric field decreases and the electrons continue to accelerate, but not as much as in the first quarter half cycle. In the ECR condition, the electron will be accelerated in correct phases will be accelerated through the entire wave cycle; electrons with wrong phases will decelerate. The decelerating electron will travel on an inward spiral until it slows to a stop, then accelerate in phase with the electric field. The accelerating electron continues to travel in an ever increasing spiral around the magnetic field line until it collide with the chamber wall, another electron, an ion, or a neutral particle, or it moves out of the ECR layer. The maximum energy the electron obtains in ECR plasma is therefore dependent on the collision frequency, or ultimately the operating pressure of the system. This continuous acceleration of energetic electrons may result in an electron energy distribution which is unusually non-Maxwellian. However, outside the ECR layer, multiple elastic collisions with neutrals, ions, or other electrons spread out the electron velocities in a more evenly distributed manner.

The microwave discharge based ECR ion source was first developed at the beginning of 1990 for the production of high current proton beams and light ions [15]. Their principle characteristic is the absence of multipole and mirror field for plasma confinement. The magnetic field is about flat within the plasma chamber. The shape of the magnetic field is designed in such a way that the injected microwave matched ECR conditions at the injection and extraction points. In the central region of the plasma chamber the field is about flat and off-resonance, i.e. $B > B_{ECR}$ [15]. The magnetic field is designed to a low value in the extraction region, in order to decrease beam emittance, which is proportional to the field at extraction.

Most of the high current ion sources operate at 2.45 GHz, with off-resonance magnetic field of 0.1 T in the center of the plasma chamber. Several measurement carried out during last decades (and reported also in this thesis) demonstrate that slightly overdense plasmas can be generated in these sources [16], which are not expected by standard theory of E. M. absorption. In particular, Sakudo [17] demonstrated that the higher plasma density is obtainable when $B_{ECR} < B < 1.3B_{ECR.}$

Different theories have been proposed [8, 18-20] to explain the plasma ignition and microwave power absorption in high current ion sources. Many authors affirm that resonances between the electromagnetic waves and the plasma electrons can occur in off-resonance magnetic field and in high densities condition. The ordinary wave can couple to the electrostatic oscillation modes, in particular the lower branch of Trivelpiece-Gould (T-G) modes, which can propagate in overdense plasmas. However, such regions needs to be reached by tunneling of the ordinary wave beyond the O cutoff, before they can be absorbed by electrostatic T. G. waves which only in second moment, could transfer the oscillation energy to the medium by means of collision or non-linear interaction of wave-electron, generating a low temperature high density plasma.

Chapter 3.

Ion beam formation and transport and review of literature on ion sources

In this chapter the ion beam emittance and brightness, ion beam extraction from plasma and ion beam transport is presented. A literature survey of high power proton accelerator and high current ion sources are presented.

3.1 Ion beam extraction from plasma

The purpose of the extraction system is to produce a beam from the plasma generator and deliver to the next acceleration stage. The extraction process consists of applying a high voltage between ion emitting surface and extractor electrode with aperture on it. The potential difference between the electrodes is usually called the extraction (acceleration) voltage, and the space between the extraction electrodes is the acceleration gap. The energy of the extracted beam is defined by the potential difference between the plasma electrode and the ground electrode. For positive ion source, the plasma electrode is kept at high positive potential and the last extraction electrode at ground potential.

The trajectories of the extracted ions determine the initial beam properties and quality and are influence by several factors. These are 1) applied electric and magnetic field strength, 2) the shape of the emitting surface, and 3) the space charge density of the ion beam. In the case of plasma sources, the emitting surface is known as meniscus. The shape of the meniscus depends on the electrical field distribution due to the applied boundary conditions and the local densities of plasma ions, electrons, and the accelerated ions.

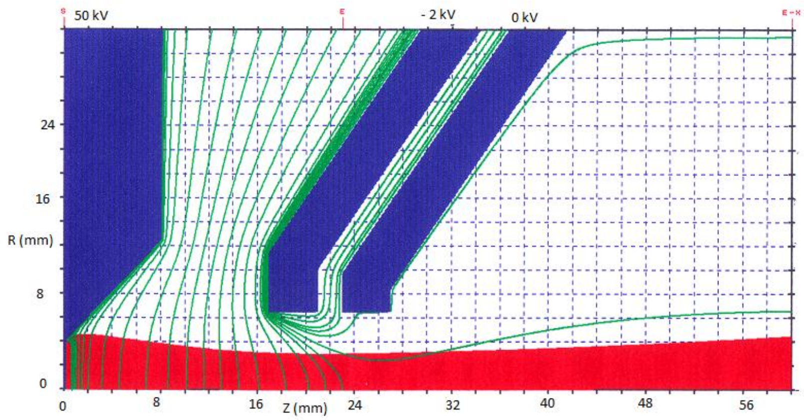

(a)

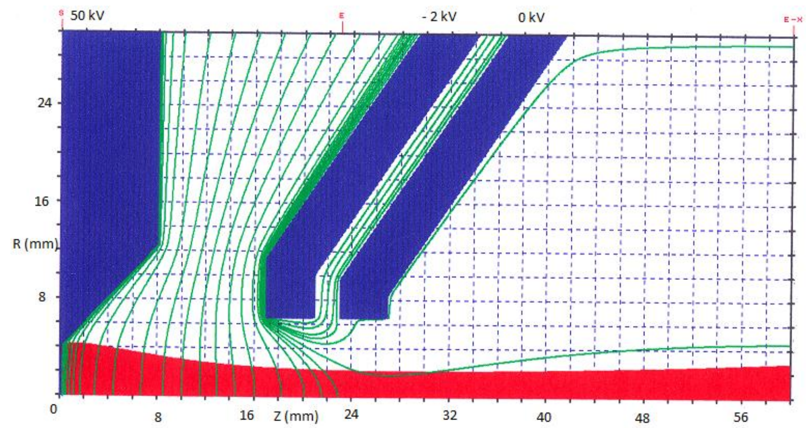

(b)

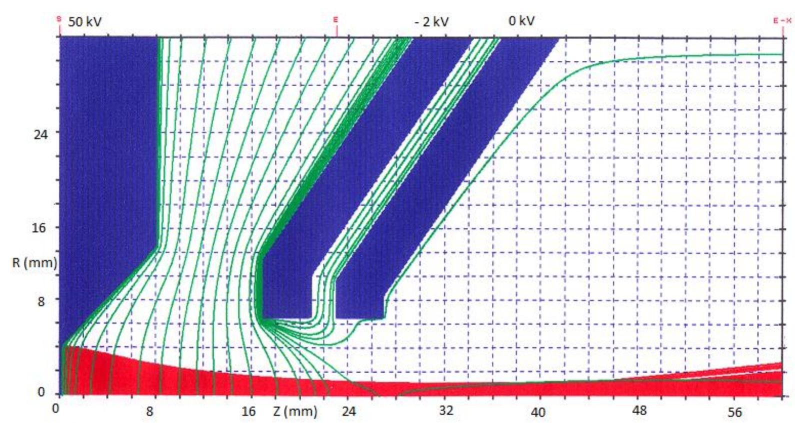

(c)

Figure 3.1 *Three cases of ion extraction from plasma sources (a) over dense plasma (b) medium density plasma (c) underdense plasma.*

The meniscus acts as the boundary layer between the discharge plasma and the accelerated beam particles. The depth and position of this layer or the shape of the meniscus, is strongly affected by the balance of plasma density, ion and electron temperatures and the electric field in the acceleration gap. Increasing the plasma density and temperature pushes the plasma sheath outward from the plasma, resulting in convex shape of the plasma meniscus. As a result, the extracted beam become diverging (Figure 3.1 (a)). When the density and temperature are lowered, or the electric field is increased, the meniscus become flat, producing almost parallel beam (Figure 3.1 (b)) and if density and temperature are reduce further, or the electric field is increased further meniscus become concave producing converging beam (Figure 3.1 (c)).

The maximum beam current that can be extracted from plasma is mainly limited by two factors: the ion production limit and the space charge limit. The ion production limit is govern by the balance of creation of ions due to ionization and losses due to diffusion, recombination etc. For a plasma source the total extracted ion beam current is given by:

$$I = j\, S_0 \qquad (3.1)$$

Where

$$j \approx 8.9 \times 10^{-14} \sum n_j \, (Z_j \, T_e / A_j)^{1/2} \ \ (\mathrm{A/\ cm^2}) \qquad (3.2)$$

where S_0 is the area of the ion emission surface; n_j (cm^{-3}), A_j and Z_j are the density, mass, mass number and charge number of the j-th kind of ions in the plasma, and T_e (eV) is the electron temperature.

The space charge limit arises from the charge of the extracted ions in the vicinity of plasma and depends on the absolute current value and the size of the emitting area, that is, on the current density. The maximum current density that can be extracted by an electric field is obtained under space charge limited conditions and follows the Child-Langmuir law [21, 22]:

$$j = 1.72\times10^{-3}\,(Z/A)^{1/2}\,U^{3/2}/d^{2} \qquad (\mathrm{A/cm^2}) \qquad (3.3)$$

Where j is the current density, Z is the ion charge state, A is the ion mass (amu), U is the extraction voltage in kV, and d is the gap width in cm.

The Eq. (3.3) shows that the space charge limited current increases with extraction voltage. When the voltage is low, the space charge is the limiting factor defining the maximum beam current, and when voltage increases the current become limited by the ion production in ECR plasma. The Eq. (3.3) is derived under the assumption that ion emitter and first electrode are in parallel configuration and the emitted ions have no initial velocity. These assumptions rarely holds for real ion source extraction systems, but the above equation can provides a practical approximation for space charge limiting current.

Equation (3.3) gives rise to two important parameters defined as: the perveance P of an ion gun,

$$P = I\,(Z/A)^{1/2}/\,U^{3/2} \qquad (3.4)$$

and the normalized, or proton equivalent, current I_n,

$$I_n = I\,(A/Z)^{1/2} \qquad (3.5)$$

The beam after extraction passes through the beam line where residual gas particles are present. The beam particle ionizes the residual gas particles present in the beam line and can generate a sufficient number of secondary electrons. These secondary electrons should be prevented from being accelerated back into the source by the extraction field. This shielding is achieved by acceleration/deceleration or three-electrode extraction system where a suppressor electrode is introduced into the main extraction gap and biased to a sufficiently negative potential to form an electron trap.

For beams extracted from ion sources, a useful estimation of the emittance is given as [23]:

$$\varepsilon_n^{rms\text{-}norm} = 0.016\, r\, (kT_i / M_i)^{1/2} + 0.032\, r^2 (ZB_0/A) \qquad [\pi \text{ mm mrad}] \tag{3.6}$$

where r is the radius of the extraction hole (mm), T_i is the ion temperature (eV), B_0 is the axial magnetic field at extraction (T), and A and Z are respectively the ion mass in *amu* and charge state of ion beam. Equation (3.6) shows that ion beam emittance depends on two parameters, the ion beam transverse temperature and the axial magnetic field on the extraction region. For the high current ECR ion source described in this thesis, the ion temperature is generally very low, because the time needed for ion heating is smaller than the ion confinement time. The presence of axial magnetic field at extraction, on the other hand, can induce beam rotation. In most high current ion sources, the thermal term of Eq. (3.6) is much smaller than the magnetic part and can be neglected. To reduce beam emittance, the magnetic system is built in such a way to reduce significantly the stray field in the extraction area.

The design of extraction system for practical ion sources is now done invariably with computer codes. There are various computer codes used for designing the ion sources e.g.;

PBGUN [24] and IGUN [25] for extractor system, POSSION [26], OPERA [27], ANSIS [28] and CST [29] for electric, magnetic fields and for microwave components, and TRANSPORT [30], TRACE [26] and GPT [31] for beam transport.

3.2 ECR ion source beam quality

The ion sources are compared by maximum ion current it produces. But more important than maximum ion current is what fraction of this current is transported and accelerated or the beam quality. The quality of beam extracted from an ECR ion source is characterized by beam emittance and brightness. These quantities are frequently used to determine the beam focusing properties and the parallelism of the beam particle trajectories and compatibility with beam transport and optical system. For good quality ion beam the emittance should be as small as possible and brightness as high as possible. The beam emittance [32] is a direct consequence of Liouville's theorem that states that the motion of a group of particles, under the action of conservative force field, is such that the local number density in six-dimensional phase volume (x,y,z,p_x,p_y,p_z) remains constant everywhere. Smaller volume means smaller emittance and good quality beam.

For paraxial beam $p_z >> p_x$, p_y, the approximate representation of the beam in trace space (x,x') and (y,y') is sufficiently accurate, where

$$x' = \tan^{-1}(p_x/p_z) \approx p_x/p_z \text{ and } y' = \tan^{-1}(p_x/p_z) \approx p_x/p_z \tag{3.7}$$

Therefore the transverse beam emittance in four-dimensional phase space is defined as:

$$\varepsilon_x = (1/\pi) \iint dx\, dx', \quad \varepsilon_y = (1/\pi) \iint dy\, dy' \tag{3.8}$$

The common unit of emittance is πmm-mrad.

For axial symmetric beam,

$$\varepsilon_x = \varepsilon_y = \varepsilon_r = (1/\pi) \iint dr\, dr' \qquad (3.9)$$

The phase diagram is an upright ellipse for a beam at waist, so

$$\varepsilon_r = r_{max}\, r'_{max} \qquad (3.10)$$

i.e. the emittance is then denoted by the product of the beam radius and semi-angle.

The emittance in trace space (Eq. (3.8)) is called the absolute emittance. Its value will decrease with an increase of beam energy, because *dx/dz, dy/dz* decreases. Thus a normalized emittance is defined as follows:

$$\varepsilon_{nr} = (\beta\gamma/\pi) \iint dr\, dr' \qquad (3.11)$$

ε_{nr} remains roughly constant throughout the accelerator.

The emittance is a measure of the quality of the geometry of the beam. A complete measure of the beam quality should include the beam current, I_i. The beam brightness, B, is defined as the mean current density in the transverse phase space for a given particle energy, i.e.

$$B = 2I_i / \pi^2 \varepsilon_r^2 \text{ and } B_n = 2I_i / \pi^2 \varepsilon_{nr}^2 \qquad (3.12)$$

The brightness is an invariant quantity for a beam transport system without loss or creation of particle. Its unit is mA/ (mm-mrad).

The phase pattern or emittance plot of a paraxial beam through any aberration-free field is usually an ellipse as shown in Figure 3.2. The acceptance (or admittance) of a beam line is defined as the largest beam emittance that the beam line can accommodate without loss, and is generally a multifaceted polygon. Several different approaches exist to determine the value of emittance from the area occupied by the beam particle in phase space [9, 33].

In the first approach the emittance value is determined directly from Eq. (3.8). This is sometimes called *area emittance*. The main shortcoming of this method is the evaluation of beam emittance value with strong distortion in phase space as in Figure 3.3 (a) and how it affects beam transport. A strongly distorted phase ellipse of the beam (due to aberrations of the ion optical system, an irregular ion-emitting-surface in the plasma source, the non-linear space charge field, as well as coupling between the transverse components of motion) may have small total area but it is not possible to transport the beam because it cannot be matched with the acceptance of the beam transport system.

In the second approach, the distorted pattern is enclosed in an ellipse of larger area sometimes called *effective emittance* as shown in Figure 3.3 (b). With the distortion in the phase space pattern, the size of the ellipse is to be enlarged, giving a better estimation of emittance value. Therefore to transmit the total beam through the beam line, the acceptance of the beam line is to be increased to the value of the effective emittance. The main drawback of this method is the overestimation of emittance value in the case where the distorted pattern has very low particle density or beam halos on the outer periphery. In such cases the emittance is normally given for a fraction of a beam, and generally 90% is taken. The emittance changes rapidly with the fraction of the enclosed beam and therefore it is important to characterize emittances with the percentage level of the included beam fraction (Figure 3.4).

These two cases mentioned above considered only the area occupied by the particle in phase space; they do not consider the variations in particle density. As a result they fail to differentiate certain parts in phase space with high particle density that is more relevant than the region with very low particle density and thus very small contribution to beam current. This aspect is taken into consideration in statistical approach to determine emittance, which has gain acceptance to accelerator community. The rms emittance is defined as second moment (variance) of particles $f(x,x')$ which form the ion beam, is defined as [34, 35]:

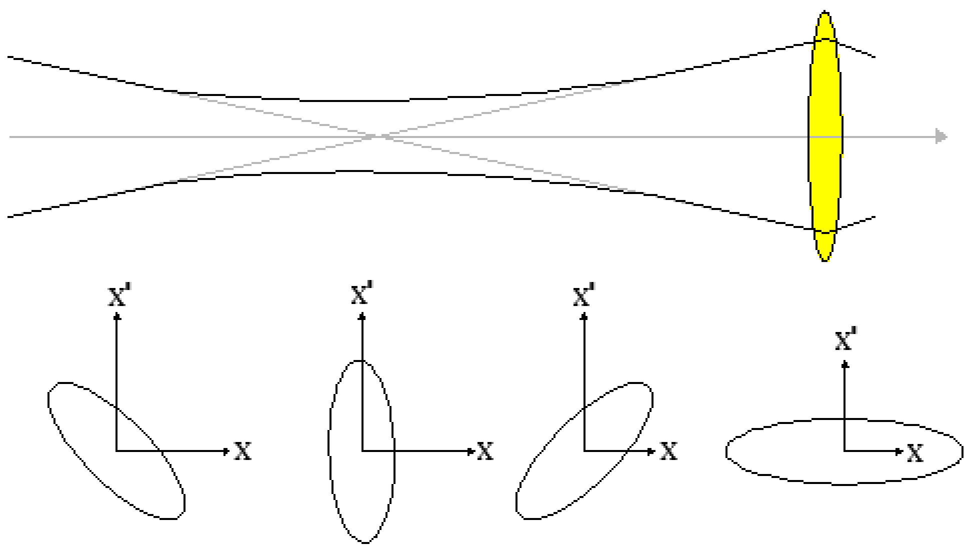

Figure 3.2 *The orientation of emittance ellipse in the case of (a) converging (b) focused (c) diverging and (d) parallel ion beam.*

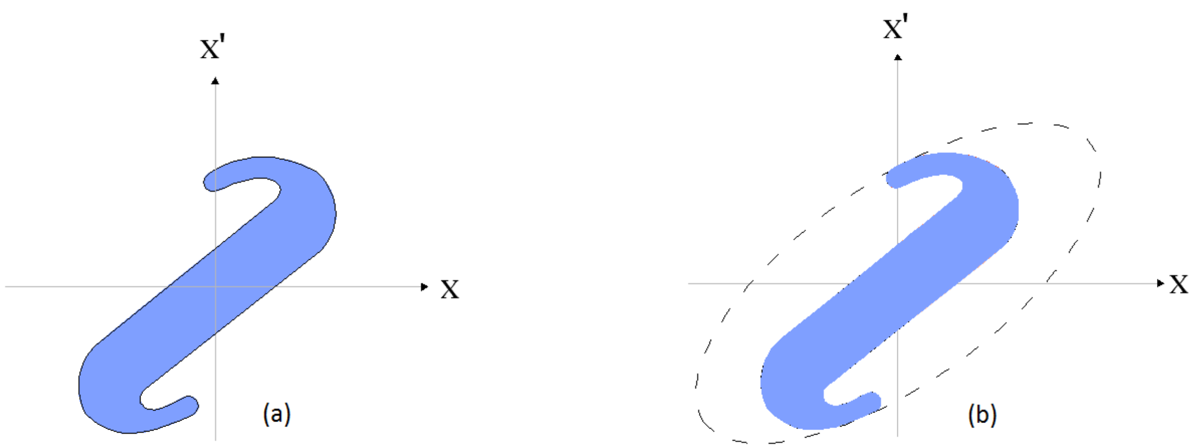

Figure 3.3 *(a) The distorted phase ellipse and (b) distorted phase ellipse enclosed in an ellipse of larger area.*

$$\varepsilon_x = \left(\langle x^2\rangle \langle x'^2\rangle - \langle x\,x'\rangle^2\right)^{1/2} \tag{3.13}$$

with

$$\langle x^2\rangle = \sum x^2 f(x,x') / \sum f(x,x'),$$

$$\langle x'^2\rangle = \sum x'^2 f(x,x') / \sum f(x,x'),$$

$$\langle xx'\rangle = \sum xx' f(x,x') / \sum f(x,x')$$

Where x is the transverse location, x' is the angular particle momentum and $f(x,x')$ is the intensity distribution in phase space at location x with an angular momentum x'.

The Eq. (3.13) is the semi axis product of the ellipse. For a Gaussian distribution, the ellipse contains 39% of the beam. A 4-rms or 6-rms emittance is frequently used which is 98% and 99.8%, respectively of the beam for a Gaussian distribution.

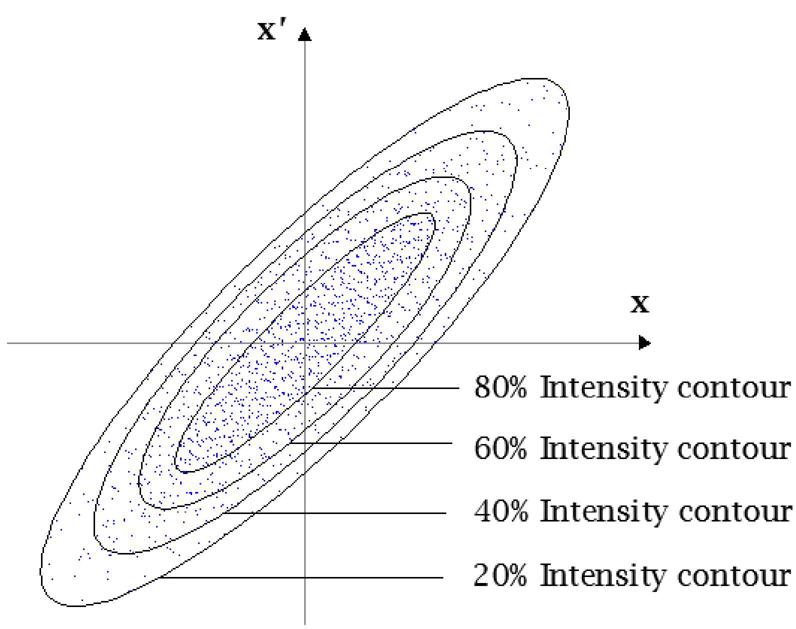

Figure 3.4 *Transverse emittance diagram showing the contours of equal intensity.*

The emittance ellipse transforms as the beam passes through the beam line. The knowledge of the area occupied by particles in phase space at the beginning of a beam transport line will allow us to determine the location and distribution of the beam at any other place along the beam transport line without calculating the trajectories of each individual particle. All particles of a beam in phase space are surrounded by an ellipse called phase ellipse in Figure 3.5 described by [36]:

$$\gamma x^2 + \alpha x x' + \beta x'^{\,2} = \varepsilon \tag{3.14}$$

where α, β, γ and ε are the ellipse parameters known as *Twiss parameters*. When the beam is transmitted through different ion optical components the ellipse rotates (Figure 3.1) in phase space and the Twiss parameters determine the shape and orientation of the ellipse. The dimensionless parameter α, relates the x, x' correlation, and it is negative for diverging beams, zero in beam waists or antinodes, and positive for converging beams. The parameter β is by definition positive

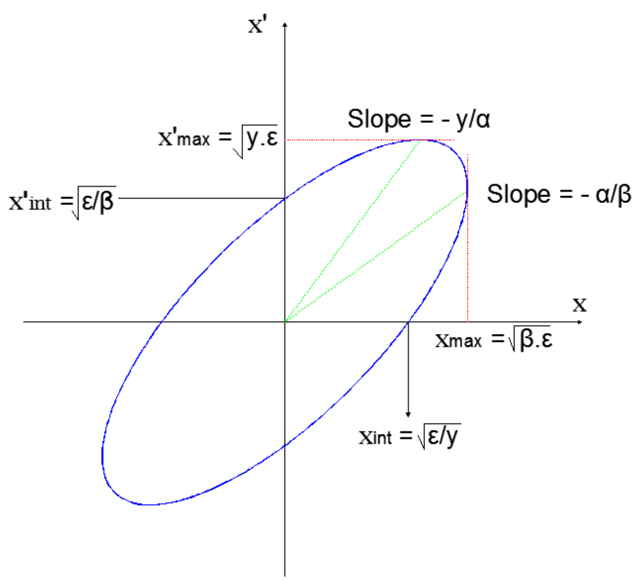

Figure 3.5 *Phase space ellipse.*

($\beta > 0$) and it is measured as length per unit angle (m/rad). The parameter γ is also positive, measured in angle per length (rad/m) and dependent on α and β:

$$\gamma = (1+\alpha^2)/\beta > 0 \tag{3.15}$$

When the beam drifts through a field free space, the Twiss parameter γ remains constant and related to maximum divergence x'_{max}:

$$x'_{max} = \sqrt{\gamma\varepsilon} \tag{3.16}$$

The Twiss parameter β however, changes because the related maximum radius x_{max} changes throughout a drift region:

$$x_{max} = \sqrt{\beta\varepsilon} \tag{3.17}$$

3.3 Low energy beam transport line ion optical elements

The ion optical elements of the beam transport line are of two categories: magnetic and electric. In case of high energy beams, where $v \approx c$, magnetic elements are used because the force due to magnetic field of 1 T equals the force due to electric field of 300 MV/m, that is difficult to produce in practical devices. In low energy beam transport line (LEBT) systems, where the beam velocity is low and the maximum electric fields are typically about 5 MV/m, the forces due to electric and magnetic field are comparable and the choice is decided by such as size, cost, and power consumption. An important factor in the selection of the beam line elements is based on fact that the electrostatic fields do not separate ion species. In electrostatic systems the particles follow trajectories defined only by the system voltages. On the other hand, in magnetic systems the particle trajectory is dependent on charge-to-momentum ratio q/p, which allows separation of particle species from each other. The common beam line elements that are used in LEBT systems are: einzel lens, solenoid, dipole and quadruple lenses. The beam line elements that are used in LEBT for ion beam characterization are described briefly.

3.3.1 Solenoid lens

Solenoid lens provides axisymmetric focusing force. It consists of rotationally symmetric coils placed around the beam tube, creating a longitudinal magnetic field peaking at the center of the solenoid. The focusing action of the solenoid is described as follows assuming a thin lens: The radial magnetic field at the entrance of the solenoid gives the particle entering the field with $v_r = 0$ at radius r_0 an azimuthal thrust

$$v_\theta = qBr/2m, \tag{3.18}$$

which makes the trajectories helical inside the solenoid. At the exit of the solenoid the particle receives a thrust cancelling the azimuthal velocity, but leaving the particle with a radial velocity

$$v_r = -\,(r_0 q^2/4m^2 v_z) \int B^2\, dz \tag{3.19}$$

This radial velocity causes the beam to converge towards the optical axis. The focal length f of the lens for particle kinetic energy E_k is given by [9]

$$1/f = (q^2/8mE_k) \int B^2 dz \tag{3.20}$$

3.3.2 Magnetic dipoles

The magnetic dipole is primarily used to deflect charged particle beams. The magnetic diploe is constructed from coil windings creating a constant magnetic field pointing in transverse direction. The particles in the magnetic field follow circular trajectories with radius

$$\rho = p/qB \approx m\mathrm{v}_z/qB = 1/B\,(2mV_0/q)^{1/2} \tag{3.21}$$

where V_0 is the voltage used to accelerate the particles from zero to v_z.

The dipole elements also have focusing /defocussing properties. For example, the magnetic dipole with straight edge angles ($\alpha = \beta = 0$) focuses the beam in the bending plane (x) as shown in Figure 3.6 (a). In this case the center of curvature of the optical axis and the two focal points

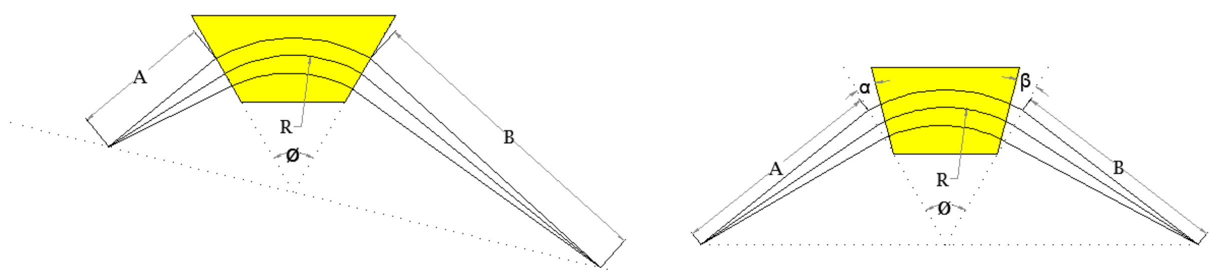

Figure 3.6 *Focusing of a magnetic dipole in bending plane (a) α = β =* 0 *(b) α and β positive.*

are on a straight line. For a symmetric setup in Figure 3.6 (b), it means that $A = B = R/\tan(\phi/2)$. There is no focusing action in y direction. If the magnet straight angles ϕ deviate from 90^0, the focusing power in x-direction can be adjusted. If the edge angle is made positive, there is weaker focusing in x-direction. If the angle is negative, there is stronger focusing in x-direction. Changing the edge angle has also an important effect on the y- direction. Overall it means that the focusing in x- direction can be adjusted for y- focusing. The focal length from the edge focusing is given by

$$f_y = R/\tan(\alpha) \tag{3.22}$$

In a symmetric double focusing dipole, with the same focal length in x and y, the angles and distances are given by:

$$2\tan(\alpha) = 2\tan(\beta) = \tan(\phi/2) \tag{3.23}$$

$$A = B = 2R/\tan(\phi/2) \tag{3.24}$$

For a $\phi = 90^0$ bending magnet edge angles become $\alpha = \beta = 26.6^0$ and the focal distances $A = B = 2R$.

For small-angle deflection typically xy steering magnets are used. This kind of system is typically used for small corrections in the beam line when the beam deviates from its defined trajectories. The xy steering magnets are typically two pairs of windings in a single frame for corrections in both transverse directions. The beam deflection is given by:

$$\theta = LB\,(q/2mV_0)^{1/2} \tag{3.25}$$

where L is the field length and B is the field strength inside the device.

3.4 Space charge effects

Ion beam is a collection of charged particles which are in collective motion. In high current ion beam, the individual particle motion is influenced by the rest of the beam through self-fields, which are generated by the beam charge and current. The electric Coulomb repulsion between the beam particles results into radial force on the individual particles, which is directed outwards from the center of the beam. The beam current exerts force on the particles through the azimuthal magnetic field it produces. This force is radially towards the center of the beam and its magnitude increases with the beam velocity. The combined radial forces is always outwards, and the beam space charge introduces defocussing effect on the beam, which increases the beam divergence and consequently the beam transverse size or beam emittance [37]. This collective effect, which is proportional to beam current, is sometimes called the space charge blow up [38].

The combined radial force exerted by the self-fields to a beam particle with charge q at radius r is given by Lorentz law, which gives

$$F_r(r) = F_r^E + F_r^B = q(E_r - \mathrm{v}B_\theta) = (qIr/2\pi\varepsilon_0 \mathrm{v} a^2)\,(1 - \beta^2) \qquad (3.26)$$

where $\beta = \mathrm{v}/c$. As the above equation shows, the space charge force of a uniform cylindrical beam is linear and defocussing in the transverse directions. Also, it is seen that when the beam velocity is increased, the force decreases and finally disappears at $\mathrm{v} = c$. In the low energy beam transport $\mathrm{v} << c$, the contribution of magnetic force is insignificant. For example for H^+ accelerated with 50 kV the ratio of magnetic to electric force is ~ 10^{-4}.

The beam potential Φ for a beam of radius a passing through grounded beam pipe of radius R is given as [39]:

$$\Phi(r) = (I/4\pi\varepsilon_0 \mathrm{v})\,(1 + 2\ln(R/a) - r^2/a^2) \quad \text{for } r < a \qquad (3.27)$$

$$\Phi(r) = (I/2\pi\varepsilon_0 \mathrm{v})\ln(R/r) \quad \text{for } r \geq a \qquad (3.28)$$

Here, the assumption of uniform density distribution may not be realistic for real ion beams extracted from ECR ion sources, the above expressions can be used to make rough approximations of the space charge effects. As an example, for an hydrogen beam extracted from ECR ion source with 50 kV extraction voltage, the total beam potential at the center of the beam, varies between 60 to 1800 V when the total extracted current is between 1 to 30 mA.

A more realistic description of the space charge related forces can be made using a Gaussian charge density distribution

$$n(r) = (I/2\pi \mathrm{v}\sigma^2)\, exp(-r^2/2\sigma^2) \tag{3.29}$$

where σ is standard deviation. This distribution yields radial force which can be described as [40]:

$$F_r(r) = (qI/2\pi\varepsilon_0 \mathrm{v}r)\,(1 - \beta^2)\,(1 - exp(-r^2/2\sigma^2)) \tag{3.30}$$

Unlike in the case of uniform charge density, the defocussing space charge force of a beam with a more realistic Gaussian distribution is nonlinear. This nonlinear force is a source of emittance growth.

If charge of opposite sign is introduced into the volume occupied by ion beam, the effective charge density of the beam decreases, reducing the space charge forces on the beam. This process is called the *space charge compensation* (SSC), and it occurs naturally when the ion beam passes through the residual gas present in the beam transport system. Interaction of the ion beam with the residual gas leads to inelastic collisions between the ions and the neutral particles, resulting in ionization and charge exchange processes. The ionization processes form slow positive ions and electrons inside or near the volume occupied by the ion beam. In case of positive ion beam, the ions are expelled from the beam due to the positive beam potential, whereas those electrons which do not have enough energy to escape are trapped by the beam.

This processes leads to accumulation of negative charge into the ion beam, resulting in formation of beam plasma with effective charge density that can be considerably lower than the charge density of the beam. It has been shown experimentally that with residual gas pressures of ~ 2×10^{-5} mbar the beam potential reduced to less than 5% of its initial values [41 - 43].

3.5 Literature survey on High Power Proton Accelerator (HPPA) and High Current Proton Ion Sources

The most important goal in the development of high power proton accelerators (HPPA) is their application in the safe and efficient production of electronuclear energies as suggested by Carlo Rubbia of CERN [44, 45]. The accelerator reactor complex known as Accelerator Driven System (ADS) where the reactor works in the sub-critical mode, and therefore makes safe nuclear energy possible. The reactor in the fast neutron mode enables the complete incineration of the most harmful radiotoxic long-lived products of nuclear reactions in nuclear fuel waste such as plutonium and other transuranic elements generating with that a great amount of the additional energy.

Other than ADS, the high energy protons in the 1 GeV range can produce a very large variety of secondary beams when impacting on secondary target: spallation neutrons, pions, muons, kaons, neutrinos, Rare Isotope Beams (RIB) etc. These secondary particles have applications in condensed matter study, nuclear physics with rare isotope beams, material irradiation study and particle physics to name a few.

The high power proton beam necessary for ADS should be about 30 MW. The optimal proton beam should be accelerated to 1 GeV and have the average current of 30 mA. The more intense proton beams are necessary for the transmutation of the long lived radionuclides from the nuclear waste for the ecologically pure tritium production. Here the proton beams are necessary with a power considerably higher than 100 MW. The important projects for ADS is the Accelerator Production of Tritium (ATP) project (Los Alamos, USA) [46] where it is supposed to create a proton linear accelerator with the energy of 1.7 GeV and average beam current of 100 mA. The main goal is the tritium production. Figure 3.7 presents the conceptual scheme of the ATP proton accelerator being developed at Los Alamos, USA. The full length of the accelerator is 1220 m.

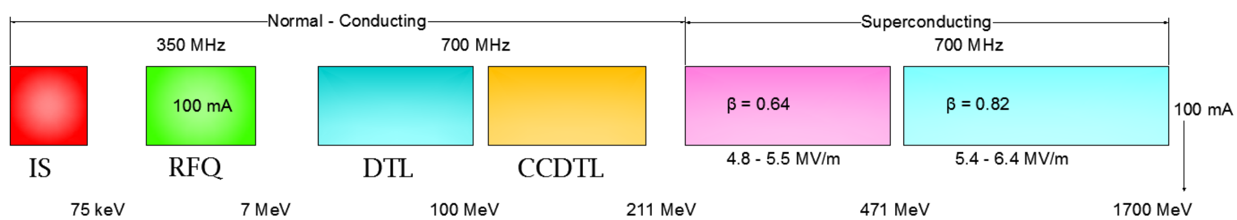

Figure 3.7 *The conceptual scheme of APT proton accelerator [46].*

A typical ~1 GeV proton linac in MW average power range consists of three main sections:

i) A front end (linac injector) is composed of an ion source and a radiofrequency quadrupole (RFQ) accelerator. The ion source has to deliver high current, low emittance and high stability beams. The RFQ which provides RF electric transverse focusing bunches and accelerates the beam from about 50 keV to a few MeV. These structures are well suited to keep the beam quality (longitudinal and transverse) to its perfection at high intensity.

ii) Intermediate-velocity structures accelerates beam to about 100 MeV in the range $\beta \sim$ 0.1 to 0.5. These structures are usually normal-conducting drift tube linac structures (DTL), Separated Drift Tube Linac (SDTL), Couple Cavity Drift Tube Linac (CDTL) etc. However, superconducting structures, as spoke type resonators, are being contemplated especially for CW beams.

iii) High-velocity structures accelerates beam up to GeV energies and consists of superconducting elliptical cavities, that offer some advantages such as higher gradient capabilities and lower operational cost.

3.5.1 High Power Proton Accelerator for Accelerator Driven System (ADS) and other applications

A few important projects for the development of HPPA are summarized below:

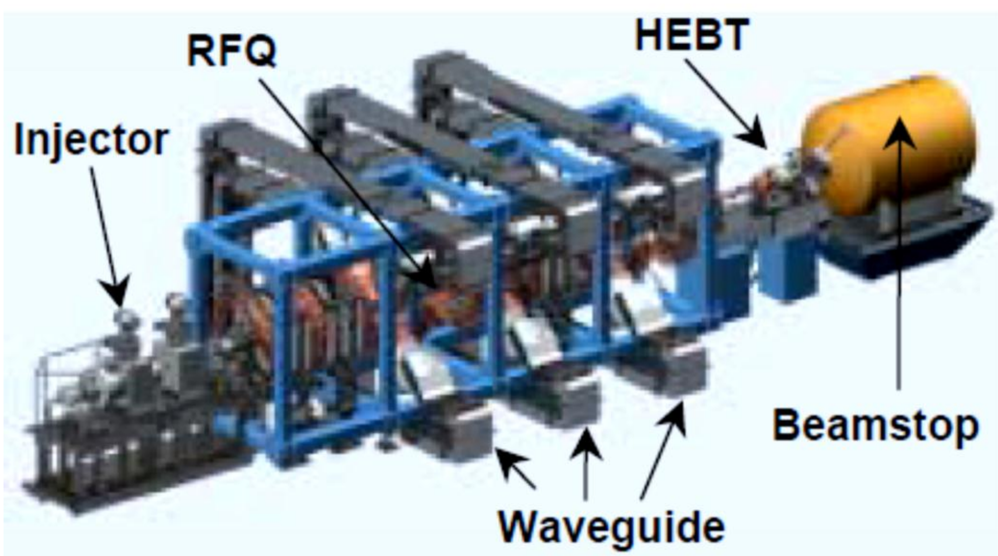

Figure 3.8 *Schematic of LEDA accelerator [47]*.

Los Alamos National Laboratory (LANL), USA is developing Low-Energy Demonstration Accelerator (LEDA), as shown in Figure 3.8 [47, 48]. The major subsystems of LEDA are the injector ion source; Low Energy Beam Transport (LEBT); Radio Frequency Quadrupole (RFQ); High-Energy Beam Transport (HEBT); and the beam stop. The ion source produces 110-mA dc proton beam at 75 keV and LEBT matches to input of RFQ. The LEDA RFQ is 8-m long, 350 MHz structure accelerated the dc, 75 keV, 110 mA H^+ beam from ion source with ~ 94% transmission to 6.7 MeV. The LEDA RFQ has operated with ≥ 99 mA CW output beam for 21 hr. cumulative.

The Commissariat Energie Atomique (CEA), Sacley and Centre National de la Recherche Scientifique (CNRS), Orsay, France are developing Injector of Proton for High-Intensity beam (IPHI) [49, 50]. The construction of the prototype is designed to accelerate beams up to 100 mA with energy up to 10 MeV.

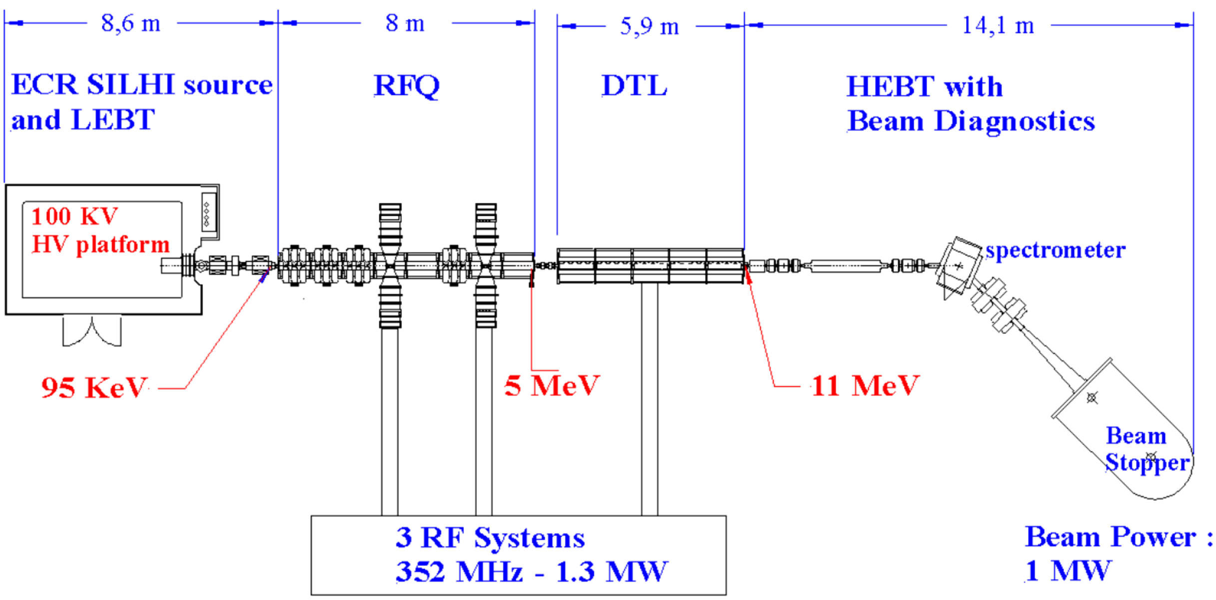

Figure 3.9: *Layout of IPHI accelerator [49]*.

Figure 3.9 represents the general layout showing the main parts of IPHI project: ECR source operating at 95 keV, 5 MeV RFQ, 10 MeV DTL and diagnostics line for accurate measurements of the beam characterization.

TRASCO (acronym for TRAsmutazione di SCOrie) is a joint Istituto Nazionale di Fisica Nucleare (INFN) / Ente per le Nuove Tecnologie (ENEA), program in Italy, started 1998 aiming at the design and the technological investigation of the main components of an accelerator driven system (ADS) for nuclear waste transmutation [51]. The linac in Figure 3.10 consists of a microwave discharge proton ion source, operating at 80 kV, capable of providing 35 mA of CW proton beam, followed by a 352.2 MHz RFQ up to 5 MeV. A 352.2 MHz superconducting linac with independently phased single phase resonators brings the energy to approximately 100 MeV, and the beam is finally brought to the nominal energy of 1 GeV by a three section superconducting linac that uses multicell elliptical cavities at 704.4 MHz.

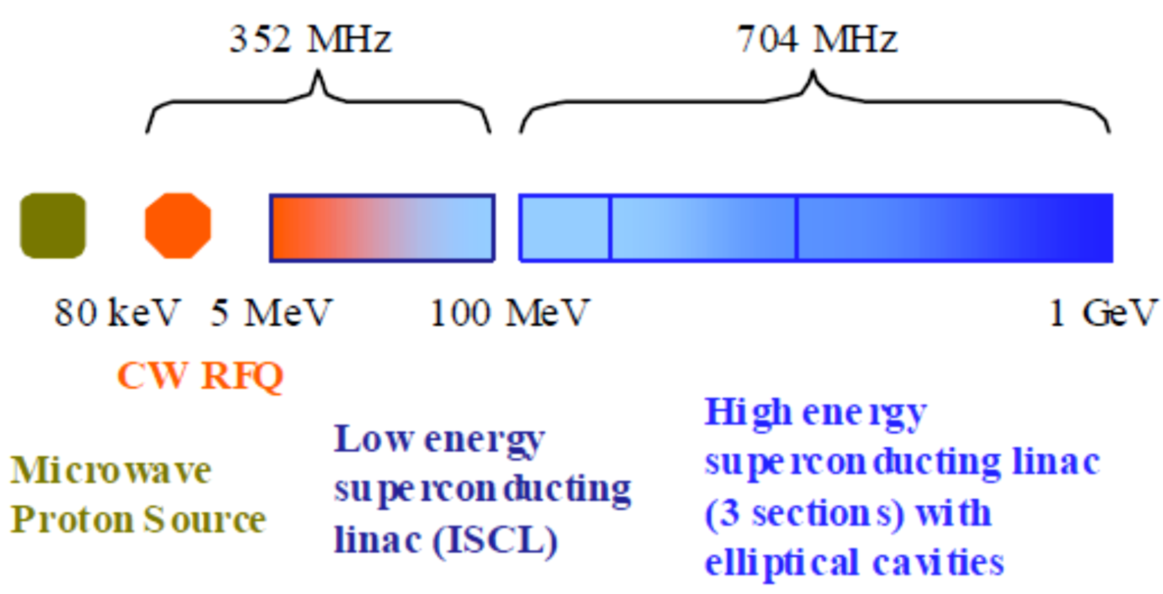

Figure 3.10: *The schematic layout of TRASCO linac [51].*

The high intensity proton accelerator facility project in Japan was formed by joint collaboration of Neutron Science Project of Japan Atomic Energy Research Institute (JAERI) and the Japan Hadron Facility project of High Energy Accelerator Research Organization (KEK) [52]. It consists of 600 MeV linac, a 3-GeV, 1-MW rapid-cycling synchrotron (RCS) and a 50 GeV main synchrotron. One half of the 400-MeV beam from the linac is injected to the RCS, while the other half further accelerated up to 600 MeV by a superconducting (SC) linac. The 3-GeV beam from the RCS is injected to the 50-GeV synchrotron.

The 600-MeV beam accelerated by the SC linac is used for an accelerator driven nuclear waste transmutation system (ADS). The 3-GeV beam from the RCS is mainly used to produce pulsed spallation neutrons and muons. The 50 GeV beam is used for particle and nuclear physics experiment.

The schematic of linac is shown in Figure 3.11. It consists of volume-production type H^- ion source with peak current 53 mA, 500 μs and repletion rate 50 Hz. A radio-frequency quadrupole linac (RFQ) accelerates the beam upto 3 MeV, a conventional DTL up to 50 MeV, and a SDTL upto 200 MeV, a CCL up to 400 MeV and superconducting linac up to 600 MeV for the ADS experiment.

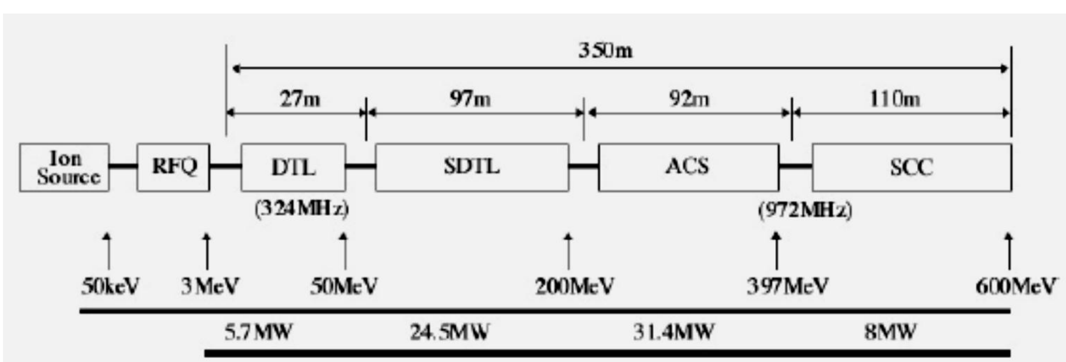

Figure 3.11 S*chematic layout of JAERI/KEK linac [52]*.

The Proton Engineering Frontier Project (PEFP) promoted by Korean Government to help realize potential application in high power proton beams [53]. The primary goal of this project is to develop a high power proton linear accelerator to supply 100 MeV proton beams. The total power of the 100 MeV beam will be 160 kW. A 20 MeV proton linear accelerator has been developed as the front end of 100 MeV accelerator, which consists of a 50 keV proton ion source, a 3-Mev RFQ, a 20-MeV DTL and RF system as shown in Figure 3.12.

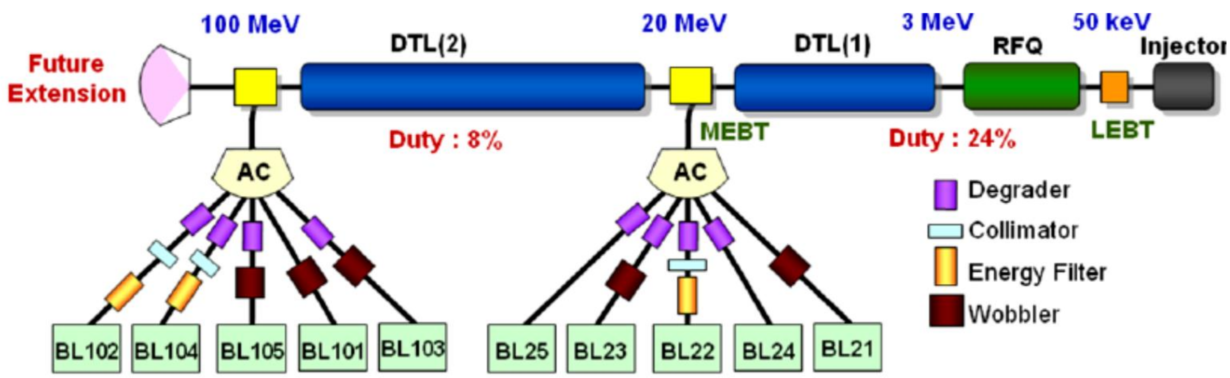

Figure 3.12 *Schematic of PEFP accelerator and user beam line [53]*.

The injector includes a duoplasmatron proton ion source and low-energy beam transport (LEBT). The beam current extracted from the source reached a current of 50 mA. The extracted beam has a normalized emittance of 0.2 π mm-mrad and the proton fraction is > 80%. The LEBT consist of two solenoid magnets that can filter the H_2^+ ions and two steering magnets that can control the beam position and angle at the entrance of the RFQ.

The PEFP RFQ is designed to accelerate a 20 mA proton beam using a voltage from 50 keV to 3 MeV and has the usual four vane type design. The RFQ has been fabricated and tested. The PFEP 20-MeV DTL consists of four tanks that accelerate the 20 mA proton beam from 3

MeV to 20 MeV. The total length of the DTL is 20 m. The PEFP DTL structures were designed for beam duty of 24% and the Focusing-Defocussing (FFDD) lattice configuration has a magnetic field gradient of 5 kG/cm and effective field length of 3.5 cm.

3.5.2 High current Ion sources for High Power Proton Accelerator

The high current ion source delivering 10 – 100 mA stable proton ion beam with good beam quality is the requirement of HPPA. Some of the high current proton ion source developed worldwide is reviewed briefly:

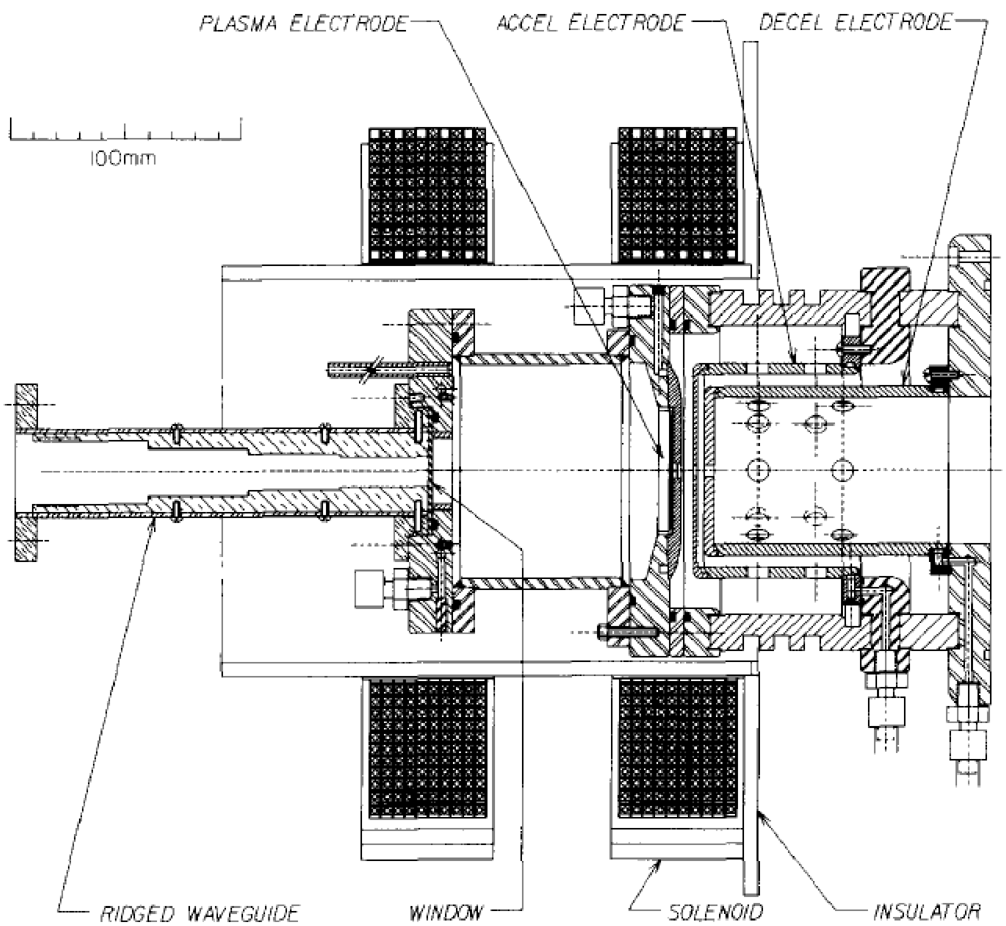

Figure 3.13 *Schematic of AECL ion source [54]*.

A dc high current, low emittance microwave based ECR proton ion source has been developed in Atomic Energy of Canada Limited (AECL), Canada [54]. The schematic of the ion source is shown in Figure 3.13. The plasma discharge was created using microwaves. Microwaves was generated using 2.45 GHz, 1 kW magnetron and transmitted to plasma chamber through circulator, bi-directional coupler, three stub tuner, DC waveguide break, ridge wave guide and Aluminum Nitride (*AlN*) microwave window. The plasma chamber was enclosed by two coils producing 875 G of ECR field. Three-electrode geometry consisting of plasma, suppressor and ground electrodes was used for beam extraction. The dc hydrogen beam of 95 mA with proton fraction in excess of 85% was extracted at beam energy 50 keV. The rms normalized beam emittance measured was 0.1 – 0.12 π mm-mrad.

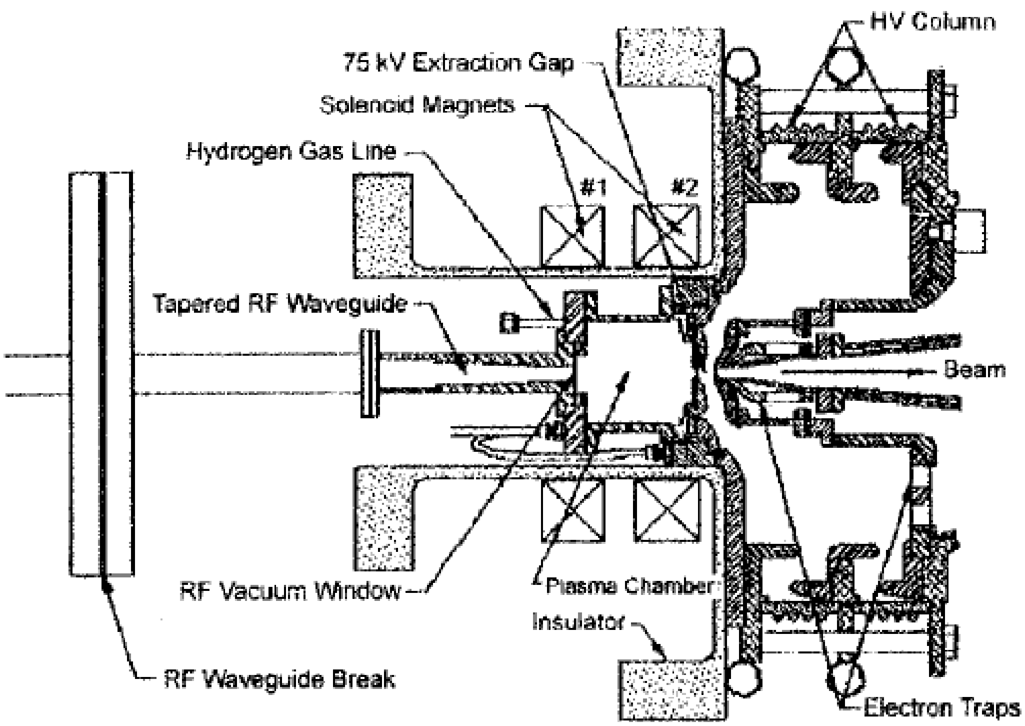

Figure 3.14 *Schematic of LEDA ion source [55]*.

The Low Energy Demonstration Accelerator (LEDA) at Los Alamos National Laboratory, USA has developed a high current microwave based ECR proton ion source as shown in Figure 3.14 [55]. The source operates at 2.45 GHz with 875 G axial magnetic field. The four electrode geometry consisting of plasma electrode, ground 1 electrode, suppressor electrode and ground 2 electrodes was used for beam extraction.

The ion source produced 110 mA of proton current at 75 keV using 600 - 800 W of 2.45 GHz discharge power. Typical proton fraction measured was 85 – 90% of the total extracted ion current and the rms normalized beam emittance measured in LEBT was 0.2 π mm-mrad. The injector operated for week-long run of 168 *h* of operation time. Of this time, the injector operated at 75 keV, > 120 mA for 161.3 *h* (96% available). The ion source accounted for 3.4 *h* of beam off time because of recovery from HV sparks which is dominated by High Voltage Power Supply (HVPS) recovery time.

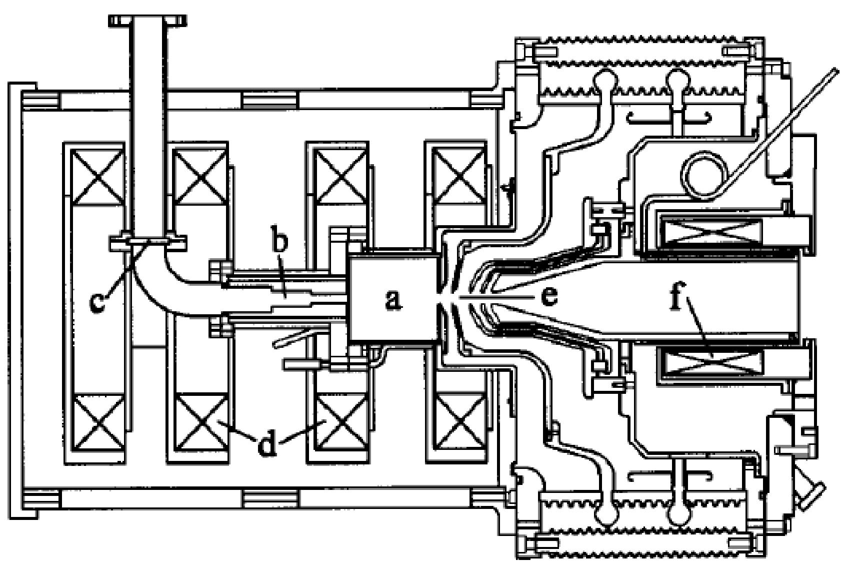

Figure 3.15 *Schematic of SILHI ion source (a) plasma chamber, (b) rf ridge waveguide transition, (c) quartz window (d) coils, (e) five electrode extractor system, (f) DCCT [56].*

The Injector of Proton for High-Intensity beam (IPHI) a CEA-CNRS-INRS, France collaboration has developed a High Intensity Light Ion Source (SILHI) for accelerator driven transmutation of waste (ADTW), and new generation of exotic ion facilities or neutrino and muon production for high energy particle physics [56]. SILHI in Figure 3.15 is a microwave based electron cyclotron resonance (ECR) source constructed and tested at CEA, Sacley. The five electrode geometry consisting of plasma electrode, puller electrode, ground 1 electrode, suppressor electrode and ground 2 electrodes was used for ion extraction. The source has produced 80 mA proton beams at 95 keV with high reliability (~1 spark/day). The proton fraction was around 90% and the typical *r-r'* rms normalized emittance after transport through a single solenoid low energy beam transport (LEBT) was 0.3 π mm-mrad. Extensive emittance measurement was performed with different gas injection in the LEBT and showed a factor of three emittance reduction.

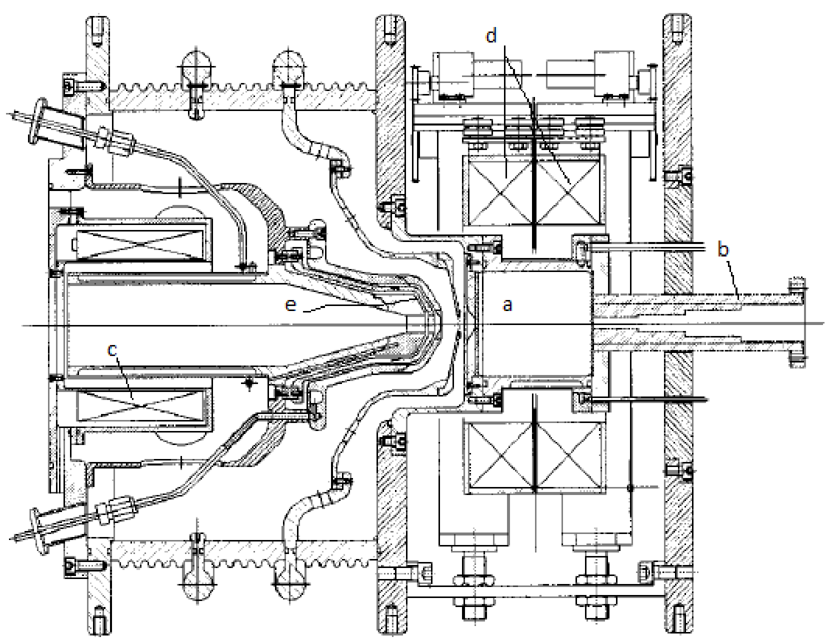

Figure 3.16 *Schematic of TRIPS ion source (a) plasma chamber, (b) rf ridge waveguide transition, (c) DCCT (d) coils, (e) five electrode extractor system [57].*

The TRASCO Project, INFN, Italy is a R&D program whose goal is an accelerator driving system (ADS) for nuclear waste transmutation [57]. The high current proton linear accelerator will drive the subcritical system to transmute nuclear waste. The TRASCO intense proton source TRIPS is a high intensity microwave ion source. The schematic of TRIPS is shown in Figure 3.16.

In TRIPS, the microwave power obtained with a 2.45 GHz, 2 kW magnetron was coupled to the cylindrical water-cooled OFHC copper plasma chamber (100 mm long and 90 mm diameter) through a circulator, a four stub automatic tuner, and a maximally flat matching transformer. Two coils, independently on-line movable and energized with separate supplies, produced the desired magnetic field configuration. The five electrode geometry was used for ion beam extraction. The source has produced 55 mA proton beams at 80 keV with high reliability (100% at 65 keV, 15 mA). The proton fraction was around 90% (estimated) and the typical rms normalized emittance was 0.2 π mm-mrad.

For the International material irradiation Facility (IFMIF) an ion source capable of producing 140 mA H^+/D^+ is being developed at Institut fur Angewante Physik in Frankfurt, Germany [58]. The ion source is filament based volume ion source as shown in Figure 3.17. The plasma chamber of the ion source is made of a water-cooled cylindrical copper chamber whose dimensions are 60 mm in diameter and 100 mm length. Close to axis, a tungsten filament (1.8 mm in diameter, 40 mm length) is installed. A water cooled solenoid surrounds the plasma chamber to confine plasma in radial direction.

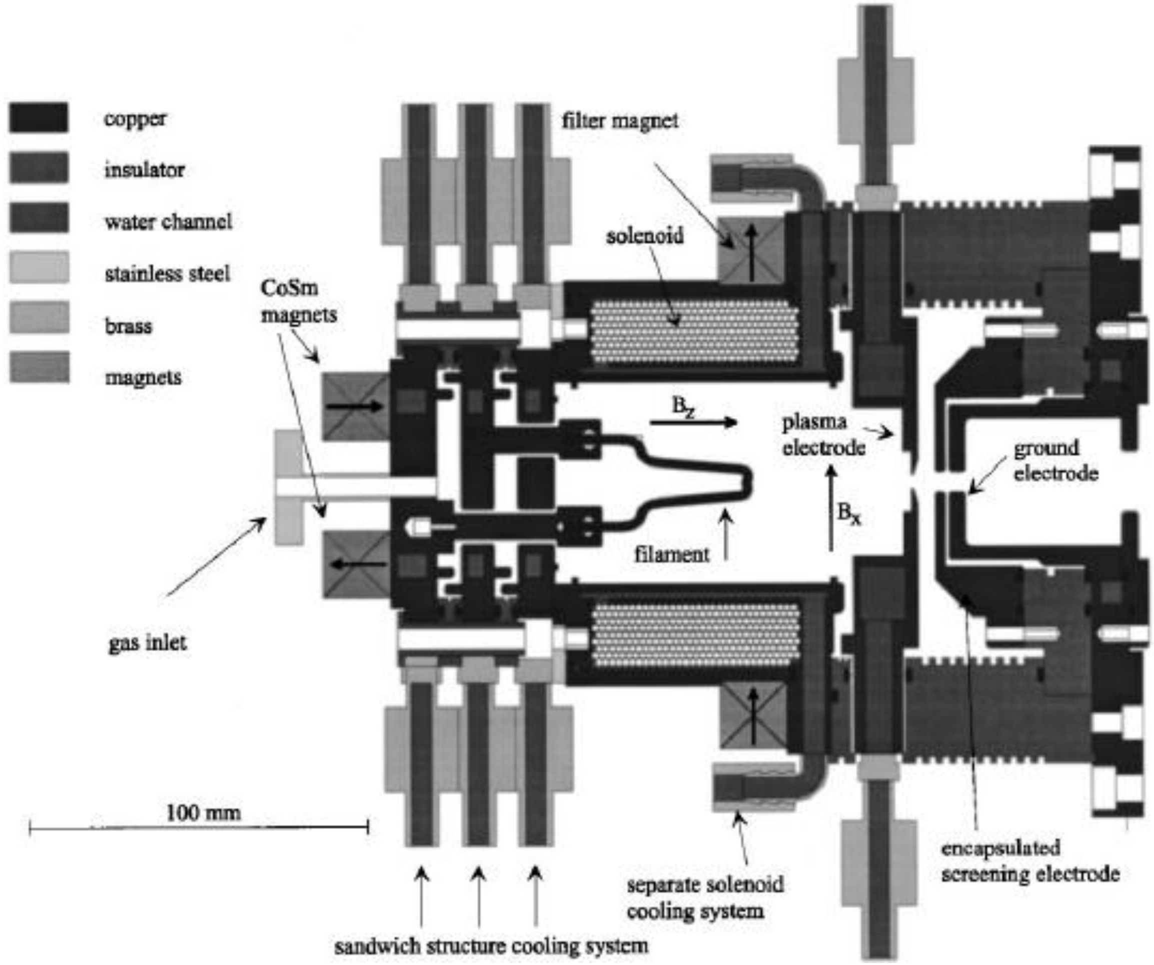

Figure 3.17 *Schematic of Frankfurt volume ion source [58]*.

There are two permanent magnets in cusp field arrangement to reduce particle losses to the back wall. On the back the gas inlet system is mounted. The ion beam was extracted using three-electrode extraction geometry. At an arc power of 10 kW and CW operation, a beam current density 400 mA/cm^2 has been achieved. The proton fraction in the beam is 93% and the divergence angle is within ± 20 mrad. In CW operation with one filament (thickness 1.8 mm), the ion source lifeline is more than 100 *h*.

Korea Atomic Energy Research Institute (KOMAC) is building a 20 MW (1 GeV, 20 mA) proton linear accelerator that will be used for nuclear-waste transmutation and energy production, basic sciences, industrial uses, and medical applications [59]. The accelerator consists of injector ion source, radio frequency quadrupole (RFQ), and couple cavity drift tube linac (CCDTL). The ion source is a high current duoplasmatron ion source as shown in Figure 3.18.

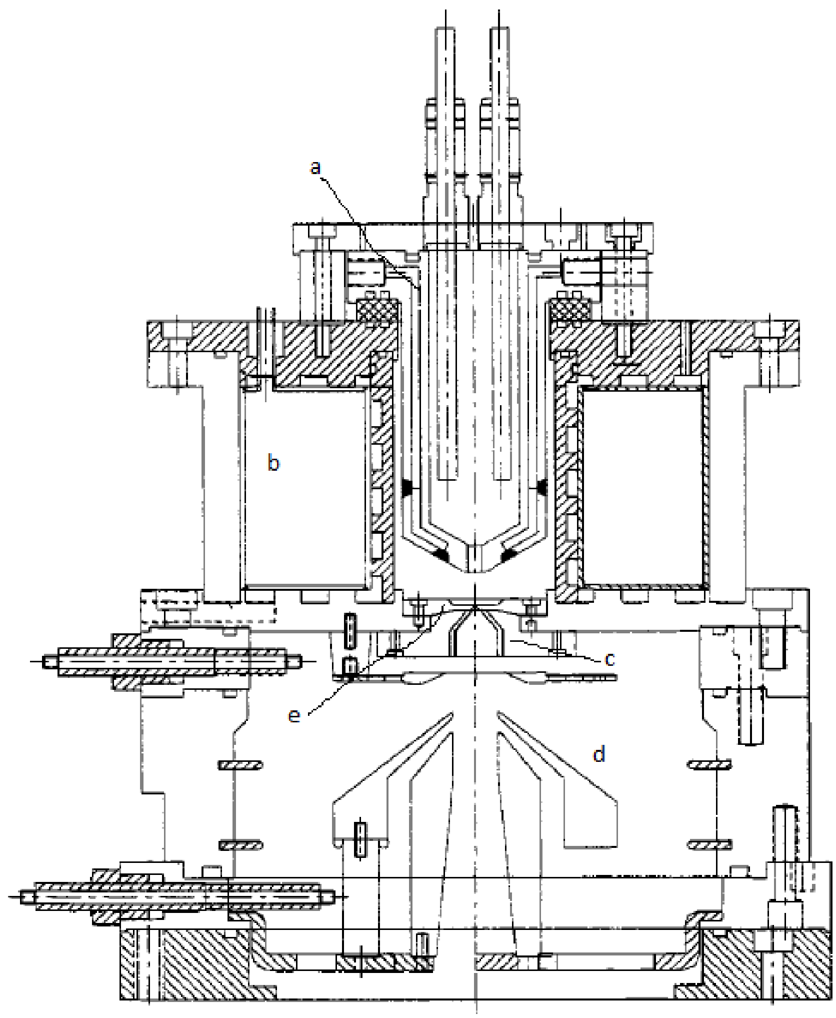

Figure 3.18 *Schematic of KOMAC duoplasmatron ion source (a) cathode, (b) coils, (c)expansion cup (d) three electrode extraction system, (e) anode [59]*.

The duoplasmatron ion source has three electrodes such as cathode, intermediate electrode and anode. Plasmas are generated by arc discharges between the cathode and the anode. High-density plasmas are formed by being compressed geometrically in a 0.7 mm diameter hole of the molybdenum anode and then transferred magnetically in the strong non-uniform magnetic field between intermediate electrode and anode. A ceramic expansion cup has been put in front of anode to reduce plasma loss.

The ion beam was extracted using three-electrode extraction geometry. The axial magnetic field from the solenoid coils in the source is used up to 4 kG. The ion source has reached beam currents up to 50 mA at 50 kV extraction voltages with 150 V, 10 A arc power. The extracted beam normalized emittance of 0.2 π mm-mrad and proton fraction over 80% has been achieved.

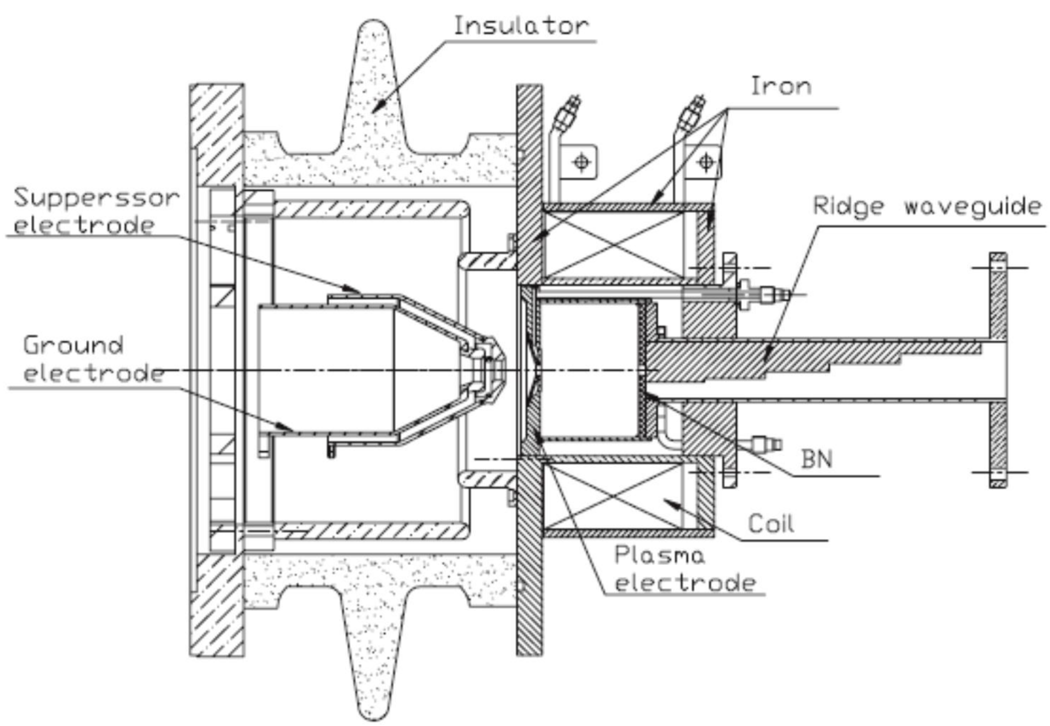

Figure 3.19 *Schematic of C-IADS proton ion source [60]*.

A project named China Initiative Accelerator Driven Sub-critical System (C-IADS) has begun construction of high power proton linac in CW mode for Accelerator Driven Sub-Critical system (ADS). The schematic of 2.45 GHz intense proton source [60] is shown in Figure 3.19. The CW 15 mA beam is extracted at 20 keV from the three-electrode system and focused into the Faraday cup (FC) unit. The measured normalized rms emittance is less than 0.14 π mm-mrad. In 2012, the source is operated more than 200 h at 75 keV, 100 mA, extracted hydrogen current.

Chapter 4

Design, construction, assembly and testing of ECR proton ion source

In this chapter**,** the design, fabrication, assembly and testing of three and five electrode ion source is presented. The design of microwave heating system, plasma chamber, magnetic system, extraction system, vacuum system, gas injection system and low conductivity process water system is described in detail. The design parameters of three-electrode ion source that is set up and its present status are shown in Table 4.1. These design beam parameters of the ion source are the input requirement of LEHIPA RFQ.

Table 4.1: *Parameters of ECR proton ion source.*

Parameters	Design specifications	Present status achieved
Beam current (mA)	50	40
Beam energy (keV)	50	40
Forward RF power @ 2.45 GHz	500 – 1000	500 – 1000
Axial magnetic field (G)	875 - 1000	875 - 1000
Duty factor (%)	100 (CW)	100 (CW) and 1 – 99 % (pulsed)
Gas pressure (10^{-3} mbar)	1 – 10	1 – 5
Emission aperture radius (mm)	8	8
Extraction gap (mm)	17	17
Proton fraction (%)	80	> 90 @ 25 keV
Beam emittance (π mm-mrad) (rms normalized)	0.2	0.05 – 0.23 @ 25 keV

4.1 Microwave system

4.1.1 Magnetron

The microwave system as shown in Figure 4.1 has been designed using WR-340 and WR-284 waveguide section. The microwave system is sourced by a variable power magnetron (2 kW) at a frequency 2.45 GHz. In CW mode, the microwave generator used was M/S National Electronics make MH2.0W-S microwave head operating at fixed frequency 2.45 GHz, ± 15 MHz and rated output power of 2.0 kW. The microwave head contains a water-cooled magnetron, filament transformer, water connections, launching sections, electrical connections and interlock switches. Output energy is coupled to additional waveguide components or into the cavity/ applicator through a standard WR340 waveguide. A magnetron is a cylindrical high-vacuum diode with a cavity resonator system embedded in the anode. In the presence of suitable crossed electric and magnetic fields, the magnetron produces continuous-wave microwave signals in the GHz frequency bands. The energy available within the cathode/anode zone is coupled out and launched in a waveguide by means of output antenna. The frequency will vary slightly as the output power is varied. A filter network is employed at the magnetron’s filament connections to keep all harmonic energy from radiating outside the filament box.

The SM745F is the controller for MH2.0W-S that was used to adjust the magnetron’s output power level by changing magnetron’s anode current through a remote interface connections or through a front panel potentiometer and provides the necessary input power to control the magnetron operation and monitors critical operating parameters of both the magnetron and power supply. The SM745F is a switch mode power supply that uses IGBT technology to generate adjustable, low ripple anode current in a compact enclosure. The SM745F is designed for an input voltage of 230 Vac, 50/60 Hz.

The magnetron was tested up to full power level of 2 kW on a dummy load on a test bench as shown in Figure 4.1 [61].

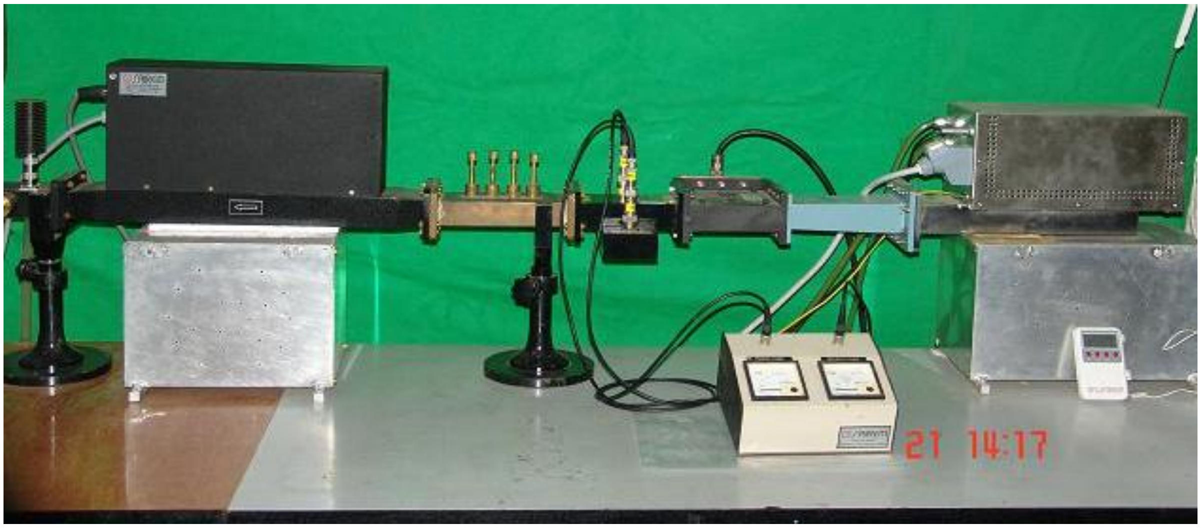

(a)

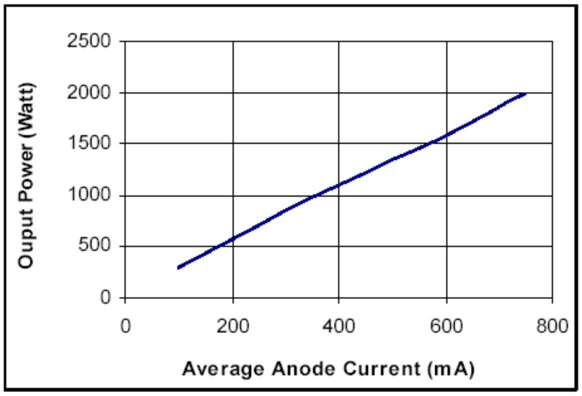

(b)

Figure 4.1 *(a) Microwave system on test bench (b) output power calibration*.

For pulsed mode operation M/S SAIREM make GMP20K microwave generator (Figure 4.2) was used that operates at frequency 2.45 GHz ± 25 MHz and maximum output power of 2 kW. In pulsed mode the magnetron can be operated in the frequency range from 2.5 kHz to 250 MHz and the duty cycle between 1 to 99%. The rising and falling time of the pulse is about 100 μs.

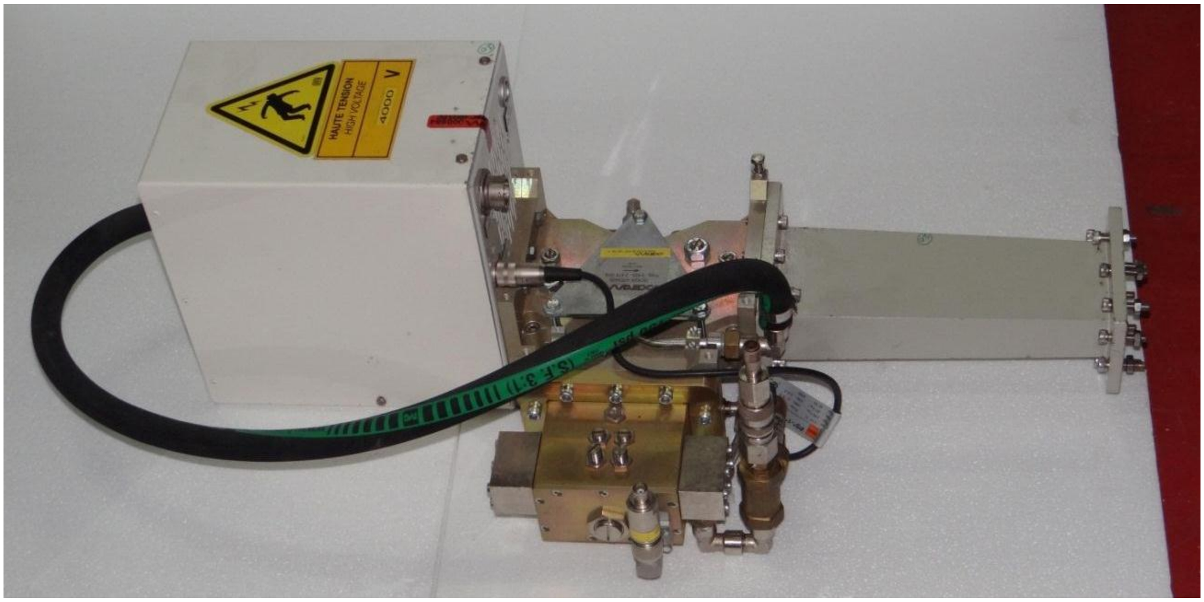

Figure 4.2 *Pulsed microwave generator and circulator*.

4.1.2. Circulator

The circulator used in the microwave transmission section was a ferrite loaded 3-port device, which allows power flow from the power source to the load, but prevents reflected power from reaching the magnetron and thus protect it from damage. Reflected power will cause overheating of the cathode and anode, resulting in shortened magnetron life or catastrophic failure. The reflected power is diverted into the dummy load. The benefits of using circulators include increased power stability, longer magnetron life, increased efficiency, increased equipment reliability and thus lower overall cost. The circulator suitable for the National-make magnetron MH2.0W-S is the WR284CIRC3A that was used to handle an average power of 3 kW at 2.45 GHz. It provides an isolation of 20 dB, with VSWR of 1.25.

4.1.3 Dual directional coupler, power sensor and power meter

A dual directional coupler of M/S GERLING make GA310× was used to measure the forward and reflected powers simultaneously. In this case, a 2-hole directional coupler was used, where the primary waveguide is coupled to a secondary waveguide by means of suitable apertures. The power sensing probe used in the coupler consists of a loop antenna mounted above a short section of waveguide and coupled to the waveguide through a round iris. One end of the loop is terminated with a 50 Ω RF resistor in a proprietary mount. This construction is important to the directivity of the coupler (ability to distinguish between forward and reverse signals). The other end of the loop delivers the attenuated output signal to the female N type connector. The coupling iris is sized and the loop position adjusted to achieve the desired coupling factor. The coupling factor for GA310× is 60 dB ± 0.1 dB @ 2.45 GHz, directivity ≥ 23 dB and output connector 50 Ω N type female.

The forward and reflected power from directional coupler was measured using M/S Agilent E-Series E9323A peak and average power sensors and EPM-P series E 4417 A peak and average power meters (Figure 4.3). The sensors have two independent measurement paths, the default normal path for continuously sampled measurements of modulated signals and the time gated measurements. The frequency, bandwidth and power range of E9323A sensor is 5 MHz, 50 MHz to 6 GHz, -60 dBm to + 20 dBm (average only mode) and - 40 dBm to + 20 dBm (normal mode) respectively. The average only path is suitable for average power measurement of continuous wave (CW). Power measurement includes peak, peak-to-average ratio and average power of RF and microwave signals. The power meter has extensive triggering features such as continuous, level, external TTL, and GPIB for making time gated measurements.

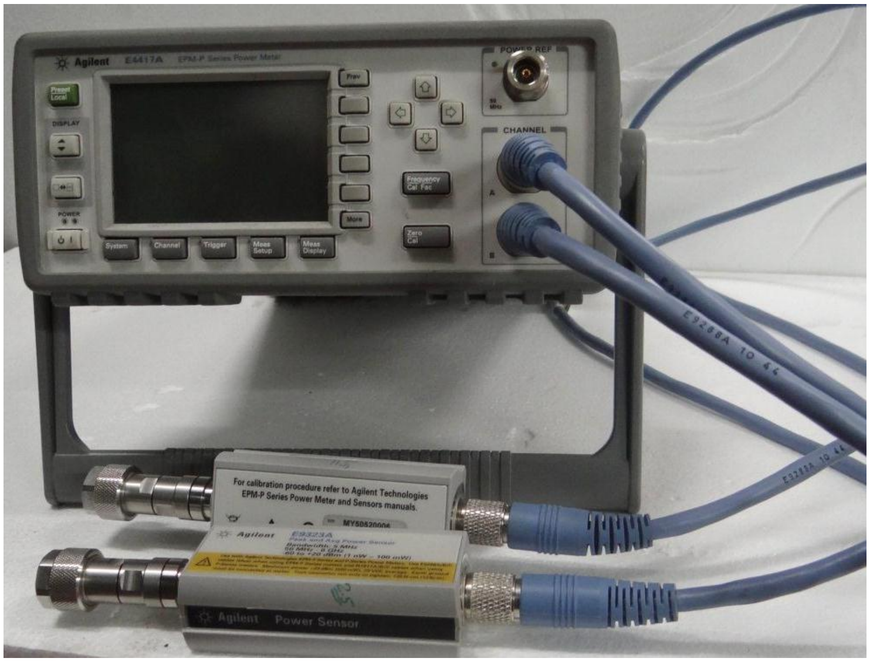

Figure 4.3 *RF power meter and power sensors*.

4.1.4 Four stub auto tuner

The M/S SAIREM makes AI4SAWR340 four stubs microwave auto tuner (Figure 4.4) and RI1567 auto tuner controller was used for waveguide to plasma impedance matching. The four stub automatic matching tuner is a waveguide component whose role is to reduce automatically the microwave reflected power that may be created by low absorbing load, a poorly matched monomode or multimode cavity etc.

The AI4S is integrated in one single unit. The impedance sensors, the four tuning stub and the electronic control system, all mounted on the WR340 waveguide. The normal operating of AI4S is between the microwave generator and the load. In principle, as soon as the microwaves are generated, the autotuner matches instantaneously the load and maintains permanently the reflected power at zero watts. The maximum travelling time of the stubs (from maximum mismatch to full match) is six seconds. The operating frequency of autotuner is 2.45 GHz and the maximum operating power is 6 kW.

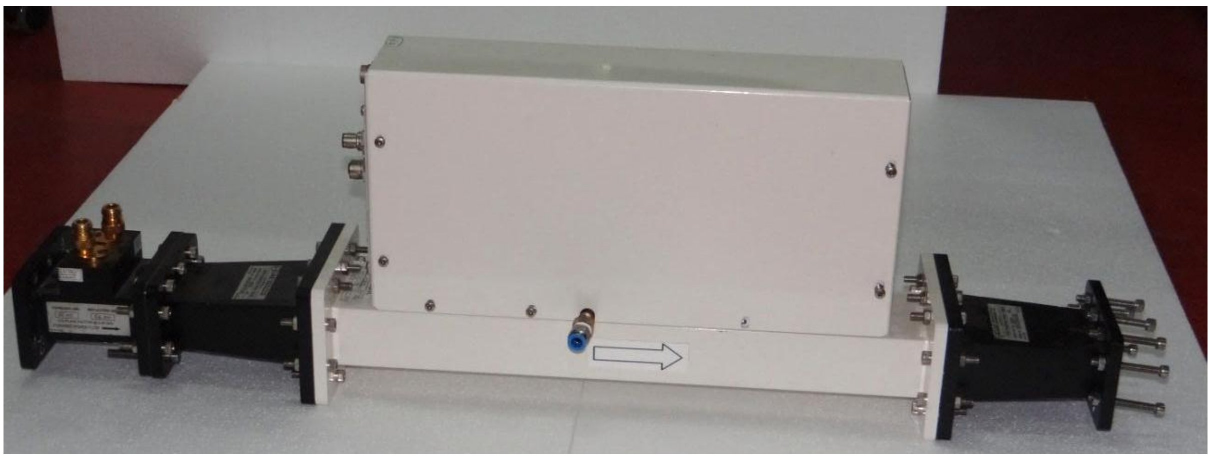

Figure 4.4 *Four stub auto tuner and directional coupler*.

4.1.5 DC waveguide break

A 50 kV dc waveguide break as shown in Figure 4.5 has been designed and fabricated so that all the active elements of the microwave power supply are at ground potential. The break consists of a 3mm thick sheet of Teflon clamped between a choke flange and a standard flange by two acrylic plates. When TE_{10} mode wave travels in the rectangular waveguide, the most intense wall current along the waveguide axis flows near the center of the wider walls. Therefore, the choke flange is designed so that the waves from near the center of the wider walls are most effectively chocked.

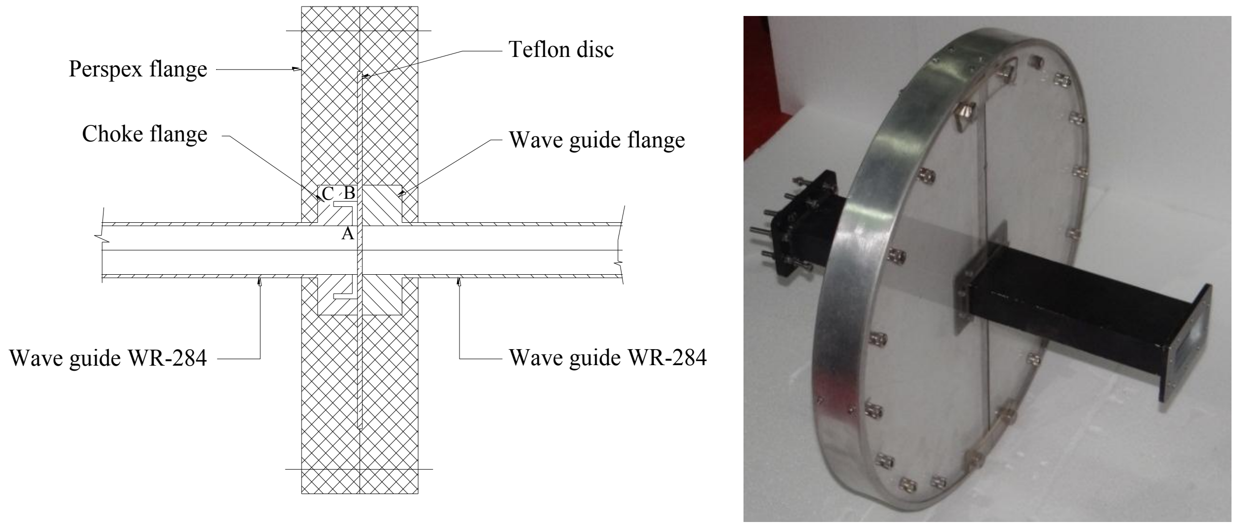

(a) (b)

Figure 4.5 *(a) Schematic and (b) fabricated DC waveguide break.*

In Figure 4.5 (a) the distances from A to B and from B to C are one-fourth the microwave wavelength. In this structure the microwave traveling from point A to the recess passes through point B and is reflected at point C to perform a standing wave corresponding to incoming waves. At point B, no current flows at the wall surface because the quarter wavelengths distance between points B and C. Therefore, there is no fear of microwave leakage from point B through the gap in which the insulator is inserted.

The design of the waveguide break was carried out using 3D calculation. The model and the S_{11} parameter are shown in Figure 4.6 (a) and (b).

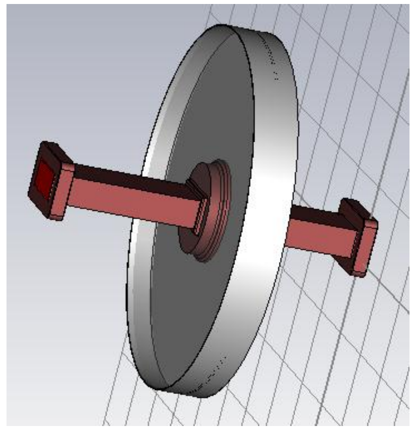

(a)

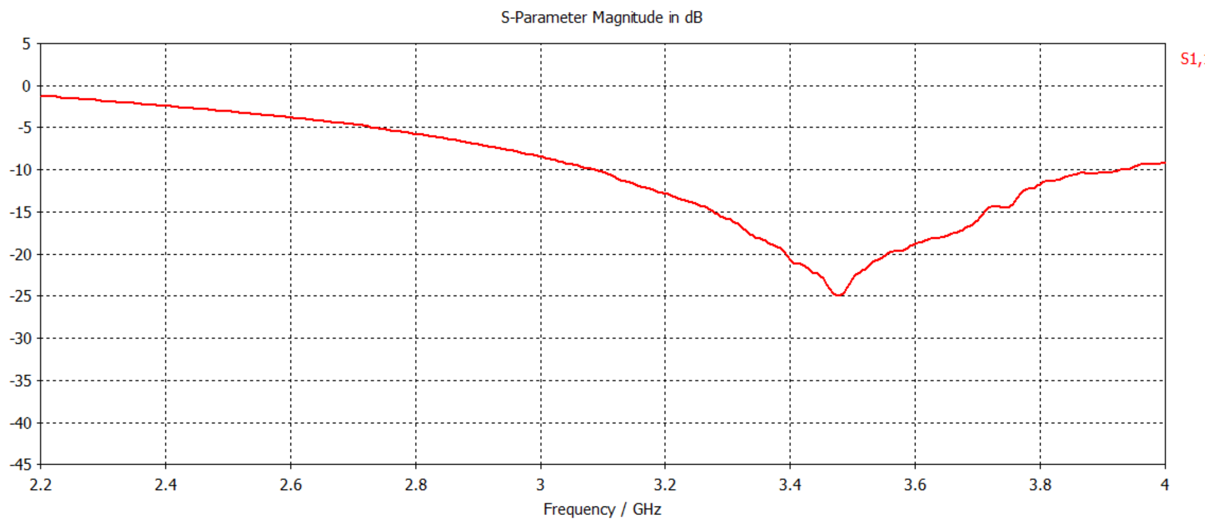

(b)

Figure 4.6 *(a) 3 D model of waveguide break and (b) S_{11} parameter*

4.1.6 Double ridge waveguide

In order to optimize the coupling between the microwave generator and the plasma chamber a four section quarter-wavelength long ridges [62, 63] also known as quarter wave transformer (binomial type), was inserted immediately ahead of the microwave window. The purpose of the ridges is to match the impedance of a WR284 waveguide working in the dominant mode (TE_{10}

mode) to the equivalent impedance of the plasma. The double ridge waveguide developed in-housed was used for (1) optimizing the coupling between the microwave generator and the plasma chamber that realizes a progressive match between the impedance of waveguide and impedance of plasma chamber and (2) concentrating the electric field at the chamber axis to maximize the resonance field.. The overall result will be a significant increase in ion current density.

The ridge realizes a progressive match between the two impedances Z_0 and Z_5 (Figure 4.7). A four-section quarter wave transformer was designed to get an improved bandwidth compared to a single-section for a given load impedance. These transformers are of two types (1) Binomial/maximally-flat design and (2) Chebyshev/equi-ripple design. Here, only Binomial transformer is considered for design. In binomial transformers, the response will be as flat as possible near the design frequency.

The design approach of double ridge waveguide is to match the impedance of WR 284 waveguide of 336 Ω to plasma impedance of ~ 50 Ω. The dimension of WR 284 waveguide is $2a_1$ = 7.213 cm, $2b_1$= 3.4 cm and a_2 = 3.6 cm (Figure 4.7).

The calculated impedances of various sections are given in appendix I and the results are summarized in Table (4.2), where index n varies from 1 to 5.

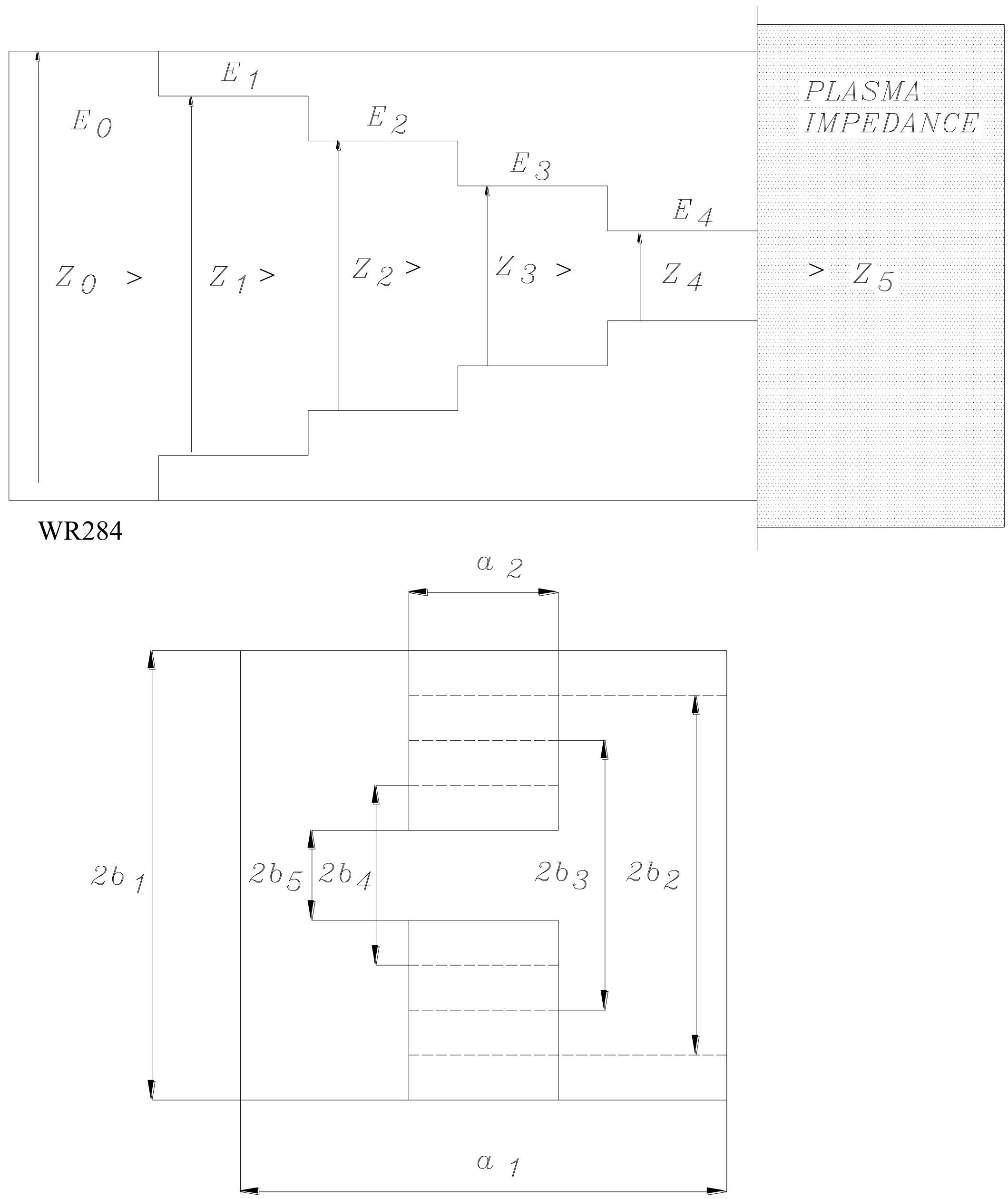

Figure 4.7 *Schematic of double ridge waveguide*

Table. 4.2: *Design parameters of double ridge waveguide*

Item	a_2 (cm)	$2b_n$ (cm)	$\lambda_g/4$ (cm)	Z_{0f} (Ω)	b_n/b_1
WR 284	3.6	3.4	5.79	336	1
Section I	3.6	2.55	4.74	222	0.75
Section II	3.6	2.04	4.25	162.2	0.6
Section III	3.6	1.36	3.76	100.74	0.4
Section IV	3.6	0.75	3.43	54.5	0.22

The design of the ridge waveguide was carried using 3 D calculation. The scattering parameter S_{11} is shown in Figure 4.8. The 2D E-field of the distribution on the input and output port of the ridge waveguide is shown in Figure 4.9. There is a field enhancement factor of 1.5.

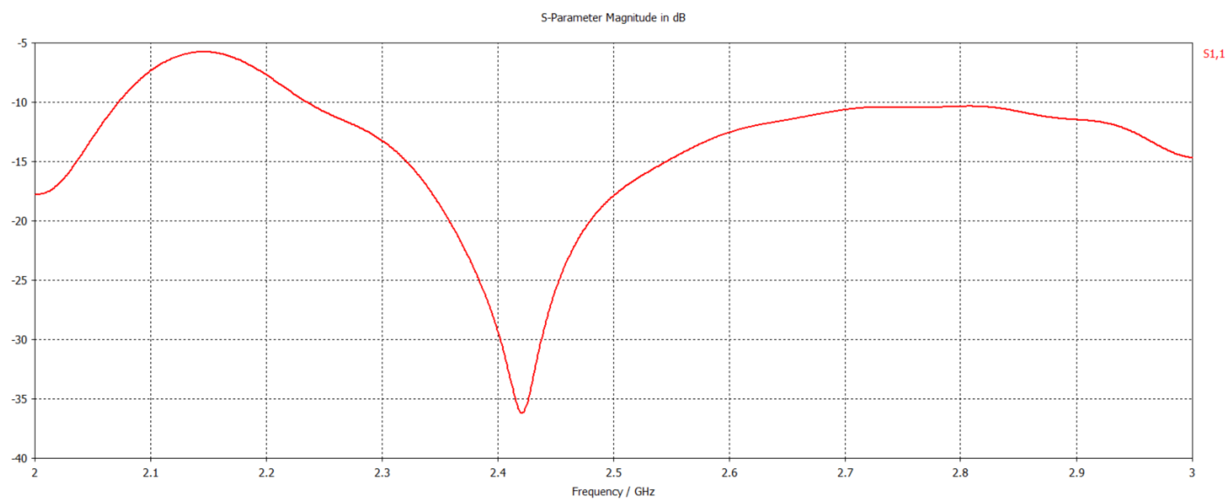

Figure 4.8 *Reflection coefficients S_{11} as a function of frequency.*

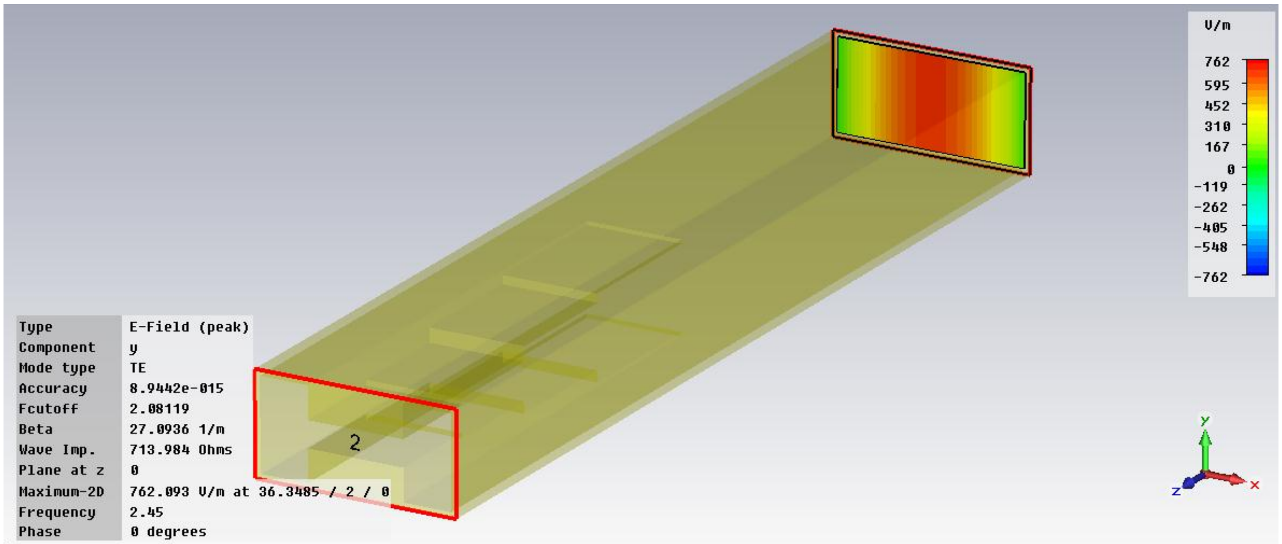

(a)

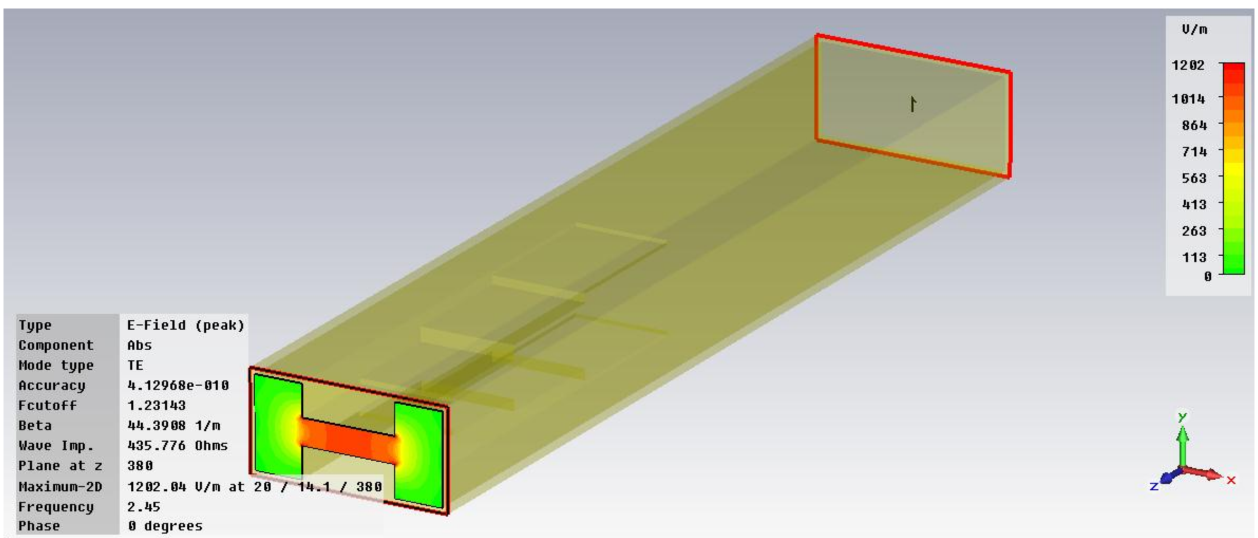

(b)

Figure 4.9 *Field pattern of (a) inlet and (b) outlet port of ridge waveguide.*

The fabricated double ridge wave guide made in OFHC copper is shown in Figure 4.10.

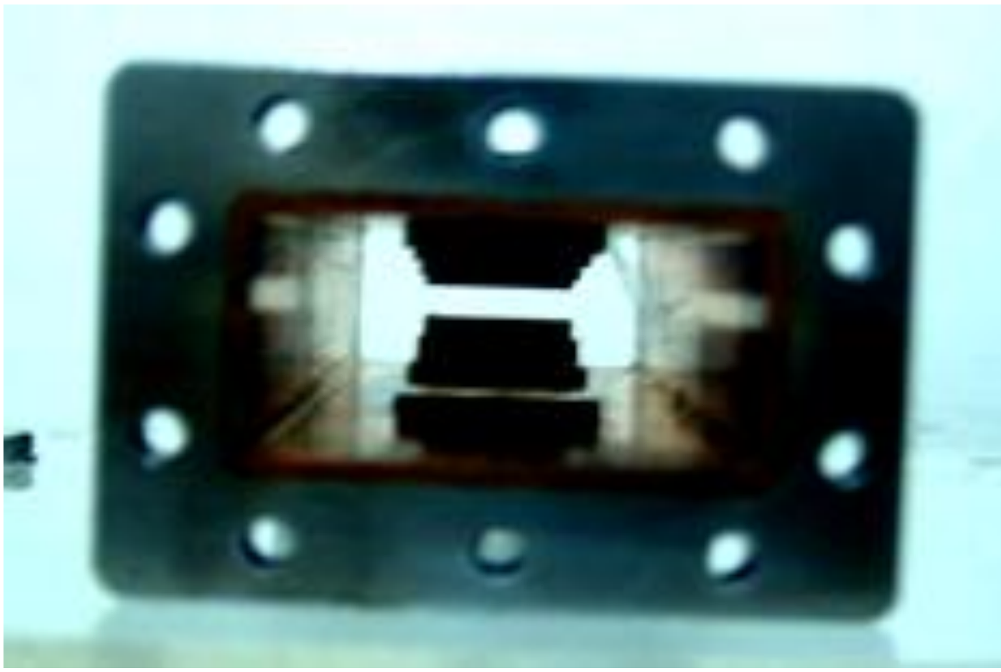

Figure 4.10 *Fabricated double ridged waveguide.*

4.1.7 Microwave window

The microwave window was introduced between the plasma chamber that is at low pressure and the microwave transmission components that are at atmospheric pressure. The design of the dielectric microwave window is very critical in order to realize longer lifetime and higher ion current. Most of the microwaves absorbed by the ECR plasma are right hand circularly polarized microwaves. The dielectric constant ε_p of the plasma for these waves, along the static magnetic field, is given by

$$\varepsilon_p = 1- [(\omega_{pe}/\omega_{RF})^2 /(1-\omega_{ce}/\omega_{RF})] \quad (4.1)$$

The dielectric constant becomes larger as the plasma density becomes higher. Therefore, the microwaves are expected to produce a strong reflection from the high-density plasma. The multi-layer dielectric plates are useful for reducing this reflection if the thickness and the dielectric constant of the plates are optimized [64].

In our design a two-layer window was used to introduce the microwave in the plasma chamber. The first layer is 6mm thick quartz plate as shown in Figure 4.11 (M/S GERLING make, waveguide: WR 284, waveguide flanges: CPR284, operating frequency: 2.45 ± 50 MHz, maximum input power: 3 kW, input VSWR: 1.2 (max), Insertion loss: 0.15 dB (max)) terminating the waveguide creates a vacuum sealing plate and impedance matching plate. The second layer, a 2.0mm thick boron nitride plate (M/S Morgan Advance Ceramic make) adjacent to the plasma, will conduct away heat generated by electrons backstreaming from the extraction column.

Figure 4.11 *Microwave quartz vacuum window*.

4.1.8 Solenoid coils and power supplies

The magnetic field is required in all high current ion sources to confine the plasma and enhance the ionization rate per electron and for ECR ion source it also enhance power absorption through ECR coupling. The magnetic field required to satisfy ECR resonance condition is $B = 2\pi f m / e$, where f = microwave frequency in (Hz), m = mass of the electron (kg), and e = electronic charge (C). The resonant magnetic field corresponding to microwave frequency of 2.45 GHz is 875 G. The required magnetic field was produced by two solenoid coils enclosed on three sides by magnetic yokes. The design parameters of solenoid coils are shown in Table 4.3. The solenoid coils were designed using magneto-static 2 D and 3 D calculations. The field contour is shown in Figure 4.12 (a) and (b) and 3D model and field arrows are shown in Figure 4.13 (a) and (b). The simulated and measured field is shown in Figure 4.14. The fabricated solenoid coil is shown Figure 4.15 (a) and the coil enclosed in yoke is shown in Figure 4.15 (b).

The coils were energized by two high current DC power supplies in Figure 4.16 of ratings: a) current range: 0 – 800 A, voltage range: 0 – 10 V and maximum power 8 kW. The power supply has line and load regulation < 0.5 ppm and stability ± 10 ppm for eight hours.

The solenoid coils placed around the plasma chamber produces the necessary magnetic field for ECR resonance condition. It can be seen from Figure 4.14, that two ECR zone exits, one located near the microwave window and the other located close to the plasma electrode. It has been reported [56] that the source efficiency increases in the presence of two ECR zones. The magnetic induction field in Figure 4.14 is more or less constant and more than 875 G in the middle region of the plasma chamber so that the plasma is confined. If the magnetic field drop significantly anywhere between the point where the plasma is generated and the point where the ions are extracted, the plasma will diffuse along the diverging magnetic field lines, proportionately reducing the density at the extraction aperture.

Table 4.3: *Solenoid coil parameters*

Coil Parameters	Design values
Coil type	Water cooled
ID of the coil (mm)	Φ 200
OD of the coil (mm)	Φ 300
Length of the coil (mm)	50
Conductors dimension (mm) Size Central hole	 7 × 7 Square OFHC copper Φ 4
Total number of pancakes	3
Ampere-turns (*NI*)	21914
Total resistance of the coil (Ohms)	0.01
Voltage drop (Volts)	7.1
Total power dissipation (kW)	5
Number of water circuit	3
Pressure drop (kg/cm^2)	3
Temperature increase (^0C)	10
Water flow per circuit (lit/min)	6

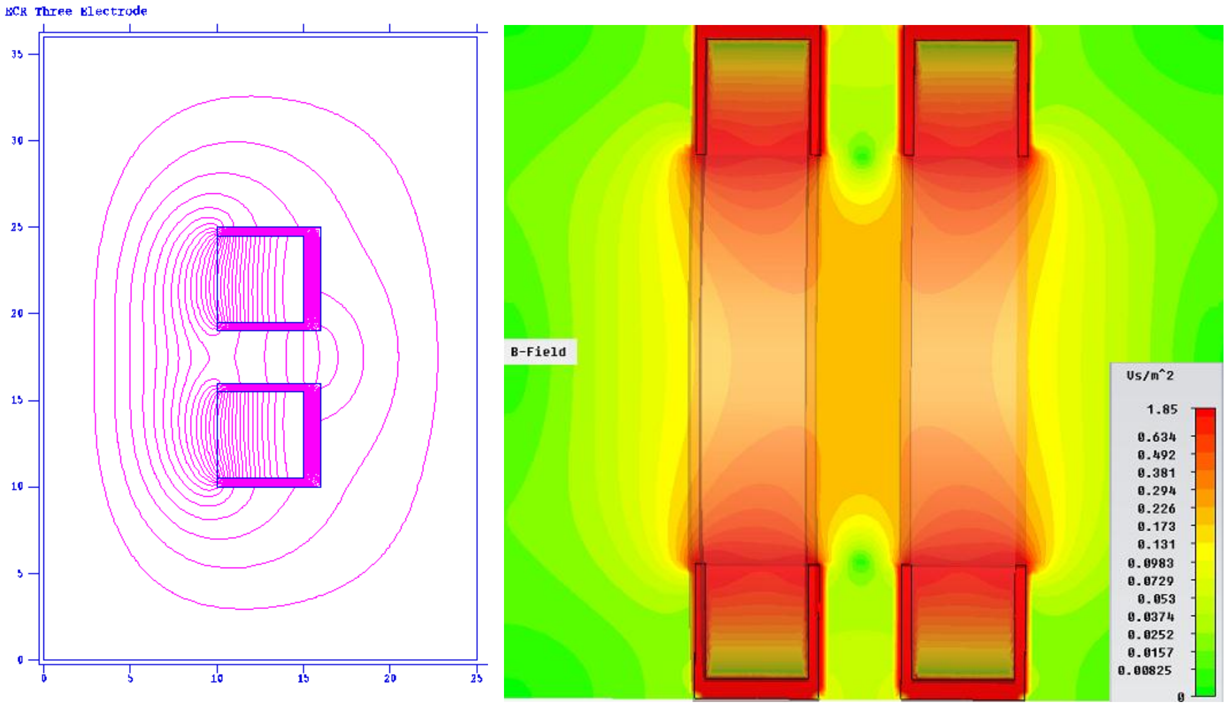

(a) (b)

Figure 4.12 *Simulated (a) field lines and (b) field contours in two coils.*

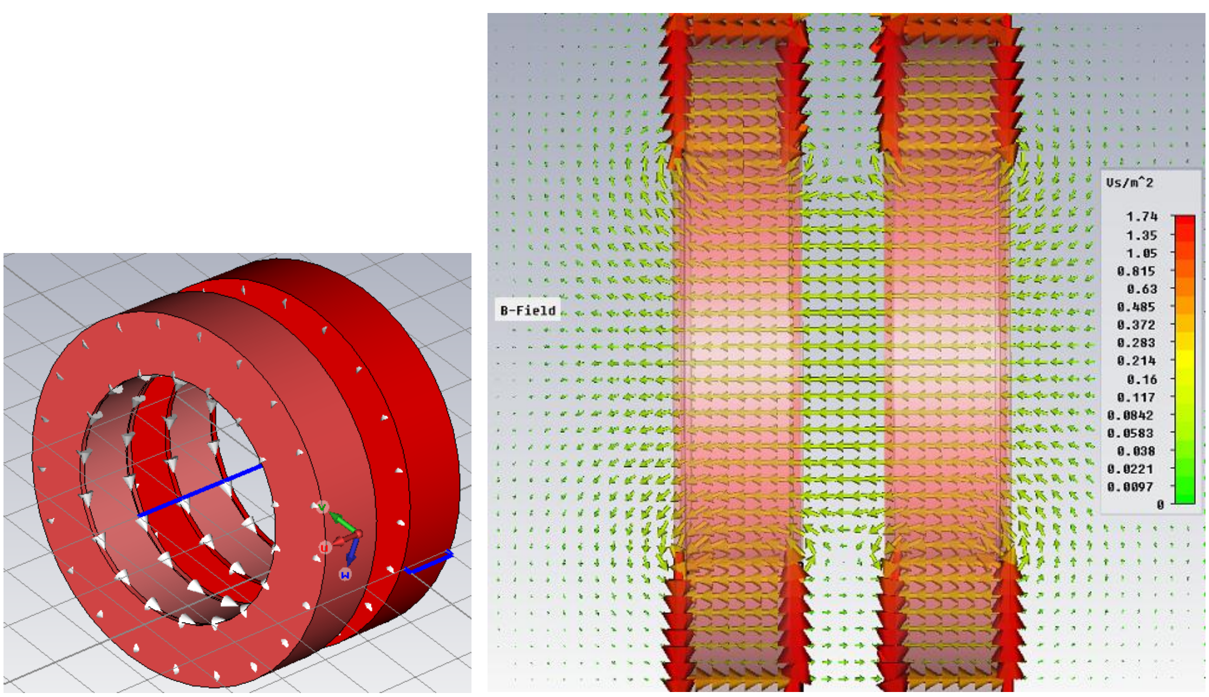

Figure 4.13 *(a) 3D Model of solenoid coils and (b) field arrows in two coils.*

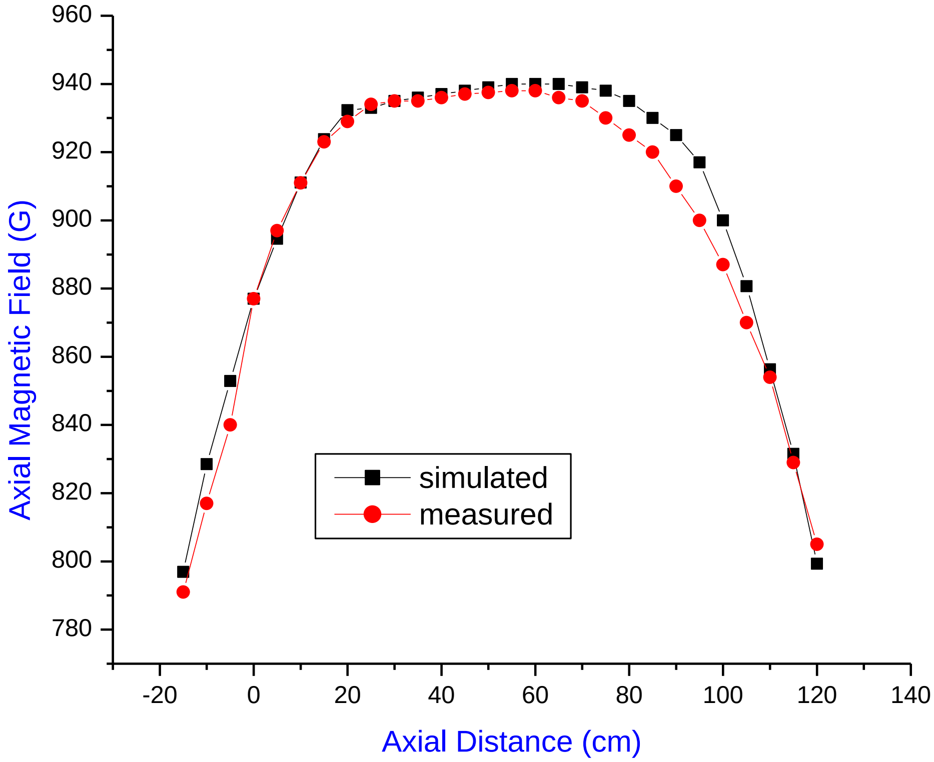

Figure 4.14 *Simulated and measured axial magnetic field*.

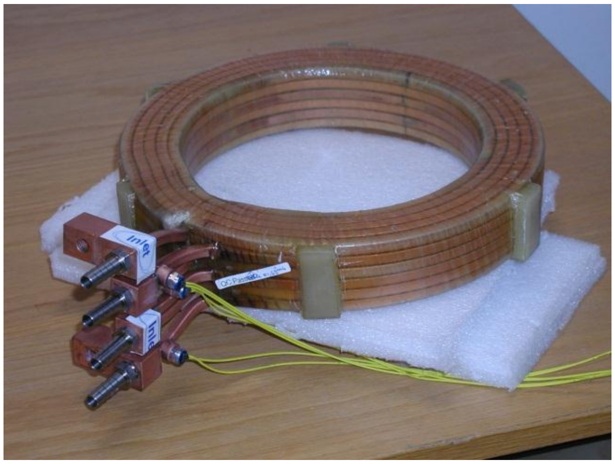

(a)

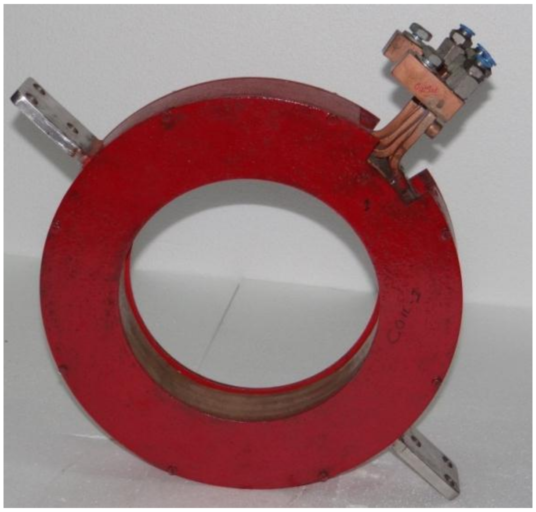

(b)

Figure 4.15 *Fabricated (a) water- cooled solenoid coil in pancake winding and (b) coil enclosed in yoke.*

Figure 4.16 *Solenoid coils power supplies*.

4.2 Plasma chamber

The plasma chamber in the ion source couples microwave power to plasma and confine plasma. The dimensions of plasma chamber are 90 mm diameter and 100 mm length and made of SS304L and OFHC copper as shown in Figures 4.17 (a) and (b). One end flange of the cylindrical plasma chamber was connected to the ridge waveguide that was sealed for vacuum. Also welded on the end flange was a gas feed line. The microwave input to plasma chamber was provided through the ridge waveguide. The other end of the plasma chamber has an end plate with an 8 mm diameter exit aperture for ion extraction. The magnetic coils were situated on axis about the both ends enclosing the plasma chamber and were positioned such that resonant field of 875 G exits at both ends.

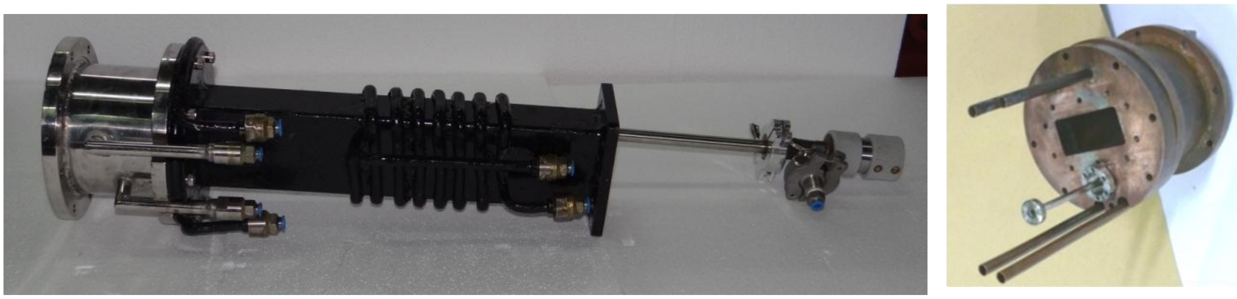

(a) (b)

Figure 4.17 *(a) Plasma chamber fabricated in SS 304 L and (b) OFHC copper.*

The mechanism of microwave power absorption for the maintenance of ECR microwave plasma is not completely understood. The widely accepted approach to the analysis of ECR type plasma is based on the perception that the presence of one or (two) ECR zones ($B = B_{ce}$) in the plasma chamber provides the complete microwave power absorption. However, it is well known that only right-hand polarized (RHP) wave can dissipate in the ECR heating. The wave with opposite polarization – left hand polarized (LHP) wave cannot be absorbed in plasma. But the ECR over dense plasma without detectable microwave leakage and with high degrees of microwave power absorption, $P_a/P_i = (P_i - P_r)/P_i > 95\%$ were reported [65-70]. Where P_i, P_r and P_a are incident, reflected and absorbed microwave power in plasma. These experimental results could be explained only if there is effective mechanism (s) that stops microwave propagation downstream and provides a very high level of microwave power absorption of both LHP and RHP waves.

One possible interpretation of efficient absorption of linearly polarized waves entering the over dense ECR type plasma is based on the experimentally observed transformation of LHP and RHP waves into short wavelength plasma waves which strongly attenuate in Landau damping. It occurs at sites where the plasma density is close to n_{cr} and the angle between the magnitude of field strength, B and the wave propagation direction is small. The presence of resonance magnetic field ω_{ce} = 875 G increase the plasma density to its critical value of $n_{cr} = 7.4 \times 10^{10}$ cm^{-3}, results in high level of absorption of microwave power (up to 95 - 98%). The transition to this region was accompanied with the decrease of reflected microwave power P_r and transmitted microwave power P_t. Microwave power absorption can occur at any place where the axial magnetic field is ~ 875 G and the plasma density is equal to n_{cr} ('plasma resonance'). The length of the plasma absorption area known as ECR region is dependent on the axial magnetic field gradient dB_z/dz and has few mm lengths.

Plasma electrons gain energy from electromagnetic waves within this area, so electron temperature reached values 10 - 20 eV that results in high ionization efficiency. This forms plasma region of very high densities ($n_e > 10^{11}$ cm^{-3}) even at gas pressures as low as $10^{-4} – 10^{-3}$ mbar. The length and the configuration of this region depends on the microwave field structure, microwave power, magnetic field configuration, 'pre-absorption' plasma density shape, gas type and pressure, and plasma chamber geometry.

The microwave electric power absorbed in plasmas is ultimately dissipated as radiation, heating the gas molecules, due to particle loss at the chamber wall surface and others. Finally, the input power should be equal to the dissipated power, and as a result in steady state the plasma parameters are stabilized. Radiation loss and heating loss are proportional to the plasma volume, and particle loss is proportional to the surface area of the chamber. The steady state density profile of the plasma is regulated by the microwave mode pattern $TE_{r,\theta}$ in the r and θ directions.

In the plasma chamber, the hydrogen plasma so formed consists both positively and negatively charged particles in approximately equal proportions along with unionized neutrals. In case of hydrogen, H_2^+ and H_3^+ ions invariably exists in the extraction beam of proton ion source, and their yields sufficiently depends on operational parameters. There are several production processes for H^+, H_2^+ and H_3^+ given as (E_{th} is the threshold energy of the reaction) [71],

$$H_2 + e \rightarrow 2H + e \qquad E_{th} = 9.2 \text{ eV}, \tag{4.2}$$

$$H + e \rightarrow H^+ + 2e \qquad E_{th} = 13.6 \text{ eV}, \tag{4.3}$$

$$H_2 + e \rightarrow H_2^+ + e \qquad E_{th} = 15.6 \text{ eV}, \tag{4.4}$$

$$H_2^+ + e \rightarrow H^+ + H + e \qquad E_{th} = 12.1 \text{ eV}, \tag{4.5}$$

$$\text{Or } H_2^+ + e \rightarrow 2H^+ + 2e \qquad E_{th} = 17 \text{ eV}, \tag{4.6}$$

$$H_2^+ + H_2 \rightarrow H_3^+ + H \qquad E_{th} \sim 0 \text{ eV}, \tag{4.7}$$

$$H_3^+ + e \rightarrow H + H_2 + e \qquad E_{th} = 9.2 \text{ eV}. \tag{4.8}$$

During discharge, H^+ produced mainly by two multiple collision processes (4.2), (4.3) and (4.5), (4.6), H_2^+ is created by direct ionization process (4.4) of hydrogen molecule while H_3^+ is produced by the dissociative attachment reaction (4.7) in a 2.45 GHz ECR ion source as the average electron temperature in the volume is about several eV. With lower electron temperature in plasma, process (4.3) will predominate the generation of H^+; with increase in electron temperature, the contribution from process (4.4) for production of H_2^+ increases. These physical processes are much related to the electron behaviors, so the electron density and temperature of plasma will obviously influence the final extracted beam.

In order to enhance proton fractions in processes (4.3), (4.5) and (4.6), a 2 mm thick boron nitride (BN) plate was placed at two extremities of the plasma chamber i.e. near the microwave window and near the extractor electrode. The nitride plate reduces the recombination processes for the formation of molecular ions. Moreover, due to high secondary electron emission coefficients of nitride plate, the electron density in the ECR discharge is enhanced leading to increased dissociative ionization of the hydrogen.

4.3 Vacuum system and gas feeding system

The vacuum chamber and the associated components of the ion source were fabricated using stainless steel 304 L. The vacuum chamber has four ports. These ports were used for connection to pump, to plasma chamber, view port, pressure gauge and Faraday cup. All the vacuum components were electro-polished and helium leak tested. The leak rate was better than 5×10^{-10} mbar-lit/sec. The objective of the vacuum system is to evacuate the plasma chamber, extractor chamber, diagnostics chamber and other vacuum components to avoid loss of beam particles due to recombination, scattering and to avoid the electrical breakdown due to high voltage. The vacuum system was designed to achieve ultimate base vacuum pressure better than 1×10^{-6} mbar without gas load and to obtain a pressure of the order of 10^{-3} mbar in plasma chamber, 10^{-5} mbar in extractor chamber with gas load. A first order estimation of pumping capacity required to evacuate the ion source with and without gas load is given in appendix II.

The schematic of vacuum system connected to vacuum diagnostic chamber of ion source is shown in Figure 4.18. It consists Turbo-molecular Pump (TP), Dry roughing Pump (DP), Gate valve (GV), Angle valve (AV), combined penning-pirani gauges (VPG) and capacitance gauges (VGC). The ultimate vacuum requirement is better than 1×10^{-6} mbar. Turbo molecular pump

TPH 2301of M/S Pfeiffer make, with the hydrogen pumping capacity of 2000 lit/s, and a dry roughing pump RevoDry 50 P of M/S Pfeiffer make with pumping capacity 50 lit/min (Figure 4.19 (a) and (b) was selected by considering gas throughput ($\approx 2\times10^{-2}$ mbar lit/s) to maintain a pressure of the order of 10^{-4} - 10^{-3} mbar in plasma chamber, 10^{-6} - 10^{-5} mbar in extractor chamber, and to get hydrocarbon free clean vacuum. The pressure difference in the plasma chamber and the extractor chamber was due to the fact that the plasma chamber was evacuated through the 8 mm hole in the plasma electrode. The vacuum gauges used for measuring pressures were capacitance diaphragm gauge heads CMR 263, 264 and compact full range cold cathode gauge head PKR 251 with TPG 256A maxi gauge controller and display unit of M/S Pfeiffer make. The vacuum diagnostic chamber is shown in Figure 4.20. The gas flow rate was measured with flow meters connected to the leak valve. The ion source was installed on non-magnetic stainless steel support with xyz adjustment for ease of installation and alignment.

The schematic gas feeding system of the ion source is shown in Figure 4.21. The gas feeding system consists of high purity hydrogen gas cylinder, a pressure regulator, shutoff valves, precision leak valve EVN 116 of M/S Pefiffer make and a flow meter to measure and control the gas flow in plasma chamber. As the hydrogen gas reservoir, flow meter and pressure sensor were kept at ground potential, it is isolated by polyethylene tube from the plasma chamber, leak valve and shutoff valve that were floated at 50 kV for ion extraction.

The plasma chamber and the extractor geometry were isolated from the solenoid coils which were at ground potential using a polypropylene tube. The extraction geometry was connected to the plasma chamber flange. The end flange of extractor geometry was connected to vacuum chamber. Two alumina rings of 35 cm inner diameter and 7 cm length were used to hold the 50 kV high voltages.

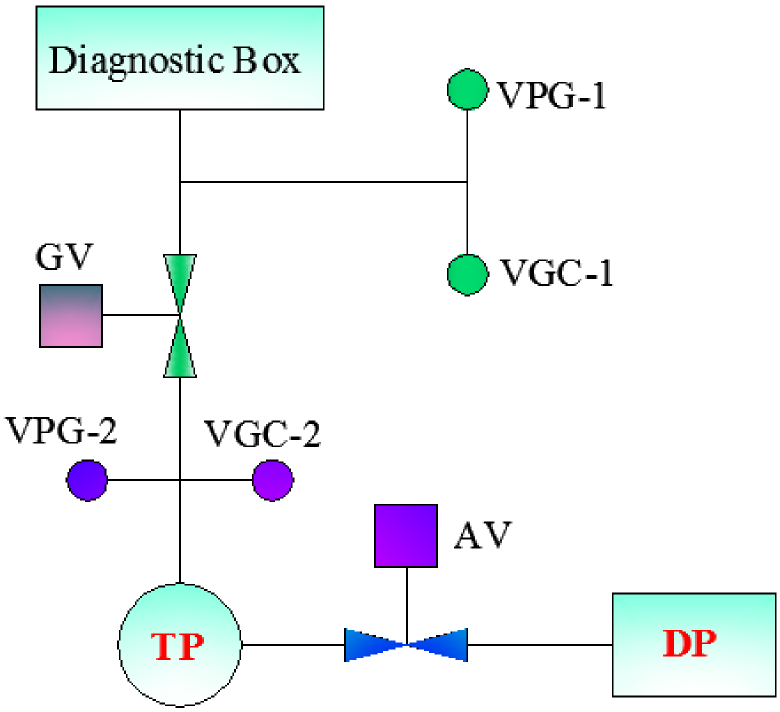

Figure 4.18 *Schematic of vacuum system of ion source. Turbomolecular pump (TP), Dry roughing pump (DP), Gate valve (GV), Angle valve (AV), combined penning-pirani gauges (VPG) and capacitance gauges (VGC).*

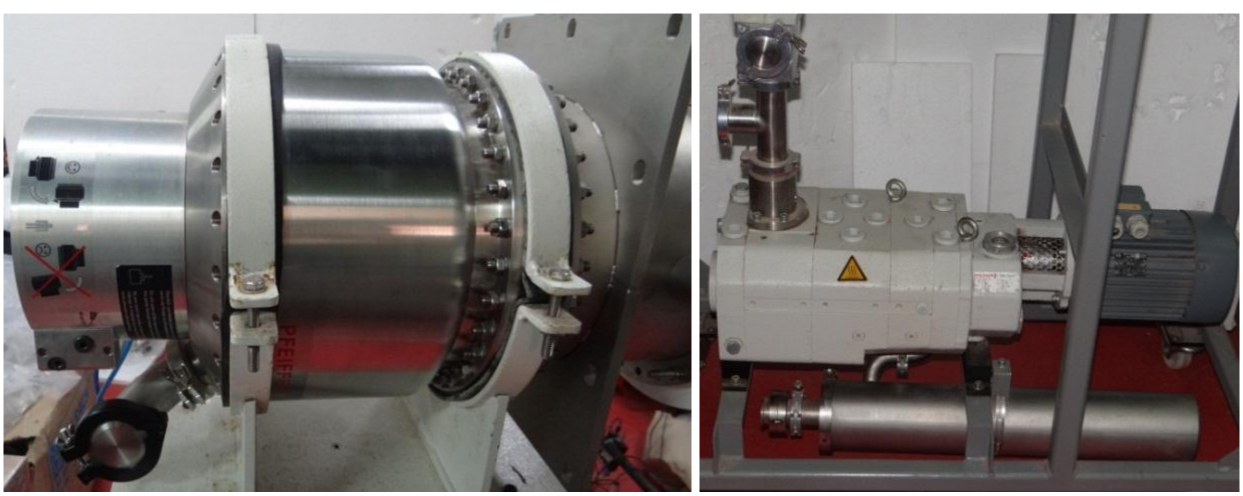

(a) (b)

Figure 4.19 *(a) Turbo-molecular pump and (b) dry roughing pump.*

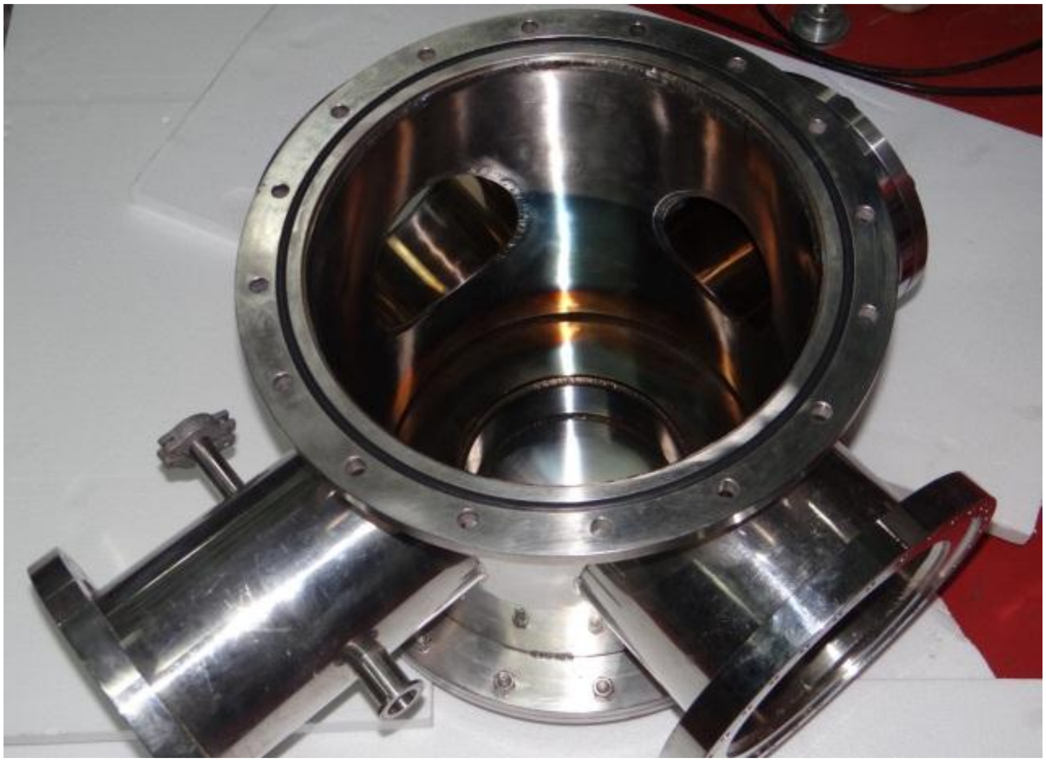

Figure 4.20 *Vacuum diagnostic chamber*.

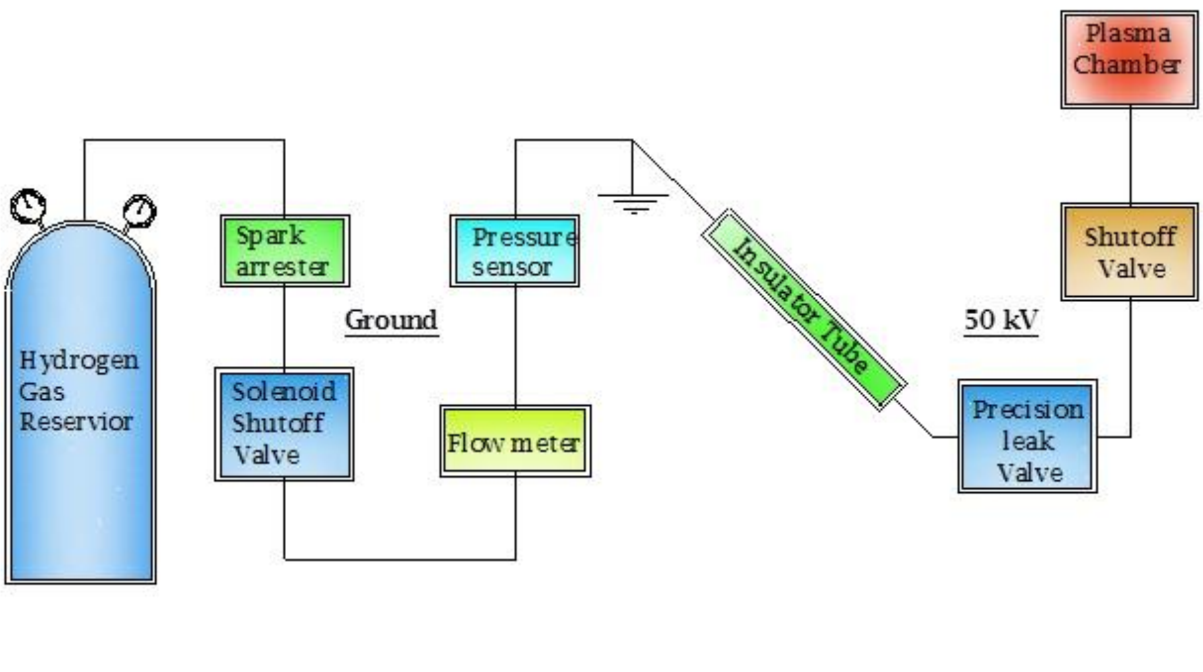

Figure 4.21 *Schematic of gas feeding system*

4.4 Extraction electrodes and high voltage power supplies

The extraction process basically consists of applying a high voltage between an ion reservoir and a perforated acceleration electrode. The trajectories of the accelerated ions, which determine the beam quality, are influenced by several factors, such as the applied field strength, the shape of the emitting surface, and also on the space charge density of the resulting beam itself. In the case of plasma sources, the shape of the emitting surface (meniscus) depends on the electrical field distribution and the local densities of plasma ions, electrons, and accelerated ions. The meniscus is convex, when the plasma density is relatively high. It is plane under intermediate conditions and concave when the plasma density is low or, if the extraction field is higher.

Ion sources using single circular aperture in their extraction electrodes are generally used to obtain low divergence beam. The ion optics of the extraction electrode system in simple terms can be considered that the total beam divergence is the sum of two effects. First the ions are emitted from a curve plasma boundary and collected on a curve extraction electrode, as a result the ion converse towards this electrode. Second the ion diverges as they pass through the aperture in the extraction electrode, this aperture being an electrostatic lens. The factors that determines the residual divergence are; (1) optical aberration in beam forming system due to (a) distortion of plasma boundary due to the use of plasma electrodes of finite thickness (b) nonuniformity of plasma density across the electrode aperture; (c) distortion of the field at the plasma due to the aperture in the second electrode; and (d) aberrations in the electrostatic lens of the second electrode aperture; (2) finite temperature of ions at the plasma boundary giving a finite transverse energy; (3) space charge expansion after extraction.

The final divergence angle of a beam extracted from an aperture of radius r is a combination of initial focusing from a concave plasma meniscus with radius R_M, focusing from the plasma

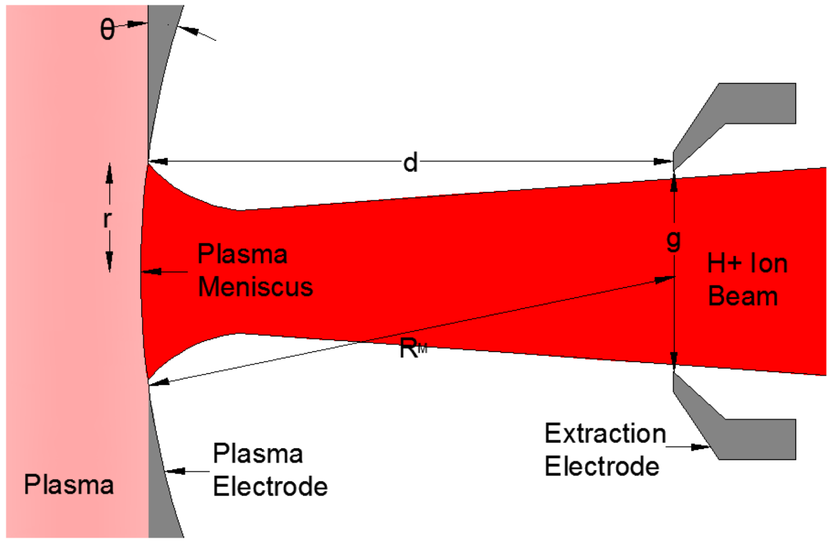

Figure 4.22 *Schematic of ion extraction system.*

electrode inclined at an angle θ, defocussing from the gap g in the extraction electrode, and defocusing due to space charge as shown in Figure 4.22. The extraction potential which tends to penetrate through the plasma electrode aperture is repelled by the plasma sheath potential; so an equipotential is formed which defines a curve boundary: the plasma meniscus. The relative strength of the plasma and extraction potentials defines the radius of curvature of the meniscus and hence on the current density within the plasma. For an uniform emission from an infinite plane, the Child-Langmuir law [21, 22] gives the current density, J, of singly ionized hydrogen gas as:

$$J = 1.74\,(V^{3/2}/d^2) \qquad \text{mA mm}^{-2} \tag{4.9}$$

where V is the applied extraction potential in kV and d is the separation between the aperture and the extraction electrode in mm. For emission from a concave surface with radius of curvature R_M, as in Figure 4.22, for small values of d/R_M it can be shown that the Eq. (4.9) is multiplied by a factor [71, 72]:

$$[1 - 1.6\ d/R_M], \tag{4.10}$$

which is smaller than unity. The total beam current is found by multiplying the current density by area of the emission aperture. For circular aperture of LEHIPA ion source, the current is:

$$I = J\pi r^2 = 1.74\ (\pi r^2/d^2)\ V^{3/2}\ [1 - 1.6\ d/R_M] \qquad \text{mA}, \tag{4.11}$$

The Perveance P, of an ion beam is defined as:

$$P = I/V^{3/2} = [1 - 1.6\ d/R_M]\ P_0 \qquad \text{mA kV}^{-3/2} \tag{4.12}$$

which from Eq. (4.12), is a function of the geometry of the system. The perveance and hence the current of a beam from a concave surface is smaller than the planer perveance, P_0. However the concave meniscus focuses the beam, reducing its divergence. Therefore a balance has to be made between a high extracted current and a low divergence by precisely shaping the plasma meniscus [71]. When this requirement is fulfilled, the extraction system perveance is matched. The overall divergence, ω, of the beam emerging from the extraction system is given by:

$$\omega = 290\ (r/d)\ [1 - 2.14\ P/P_0] \qquad \text{mrad}, \tag{4.13}$$

when $P = 0.47\ P_0$, $\omega = 0$. Inserting this into Eq. (4.12) implies that the perveance match occurs when $R_M = 3.02\ d$. Using this value in Eq. (4.11) gives an expected beam current of 50 mA for $V = 50$ kV, $r = 4$ mm and $d = 17$ mm of the LEHIPA ion source.

A series of simulation studies were made in order to determine optimum condition for extraction of space charge dominated proton beam extracted from LEHIPA ion source. The curvature of the plasma emission surface tends to converge/diverge during extraction of ion beam. Highest quality beams result whenever the plasma-emission boundary is concave and has an optimum radius of curvature. The optimum radius of curvature can be achieved by carefully balancing the plasma density in relation to the strength of the electric field. Under this condition the angular divergence is minimum. To optimized the extraction system some critical points to be considered: 1) matching the current required by adjusting the plasma electrode aperture and the current density which is directly connected to microwave power injected in the source, 2) matching the emittance requirement by optimizing the plasma electrode shape and varying the accelerating field and 3) minimizing the electric field peak value to avoid breakdown by carefully smoothing electrode shape. To achieve high beam current transport after extraction it is necessary that the beam ionizes residual gas in the vacuum chamber and become neutralized by the produced electrons. To avoid back streaming electrons being accelerated back into the source and damaging the source, a suppressor electrode with negative potential is inserted into the extractor system. Downstream this location, the beam space charge is partially compensated by those electrons.

The extraction system was designed and optimized to minimize beam size and divergence. The three and five electrode extraction was designed and fabricated for ion extraction. The geometrical parameter of the three and five electrode extraction is shown in Table 4.4 and 4.5. The electrical potential distribution of three electrode and five electrode extraction is shown in Figure 4.23.

The design parameters of the three and five electrode extraction geometry viz. electrode apertures, electrode gaps and electrode shapes were optimized to reduce beam divergence and emittance using beam trajectory simulation software PBGUNS and IGUN. The space charge effect of the beam is incorporated in the code. Figures 4.24 and 4.25 shows the beam extraction electrodes, equipotentials, and trajectories for the actual three and five electrode geometry obtained from PBGUNS and IGUN simulations for the injected current density of 995 A/m^2. The emittance plot of three and five electrode ion source is shown in Figure 4.26.

Table 4.4: *Geometrical and Electrical parameters of the three-electrode extractor*.

Parameters	Designed values
Plasma electrode (PE) aperture diameter (mm)	Φ 8
Suppressor electrode (SE) aperture diameter (mm)	Φ 13
Ground electrode aperture (GE) (mm)	Φ 13
Angle on PE, SE and GE	45^0, 56^0, 56^0
Gap between PE and SE (mm)	17
Gap between PE and GE (mm)	23
Material of the electrodes	SS 304 L
Insulator	Alumina ceramic
PE potential (kV)	+ 50 kV
AE potential (kV)	- 2 to - 4 kV

Table 4.5: *Geometrical and electrical parameters of the five-electrode extractor.*

Parameters	Designed values
Plasma electrode (PE) aperture diameter (mm)	Φ 8
Puller electrode (PUE) aperture diameter (mm)	Φ 13
First Ground electrode aperture (FGE) (mm)	Φ 13
Suppressor electrode (SE) aperture diameter(mm)	Φ 13
Second Ground electrode (SGE) aperture diameter (mm)	Φ 13
Angle on PE, PUE, FGE, SE and SGE	45^0, 77^0, 56^0, 56^0, 56^0
Gap between PE and PUE (mm)	9
Gap between PE and FGE (mm)	18
Gap between PE and SE (mm)	27
Gap between PE and SGE (mm)	36
Material of the electrodes	OFHC copper
Insulator	Alumina ceramic
PE potential (kV)	+ 50 kV
PUE potential (kV)	+ 30 to + 45 kV
SE potential	- 2 kV to – 4 kV

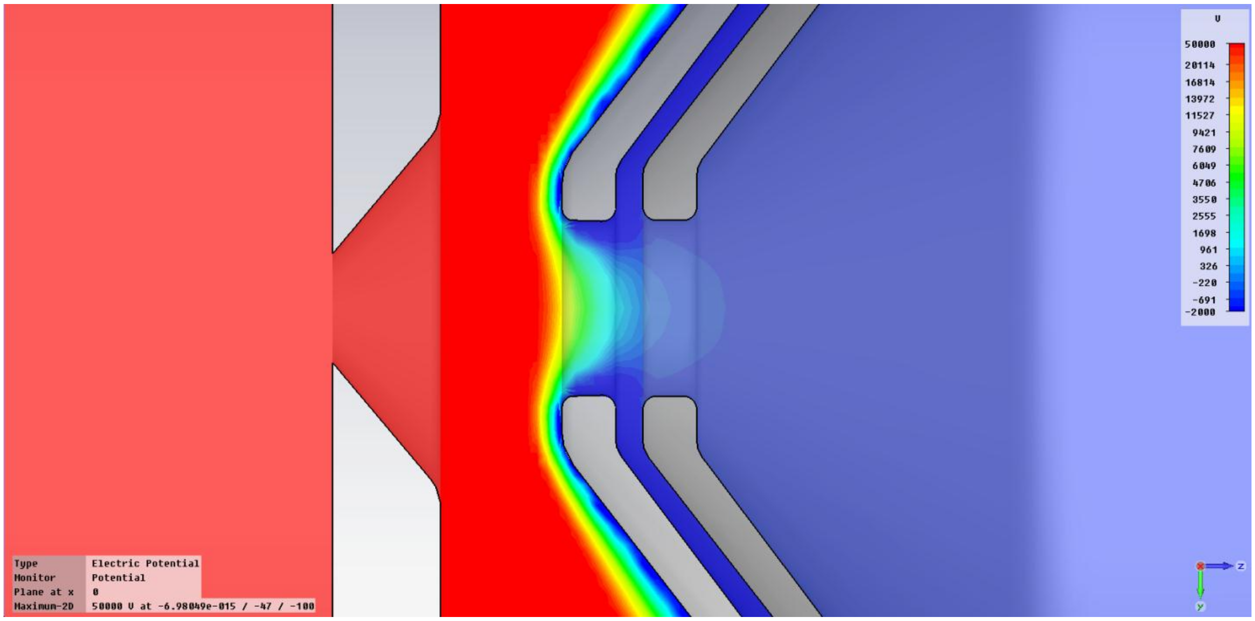

(a)

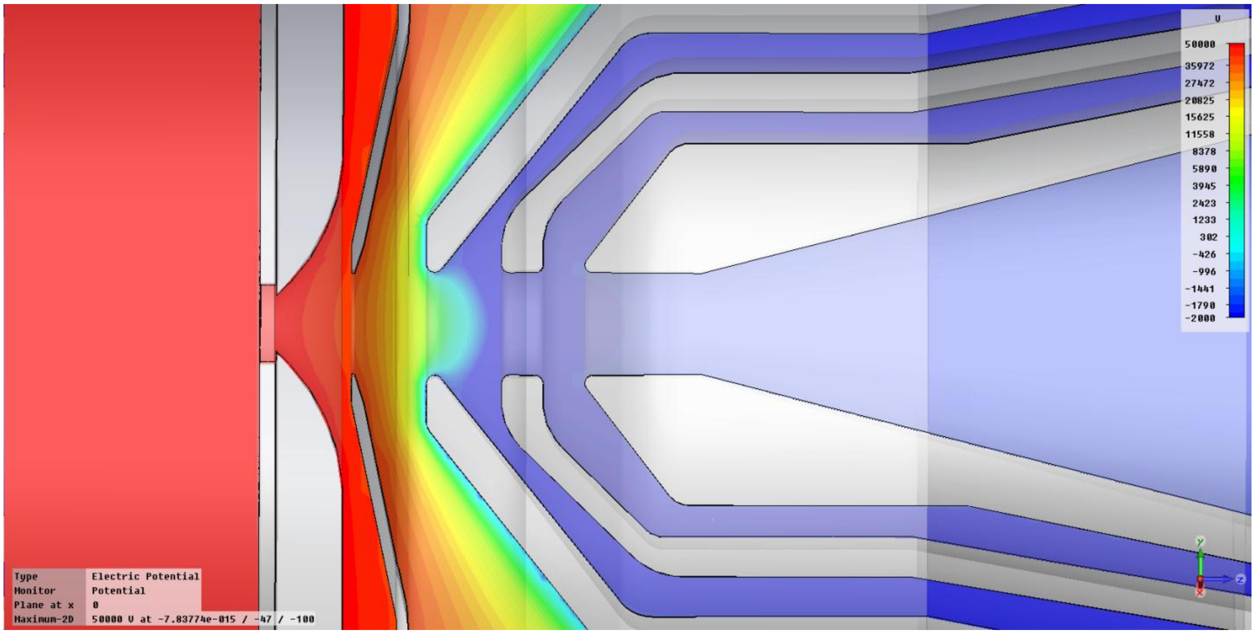

(b)

Figure 4.23 *Electrical potential distribution of (a) three electrode (b) five electrode ion source extraction system.*

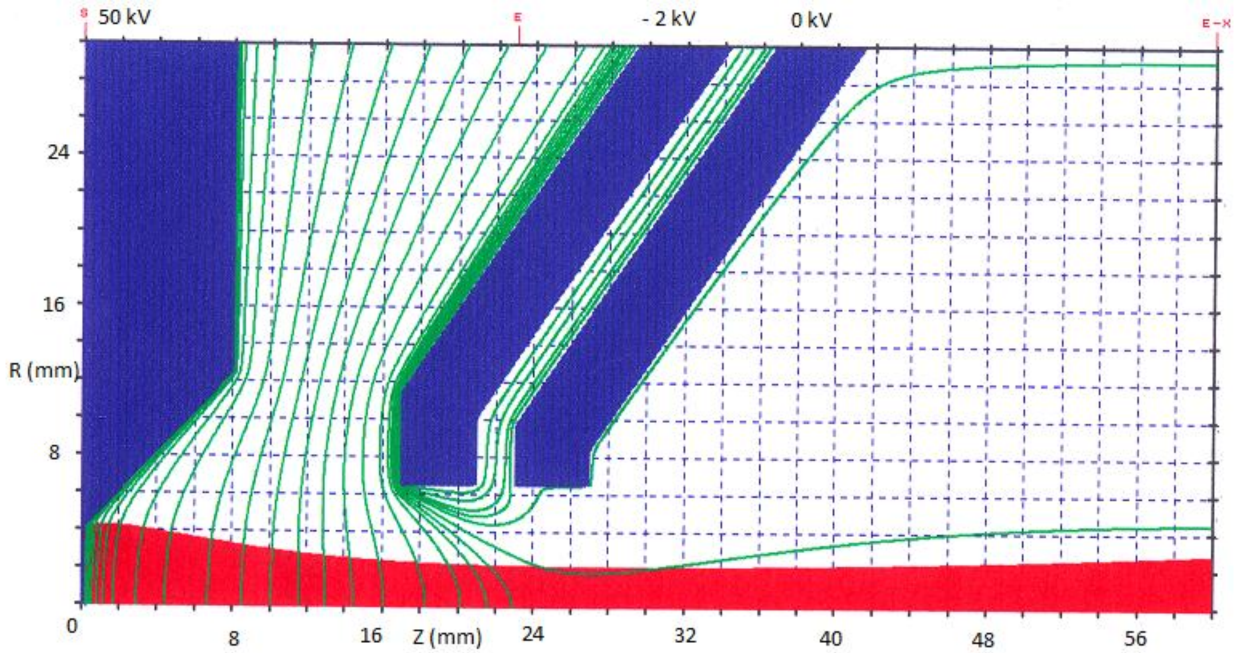

(a)

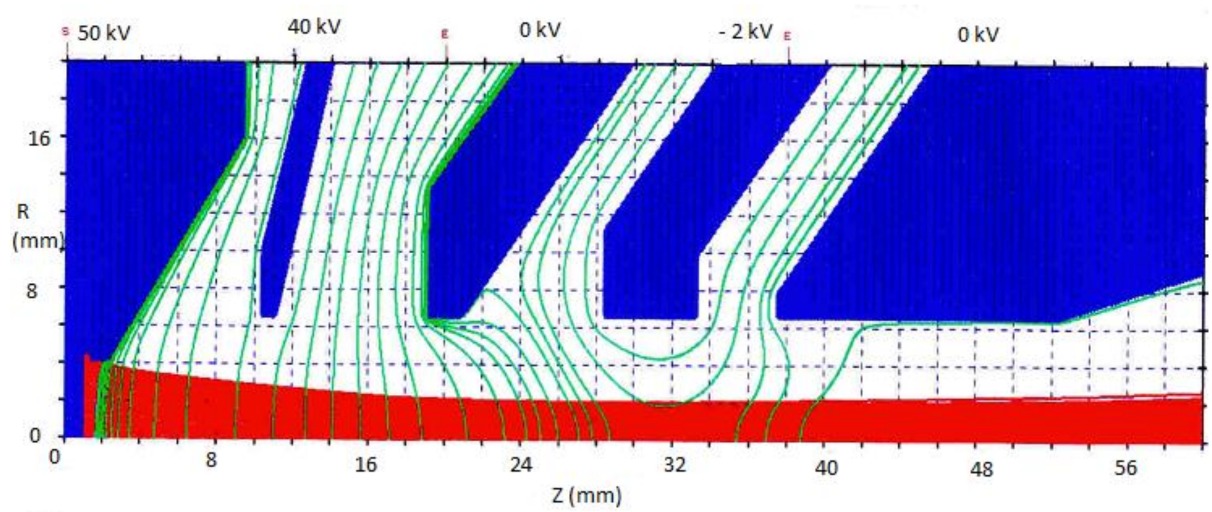

(b)

Figure 4.24 *PBGUNS simulation of equipotential and trajectories of (a) three and (b) five electrodes ion source extraction system.*

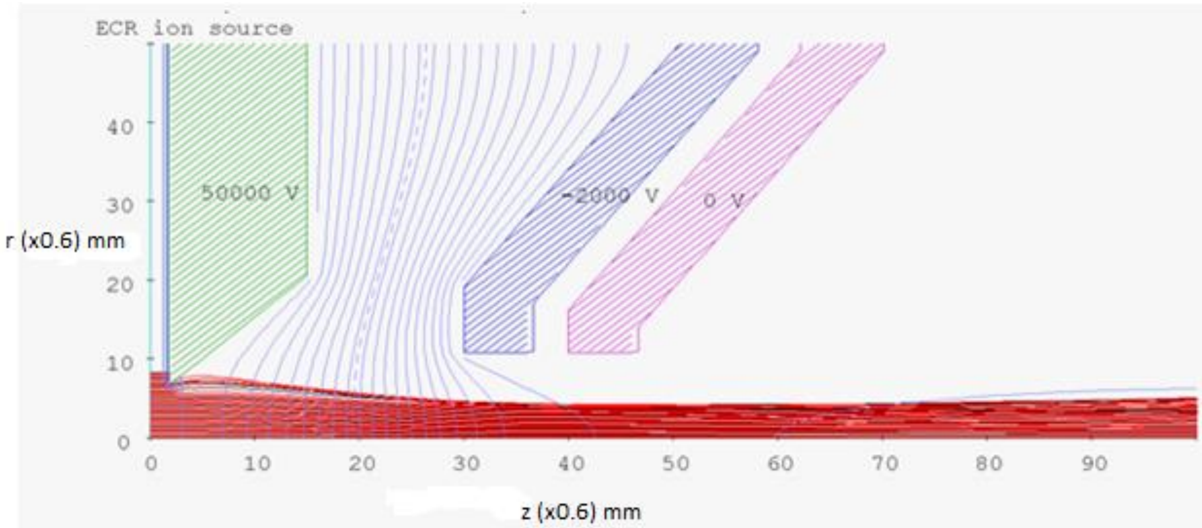

(a)

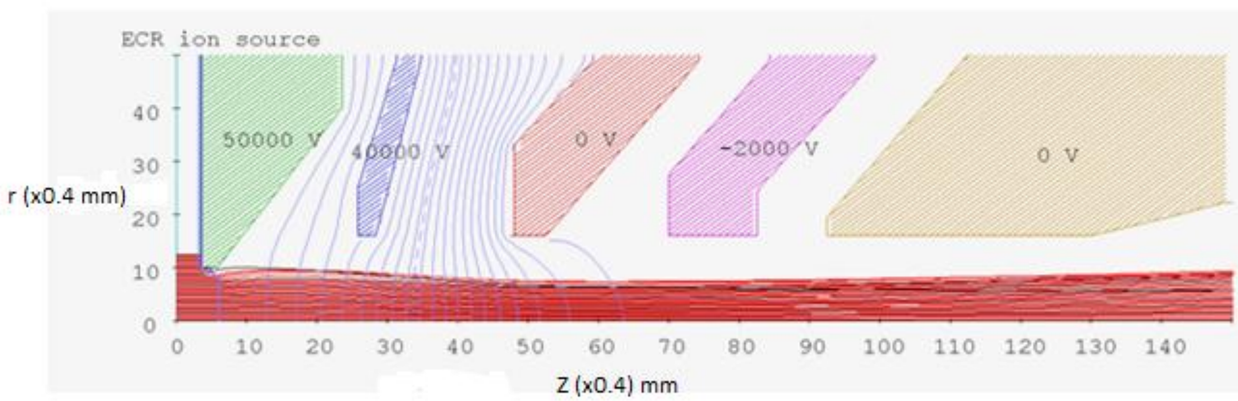

(b)

Figure 4.25 *IGUN simulation of equipotential and trajectories of (a) three and (b) five electrodes ion source extraction system.*

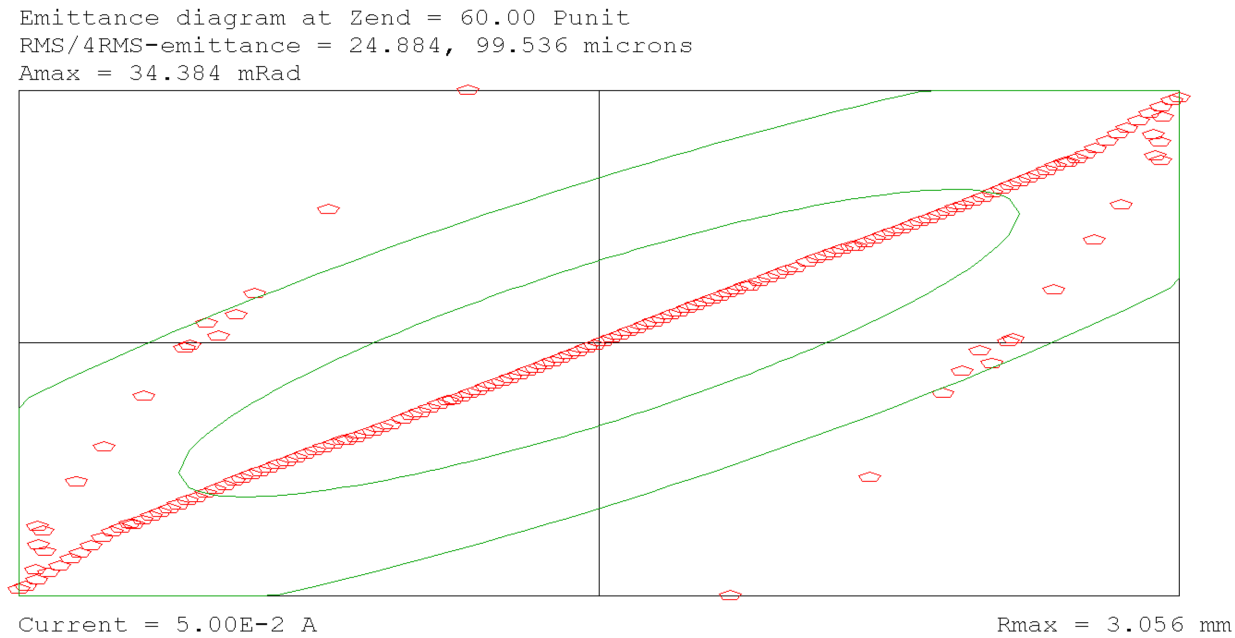

(a)

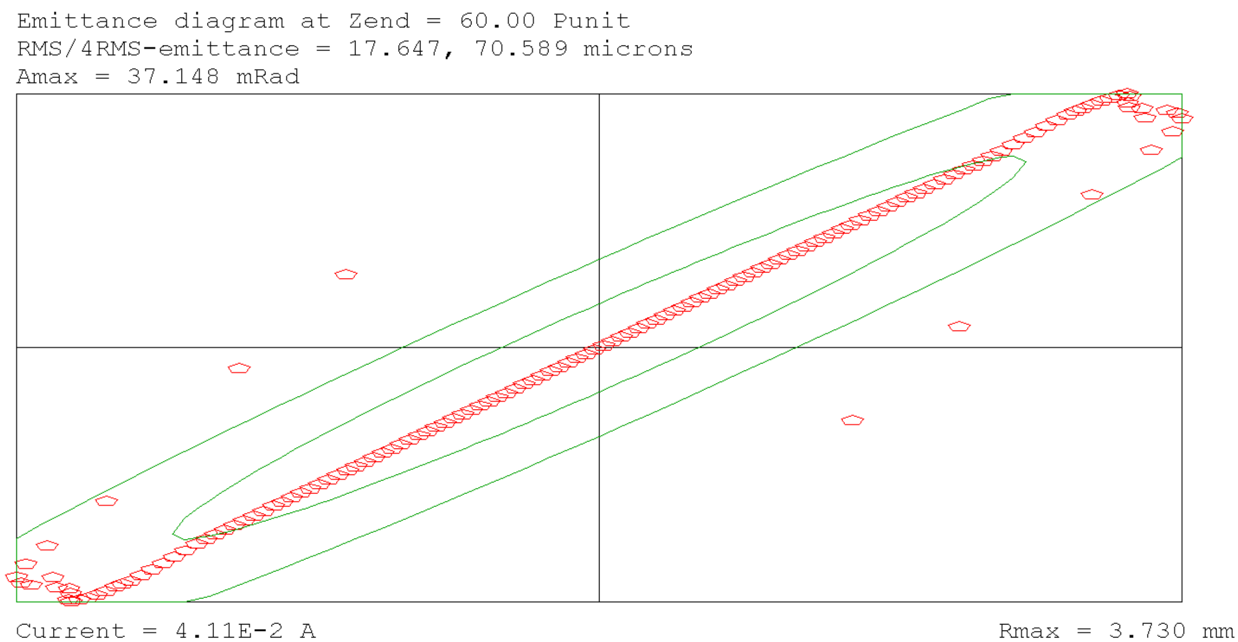

(b)

Figure 4.26 *Emittance plot of (a) three and (b) five electrode extraction.*

The PBGUNS and IGUN codes are widely used to solve the plasma meniscus by matching equipotential inside and outside the plasma region and compute the resultant particle trajectories for steady state beam transport. IGUN self-adjusts the ion extraction current on successive iteration cycles, adjusting the Debye length within the plasma region until the self-consistent solution for the shape and the location of the plasma meniscus is reached. PBGUNS utilizes a fine mesh region near the plasma emission surface, solving the plasma meniscus by matching the particle trajectories and the resultant space charge density distribution on adjacent mesh positions until the solution converses. These codes have two dimensional capabilities and are useful for simulation of cylindrically symmetric or rectangular slit extraction geometries.

In PBGUNS code the electrodes are described by line segments sketched onto a grid. The geometry is defined in axis symmetric terms. The axial magnetic field for the ECR proton ion source is entered by specifying a series of breakpoints along the beam axis. The program then interpolates between these points to give a distribution. It has been observed that the presence of an axial magnetic field did not appear to affect the beam trajectories in the PBGUNS simulations. PBGUNS simulation utilizes a self-consistent solver to define the shape of the ion emission surface at the extraction aperture. PBGUNS require initial ion energies of 2 - 10 eV with the velocity vector oriented in the direction of beam extraction for the simulation to work. Multispecies beams (such as hydrogen) are interactively specified in PBGUNS during the initial setup.

IGUN software calculates the electric fields and the trajectories of charged particles for a given configuration of electrodes, with applied voltages and particle initial conditions. It is a two-dimensional code, suitable for simulating the extraction of positive ions from plasma using ion ray optics, and electrostatic field based on solution of Poisson equation. The code starts with mesh independent input data containing coordinates of the electrodes (either axis-symmetric or rectangular, as entered), boundary conditions, number of the electrodes, potential of each electrode, plasma potential, current or plasma density or ion current density, fractions of ion species and or mass, electron and ion temperature etc. The mesh points are generated once potentials are applied to the fixed electrodes. It automatically determines the ion extraction current during successive cycles, by matching the electric field gradient outside and inside of the plasma. This process is repeated until a self-consistent solution of the Poisson equation for a good quality extracted particle beam is determined. The resulting distribution of potential along the beam edge is used to match the Laplace's solution in the region external to the beam that will support the charge flow. The code first check the input file and then provide the interactive colored graphics plots of equipotential lines, beam trajectories, electrode log tables for different ion species, emittance diagrams, beam profiles, surface fields along the beam axis, surface fields along the problem boundary, the data files for all the plots, twiss parameters etc. The ray tracing is simulated by numerical integration and fields are differentiated and interpolated from the previous potential map. It also provides extensive supporting functionality in geometry definition, data recording, visualization etc.

Figure 4.27 shows the plot of ion beam current with extraction voltage. The ion beam current increases with the increase of extraction voltage govern by space charge limiting current. Figure 4.28 shows the plot of extracted beam current versus plasma density. The beam current varies more or less linearly with plasma density. For 50 mA beam current the plasma density requirement is 2.9×10^{11} cm^{-3}. Figure 4.28 shows the plot of beam current and RMS emittance. For 50 mA beam current the RMS emittance is 25 mm - mrad. It is seen from Figure 4.29 that the RMS emittance increases with increase in beam current. This is because the beam emittance increases with the space charge forces due to increase in beam current. Figure 4.30 shows the plot of beam RMS emittance versus suppressor voltage. The RMS emittance is minimum for suppressor electrode voltage between - 2 to - 4 kV. Figure 4.31 shows the plot of RMS emittance versus plasma electrode angle. The RMS emittance is minimum for plasma electrode angle of 45^0.

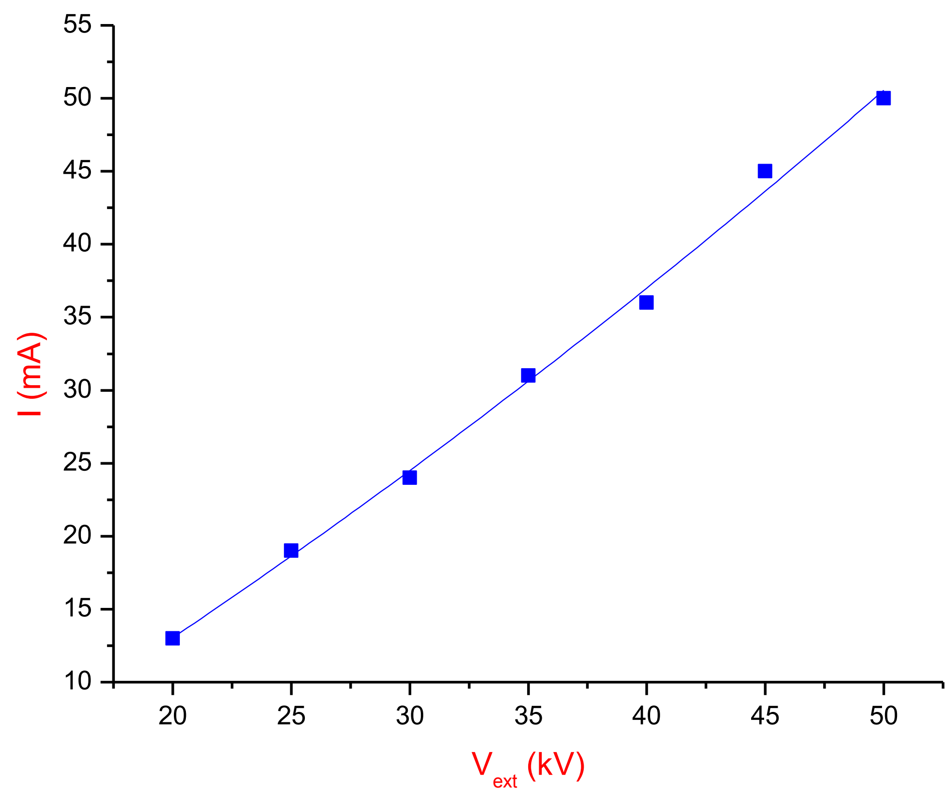

Figure 4.27 *Beam current versus extraction voltage for suppressor electrode voltage -2 kV.*

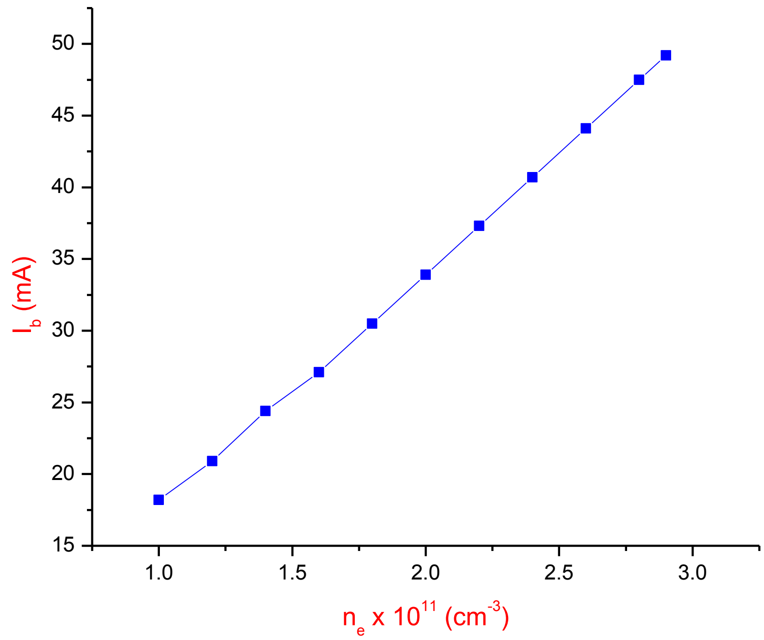

Figure 4.28 *Beam current versus plasma electron density for plasma electrode voltage +50 kV and suppressor electrode voltage -2 kV.*

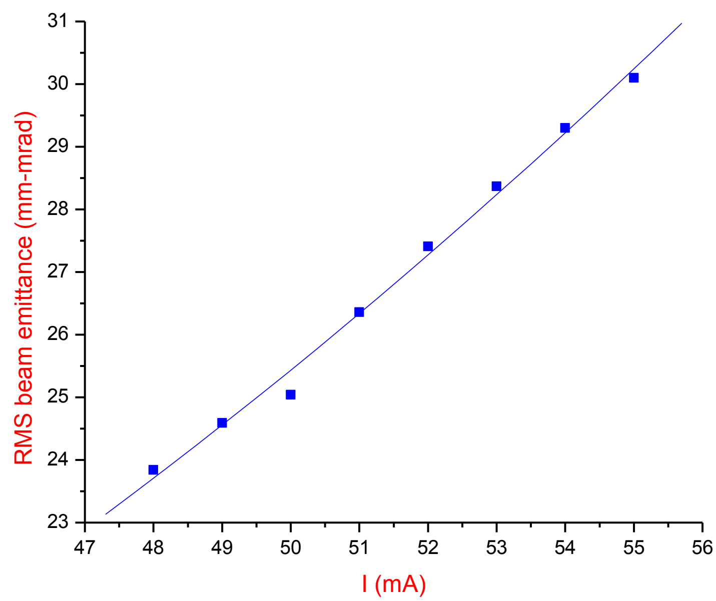

Figure 4.29 *RMS beam emittance versus beam current for plasma electrode voltage +50 kV and suppressor electrode voltage -2 kV.*

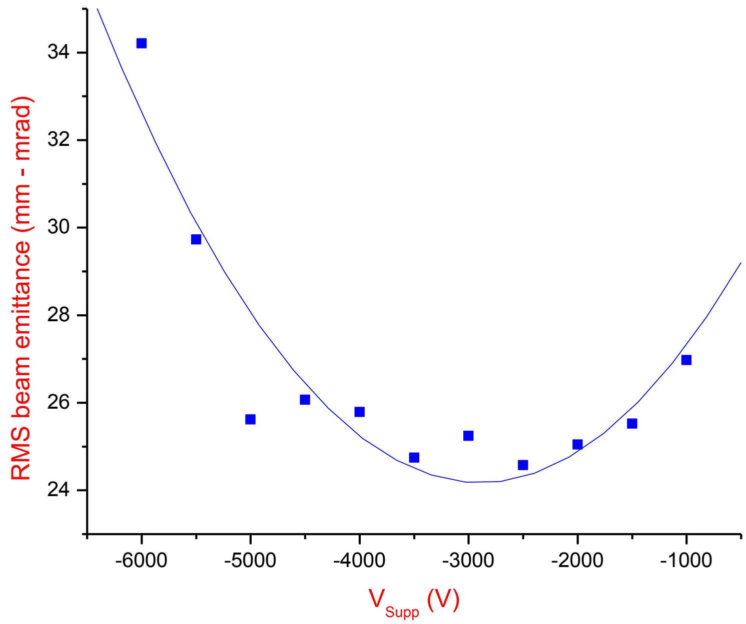

Figure 4.30 *RMS beam emittance versus suppressor electrode voltage for plasma electrode voltage +50 kV, suppressor electrode voltage -2 kV and beam current of 50 mA.*

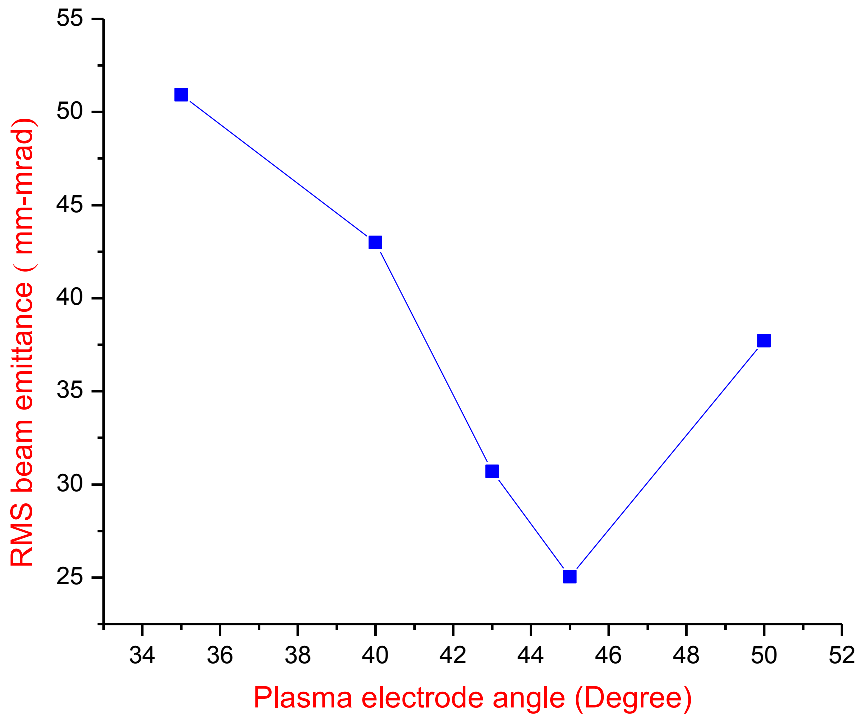

Figure 4.31 *RMS beam emittance versus plasma electrode angle for plasma electrode voltage +50 kV, suppressor electrode voltage -2 kV and beam current of 50 mA.*

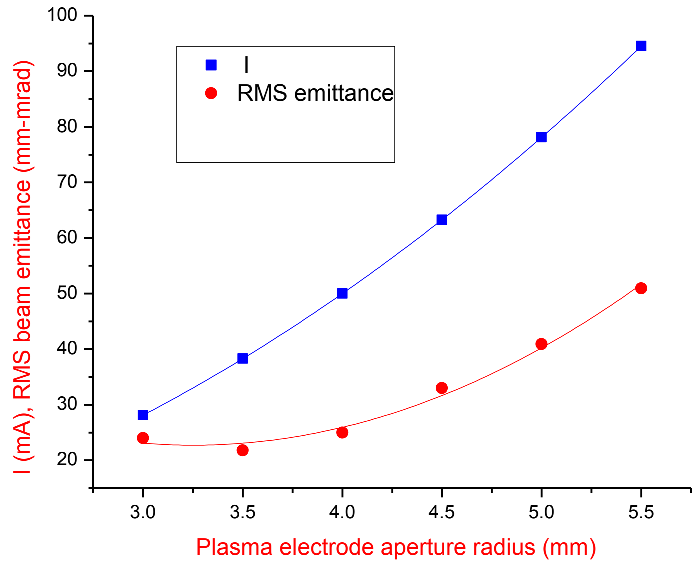

Figure 4.32 *Beam current (square dots) and RMS beam emittance (round dots) versus plasma electrode aperture radius for plasma electrode voltage +50 kV and suppressor electrode voltage -2 kV.*

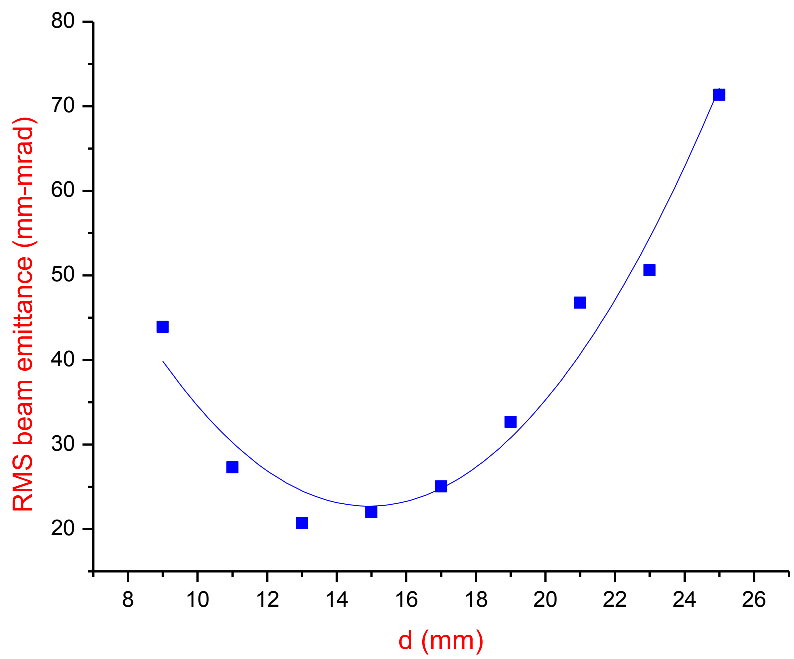

Figure 4.33 *RMS beam emittance versus acceleration gap d for plasma electrode voltage +50 kV, suppressor electrode voltage -2 kV and beam current of 50 mA.*

Figure 4.32 shows the plot of extracted beam current and RMS emittance versus plasma electrode aperture radius. The extracted beam current increases as r^2, where r is the plasma electrode aperture radius. The RMS emittance is near minimum for plasma electrode aperture radius of 4 mm. Figure 4.33 shows the plot of RMS emittance versus accelerating gap between the plasma electrode and suppressor electrode. The RMS emittance is near minimum for accelerating gap of 17 mm.

Based on this analysis the extraction electrodes of three and five electrode ion source were fabricated. The schematic of plasma chamber and extraction electrodes of three electrode ion source is shown in Figure 4.34 to 4.37 and that of five electrodes is shown in Figure 4.38 to 4.43. The fabricated electrodes are shown in Figure 4.44 (a) and (b).

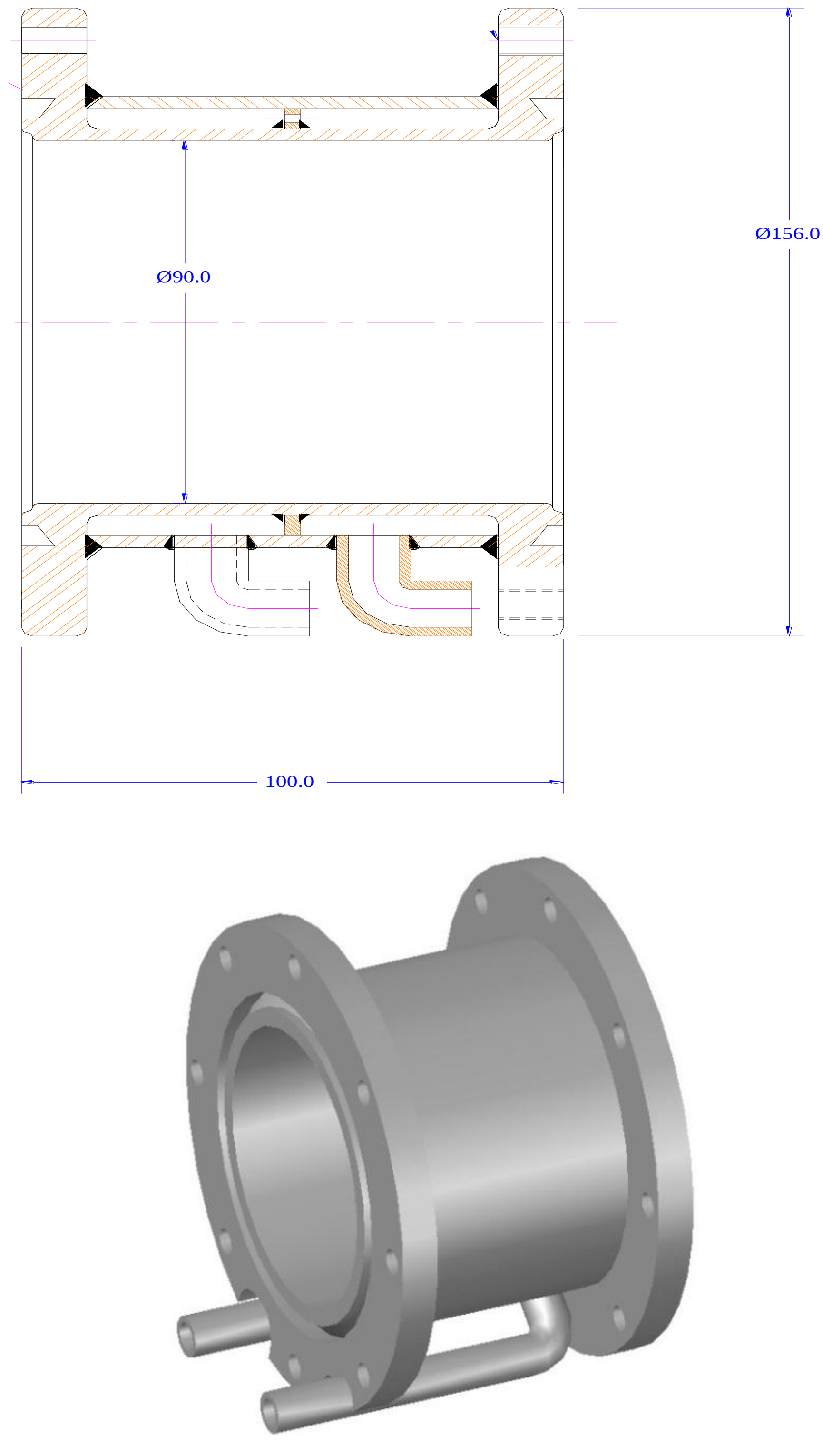

Figure 4.34 *Schematic of water cooled plasma chamber made of SS 304L*.

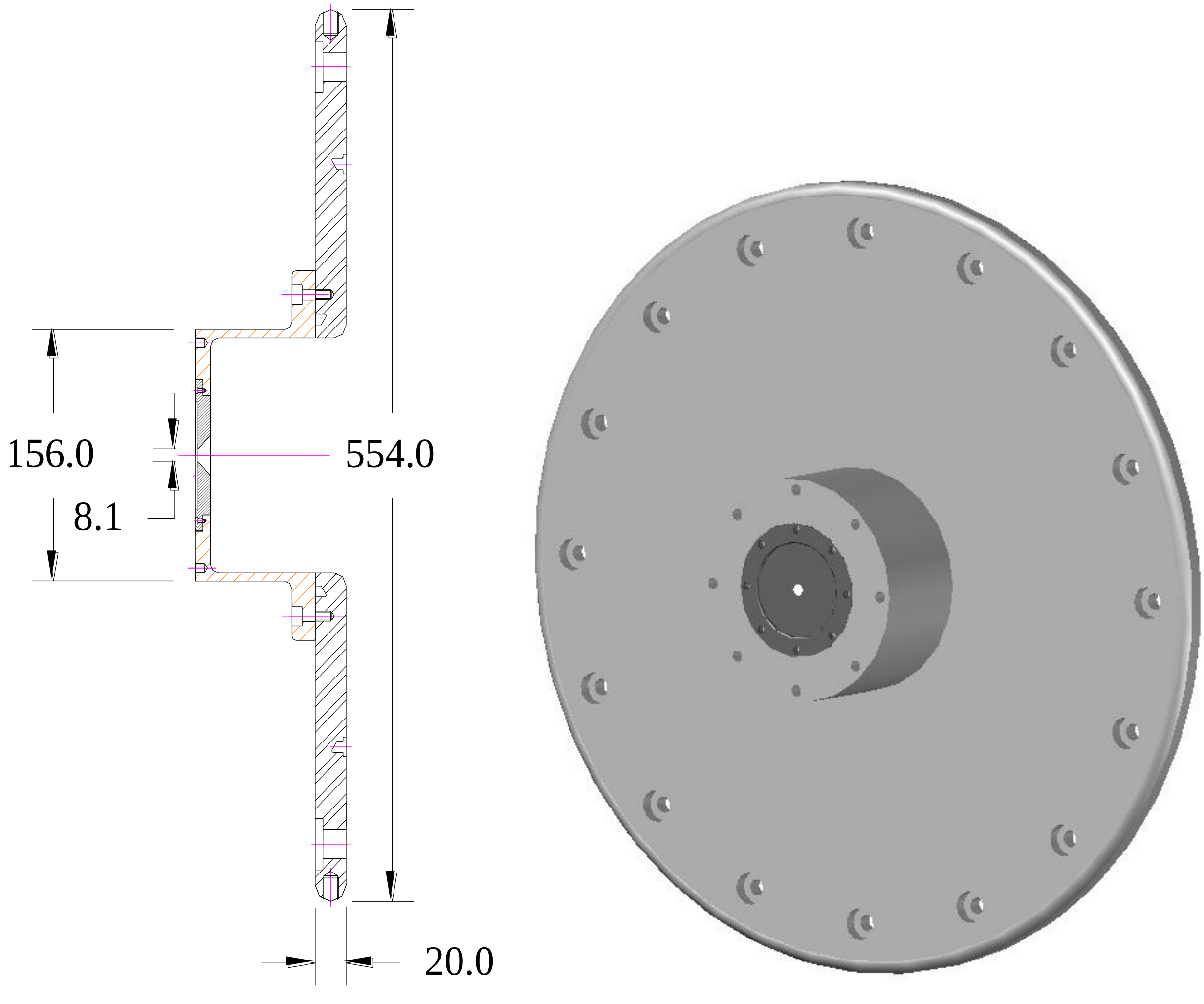

Figure 4.35 *Schematic of plasma electrode made of SS 304L.*

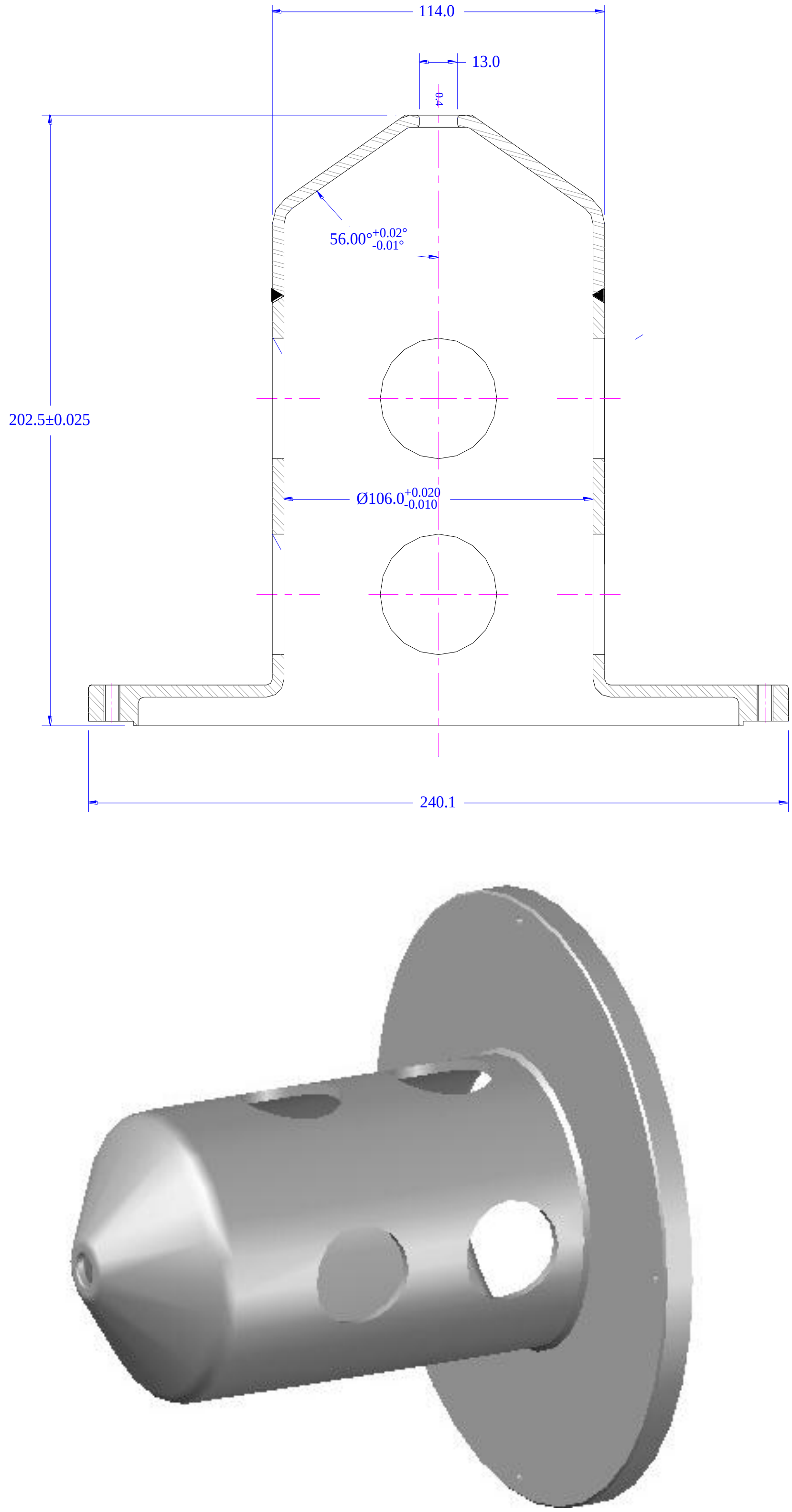

Figure 4.36 *Schematic of suppressor electrode made of SS 304 L.*

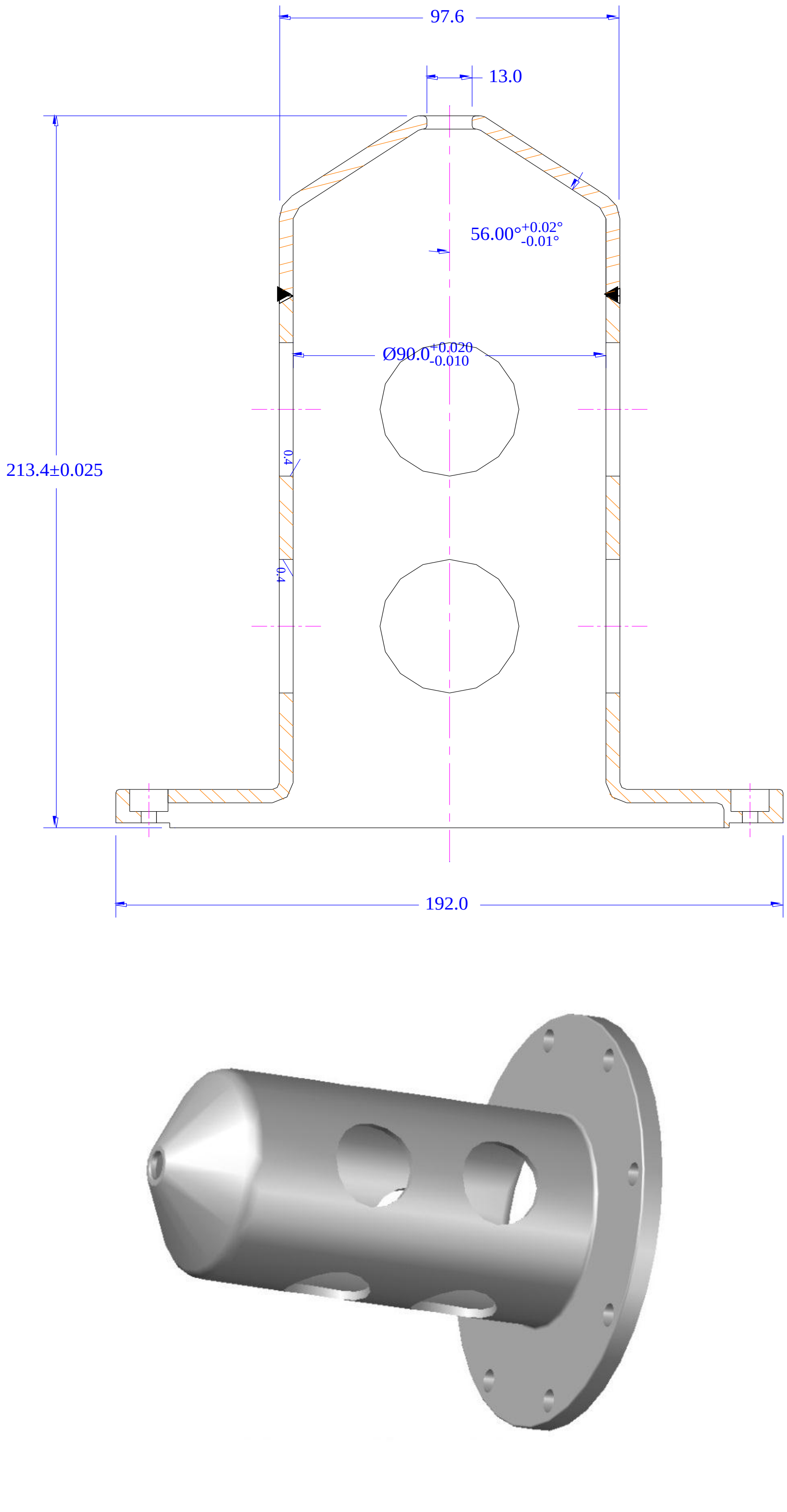

Figure 4.37 *Schematic of ground electrode made of SS 304 L.*

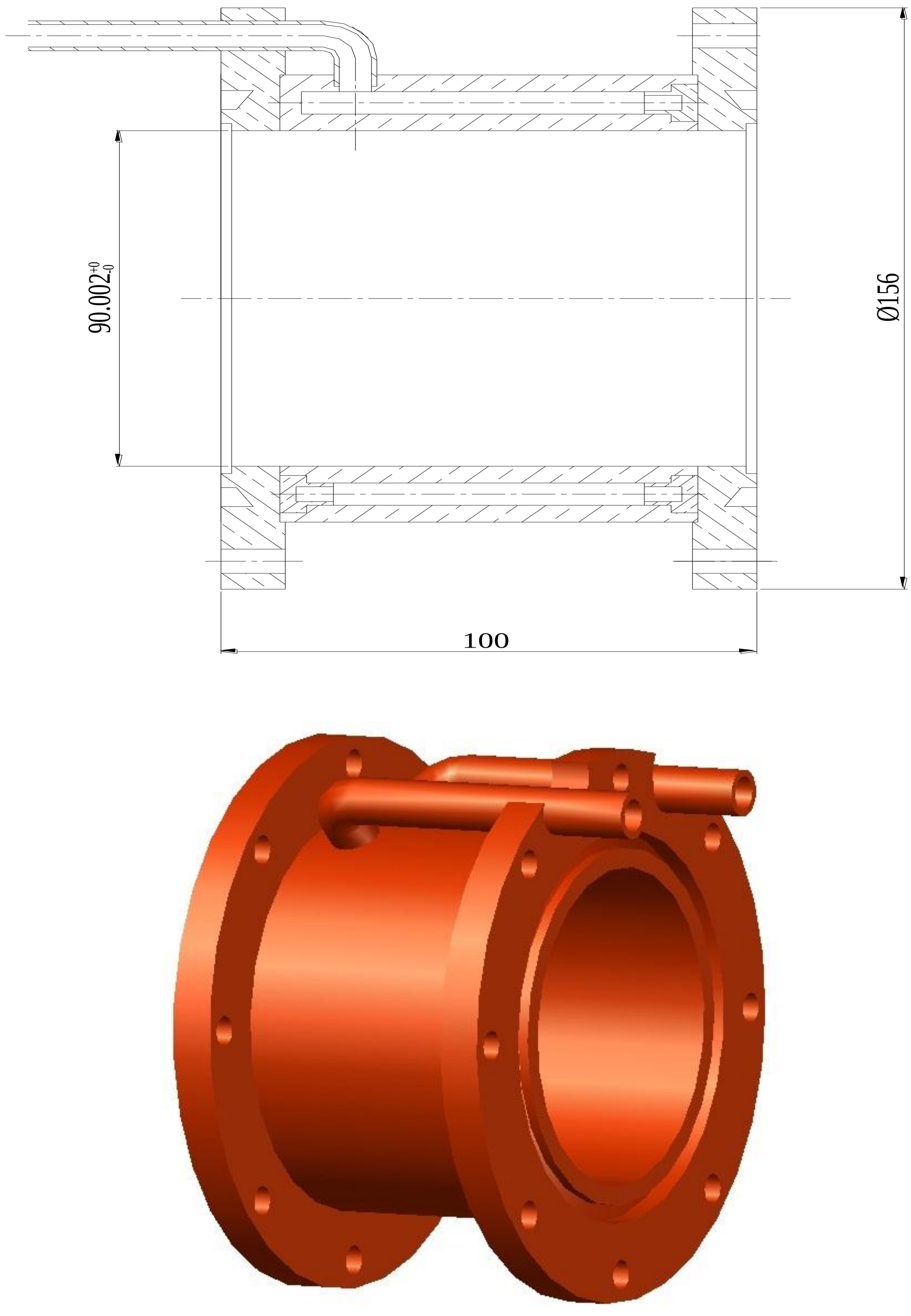

Figure 4.38 *Schematic of water-cooled plasma chamber made of OFHC copper.*

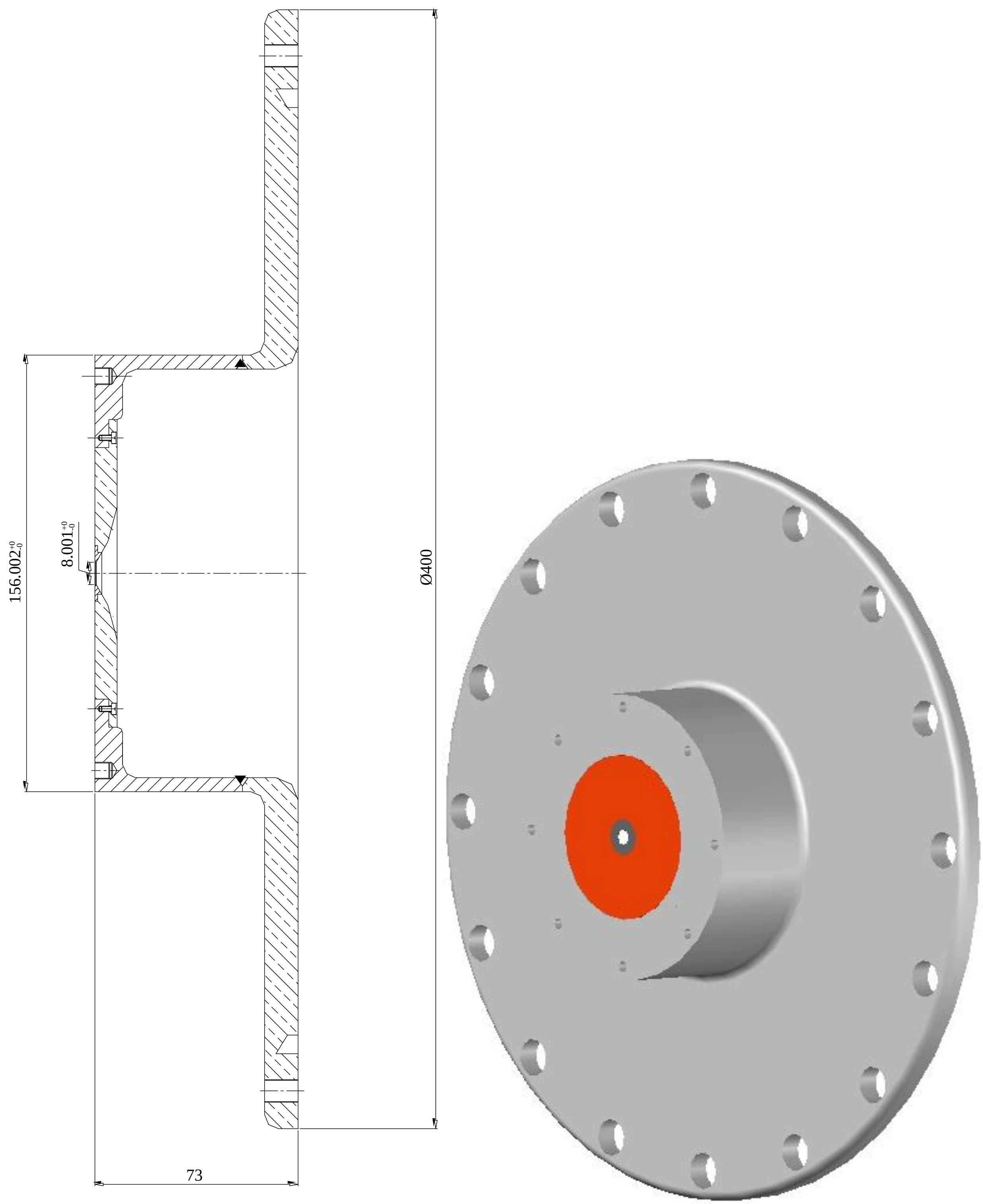

Figure 4.39 *Schematic of plasma electrode made of OFHC copper.*

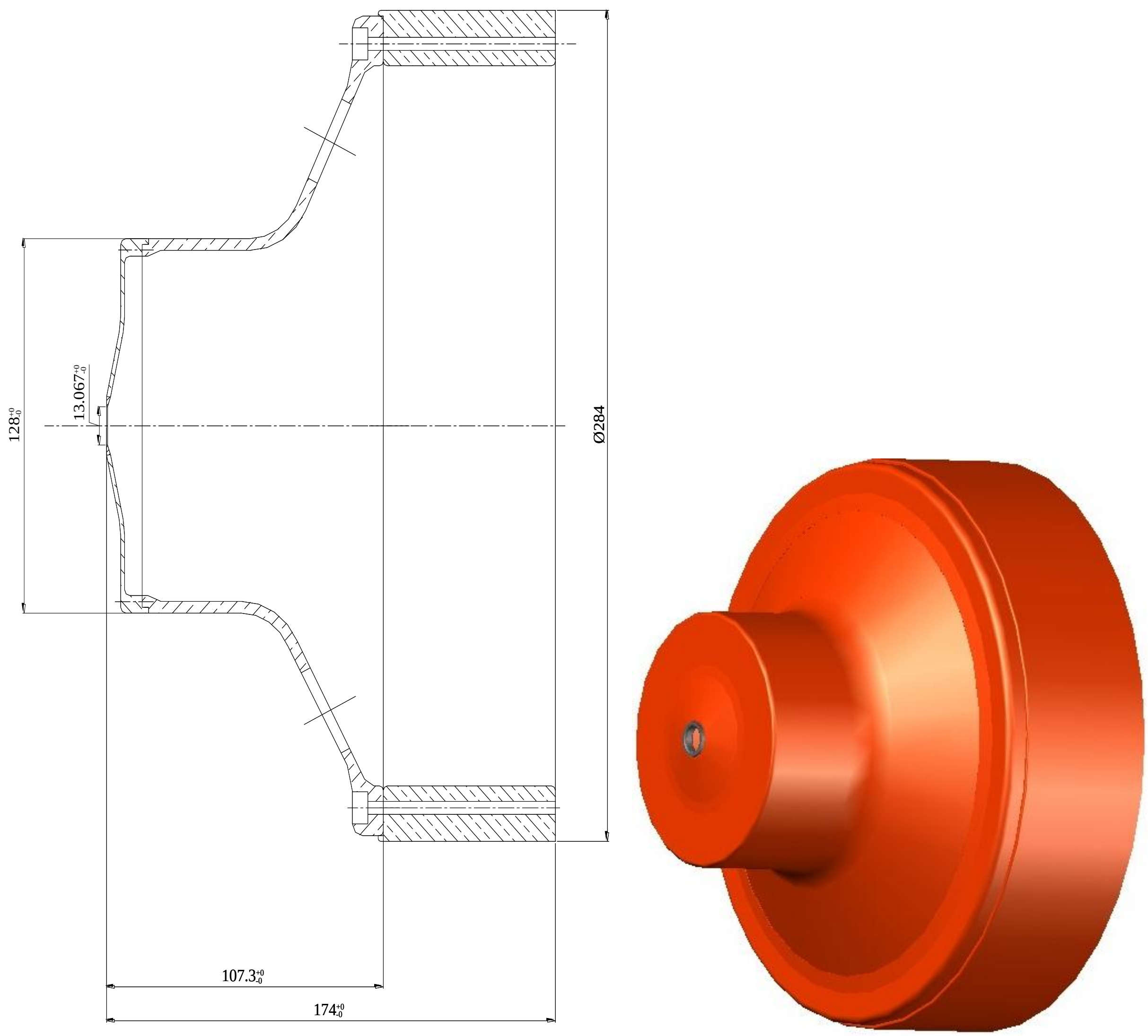

Figure 4.40 *Schematic of puller electrode made of OFHC copper.*

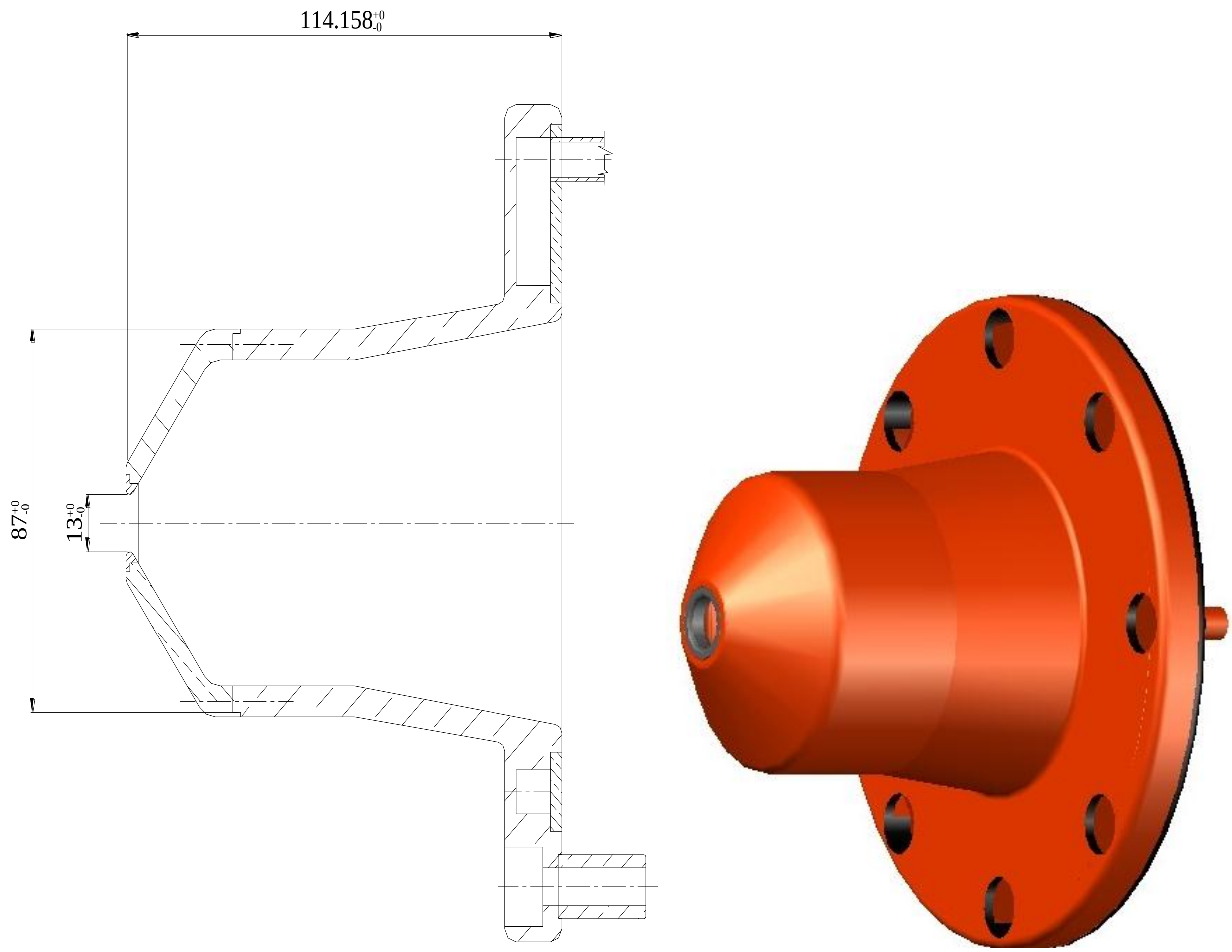

Figure 4.41 *Schematic of first ground electrode (water-cooled) made of OFHC copper.*

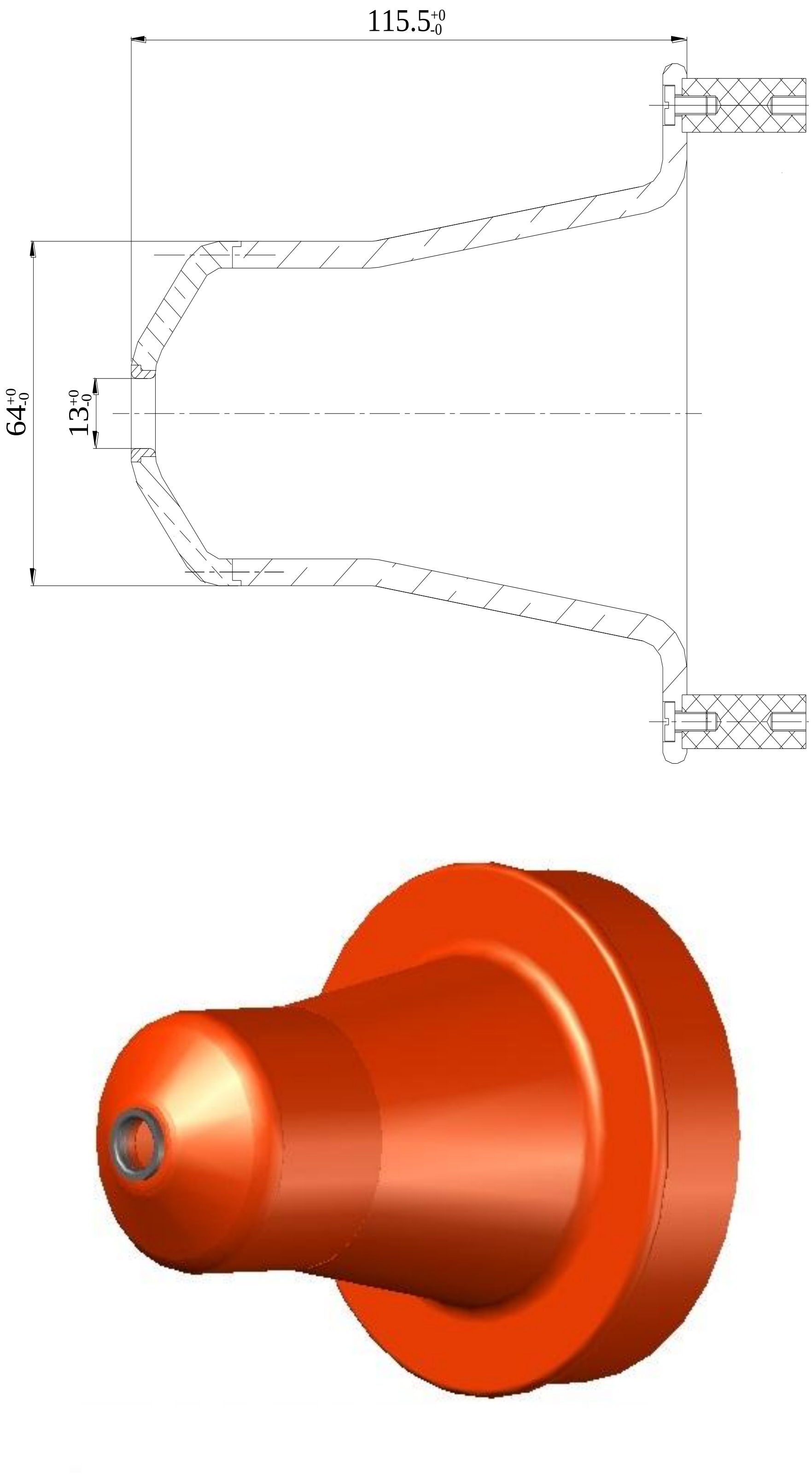

Figure 4.42 *Schematic of second ground electrode made of OFHC copper*.

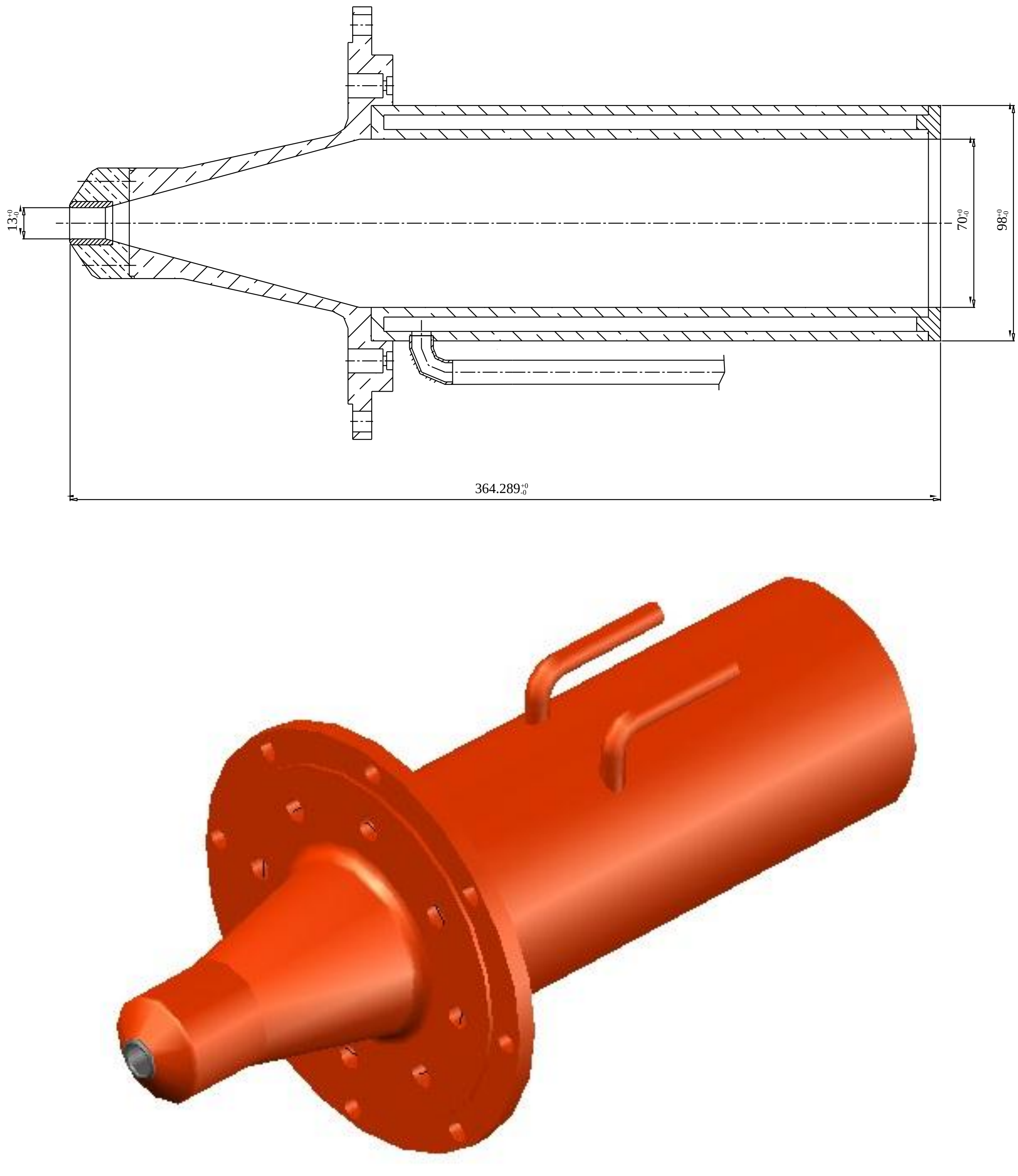

Figure 4.43 *Schematic of second ground electrode (water-cooled) made of OFHC copper.*

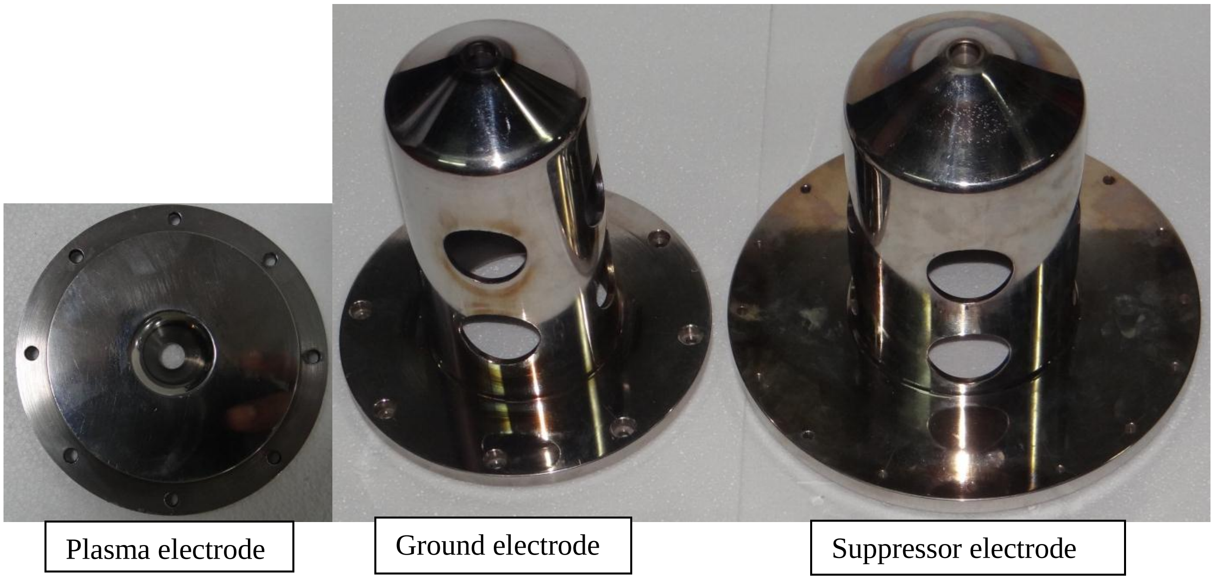

(a)

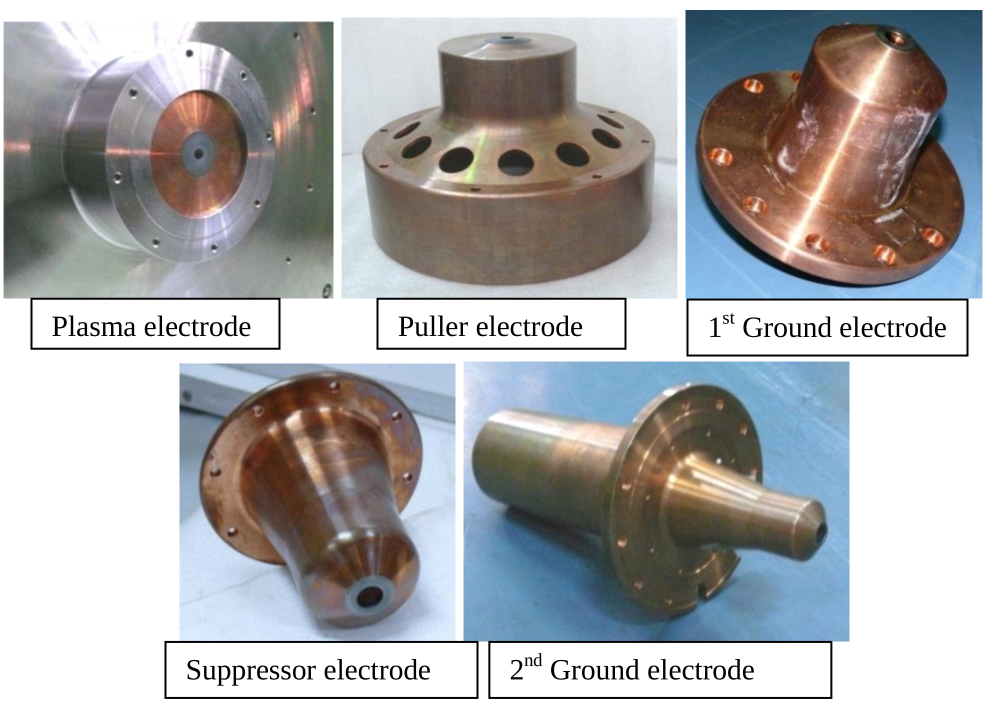

(b)

Figure 4.44 *Fabricated extraction electrodes of (a) three and (b) five electrode ion source.*

The extraction electrode power supplies of the ion source are shown in Figure 4.45(a) and (b). The high voltage power supplies of M/S Gamma and M/S Spellman make were used for ion extraction. The M/S Gamma make regulated high voltage DC power supplies are of following specifications: (1) 0 – 50 kV, 0 – 100 mA and (2) 0 – (-5) kV, 0 – 100 mA with ± 0.01% voltage and current regulation, 0.1% ripple, 0.01% stability and remote control operation via RS 232. The M/S Spellman make power supplies are of following specifications: (1) 0 – 60 kV, 0 – 100 mA and (2) 0 – (-6) kV, 0 – 100 mA with ± 0.005% voltage and current regulation, 0.1% ripple, 0.01% stability and remote control operation via RS 232.

(a) (b)

Figure 4.45 *High voltage power supplies (a) M/S Gamma (b) M/S Spellman make.*

4.5 Assembly of Three and Five Electrode Ion Source on Test Stand

After fabrication of all the components of the three and five electrode ECR proton ion source, the components have been assembled on the test stand [3, 73-76]. For ion source assembly, the vacuum diagnostic chamber was first installed on the support stand and leveled. Then the suppressor and ground electrode were assembled on one of the end flanges. The suppressor and the ground electrode were separated by MACOR insulator that isolates – 6 kV of suppressor voltage. Two alumina ceramic insulator rings of 352 mm inner diameter, 374 mm outer diameter and 74 mm length were used to isolate the 50 kV high voltages between plasma electrode and ground electrode as shown in Figure 4.46.

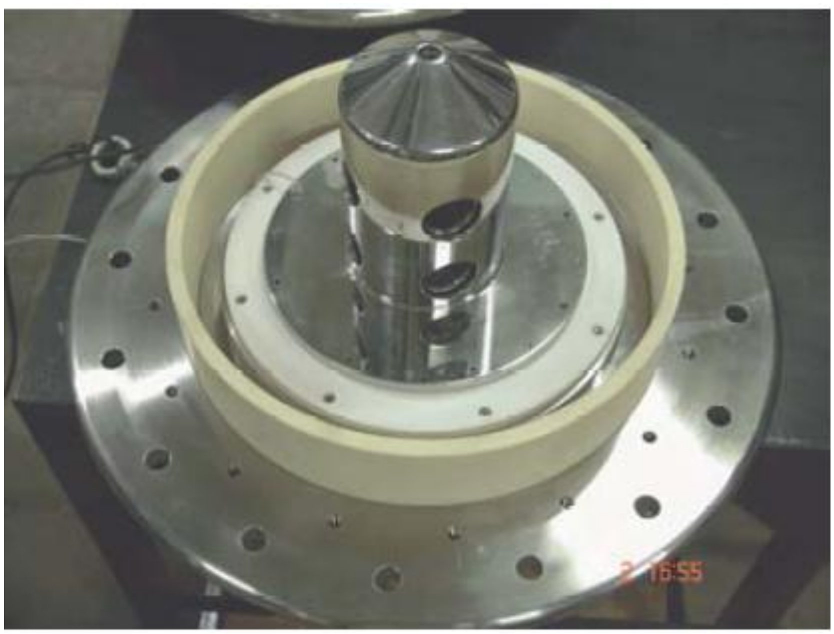

Figure 4.46 *Assembly of suppressor electrode and ground electrode on end flange.*

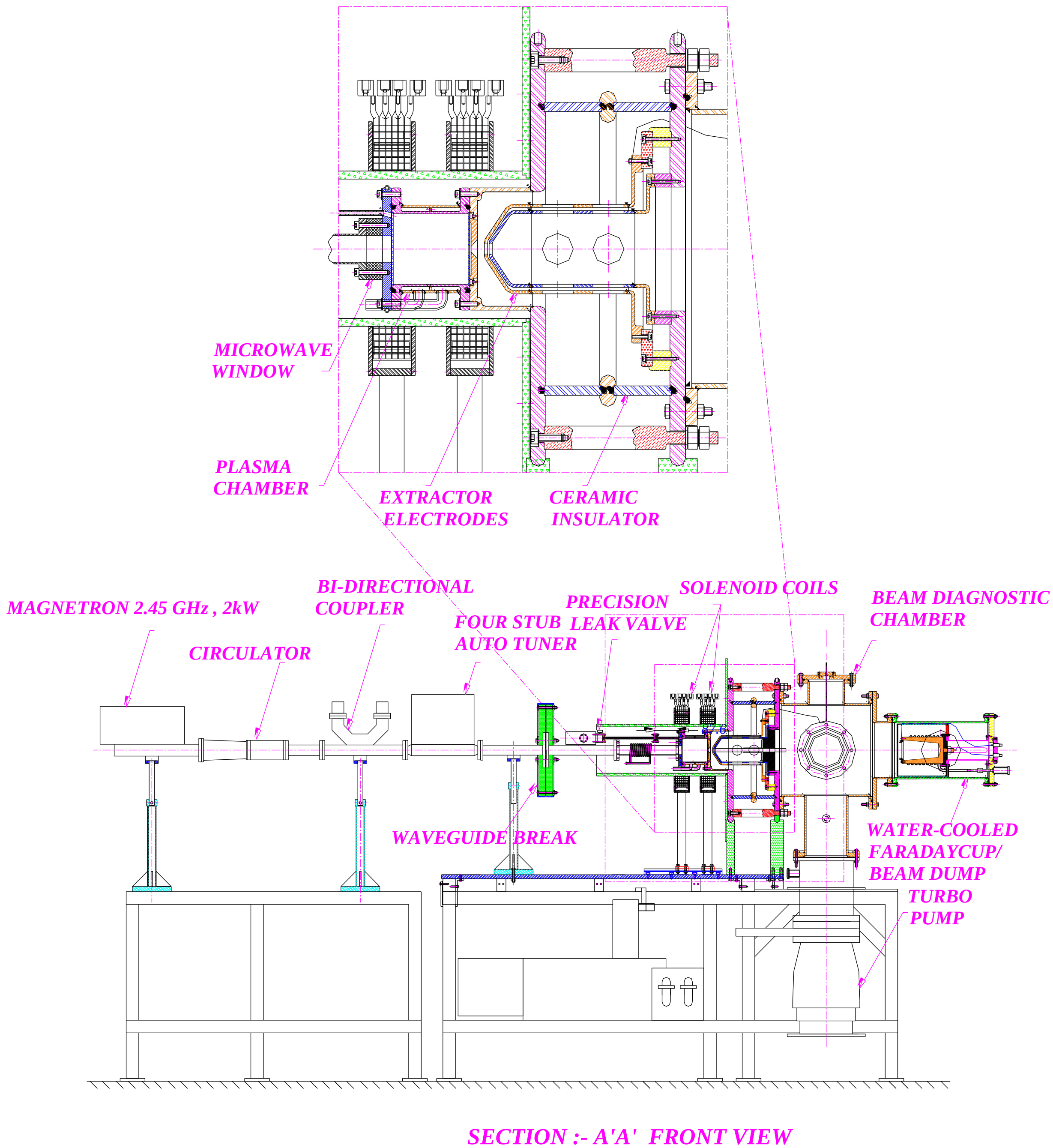

Figure 4.47 *Schematic of three electrode ion source.*

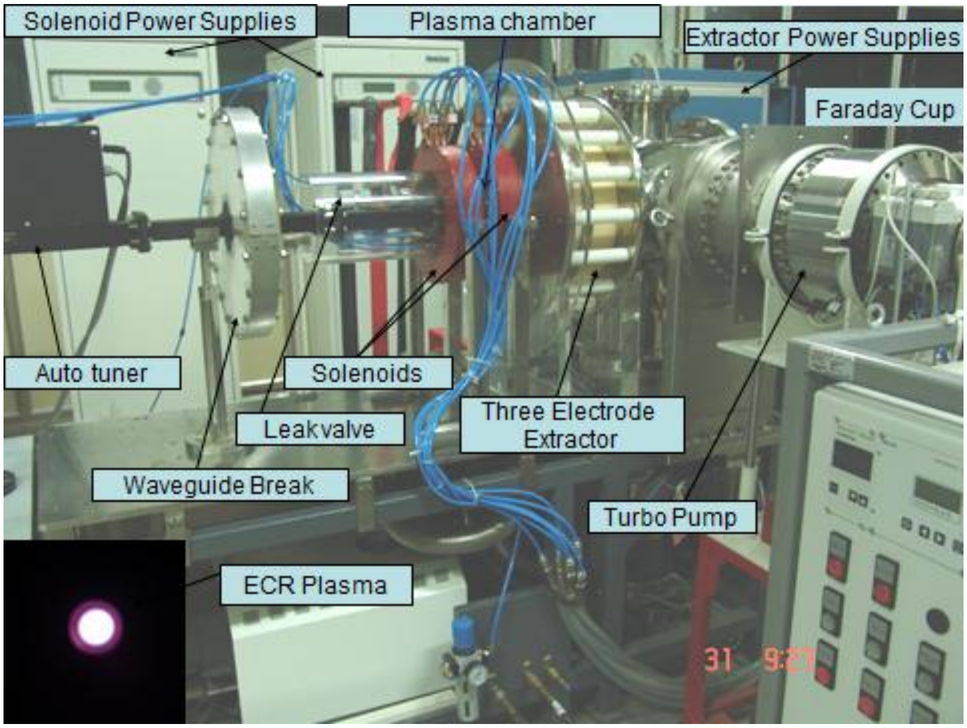

Figure 4.48 *Assembled three-electrode ion source.*

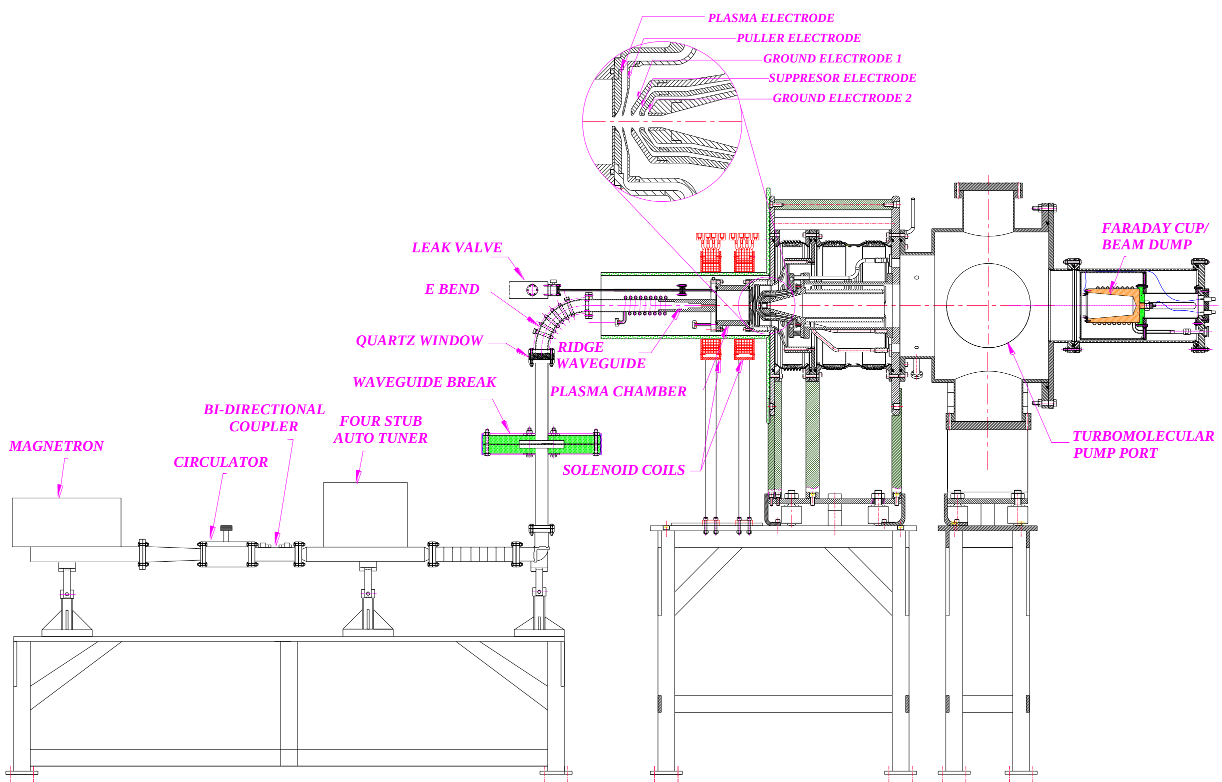

Figure 4.49 *Schematic of five electrode ion source.*

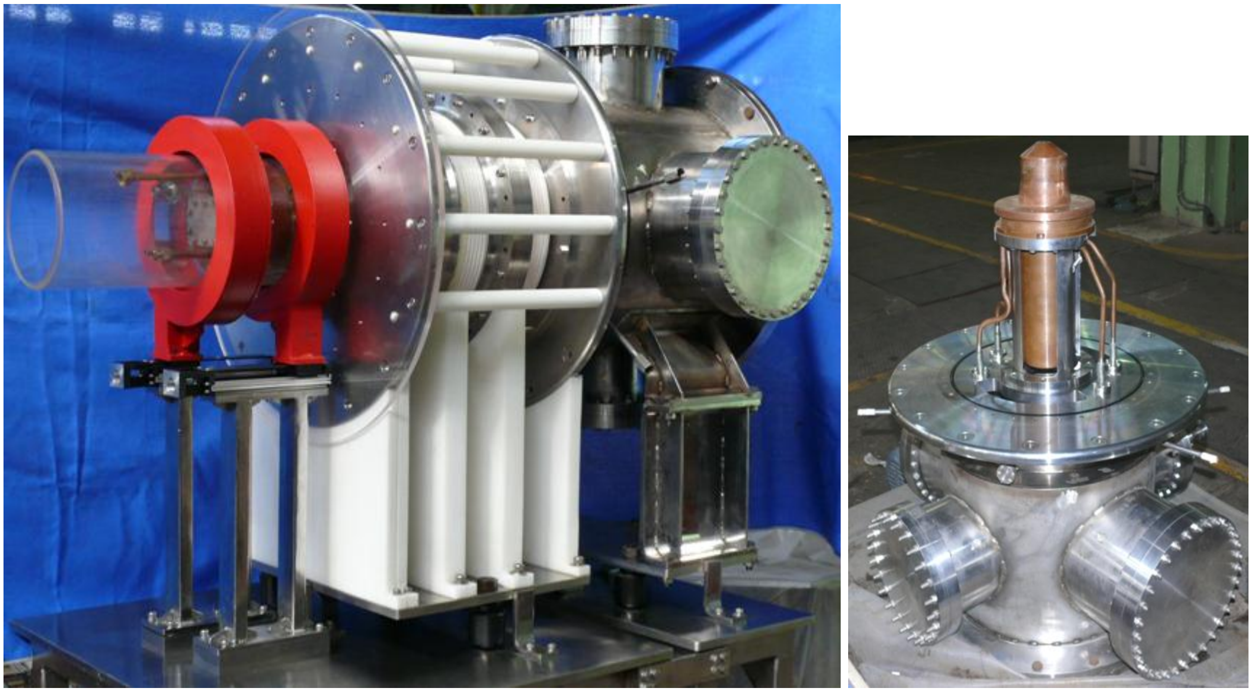

Figure 4.50 *Assembled five electrode ion source on test stand.*

The plasma chamber was assembled at one end flange of the extractor electrode assembly. The other end flange of extractor assembly was connected to the vacuum diagnostic chamber that was installed on the test bench. The extractor assembly was supported on the test bench using Perspex insulator.

The assembly was aligned to an accuracy of 0.2 mm over length of 2m. The turbo-molecular pump and dry roughing pump were connected to one of the side ports of the vacuum diagnostic chamber. The vacuum gauges were connected to the port provided in the diagnostic chamber. The whole assembly was then enclosed by blank flanges at two ends and vacuum tested to better than 10^{-6} mbar. The high voltage test was also performed under vacuum to the voltage up to 60 kV. Two solenoid coils were assembled on the test bench support plate enclosing the plasma chamber. The microwave generator and transmission components were assembled and connected to the plasma chamber with microwave quartz window. The schematic and actual set up three electrode ion source is shown in Figures 4.47 and 4.48. The schematic and actual setup of five electrode ion source is shown in Figures 4.49 and 4.50.

4.6 Low Conductivity Process Water System

For cooling the ion source components, a low conductivity process water system has been designed, fabricated, installed and commissioned to remove heat dissipation due to joule heating [77]. Low conductivity water (LCW) helps in avoiding corrosion and scaling on heat exchanging surface. It provide water with very low silica content (< 0.01 ppm) and it is well known that the efficiency of the cooling system decreases if there is silica content in cooling water. It also increases the leakage current when used as cooling media at 50 kV potential. Typical values of water characteristics obtained from these systems are: (1) conductivity < 1 μS/cm, (2) total dissolved solids < 1 ppm and (3) pH variation is within 6.8 – 7.2. The LCW system was used for cooling twenty components of the ion source and was designed for 65 kW heat removals, with pumping capacity 200 lit/min ($12m^3/h$). It comprises of makeup water system (demineralized water column) and self-circulation through ion exchange beds (resin column) for improving conductivity (polishing), recirculation pumps, SS-304 storage water tank, flexible tubing connections and instrumentation system.

The salient features of the LCW system are: (i) automatic improving conductivity (polishing) of demineralized water if conductivity goes beyond the set limit, (ii) independent make-up water facility from raw water source, (iii) recirculation pumping system to cope with 200 lit/min requirement at 5 kg/cm^2 and (iv) measurement and interlock system with remote signals for processing the ion source subsystem controls. More than 50 m of metallic piping ranging from 1” to 2” and 100 m metallic and nylon braided PVC flexible piping carry the treated and cooled demineralized water from recirculation system to various components of the ion source. The piping is made of SS-304 stainless steel. The cooling system parameters are listed in Table 4.6.

Table 4.6: *Cooling system parameters of ion source*

Parameters	Designed values
Cooling power (kW)	65
Inlet Temperature (^{0}C)	30
Volume of demineralized water (liters)	1200
Flow rate of demineralized water (liters/min)	200
Flow rate of chill water (liters/min)	100
Flow rate of polishing and make-up water (liters/hour)	300
Supply pressure (kg/cm^2)	5
Pumps	3
Outlet temperature (^{0}C)	35
LCW conductivity (μS/cm)	1

The cooling system has to fulfill three main requirements: reliability and safety, low level of mechanical vibration (dB) and temperature stability (within ± 1^{0}C). For reliable functioning of the system, a spare recirculation pump has been provided on-line, and both pump work alternately. Safety is ensured in case of leakage, by high sensitivity flow switches on each distribution manifold. Continuous water conductivity monitoring and set limit has been adopted (< 1 μS/cm) using on-line conductivity meter. In order to reduce vibrations, suitable pipe diameter has been selected for required flow, so as to keep the water velocity in the piping low (less than 1 m/s). Reinforced concrete foundation with 10 mm thick rubber pad has been used for the pumps to arrest vibration.

The cooling system has four loops: (i) primary loop of LCW which extract the heat generated in various sub-systems of the ion source, (ii) secondary loops of soft water which exchanges heat from primary loops through plate type heat exchanger (PHE) and dissipate to chilled water, (iii) DM loops (make-up system) provides an initial charge of LCW which is to be stored in the storage tank through the ion exchanger stage, and (iv) conductivity improving (polishing) system. Figure 4.51 shows the schematic and Figure 4.52 shows the cooling system of the ion source.

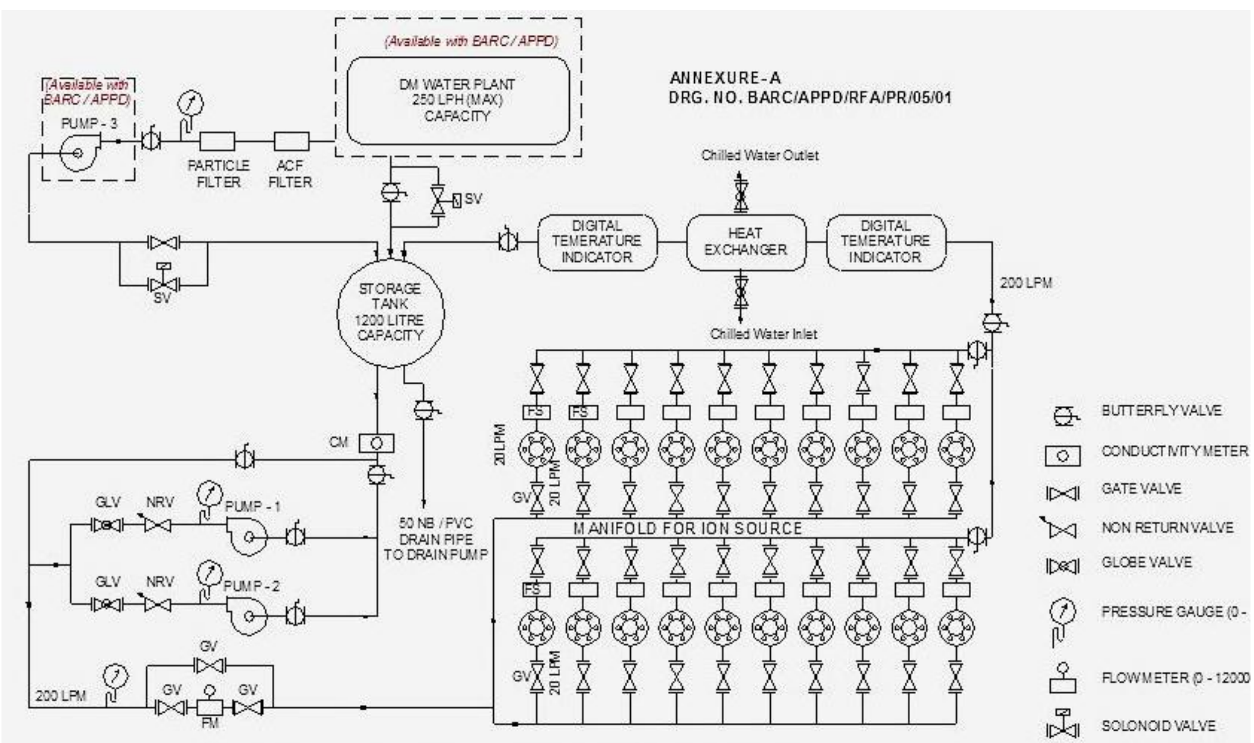

Figure 4.51 *Schematic of low conductivity process water system for the ion source.*

Figure 4.52 *Low conductivity process water system of the ion source*.

In Figure 4.52, the raw water is initially passed through polyethylene cartridge filter (5 μ size), activated carbon filter, cation, anion and mixed bed exchange resins. When raw water passes through cation exchange resin, all cation from water are captured and H^+ ions are released. The released H^+ ions react with OH^- released by anion exchanger to from water. Thus all ions or minerals from water are removed by two exchangers. The capacity of each column is 300 lit/h. The deionized water after passing through ion exchanger are stored in SS 304 storage tank of 1200 liters capacity and circulated through fully closed type centrifugal pump, to provide 200 lit/m flow at 5 kg/cm^2 pressure to cool various subsystem of the ion source. Flow-control valves are used in each subsystem, to balance constant volume flow, reducing high installation cost and complex piping network.

The major components of the ion source to be cooled are: solenoid coils and power supplies, RF generator, waveguides, plasma chamber, extractor electrodes, vacuum system and Faraday cup/beam dump etc. given in Table 4.7.

Table 4.7: Cooling requirement of ion source

Subsystems	Wattage (kW)	Flow rate (lit/m)
Solenoid coil power supply (2 Nos.)	8 each	20 each
Solenoid coils (2 Nos.)	5 each	10 each
Microwave systems (magnetron, window and water load)	2	5
Plasma chamber	2	5
Ridge waveguide	1	3
Waveguide bend	2	5
Suppressor and ground electrode	2	5
Faraday cup / beam dump	2	6
Turbo-molecular pumps (2 Nos.)	1.6 each	2 each
Dry roughing pumps (2 Nos.)	1.6 each	2 each
Solenoid focusing magnet	14.8	10
Analyzing magnet	3.7	6

The parameters of water e.g., temperature, conductivity and flow rates are monitored at various point of distribution line. RTD based digital temperature indicator and conductivity meter provides analog signals for remote transmission. Conductivity improving (polishing) operation is automated by means of a solenoid valves interlocked with conductivity meter. Automated controls and interlocks of process parameters have been designed and implemented for reliable and safe operation.

The reliable and longtime stable operation of LCW system has been established. The demineralized water having pH of 6.5 – 7.2 and conductivity < 1 μS/cm has been achieved. The successful operation of LCW system has resulted in stable operation of ion source for several hours.

4.7 Summary

This chapter describes the design, fabrication, assembly and testing of three and five electrode ion source. The design detail of microwave heating system, plasma chamber, magnetic system, extraction system, vacuum system, gas injection system and low conductivity process water system is presented. The microwave system consists of magnetron, circulator, dual directional coupler, four stub automatic tuner, DC waveguide break, double ridged waveguide, waveguide bend and microwave window. The DC waveguide break and double ridged wave guide have been designed and fabricated. The magnetic field configuration of the ion source was generated using two solenoid coils. The solenoid coils were designed and fabricated. The vacuum system has been designed and the vacuum chamber and interconnections were fabricated. The vacuum pumps of designed capacity, vacuum gauges and vacuum valves were procured. The gas injection system has been designed and the leak valve, shut off valve, flow meter and pressure sensor were procured. The ion extraction system is critical part of the ion source and was designed and fabricated. The parametric studies were performed to reduce the beam size and divergence. For three electrode ion source the electrodes were fabricated in SS 304 L and for five electrode ion source it were fabricated in OFHC copper. The ion source components has been assembled in the test stand and tested for vacuum better than 10^{-6} mbar. The high voltage insulation test of the ion source was carried out up to 60 kV. The low conductivity process water system has been designed, fabricated, installed and commissioned to cool the ion source components.

Chapter 5.

Plasma Characterization of ECR Proton Ion Source

In order to understand about the plasma produced by ECR ion source that qualifies the ion beam, plasma diagnostic using electrostatic probes were performed. The magnetic fields produced by the solenoid coils were characterized to determine the operating range necessary to satisfy resonance condition under minimum reflected microwave power. A single electrostatic (Langmuir) probe was used to measure electron temperature and plasma density under various operating conditions.

The plasma diagnostic technique using electrostatic probe was chosen for their physical simplicity and universality. The Langmuir probe is an easy device to implement, but the data analysis and interpretation becomes involved, especially in the presence of magnetic field. The bulk of Langmuir probe theory relies on electron energy distribution function to be Maxwellian in form, which may not be true in the case of ECR plasma.

5.1 Magnetic Field Characterization

The magnetic field was measured using an F.W. Bell 5070 Gauss/Tesla meter as shown in Figure 5.1. The field mapping of plasma chamber was performed every 5mm along z axis at $x, y = 0, \pm 15$ and ± 30 mm. The probe was oriented along the axis of the chamber and since the transverse fields were considered negligible in this case, only the axial probe was used. The $x, y = 0$ on the axis of the plasma chamber under the microwave entrance port was probed at various coil currents to establish the approximate current necessary to meet two resonant field at the entrance and exit of plasma chamber. Further adjustment for optimum resonance conditions was done by maximizing plasma brightness. The probe for this Gauss meter is 15 cm in total length, and has a maximum diameter 5 mm. It is attached to the meter by a 1.2 m long wire cable. The probe was held in place by the cavity made at various radial locations on Perspex solid cylinder that fits on the plasma chamber. The probe was pulled along the inside of the Perspex cylinder marked in 5 mm increments and magnetic field recording was made.

A graph comparing the magnetic fields along z and at x and y = 0, ± 15 mm and ± 30 mm is shown in Figure 5.2. The resonance field of 875 G is present in the plasma chamber region. The magnetic field is more or less uniform along z in both x and y direction with maximum variation of ± 50 G. The configuration of magnetic field is obtained under the minimum reflected microwave power condition.

Figure 5.1 *Gauss/Tesla meter with axial Hall probe.*

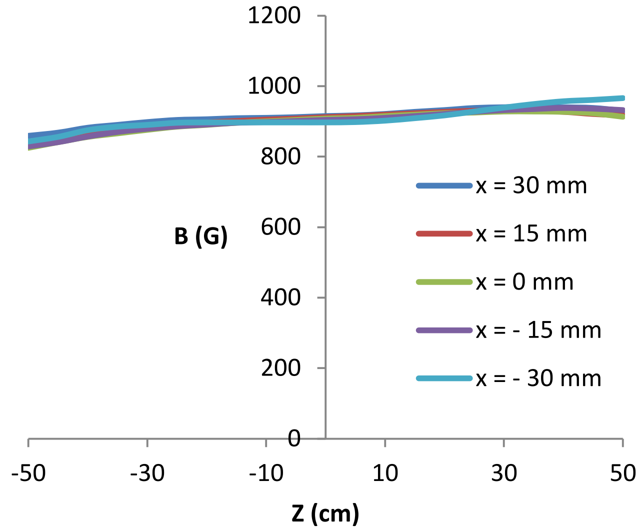

(a)

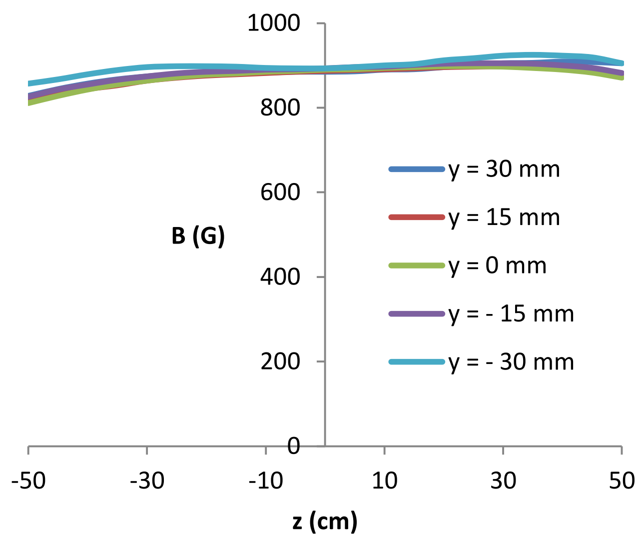

(b)

Figure 5.2 *Measured axial magnetic field in the plasma chamber for (a) x and (b) y = 0, ±15 and ±30 mm.*

5.2. Plasma Characterization using Langmuir Probe

A cylindrical Langmuir probe was used to characterize the microwave generated ECR plasma. In Langmuir probe, a conductor, usually a wire is immersed in the plasma and biased at various voltages, positive and negative, with respect to the potential of plasma. A current is drawn by the wire, which is recorded and plotted vs. the voltage applied to the probe. This I-V plot is referred to as the probe characteristic, and is analyzed to determine various plasma parameters, mainly electron temperature, electron and ion density, plasma potential and electron energy distribution function.

A typical probe characteristics plot is shown in Figure 5.3. It is divided into three regions, labeled A, B and C as shown. In region A, the probe's potential is much more positive than the potential of the surrounding plasma. Electrons in the plasma are attracted and ions repelled, so the current flowing to the probe is due to the electrons. This region is of pure electron current and is in the upper right corner of the plot.

As the applied probe voltage increases to collect higher flux of electrons, the probe reaches a point where the electron current fails to increase. This is called electron saturation and is a function of electron temperature and density.

When the potential of the probe is still positive with respect to ground, but less than the plasma space potential, electron current reduces. Electrons are not attracted as strongly, and more energetic electrons reach through the sheath surrounding the probe. This is represented by region B in Figure 5.3. Ion current is present here, but because of the mass difference and usually the cooler temperature of the ions, it is negligible compared to the electron current. The electron energy distribution of most of the plasma is Maxwellian, so the electron current should have an

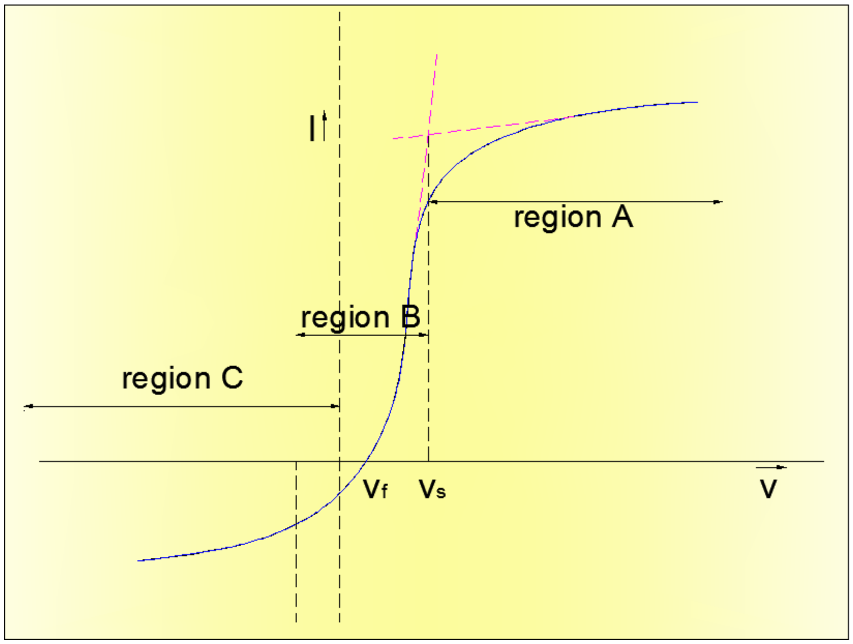

Figure 5.3 *Typical single probe characteristics.*

exponential dependence on the applied probe voltage. The most common way of determining electron temperature uses this region of the characteristic.

When the probe potential becomes large negative with respect to plasma potential, ion current dominates electron current, and eventually the electron current disappears altogether. This is known as ion saturation current in region C of Figure 5.3. The ion saturation current is usually much smaller than the electron saturation current in plasma as shown in Figure 5.3. Similar to electron saturation current, the ion saturation current depends on ion density, temperature, and the shape of the probe. The probe characteristics touches the I = 0 line, when the ion current is exactly equal to the electron current and no net current is drawn by the probe. The voltage at which this happens is called the floating potential V_f in Figure 5.3, and is the voltage which will be reached by any unbiased conducting body placed within the plasma.

For any probe immersed in real plasma, a sheath will formed around the probe, in which the electric field disturbs the characteristics of the bulk plasma. Beyond this sheath, the electric field is shielded, and the plasma continues undisturbed. The size of the sheath is few times Debye length. If the size of the sheath is small compared to the size of the probe in a collisionless (low pressure) plasma, so that all particles entering the sheath are absorbed by the probe, the probe current is: $I = j_r A_s$, where j_r is the current density in one direction, and A_s is the area of the probe and sheath. In the case of the electron saturation region of the probe, if the electron velocity distribution is Maxwellian at the sheath edge, the current density is given as:

$$J_r = \frac{1}{4} n\bar{v} = \frac{1}{2} n\,(2kT_e/\pi m_e)^{1/2}, \tag{5.1}$$

Where n is the plasma density, kT_e the electron temperature, and m_e, the mass of the electron. In one fourth factor, half comes from the density at the sheath edge being one-half the bulk density, and the other half comes from the average of the direction cosine over a hemisphere from which electrons can randomly originate. It is important to note that the electron current in this case does not depend on probe voltage; hence it is referred to as electron saturation current. For most laboratory plasmas, the size of the space charge sheath is not known, but it can be predicted from the voltage applied and the shape of the probe. For the case of cylindrical probe, the electron current is given in many references [78-80] to depend on probe voltage. But the relationship is not hold good in the presence of strong magnetic field.

For less dense or hotter plasmas, the sheath will be large compared to probe. In that case it is possible for the particle to leave the sheath without encountering the probe. An electron in the sheath can orbit around the positively charged probe, much like an attractive central force field, and depending on its velocity, may not always be absorbed by the probe. For a cylindrical probe, the current is proportional to the square root of voltage above the space potential [79].

Therefore, if I^2 is plotted against the applied voltage in the electron saturation region, it should from a straight line. From this line the space potential V_s can be found if e/kT_e is known. The slope of this line can also be used to determine the plasma density. This is preferable to the collisionless case, because it can calculate the electron temperature and plasma density separately, whereas in most cases one of these values must be known to calculate the other.

The electron temperature is found from region B of probe characteristic known as transition region. If the electron velocity distribution is Maxwellian, the electron density around the probe will be affected only by the probe voltage. The effect of density will be exponential in eV/kT_e, so that the random current hitting the probe is,

$$I = A_s n_0 (kT_e/2\pi m_e)^{1/2} e^{eV/kTe} \tag{5.2}$$

where A_s is the area of the sheath around the probe, and n_0 is the particle density [79].

Therefore if in the transition region $ln(I)$ is plotted against the probe voltage, a straight line results. The slope of this line is e/kT_e, and the reciprocal of the slope is the electron temperature in eV.

If the electron energy distribution is not Maxwellian, the transition region can be used to determine the actual energy distribution. When the energy distribution is isotropic and the electrons can reach the probe from any direction, the current to the probe will only depend on electron energy and is given by [80]:

$$I = A_p e\pi \int_0^\infty f_p \left(\frac{1}{2} m_e v^2\right) v^3 \, dv \tag{5.3}$$

Where f_p is the distribution function at the probe surface and A_p is the collecting area of the probe, e the electronic charge, m_e is the mass of the electron and v is the velocity at the probe surface. If the potential difference between the probe and the plasma drops over a distance less than the mean free path, the total energy E must be conserved and is given by:

$$E = \frac{1}{2}\, m_e\, v^2 - eV \tag{5.4}$$

where in this case, v decreases as the electron nears the probe due to retarding potential on the probe. The energy distribution function of the bulk of the plasma is one mean free path away if the size of the probe is small compared to the mean free path length. Thus the electron energy distribution function $f(E)$ is equal to $f_p(\frac{1}{2}\, m_e\, v^2)$, and the current to the probe is given as:

$$I = A_p\,(2e\pi/m_e^2) \int_{-eVp}^{\infty} f(E)\,(E+eV_p)\, dE \tag{5.5}$$

Differentiating twice with respect to V_p gives us:

$$d^2I/dV_p^2 = A_p\, 2e\pi(e/m_e^2)\,[f(E)]_{E=-eVp}, \tag{5.6}$$

The electron energy distribution function is given as [76]:

$$f(\varepsilon) = (4/A_p e^2)\,(-m_e V_p/2e)^{1/2}\, d^2I/dV_p^2 \tag{5.7}$$

Using this equation, the form of the distribution function can be calculated from the second derivative of the transition region curve. From the distribution function, an average energy can be determined given as:

$$\langle\varepsilon\rangle = \int_0^{\infty} \varepsilon F(\varepsilon) d\varepsilon \,/\, \int_0^{\infty} F(\varepsilon) d\varepsilon \tag{5.8}$$

This can be compared to the electron temperature of plasma with a Maxwellian distribution.

For modeling the region C of the probe characteristics, the ion saturation region, a theory different from electron current region is required. Because of their larger mass, ions are usually colder species in plasma, and must have a drift velocity upon entering the sheath in order to reach the probe. This necessarily involves ion orbits around the probe, and no simple theory exists. Many numerical models exist, which calculates various normalized plasma parameters for spherical and cylindrical probes [77-81].

The addition of magnetic field brings an added anisotropy into the theory of Langmuir probes. The normally random current to the probe changes by the reduced diffusion constant in the directions perpendicular to the magnetic field. A field of 875 G, as used in the ECR systems, falls into the "moderate" field strength category. The field is strong enough that the Larmor radius of an electron is small compared to the dimensions of the probe, but r_L for the ions is still very large. In this situation, the analysis of ion saturation region will not be affected by the magnetic field.

Classically, the diffusion coefficient perpendicular to the magnetic field will be reduced by collision with neutral particles [79]:

$$D_\perp = D/(1 + \omega^2\tau^2), \tag{5.9}$$

where ω is the cyclotron frequency and τ the time between collisions. This will result in a large reduction of electron saturation current. At large magnetic fields, however, anomalous diffusion almost always occurs [79], raising the current above the classical level. Probe data is then used to determine this diffusion coefficient, with known electron temperature or plasma density, rather than calculating the diffusion and then determining the temperature or density.

Because diffusion is involved, the probe theory is similar to that in collision dominated plasma. In plasma with collisions, a small area around the probe can be considered collisionless, while outside this area the plasma is still collision dominated. This area is delineated by the length of the mean free path, or how far on average, an electron can come from and not have collided with anything. For a probe in a magnetic field, the mean free path is still the limit in the direction of magnetic field, but the Larmor radius is the limit within which the electron has not collided in directions transverse to the magnetic field. The Larmor radius is generally much smaller than the mean free path. This anisotropy can be reduced back to a one dimensional analysis by contacting lengths in the B field direction by $(D_\perp/D)^{1/2}$. A good approximation of the electron current is then [79],

$$I = [n_0 \bar{v} A_p \lambda / 3 r_p] \, (D_\perp / D)^{1/2} \quad (5.10)$$

where n_0 is the plasma density, $\bar{v}$ the mean velocity (from the electron temperature), A_p the area of the probe, λ the mean free path, and r_p the probe radius. This approximation of the electron current does not depend on probe voltage, and is not specific for cylindrical probes. A reduced electron saturation current is predicted here, and if the effect of the magnetic field is not taken into account, can result in a calculated electron density which seems much lower than the electron density actually is. Calculating this diffusion coefficient, $D_\perp/D$, can help quantify the effect of the magnetic field.

The transition region analysis is not as sensitive to the addition of a magnetic field, because the field cannot change the velocity distribution of the electrons. The anisotropy, though, if strong enough, may complicate the concept of a collective electron temperature. Especially with ECR generated plasma, where the acceleration is in the directions transverse to the magnetic field only, there can be separate temperatures in the different directions.

5.3 Probe Construction

The automated Langmuir probe used in the present study was designed and developed in housed. The single probe used in the study is shown in Figure 5.4. The probe tip consisted of 0.5 mm diameter tungsten wire and lengths 1 mm and 3 mm. The wire was insulated by alumina tube. The probe was shielded by quarter inch O.D. stainless steel tube to protect the probe from noise of stray fields, and to provide good vacuum sealing surface. The junctions between the tungsten and alumina and alumina and stainless steel were sealed against vacuum leaks with torr-seal. The probe end was connected to a vacuum BNC feedthrough. The probe movement in radial direction was provided through Wilson seal arrangement on KF flange. The probe was introduced in the plasma chamber through the diagnostic port mating KF flange. The reference electrode was the wall of the plasma chamber that was grounded.

Figure 5.4 *Single Langmuir probe*

5.4. Probe Circuit

An automated Langmuir probe diagnostics unit with data acquisition system was developed to measure plasma parameters [16, 82-90]. The current – voltage (I – V) characteristics of the probe were taken by sweeping the voltage on the probe from – 115 V to + 53 V. These data were recorded on the digital storage oscilloscope (DSO) and were then transferred to the personal computer. The probe was inserted radially into the plasma so that the probe tip can be located at the center of the plasma and at any point along the radius to the outer edge of the plasma.

The probe circuit used in the experiment is shown in Figure 5.5. Voltage sweep pulse - 115 V to + 53 V / 90 ms was generated using triangular wave generator and ± 200 V, 2 A Kepko bipolar operational amplifier power supply (BOP) as shown in Figure 5.6 (a). The “active” terminal of the BOP drives the probe tip via current-to-voltage converting circuits. The “common” terminal of the BOP was connected to the electrical ground of the plasma generation system. The voltage sweep was applied to the tungsten tip of the Langmuir probe and the current was detected using a current shunt. Shunt resister was connected in the signal path to avoid stray capacitance effect which was present in ground path. There are many kinds of electromagnetic noise associated with high power RF and high magnetic field. Under the harsh environment, it is important for an electronic circuit to have the capability of noise immunity during measurement. One way to accomplished it is to have separate electrical grounds such as the ground of the plasma generation system, the casing ground of the electronics devices, and the signal ground of the data acquisition system. In order to make the ground line impedance as small as possible, cables of large cross-section area were used as ground lines. The electronic circuits were encased by metal shield that are connected to the shielding mesh of the signal line cables. For the signal line from the function generator to the BOP, coaxial cables were used to minimize the noise induced from electromagnetic interference. The shunt resistor for converting the probe current to voltage signal was placed between the active terminal of the BOP and the probe as shown in Figure 5.5. In this case the ground of the data acquisition system should not be connected directly to the common point of the shunt resistors because the common voltage varies by hundreds of volts. Therefore the voltage signal across the shunt resistor was acquired through an isolation amplifier which electronically separates the shunt resistor common from the ground of the data acquisition system. The isolation amplifier used in the system was AD 210, and it provided ± 2000 V peak common mode isolation between the probe current pickup port and the signal output port, which was high enough for sweeping the common voltage. The current and voltage were recorded on a digital oscilloscope as shown in Figure 5.6 (b).

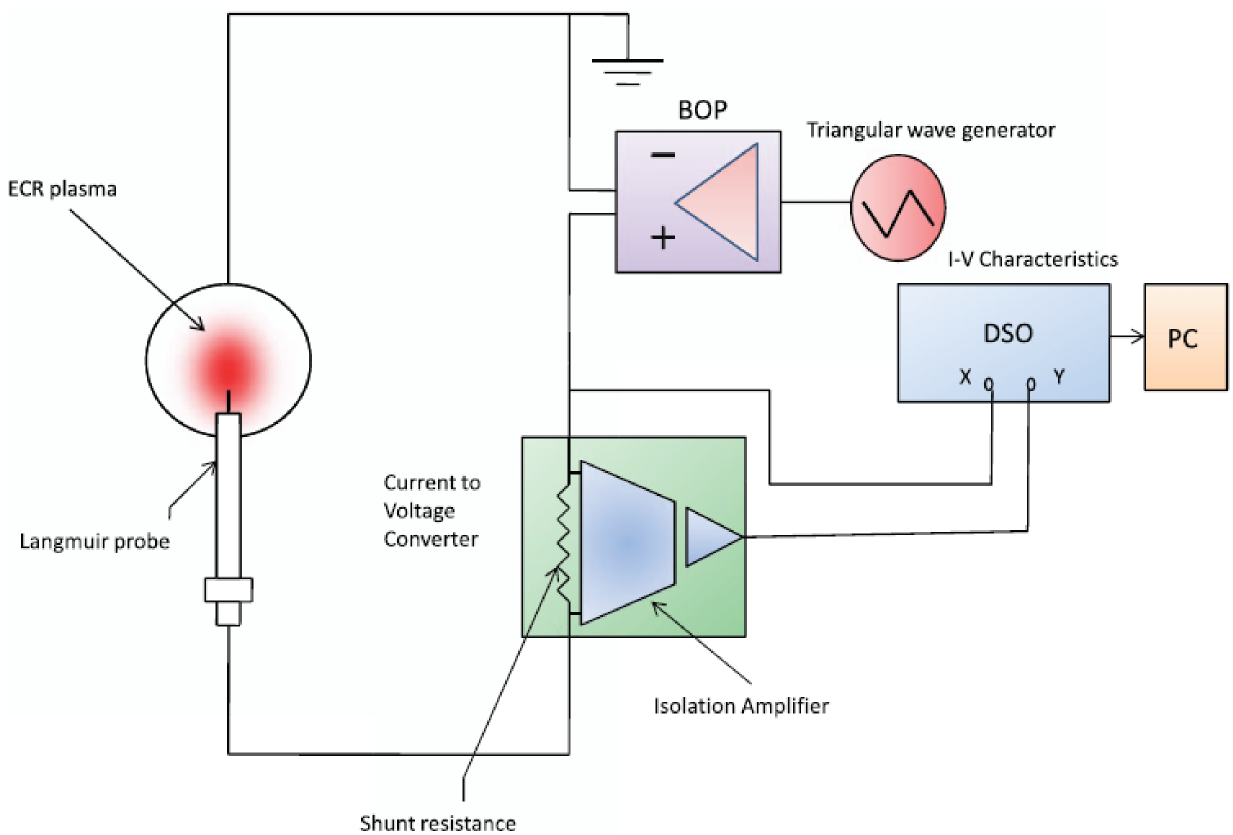

Figure 5.5 *Automated Langmuir probe circuit*

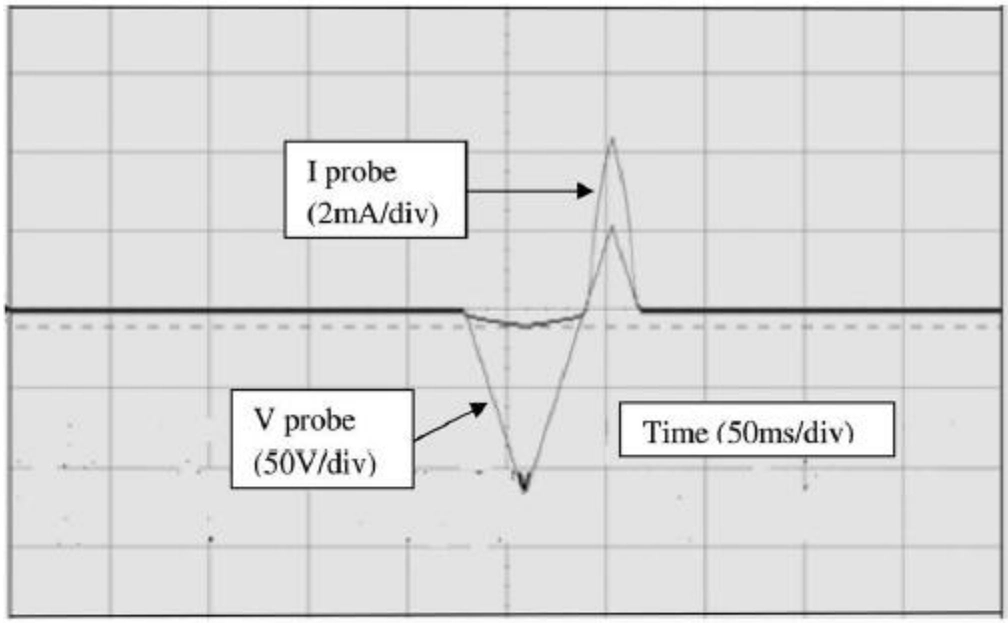

(a)

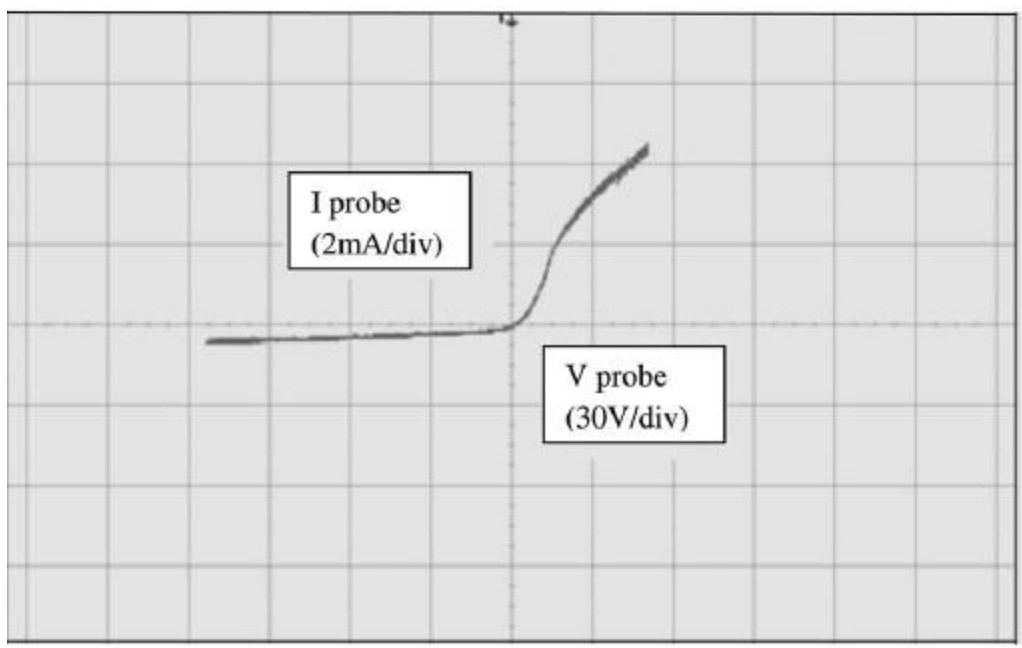

(b)

Figure 5.6 *Oscilloscope traces of (a) Triangular voltage pulse to probe (upper trace) and current collected by probe (lower trace) and (b) I – V characteristics of probe.*

5.5. Probe Data Analysis Method

In this study, standard analysis techniques are used to determine the plasma potential, plasma electron density, plasma electron temperature and plasma electron energy distribution function (EEDF). The plasma potential V_p is determined from the probe I –V curve where the second derivative of the I – V curve are taken and the location of the voltage where the second derivative goes to zero is taken as plasma potential.

The plasma electron temperature T_e is determined from the electron current in the retarding region of the probe characteristics given as

$$I_e = I_{e0}\, exp\, [e\, (V - V_p) / kT_e\,] \quad \text{with } I_{e0} = n_e\, e\, A\, (kT_e / 2\pi m_e) \tag{5.11}$$

where, V_p is the space potential and V is the probe potential. One way of determining electron temperature kT_e in eV is to plot $ln\, (I_e)$ against V and the straight line is fitted to the voltage region less than but close to the plasma potential V_p. The measured value of kT_e is given by the inverse slope of the line. The other way of determining the electron temperature is from the electron energy distribution function (EEDF) given as

$$f(E) = [(8m_eV)^{1/2} / Ae^{3/2}n_e]\, d^2I/dV^2 \tag{5.12}$$

The plasma electron temperature is calculated as

$$T_e = (2/3) \int E\, f(E)\, dE, \tag{5.13}$$

Where $f(E)$ is the EEDF and E is the energy. The units of T_e and E are in electron volt. As there is little difference found in the estimation of plasma electron temperature using the two methods, the second method is adopted here.

The ion density n_i, is estimated from the ion saturation current using the standard thin sheath probe theory since the probe radius is much larger than the Debye length, $r_p/\lambda_D \sim 30$ and assuming quasi-neutrality $n_e \sim n_i$

$$I_{is} = 0.61\, e\, n_e\, A\, C_s, \tag{5.14}$$

Where A is the surface area of the probe and C_s is the acoustic speed given as $C_s = (kT_e / 2.72\, M_i)^{1/2}$, and M_i is the mass of the ion.

The effect of applied magnetic field on the Langmuir probes [91-94] is categorized as (a) weak B field regime ($r_p > r_{Le}$), (b) moderate B field regime ($r_{Le} < r_p < r_{Li}$) and (c) strong B field regime ($r_{Li} < r_p$). Where r_p, r_{Le} and r_{Li} are probe radius and Larmor radius of electron and ion. For the present typical ECR Hydrogen plasma parameters $B \approx 0.1$ T, $n_e \approx 10^{11}$ cm^{-3}, $T_e \approx 10$ eV, and $T_i = 0.5$ eV, r_{Le} , r_p and r_i are turned out to be 0.1 mm, 0.25 mm and 0.69 mm respectively. Thus it falls in moderate B field regime. In this regime, electrons with Larmor radius smaller than the dimensions of the probe can either be collected through cross-field diffusion or from flux tubes intersecting the probe. The diffusion coefficient $D_\perp$ across the magnetic field lines is given by

$$D_\perp = D_\parallel / (1 + \omega_{ce}^2 / \nu_{ei}^2) \approx D_\parallel / (\omega_{ce}^2 / \nu_{ei}^2) \tag{5.15}$$

where ω_{ce} is the electron angular cyclotron frequency, ν_{ci} is the electron-ion collision rate and $D_\parallel$ is the diffusion coefficient along the magnetic field lines. The values of ν_{ei} and ω_{ce} are $\approx 10^5$ s^{-1} and 10^{10} s^{-1} respectively. For electrons $(\omega_{ce}/\nu_{ei}) \approx 10^5$ and from Eq. (5.15), the electron radial diffusion is strongly inhibited. But for ions, $(\omega_{ce}/\nu_{ei})\ \alpha\ (m_e/M_i)$, the ion diffusion is not severely limited. So, the electron saturation current is reduced and the ion saturation current remains unchanged. Moreover, in the presence of a magnetic field, the tip of Langmuir probe should be aligned perpendicular to the magnetic field so as to eliminate any discrimination of low energy particles by the probe. For a cylindrical Langmuir probe, aligned along the magnetic field, the electric field (E) between plasma and the probe acts perpendicular to the magnetic field (B) lines which results in changing the direction of $E \times B$ drift of the guiding center of the plasma particles in azimuthal direction with respect to the axis of the probe. Thus, the low energy plasma particles, owing to a smaller Larmor radius than the probe sheath thickness, are restricted to reach the probe due to the superposition of cyclotron motion on the guiding center motion. The resulting discrimination of low energy particles by the probe leads to a higher measured value than the actual value of temperature. This effect is eliminated by orienting the probe tip perpendicular to the magnetic field so that the orbit effects are taken off the scenario by keeping $E \times B$ zero. Thus, the cylindrical probe in the experiment is located in the plasma chamber with axis oriented perpendicular to the magnetic field and it measures the electron temperature parallel to magnetic field $T_{\parallel}$ [95].

5.6. Experimental Setup

The schematic and actual setup of the plasma characterization studies carried out in electron cyclotron resonance (ECR) proton ion source is shown in Figures 5.7 and 5.8. During the experiments, a base pressure < 10^{-6} mbar was maintained in the ion source for several hours, prior to the commencement of the actual measurements. The working gas was introduced in the plasma chamber in a controlled fashion using a precision leak valve and maintained in the pressure range of ~ 10^{-4} - 10^{-3} mbar in the plasma chamber and ~ 10^{-6} - 10^{-5} mbar in the extractor region.

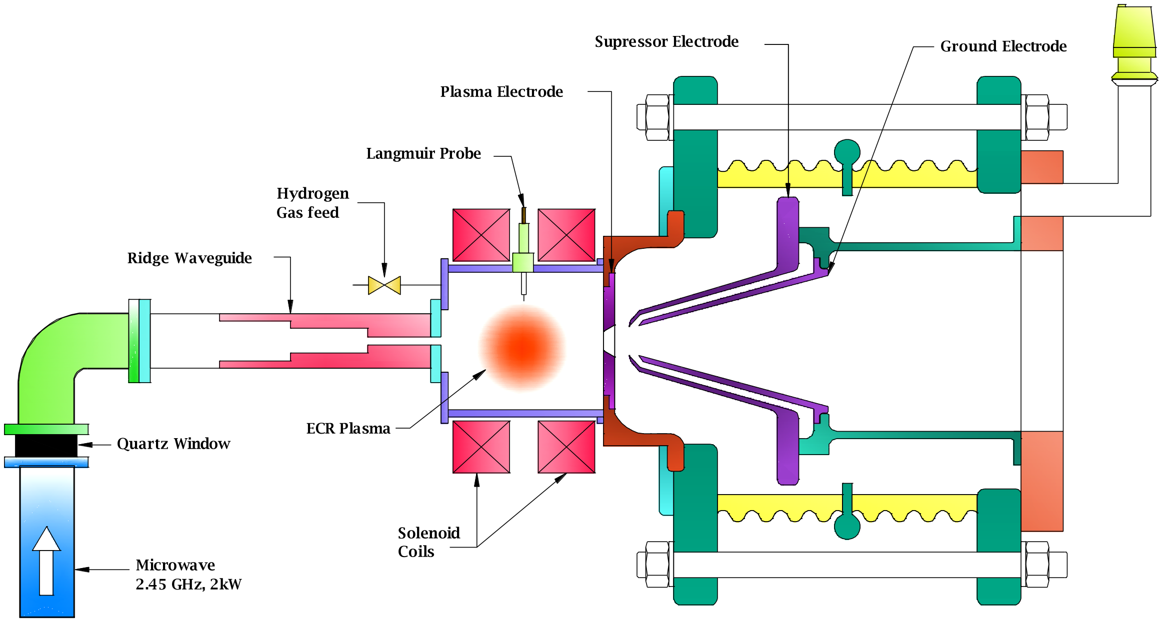

Figure 5.7 *Schematic of Langmuir probe plasma characterization setup.*

Figure 5.8 *Langmuir probe measurement setup.*

The current in the solenoid coils was adjusted to obtain the desired magnetic field configurations. The measured magnetic field was 850 – 900 G along the axial direction in the plasma chamber of length 100 mm as shown in Figure 5.2. The incident and reflected microwave powers were measured using a digital power meter connected to a directional coupler. The reflected power was minimized using a four stub auto-tuner. Once the plasma discharge was established, a ramp voltage was applied to the probe and the probe characteristics were recorded on the digital oscilloscope and then transferred to personal computer for data analysis.

The pulsed plasma was generated in μs to ms time duration by operating the magnetron in a pulsed mode. The magnetron was operated at frequency of 2.45 GHz with 400 - 1000 W output power for μs to ms pulse duration and 1% to 99% duty cycle.

5.7. Results and Discussions

The typical probe characteristics, its second derivative and EEDF as deduced from reference [96] are shown in Figures 5.9 and 5.10 for microwave power of 900 W and operating pressure 2.5×10^{-3} mbar. It is seen from Figure 5.10 that ECR plasma discharge have two electron temperature populations (i.e., hot and cold (bulk) electrons) that are also reported by others [97-100]. This happens due to ECR heating and magnetic confinement of electrons in the ECR zone and results in non-Maxwellian nature of electron population. Some electron gain higher energy compared to the bulk electrons in the ECR zone and therefore results in plasma with two electron temperatures. The hot electrons in the tail of the distribution in Figure 5.10 are responsible for ionization of hydrogen gas. In further study only bulk electron temperature is considered.

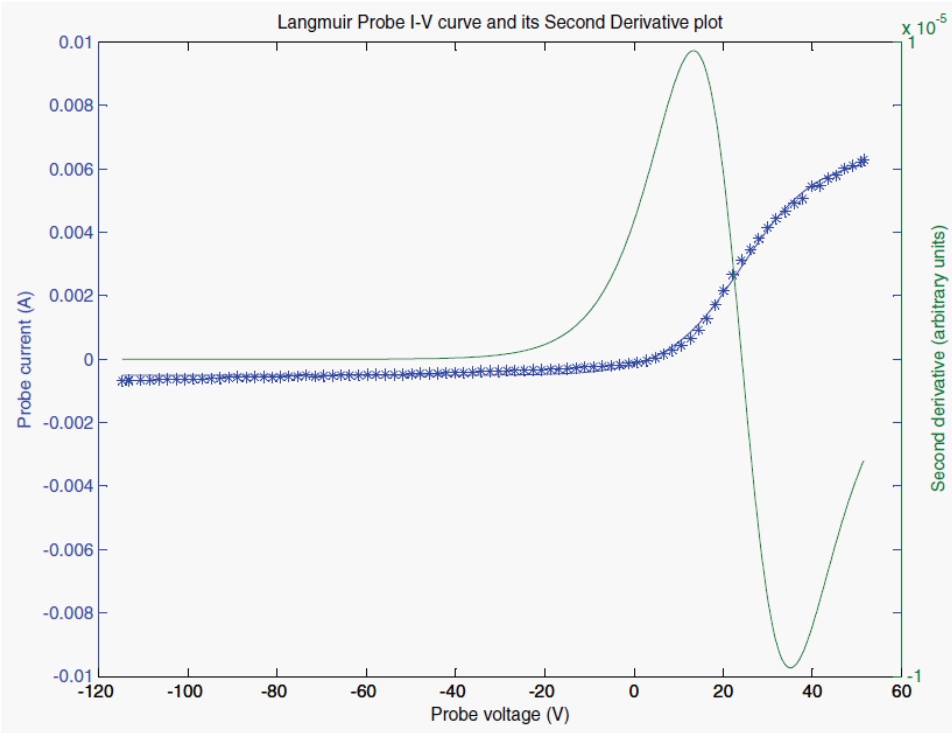

Figure 5.9 *Langmuir probe characteristics and its second derivative at 900 W, 2×10^{-5} mbar.*

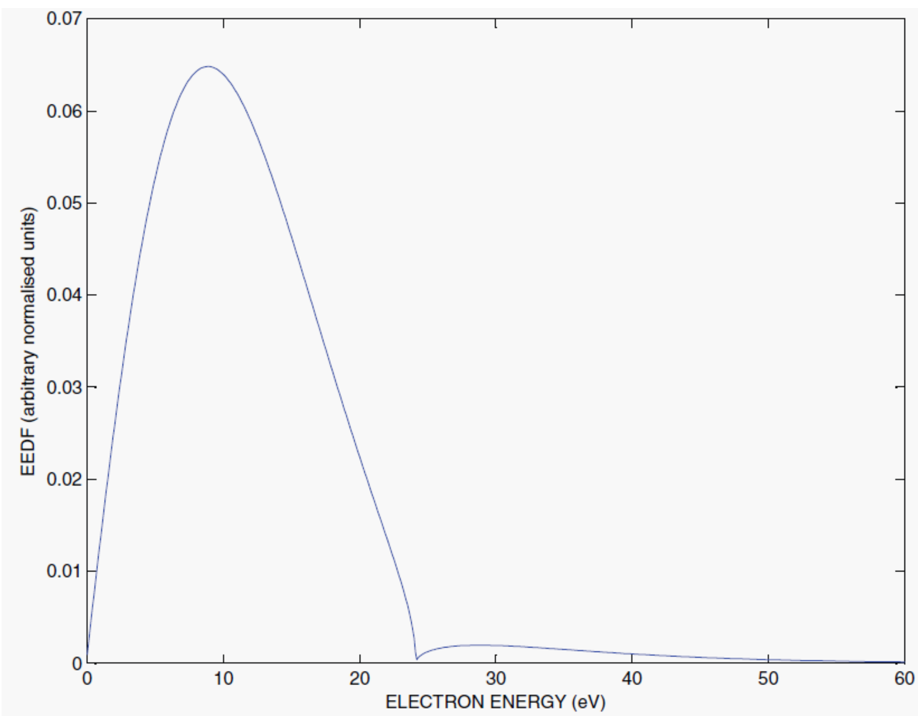

Figure 5.10 *EEDF of probe characteristics.*

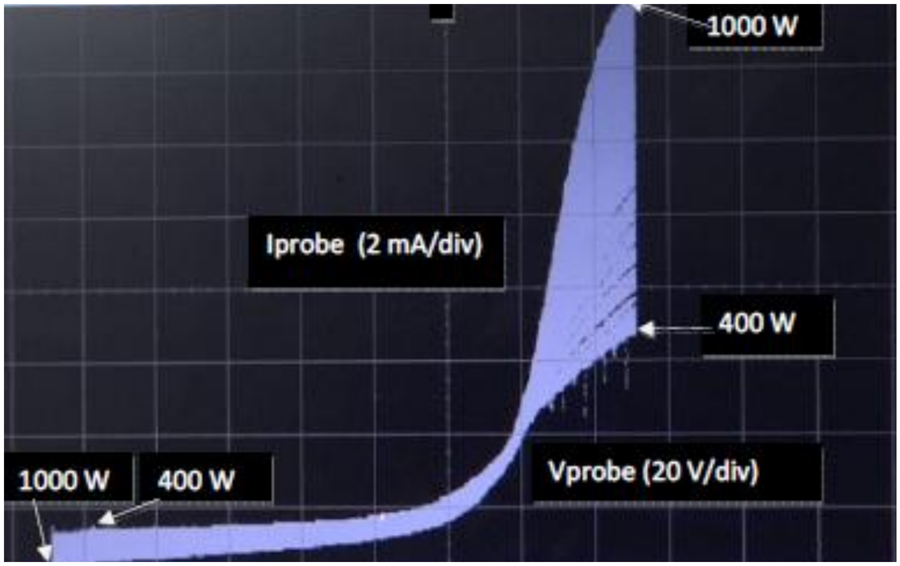

Figure 5.11 *Snapshots of probe I-V characteristics on oscilloscope for continuous variation of microwave power from 400 W to 1000 W.*

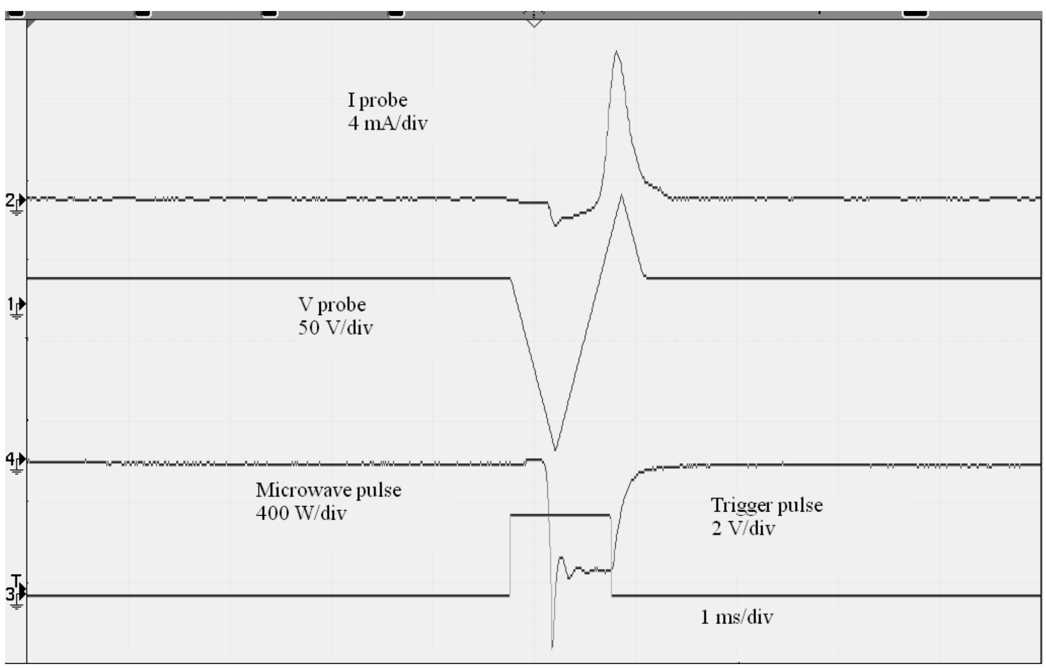

Figure 5.12 *Oscilloscope traces of master trigger pulse, microwave pulse, probe voltage pulse and probe current pulse for pulsed plasma operation.*

The Figure 5.11 shows the snap shots of the probe characteristics recorded on digital storage oscilloscope by varying the microwave power continuously from 400 W to 1000 W. In pulsed mode operation, the synchronization of the microwave pulse and the probe voltage pulse was achieved using a master trigger pulse as shown in Figure 5.12. The plasma parameters are deduced from the probe characteristics and the dependence of plasma parameters on microwave power and gas pressure were studied.

The probe data were recorded for five operating pressures and seven microwave powers, i.e., 1.2×10^{-3} mbar, 1.9×10^{-3} mbar, 2.5×10^{-4} mbar, 3.2×10^{-4} mbar and 3.9×10^{-4} mbar and 400 W, 500 W, 600 W, 700 W, 800 W, 900 W and 1000 W respectively.

5.7.1. Dependence of reflected microwave power on forward microwave power for different neutral gas pressures

As a result of ECR breakdown the self-sustained plasma was generated in the chamber. In the gas pressure range of 1.2×10^{-3} mbar to 3.9×10^{-3} mbar and incident microwave power 400 W – 1000 W, the reflected microwave power of 5 W – 17.5 W (Figure 5.13) was recorded. The reflected power is 1.25% ~ 1.75% of incident microwave power. This drastic decrease of reflected microwave power (down to two percent) accompanied with appearance of bright plasma was observed when the plasma density reaches the value $n_e = n_{cr} = m\omega_{rf}^2/4\pi e^2 = 7.4\times10^{10}$ cm^{-3} of critical density at sites where the magnetic field is ~ 875 G. The shape size and location of this area known as ECR region can be controlled by proper matching, magnetic field configuration, and microwave power label. Experimentally the high absorption regime or ECR region has been achieved in four ways first by increasing of incident microwave power, second by microwave tuning, third by increasing gas pressure and fourth by varying the magnetic field.

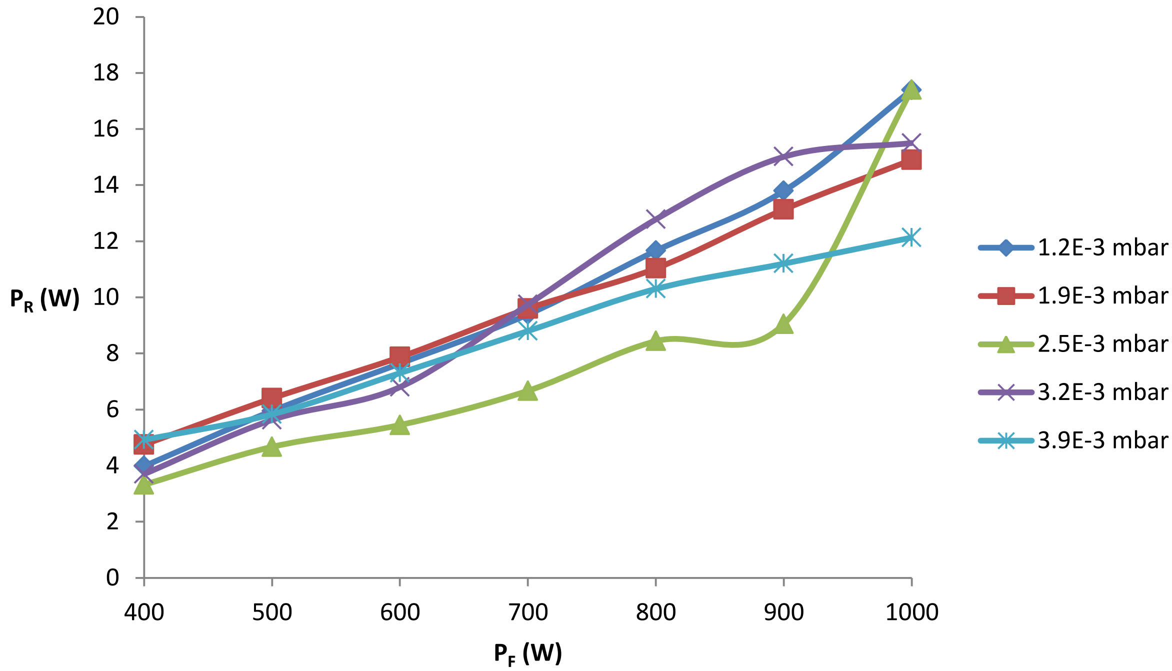

Figure 5.13 *Variation of reflected microwave power P_R (W) with forward microwave power P_F (W) for pressures 1.2×10^{-3} mbar, 1.9×10^{-3} mbar, 2.5×10^{-3} mbar, 3.2×10^{-3} mbar, and 3.9×10^{-3} mbar.*

5.7.2. Dependence of plasma electron density, plasma electron temperature and plasma potential on neutral gas pressure

The plots of plasma electron density n_e, plasma electron temperature T_e and the plasma potential V_P versus hydrogen gas pressures p in the ECR region for microwave powers 400 W, 500 W, 600 W, 700 W, 800 W, 900 W and1000 W are shown in Figures 5.14 (a) – (c).

In Figure 5.14 (a), n_e as a function of pressure for 400 W increases from 8.2×10^{10} cm^{-3} to 1.42×10^{11} cm^{-3} and for 1000 W increases from 1.6×10^{11} cm^{-3} to 2.6×10^{11} cm^{-3}. In Figure 5.14 (b), T_e as a function of pressure for 400 W decreases from 12 eV to 6.5 eV and for 1000 W decreases from 10.2 eV to 7.1 eV. In Figure 5.14(c), V_P as a function of pressure for 400 W increases from 25.4 V to 25.7 V and for 1000 W increases from 33.4 V to 37.8 V. The plots of n_e, T_e and V_P as a function of pressure for intermediate power ranges are similar in nature for all the cases.

As evident from Figure 5.14 (b) there is a general tendency that the plasma electron temperature decreases with increase of neutral gas pressure. The decrease in electron temperature with increase in neutral gas pressure is due to the increase in number of collisions electrons undergo with neutrals and the fact that the loss of plasma is controlled by magnetic confinement. It is also found that low-electron temperature ECR plasma could be obtained by raising the gas pressure. From Figure 5.14 (a) and Figure 14 (c) it is seen that the plasma electron density and plasma electric potential increases with the increase of neutral gas pressure. The plasma electron density is low at lower pressures due to the decrease in the number of particles available for ionization. The general expression of the dependence of plasma electron temperature T_e on neutral gas pressure p is deduced from the following fact that when a microwave electric field is applied to a gas volume,

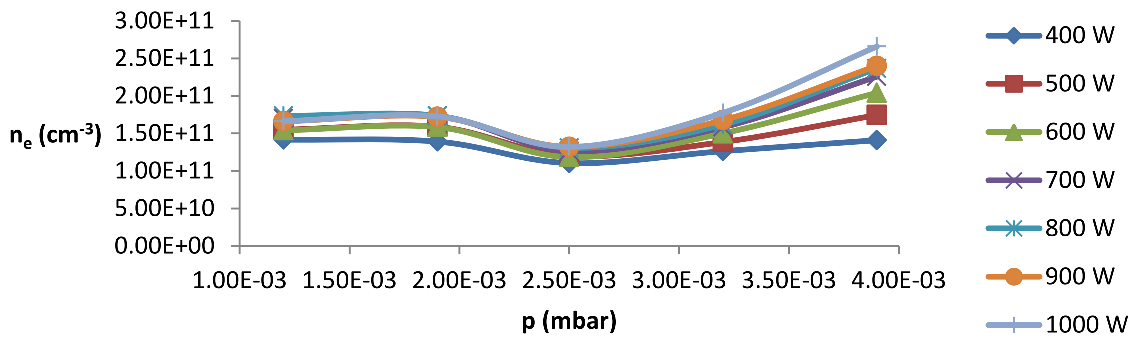

(a)

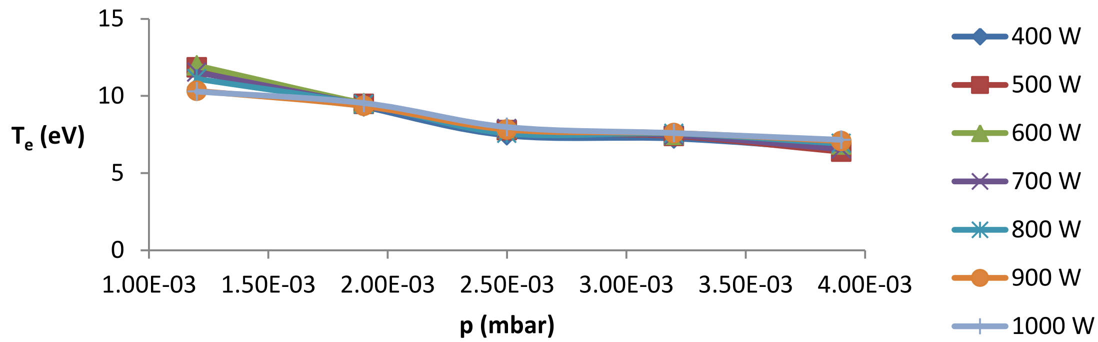

(b)

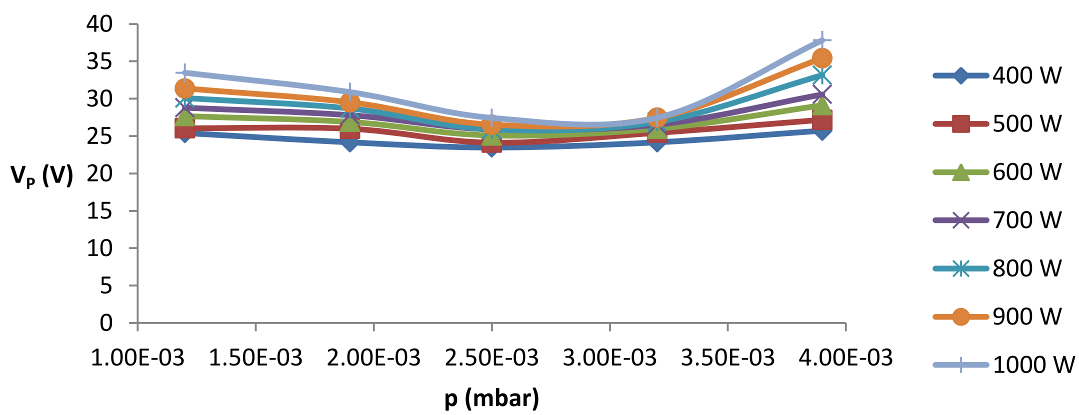

(c)

Figure 5.14 *Variation of (a) plasma density n_e, (b) plasma electron temperature T_e and (c) plasma potential V_P at the ECR region with the hydrogen gas pressure p for microwave powers 400 W, 500 W, 600 W, 700 W, 800 W, 900 W and1000 W.*

electrons in the volume are accelerated and collide with neutral gas molecules, producing ions and secondary electrons.

The gas breakdown sustains when the electron production rate in the volume is larger than the loss rate. After the gas breakdown is initiated and microwave discharge is developed, the electron temperature is increased by the electron-cyclotron resonance heating when the microwave frequency is very close to the electron cyclotron frequency $\omega_{rf} \approx \omega_{ce}$. The average electron energy (or the electron temperature) in the Ohmic heated plasma is directly proportional to the microwave electric field and inversely proportional to the collision frequency of electrons by neutrals.

The collision frequency in turn is proportional to the gas pressure p in the chamber. The collision frequency is also proportional to collision cross section of neutral by electrons and is proportional to the square root of electron temperature T_e. The electron temperature is then expressed as function of gas pressure p as [101]:

$$T_e = \alpha + \beta\, p^{-1/2} \qquad (5.16)$$

where p is the pressure in the plasma chamber. The coefficient α and β are determined from various system parameters.

Figure 5.15, shows the plot of electron temperature T_e versus the pressure p in the plasma chamber. The square dots and round dots in Figure 5.15 represent the measured electron temperature in the hydrogen plasma in the ECR region for microwave power of 400 W and 1000 W respectively.

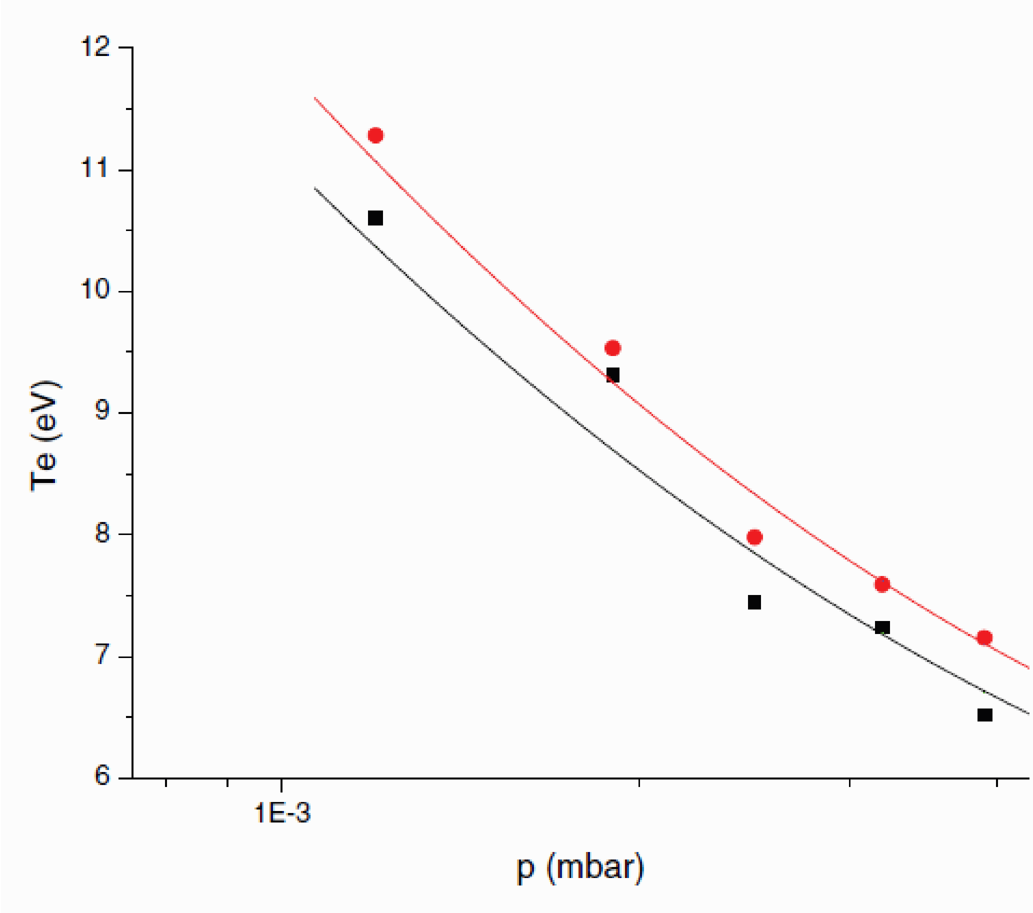

Figure 5.15 *Variation of electron temperature T_e versus chamber pressure p. The square dots and round dots represent the measured electron temperature for 400 W and 1000 W. The solid line represents the theoretical fit to experimental data.*

The solid lines represent the results obtained empirically from Eq. (5.16), with α and β determined from a least square fit to the experimental data. The values of (α, β) for 400 W and 1000 W are (2.16, 9.0) and (2.16, 9.77) respectively where the pressure p and temperature T_e are in the units of bars and eV respectively. Note from Figure 5.15 that Eq. (5.16) represents the electron temperature reasonably well in the board range of operation of the plasma chamber pressure of the ion source.

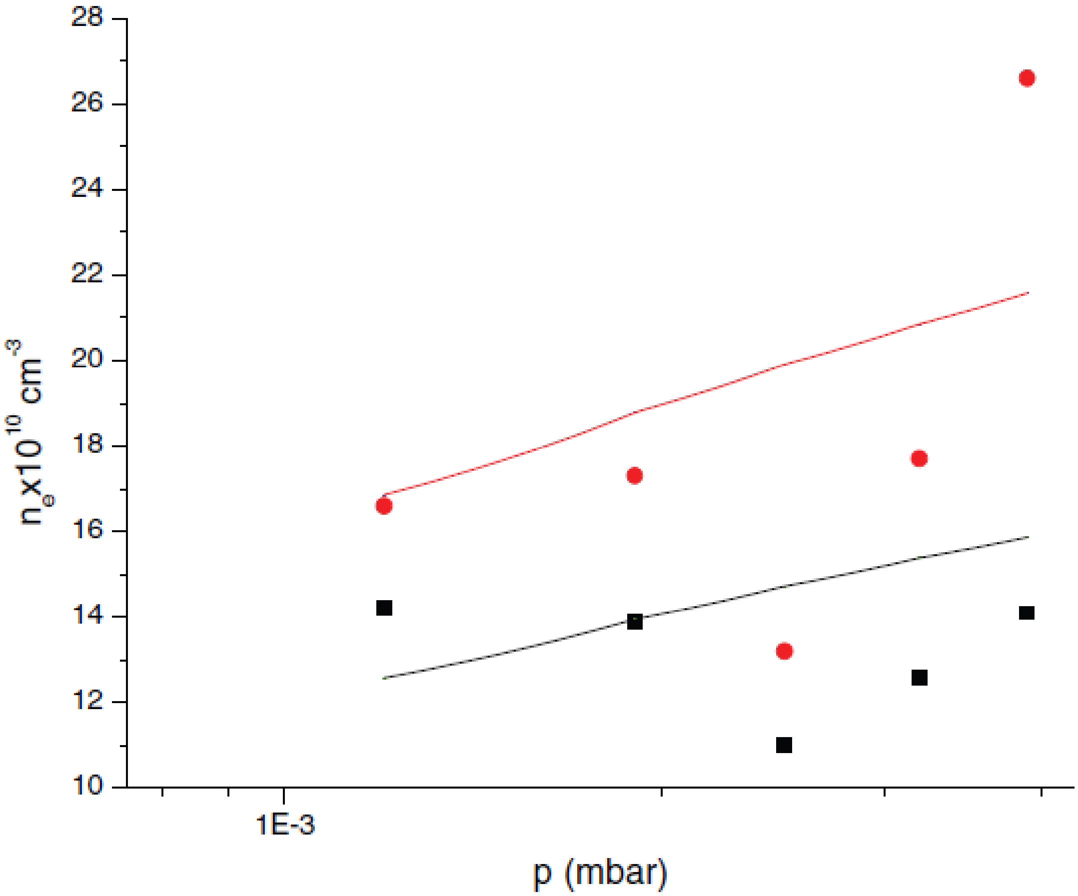

Figure 5.16 *Variation of plasma density n_e with chamber pressure p. The square dots and round dots represent the measured electron densities for 400 W and 1000 W respectively. The solid line represents the theoretical fit to experimental data.*

Figure 5.16 represents the plot of plasma density versus the operating pressure. The square dots and round dots in Figure 5.16 represent the measured plasma density for 400 W and 1000 W respectively. It is seen that electron density shows a dip at pressure 2.5×10^{-3} mbar. At this pressure probably the microwave mode structure at the probe location has changed resulting in shifting of ECR zone. This needs further investigation. The solid curve in Figure 5.16 represents the general expression of plasma density as a function of pressure and given as

$$n_p = \eta\, p^{1/2} e^{-\varepsilon i/2Te} \tag{5.17}$$

where ε_i is the ionization energy. In obtaining the solid curves use has been made of Eq. (5.17). The numerical constant $\eta = 7\times10^{10}$ was determined from the least square fit of the experimental data.

5.7.3 Dependence of plasma electron density, plasma electron temperature and plasma potential on microwave power

The variations of plasma parameters n_e, T_e and V_P with microwave power are shown in Figure 5.17 (a) – (c). For pressure 1.2×10^{-3} mbar the plasma electron temperature decreases from 11.9 eV at 400 W to 10.3 eV at 1000 W. The plasma electron density increases from 1.42×10^{11} cm^{-3} at 400 W to 1.6×10^{11} cm^{-3} at 1000 W and its value exceed the critical density $n_{cr} = 7.4\times10^{10}$ cm^{-3}. The plasma potential increases from 25 V at 400 W to 37 V at 1000 W. The confinement of plasma electrons depends on plasma electron temperature and plasma potential. The decrease of plasma electron temperature with increase of microwave power results in smaller value of Bohm Diffusion coefficient across magnetic field $D_B = k\, T_e/16\, B$, where B is magnetic field and results in controlling the losses of electrons. Further, the electrons are confined in the plasma by the potential well i.e., by the large positive potential V_P. The value of V_P increases from 25 V to 37 V with the increase of microwave power thereby controlling the losses of electrons.

For other pressures i.e., 1.2×10^{-3} mbar, 1.9×10^{-3} mbar, 2.5×10^{-3} mbar, 3.2×10^{-3} mbar and 3.9×10^{-3} mbar the plasma electron density and plasma potential increases with the increase of microwave power absorbed and plasma electron temperature either decreases slightly or remains constant with the increase of microwave power absorbed.

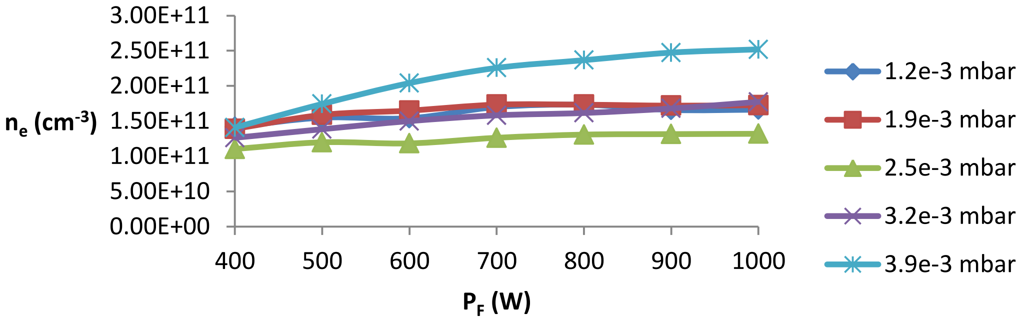

(a)

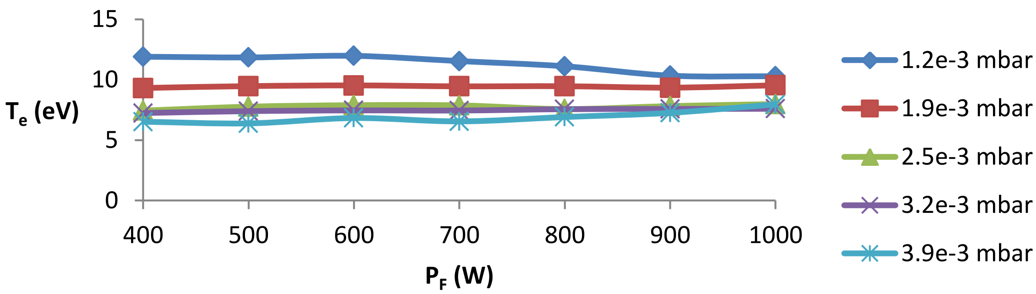

(b)

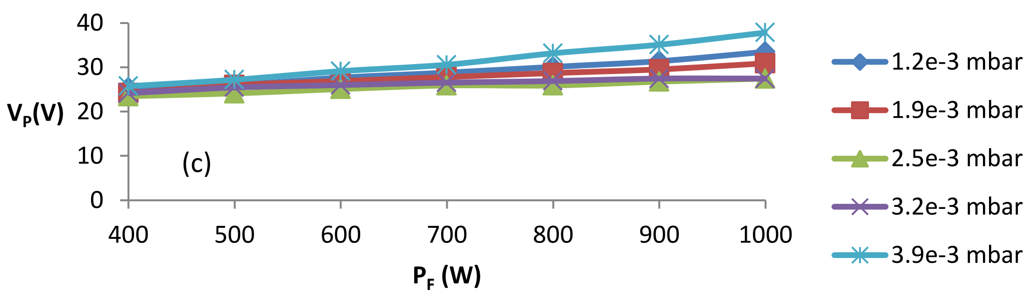

(c)

Figure 5.17 *Variation of (a) plasma density n_e, (b) plasma electron temperature T_e and (c) plasma potential V_P at the ECR region with the microwave forward power P_F for neutral gas pressures 1.2×10^{-3} mbar, 1.9×10^{-3} mbar, 2.5×10^{-3} mbar, 3.2×10^{-3} mbar, and 3.9×10^{-3} mbar.*

Figure 5.18 represents the plot of plasma density versus the microwave power. The square dots and round dots in Figure 5.18 represent the measured plasma density for 1.2×10^{-3} mbar and 3.9×10^{-3} mbar respectively. The solid line represents the general expression of plasma density n_e as a function of microwave power P as

$$n_e = \gamma P^{\delta} \tag{5.18}$$

where γ and δ are constants determined from the least square fit to the experimental data and are given by (0.4, 0.61) and (2, 0.32) for 1.2×10^{-3} mbar and 3.9×10^{-3} mbar respectively.

Figure 5.19 represents the plot of electron temperature T_e versus microwave power. The square dots and round dots in Figure 19 represent the measured plasma electron temperature for 1.2×10^{-3} mbar and 3.9×10^{-3} mbar respectively. The solid line represents the general expression of plasma electron temperature as a function of microwave power

$$T_e = \alpha + \beta\, p^{-1/2}(P/P_0)^{(1-\kappa)/2} \tag{5.19}$$

Where, P_0 is the normalization factor of power and κ is constants determined from the least square fit to the experimental data and is given by 0.98 for 1.2×10^{-3} mbar and 0.8 for 3.9×10^{-3} mbar respectively.

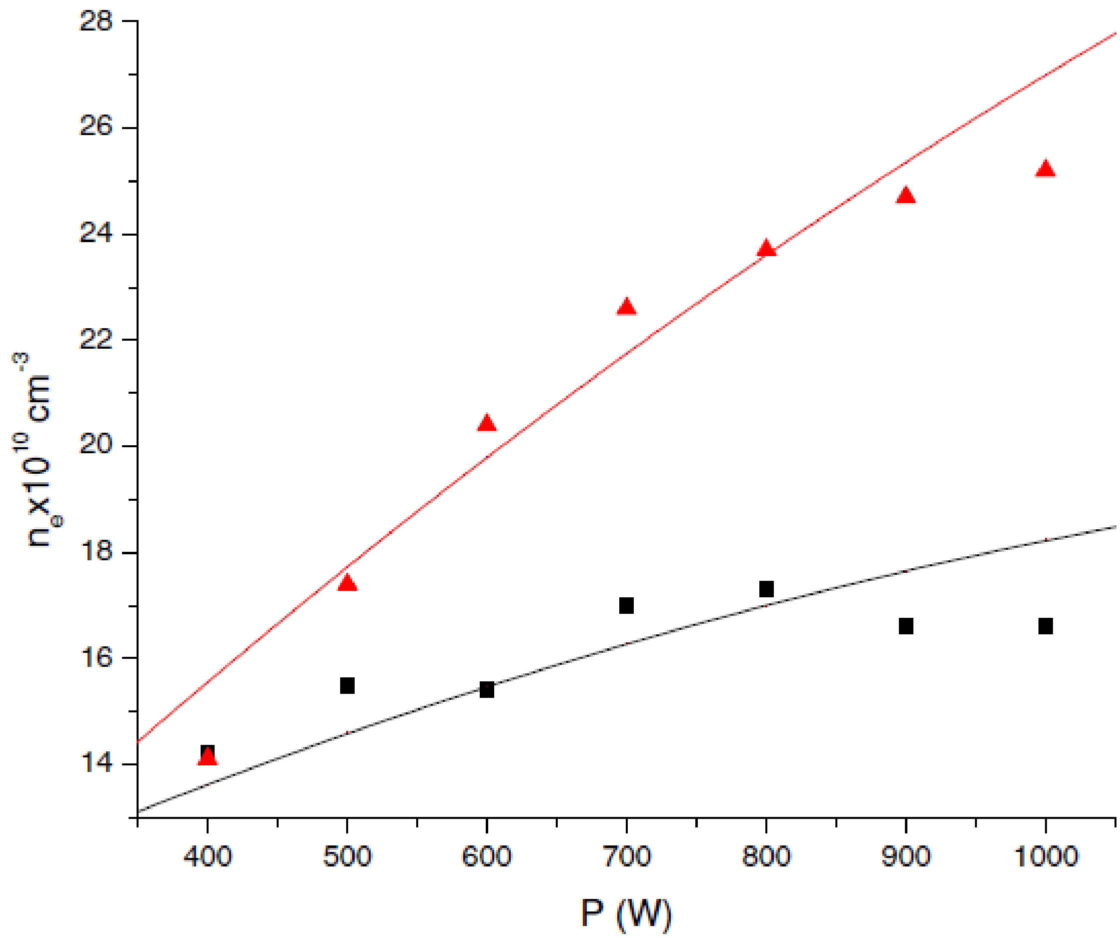

Figure 5.18 *Variation of plasma density n_e with microwave power P. The square dots and round dots represent the measured electron density for 1.2×10^{-3} mbar and 3.9×10^{-3} mbar. The solid line represents the theoretical fit to experimental data.*

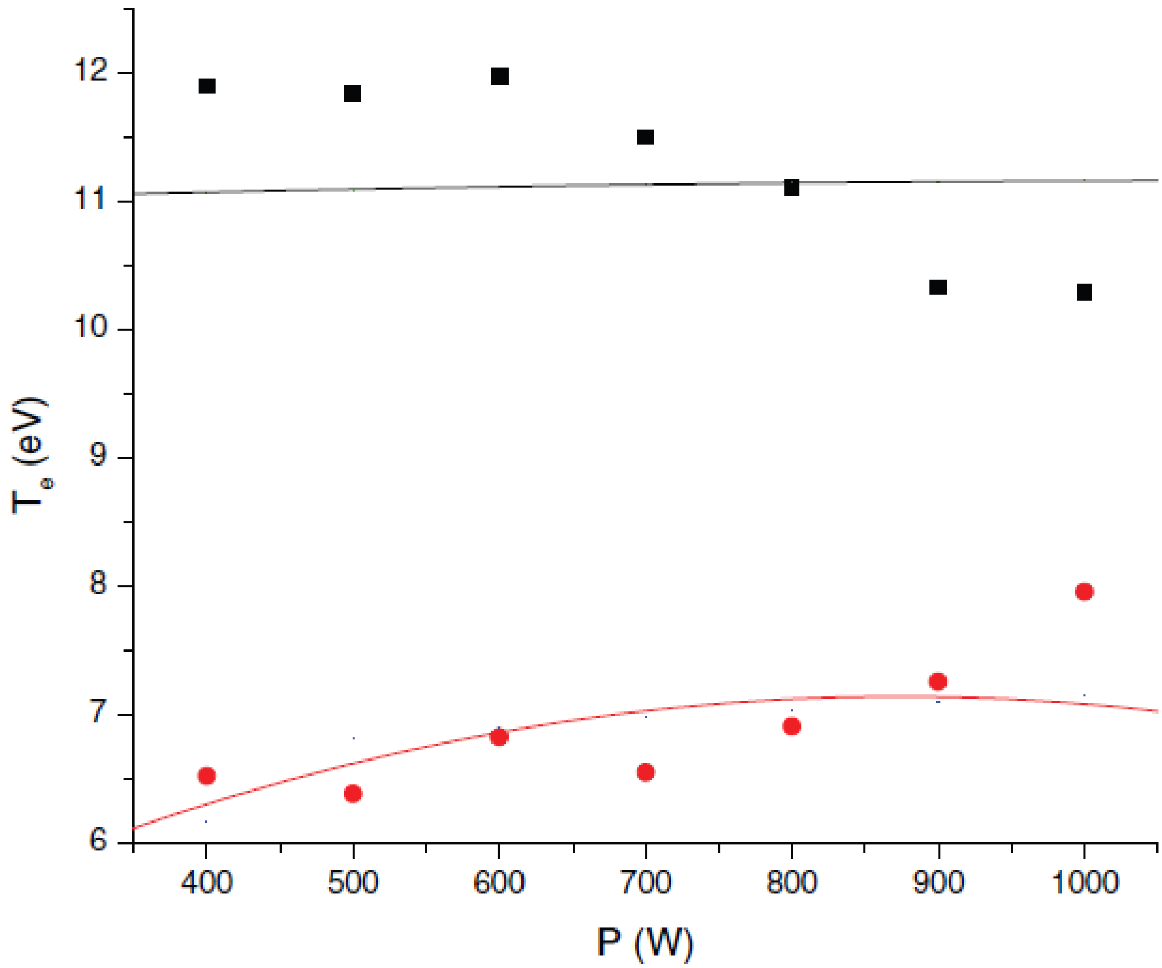

Figure 5.19 *Variation of electron temperature T_e with microwave power P. The square dots and round dots represent the measured electron temperature for 1.2×10^{-3} mbar and 3.9×10^{-3} mbar. The solid line represents the theoretical fit to experimental data.*

5.7.4. Radial variation of plasma parameters

The radial profile of plasma parameters for microwave power 400 W – 1000 W and gas pressure 2.5×10^{-3} mbar is shown in Figures 5.20 (a) – (c). In Figure 5.20 (a), the plasma density gradually decreases from center of the plasma chamber at *r* = 0 mm to the outer edge at *r* = 45 mm for all powers. At all radial locations of *r* i.e., 0 mm, 10 mm, 20 mm, 30 mm, 40 mm and 45 mm, the plasma electron density increases with the increase of microwave power from 400 W to 1000 W. The plasma density at *r* = 0 mm for microwave powers 400 – 800 W is lower than at *r* = 10 mm but increases at higher powers of 900 W and 1000 W. This effect is due to changes in microwave power distribution as the plasma absorbs the power radially.

The Guassian like profile of Figure 5.20 (a) has many possible origins. In the plasma chamber, electron loss at the grounded side wall is the major factor in determining the radial plasma profile. Other important factors in the ECR chamber include the fact that the microwave power distribution is not uniform and depend on the selection of microwave modes. Also, the magnetic field, if not uniform can cause plasma density variation. Figure 5.20 (b) shows the radial profile of plasma electron temperature. At *r* = 0, the plasma electron temperature lies between 4 eV to 6 eV for all powers and decreases with increasing power. At other locations i.e, *r* = 10 mm, 30 mm, 40 mm and 45 mm it is within 6 eV to 8 eV and at *r* = 20 mm it increases to 12 eV to 14 eV for all powers. Figure 5.20 (c) shows the plasma potential at *r* = 0 mm and *r* = 10 mm that lies between 30 V to 40 V and then gradually decreases and at *r* = 45 mm and lies between 14 V to 18 V for all powers.

Therefore, it is concluded that the radial profiles as shown in Figure 5.20 are mainly caused by the sidewall loss of electrons and nonuniform power distribution of microwave in the ECR plasma.

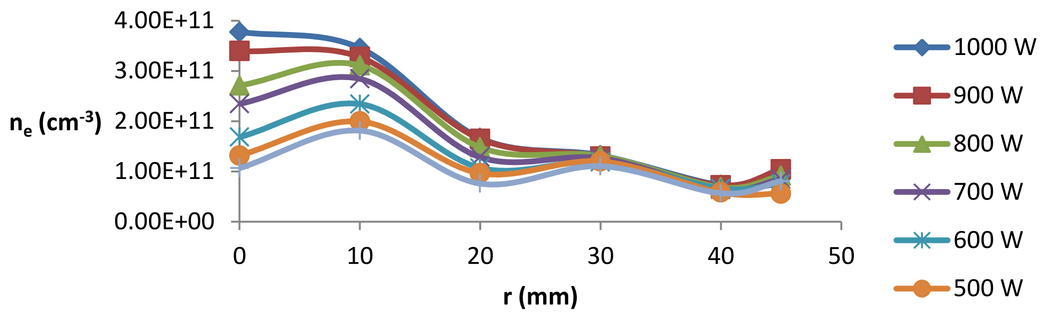

(a)

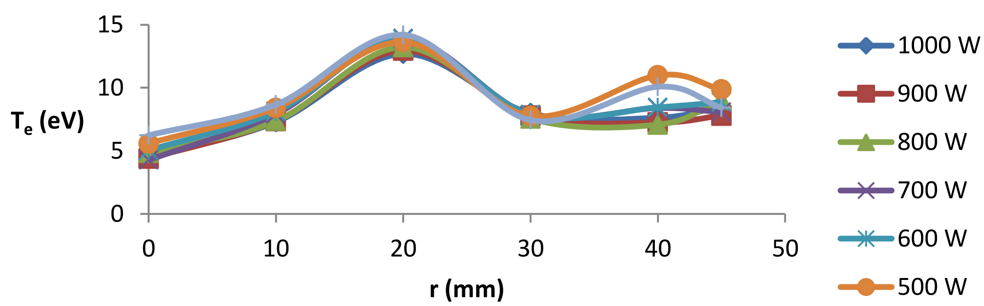

(b)

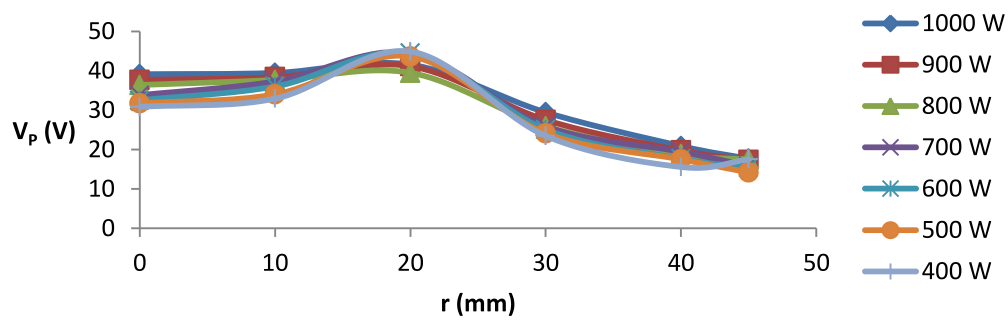

(c)

Figure 5.20 *Variation of (a) plasma density n_e, (b) plasma electron temperature T_e and (c) plasma potential V_P at the ECR region with the radial location of probe at neutral gas pressure 2.5×10^{-3} mbar.*

5.8 Summary

In this chapter the plasma characterization of the ECR proton ion source is described. The ECR plasma in the ion source was generated in a cw and pulse mode using microwave power 400 W – 1000 W at 2.45 GHz and axial magnetic field configuration of 820 – 950 G. The pulsed plasma was generated by operating the magnetron in pulsed mode. The plasma parameters were measured in the ECR zone using automated Langmuir probe measurement unit that was developed in housed. Dependence of reflected microwave power was studied as a function of forward microwave power for various neutral gas pressures. It is found that the reflected microwave power is 1 to 2 % of forward microwave power for the pressure range studied. The Langmuir probe measurement indicate that the plasma density and plasma electron temperature measured are in the range 5.6×10^{10} cm^{-3} to 3.8×10^{11} cm^{-3} and 4 eV to 14 eV respectively. The dependence of plasma parameters with microwave power, neutral gas pressure and radial location of probe were studied. The investigations show that the plasma electron temperature decreases with the increase of neutral gas pressure where as the plasma electron density increases with the increase of neutral gas pressure. The variations of plasma parameters with microwave power shows that the plasma density increases steadily with the increase of microwave power whereas the plasma electron temperature decreases or remains constant with the increase of microwave power. An empirical scaling law is found to explain the variations of plasma parameters with gas pressure and microwave power that matches well with the experimental data. The radial variation of plasma parameters with microwave power shows that the plasma density and plasma potential gradually decreases from the center of the plasma to the outer edge while plasma electron temperature on the average remains constant.

Chapter 6

Beam Characterization of ECR Proton Ion Source

This chapter discusses about the ion beam extraction in continuous and pulsed mode and its characterization in terms of beam current, emittance and proton fraction. A low energy beam transport line that was designed and developed for ion beam characterization is also discussed.

6.1 Beam Current Measurement

The schematic of the high current electron cyclotron resonance (ECR) ion source apparatus that was used for beam current measurement is shown in Figure 6.1. The ion source in the test stand is shown in Figure 6.2 [102].

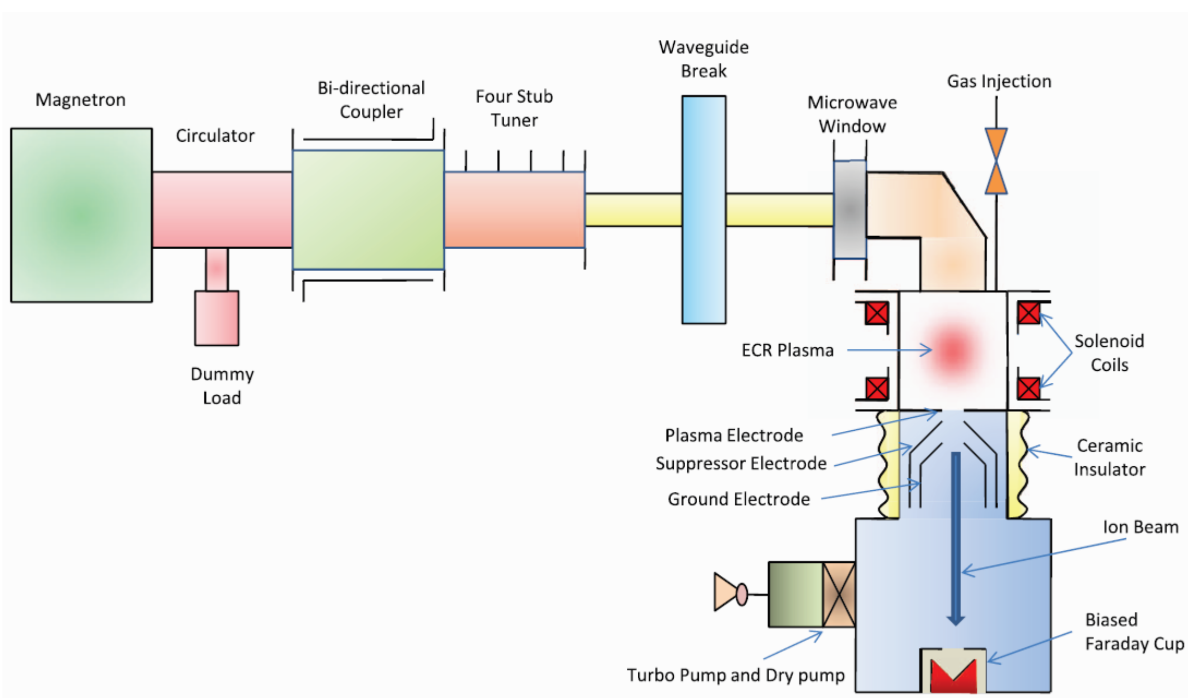

Figure 6.1 *Schematic of beam current measurement setup.*

Figure 6.2 *Beam current measurement setup of ECR proton ion source.*

6.1.1 Experimental Setup

The ion extraction and ion beam current measurement experiment was performed by first isolating the plasma chamber that was floated at extractor voltage of 50 kV from the microwave components and solenoid coils that were at ground potential using a DC waveguide break and a Perspex cylindrical insulator. The ion source was evacuated to a base pressure of 6×10^{-7} mbar and maintained for several hours, prior to the commencement of the experiment. The working gas was introduced in the plasma chamber in a controlled manner using a precision leak valve and maintained in the pressure range ~ 10^{-4} - 10^{-3} mbar in the plasma chamber and ~ 10^{-6} - 10^{-5} mbar in the extractor region. The pressure difference in the plasma chamber and the extractor region was due to the fact that the plasma chamber was evacuated through the 8 mm aperture in the plasma electrode. Prior to beam extraction, pressure measurements were carried out in the above range by introducing the working gas and measuring the pressures in the plasma chamber and the vacuum chamber of the extractor region. When the source was in operation with high voltage on, only the pressure in the vacuum chamber of extractor region was monitored. The currents in the solenoid coils were adjusted to obtain the desired magnetic field configurations of 850 – 900 G along the axial direction in the plasma chamber of length 100 mm. The microwave generator was energized for initiating the discharge. The microwave power of 400 – 1000 W was coupled to the plasma chamber. The incident and reflected power were measured using a diode detector and digital power meter connected to a directional coupler. The reflected power was minimized using a four stub auto-tuner. Once the plasma discharge was established, the ion beam was extracted by biasing the extractor electrodes. An electron suppressed Faraday cup was used to measure the total ion beam current.

6.1.2 Results and Discussions

The assembled ion source on the test stand in Figure 6.2 was operated with all subsystems connected. The ion beam current of 42 mA (all species) was extracted at beam energy of 40 keV [3]. The long time operation of the ion source was found to be hampered by (i) damage of microwave quartz window and (ii) rise in cooling water temperature. When the source was operated at beam current of 20 - 30 mA, it was observed that the vacuum in the chamber was deteriorated after half an hour of source operation. After careful observation, it was found that 6 mm thick quartz microwave window was damaged. This was caused by the bombardment of back-streaming electrons on the quartz window. The back-streaming electrons were created by ionization of residual gas in the extractor region. The secondary electrons from gas ionization experience an accelerating field in opposite direction and entered in the plasma chamber where they get focused due to strong solenoid focusing field present and these electrons then hit the quartz window plate. The impression seen on the quartz window as shown in Figure 6.3 (a) is a tapered hole of 8 mm diameter (same as extraction electrode aperture) in front and 0.5 mm diameter at back. Subsequently, a 2 mm thick boron nitride plate was incorporated with the 6 mm thick quartz plate making it a two layered window. But the two layer window as shown in Figure 6.3 (b) was also damaged after three hours of source operations. It was also observed during source operation that the cooling water temperature rises steadily resulting in steady rise of reflected microwave power.

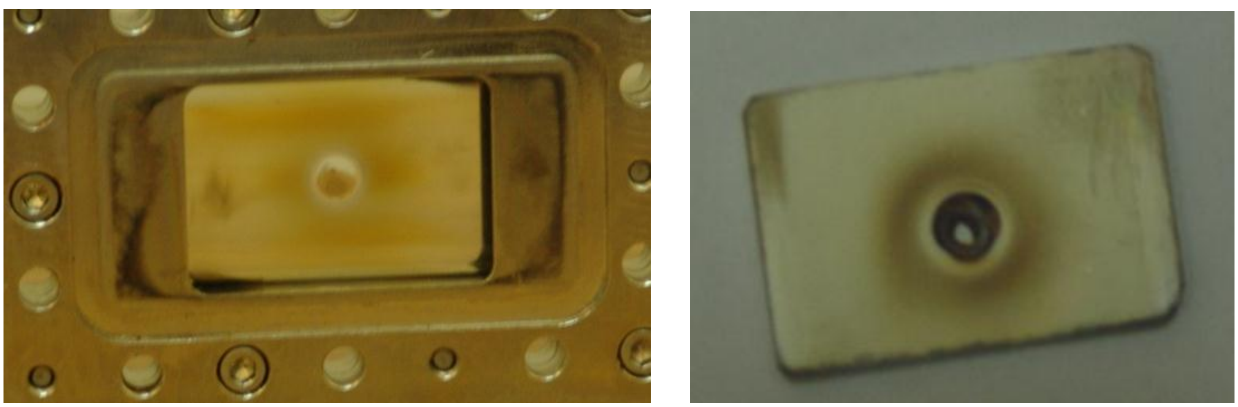

(a) (b)

Figure 6.3 *Damaged microwave windows (a) quartz and (b) Boron nitride.*

The reflected power could not be controlled using four stub auto tuner as the ion source components were heated up. These two problems were resolved by relocating the microwave window from the line of sight of back streaming electrons and by increasing the chill water flow in the heat exchanger. The ridge waveguide was redesigned because it is to be operated under vacuum. Also a water-cooled H plane bend waveguide was designed and fabricated with vacuum compatibility and incorporated in the microwave transmission line section. In this new configuration it was felt necessary to stabilize the plasma and characterize it (chapter 5) before extracting ion beam as the microwave coupling to plasma has changed by the presence of H plane bend waveguide and ridge waveguide in the low pressure region.

With these modifications the ion source was operated but the stabilization of plasma was found to be difficult as it was not possible to reduce the reflected microwave power. The coupling of microwave power to ECR plasma was poor by the presence of ridge waveguide and H-plane

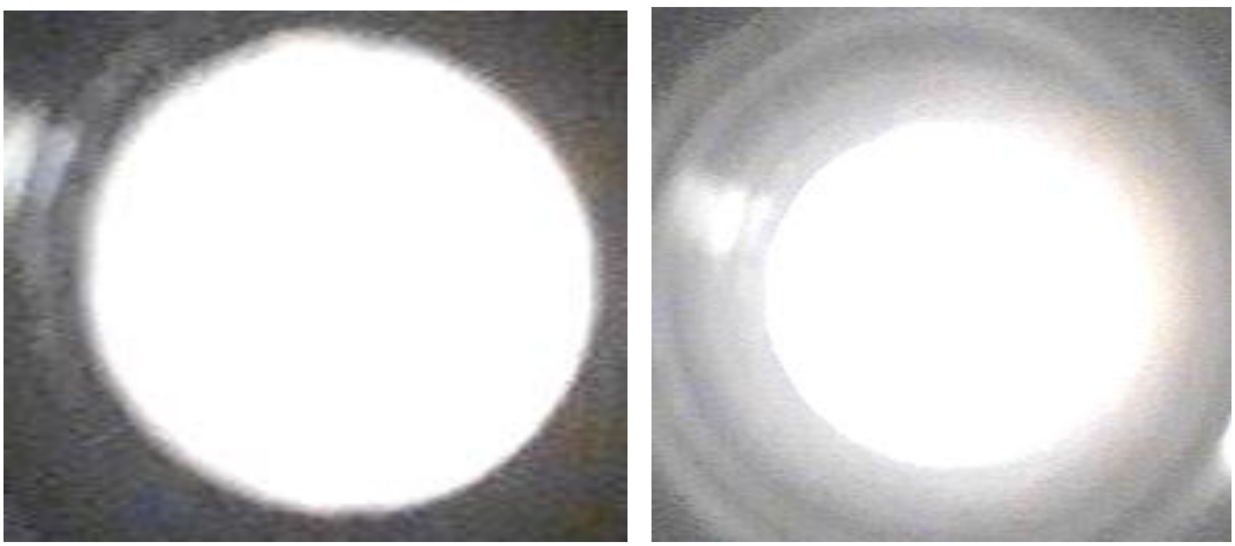

(a) (b)

Figure 6.4 *ECR plasma discharge at microwave power of (a) 500 W and (b) 800 W.*

bend waveguide in low pressure region and non-sustainable plasma discharge was observed by the continuous fluctuations of reflected microwave power. Considerable efforts were made to reduce the reflected microwave power and finally it has been achieved by tuning with the magnetic field. Reduction in the reflected microwave power leads to ECR breakdown and self-sustained plasma in the chamber as stated in chapter 5. The ECR discharge as shown in Figure 6.4 is for microwave power of (a) 500 W and (b) 800 W. Other than ECR mechanism there are off-resonance mechanisms that also contribute significantly to the production of high density plasma [17-20, 65-70].

After plasma stabilization, a detailed ECR plasma characterization studies were performed in CW and pulsed mode using hydrogen as working gas in the pressure range 10^{-4} - 10^{-3} mbar and microwave power of 400–1000W as described in chapter 5. These are the pressure and power range of interest where the ion source was operated. The measurement of plasma parameters is important as it is related to the beam parameters of the ion source, i.e. beam current, emittance and species. The investigations indicate that in the above mentioned microwave power and pressure range the plasma density and plasma electron temperature measured were 5.6×10^{10} - 3.8×10^{11} cm^{-3} and 4 – 14 eV respectively. From Figure 4.26, it is seen that tens of mA's ion beam current can be extracted with the above mentioned plasma density.

The ion beam was extracted when the plasma was stabilized. The ion beam was extracted by applying bias of +10 to +50 kV on plasma electrode and -2 to -4 kV on suppressor electrode. While extracting the ion beam in CW mode, there were few sparks initially inside the extractor chamber that got subsided with time. The ion beam current was found stable for several hours of source operation. The extracted ion beam current was measured using movable water cooled electron suppressed Faraday cup developed in housed as shown in Figure 6.5. The extracted beam current recorded on Faraday cup and beam image recorded on CCD camera are shown in Figures 6.6 (a) and (b).

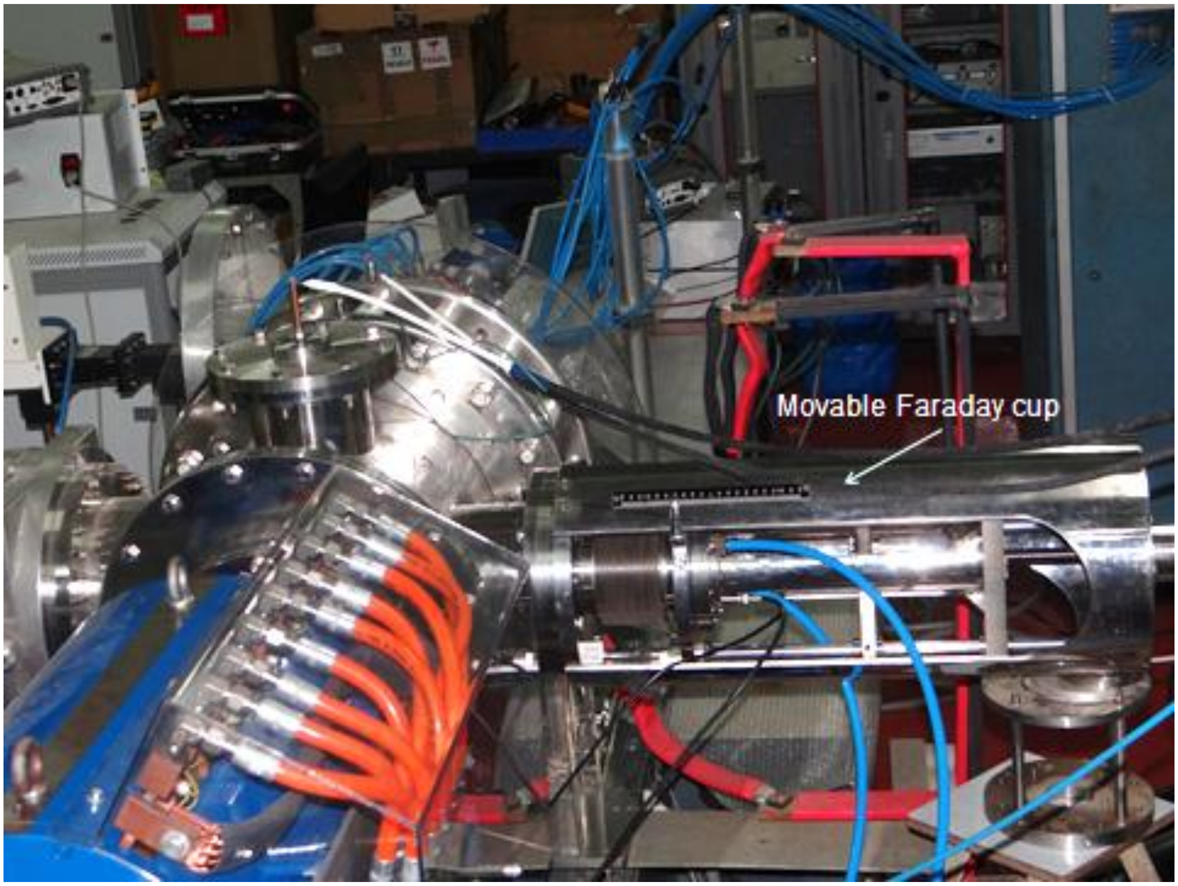

Figure 6.5 *The movable Faraday cup installed in the ion source test stand*.

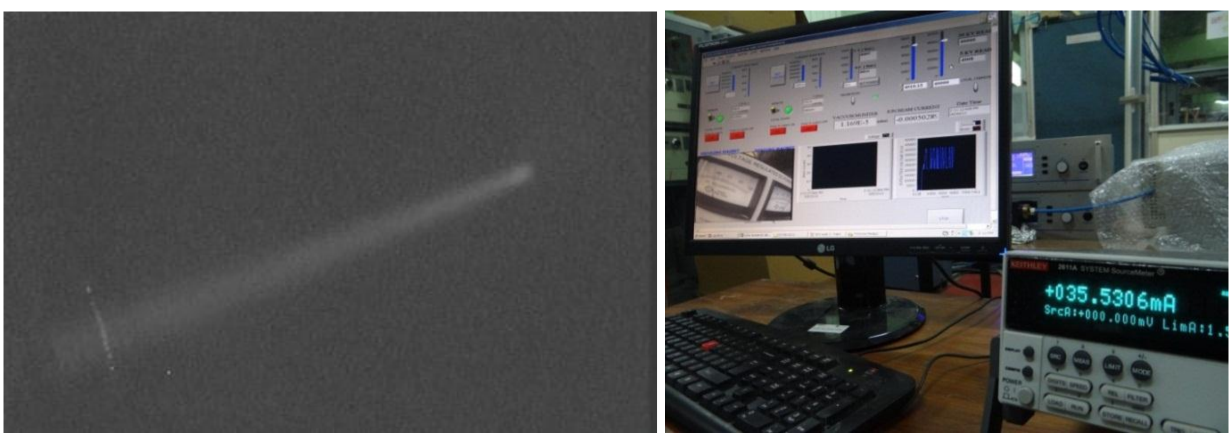

Figure 6.6 *(a) Beam image recorded on CCD camera and (b) beam current recorded on current meter.*

6.1.2.1 Dependence of beam current on extraction voltage

Figure 6.7 (a-c), show~~s~~ the plot of beam current versus extraction voltage for different values of microwave power at a residual gas pressure of 1×10^{-5} mbar. Also shown in Figures are the simulation results for -2, -3 and -4 kV of suppressor voltage. It is seen from Figure 6.7 (a) that the extracted beam current increases as $V^{3/2}$ (space charge limiting current) with the rise in extraction voltage for all microwave powers. The beam current is 9 - 10 mA at 20 kV and increases to 30 – 31 mA at 40 kV. Figure 6.7 (b) shows that the beam current increases as $V^{3/2}$ with extraction voltage up to 35 kV and then saturates for all microwave powers. Here, the beam current is 7.5 – 9.2 mA at 20 kV and increases to 29.4 – 31 mA at 40 kV. Figure 6.7 (c) shows that the beam current increases as $V^{3/2}$ with extraction voltage for microwave powers of 800, 900 and 1000 W but saturate after extraction voltage of 35 kV for microwave powers of 600 and 700 W. Here, the beam current is 7.7 – 9.2 mA at 20 kV and increases to 32 – 35.5 mA at 40 kV.

Figure 6.8 (a-c), show the plot of beam current versus extraction voltage for different values of microwave power at a residual gas pressure of 1.5×10^{-5} mbar. Figure 6.8 (a) shows that the beam current increases from 9.8 – 10.4 mA at 20 kV to 29.5 – 32 mA at 40 kV. From Figure 6.8 (b), it is seen that the beam current increases as $V^{3/2}$ with extraction voltage up to 35 kV and then saturates for all microwave powers. Here, the beam current is 8.7 – 10.1 mA at 20 kV and increases to 31 – 34 mA at 40 kV. Figure 6.8 (c) indicate that the beam current increases as $V^{3/2}$ with extraction voltage up to 35 kV and then saturates for all microwave powers. Here, the beam current is 9.1 – 10.4 mA at 20 kV and increases to 31 – 35.7 mA at 40 kV.

Figure 6.9 (a-c), shows the plot of beam current versus extraction voltage for different values of microwave power at a residual gas pressure of 2×10^{-5} mbar. In Figure 6.9 (a) it is seen that the beam current for microwave powers 500 – 700 W increases from 12.2 – 14.2 mA at 20 kV to

21.4 – 24.8 mA at 40 kV. For microwave power of 800 – 1000 W the beam current increases from 10.4 – 11.5 mA at 20 kV to 36.4 – 40.0 mA at 40 kV. Figures 6.9 (b) and (c) indicate similar features. There is change in the pattern as shown in Figure 6.9 for microwave power of 500 – 700 W and 800 - 1000 W. This is observed when the microwave power is reduced from 800 W to 700 W and the reflected power is increased to a large value. It was not possible to reduce it with auto tuner so the magnetic field value was changed slightly to reduce the reflected power. This resulted in the change of electric field pattern or mode structure in plasma and the measured beam current at 40 kV, 500 – 700 W reduces to 25 mA at 2×10^{-5} mbar as compared to 30 mA for 1×10^{-5} mbar.

6.1.2.2 Dependence of beam current on microwave power

Figure 6.10 (a-c), show the plot of beam current versus microwave power for different values of extraction voltages at a residual gas pressure of 1×10^{-5} mbar. The beam current in Figure 6.10 (a) increases from 600 – 800 W and then reduces for 900 - 1000 W for all extraction voltages. Similar features are seen from Figures 6.10 (b-c). The beam current does not change significantly with the increase of microwave power because the plasma density does not change significantly with the increase of microwave power as seen in Figure 5.17. Here, the residual gas pressure of 1×10^{-5} mbar in the extractor region of Figure 6.10 corresponds to gas pressure of 1.2×10^{-3} mbar in the plasma chamber of Figure 5.17.

6.1.2.3 Dependence of beam current on gas pressure

Figure 6.11 (a-c), show the plot of beam current versus residual gas pressure for different values of extraction voltages and microwave power of 800 W. From Figure 6.11 (a), the beam

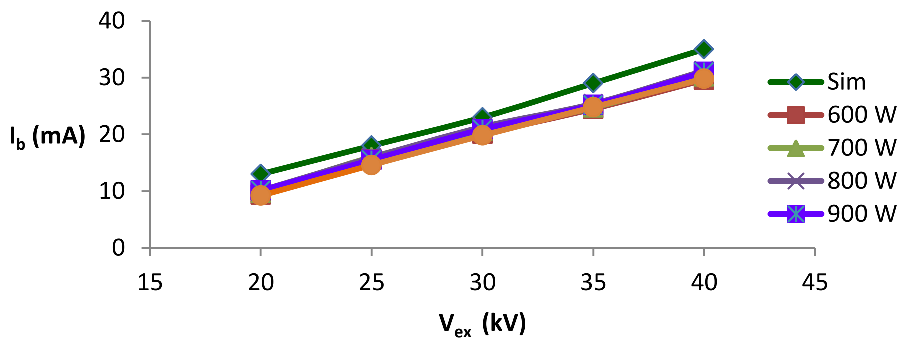

(a)

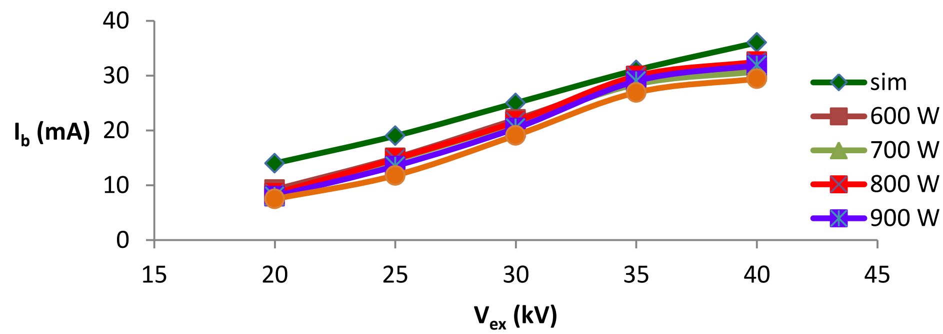

(b)

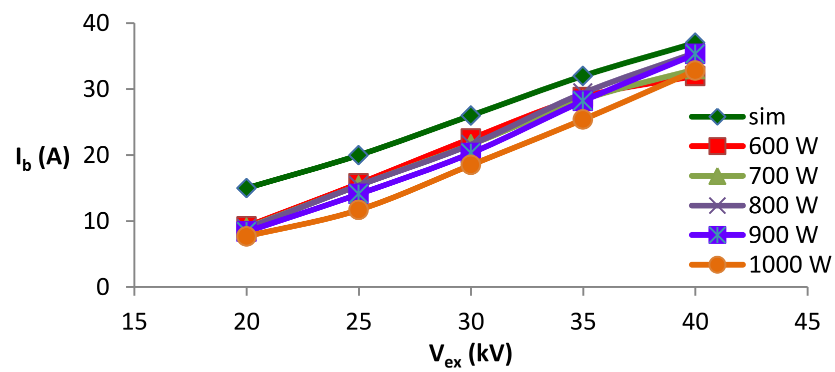

(c)

Figure 6.7 *Beam current versus extraction voltage (along with simulation results) for different values of microwave powers at* 1×10^{-5} *mbar of gas pressure and suppression electrode voltage (a) –2 kV, (b) –3 kV and (c) -4 kV.*

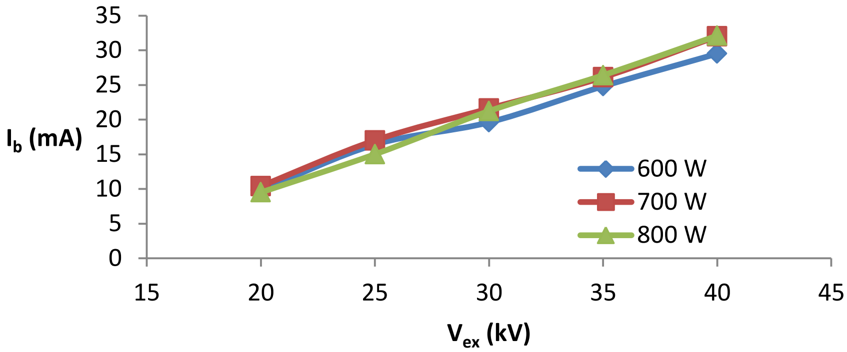

(a)

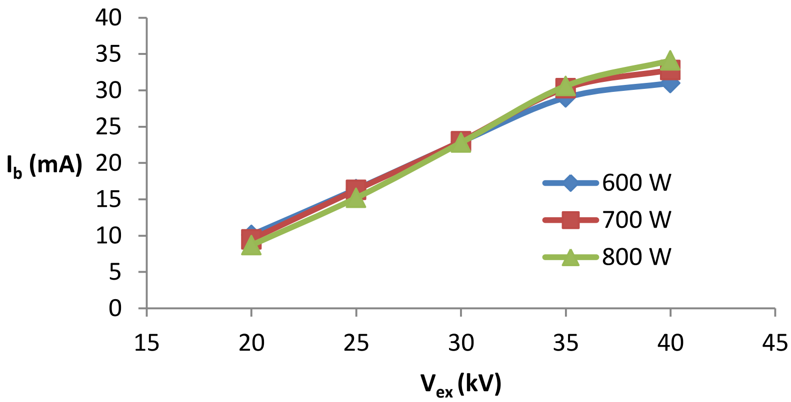

(b)

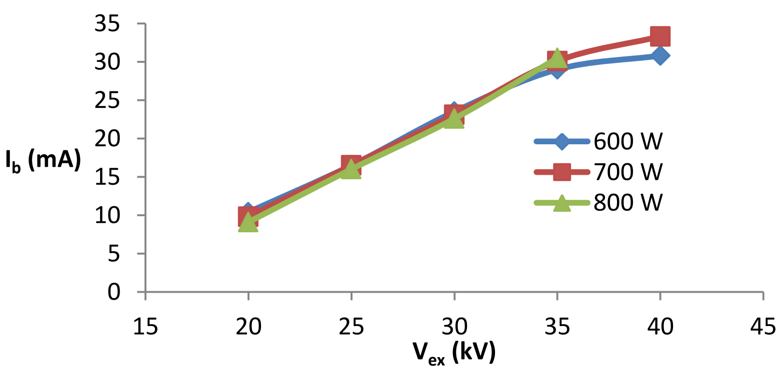

(c)

Figure 6.8 *Beam current versus extraction voltage (along with simulation results) for different values of microwave powers at* 1.5×10^{-5} *mbar of gas pressure and suppression electrode voltage (a) –2 kV, (b) –3 kV and (c) -4 kV.*

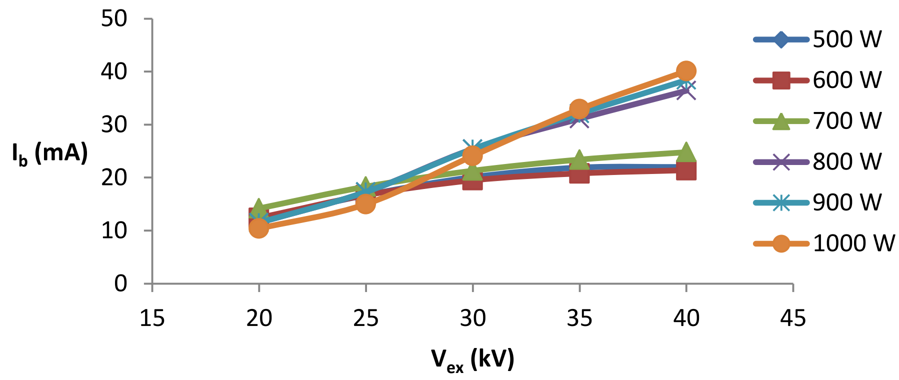

(a)

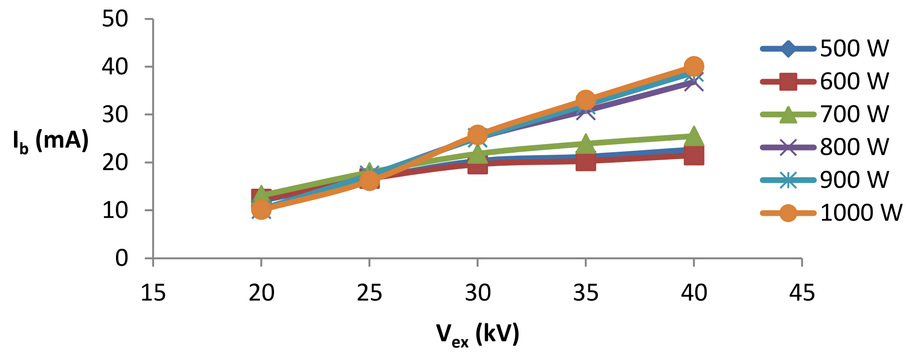

(b)

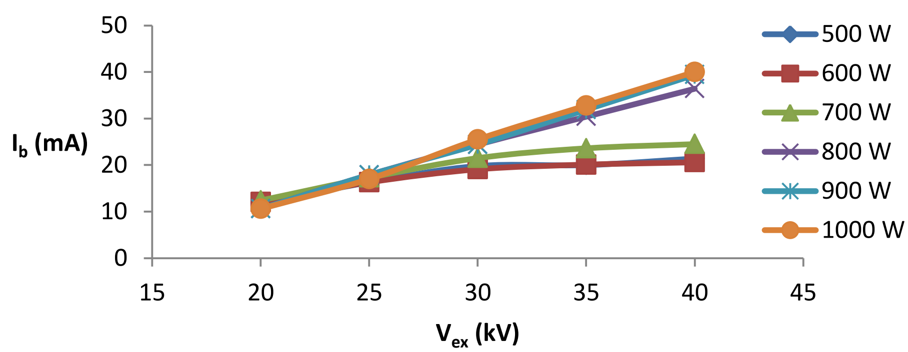

(c)

Figure 6.9 *Beam current versus extraction voltage (along with simulation results) for different values of microwave powers at* 2×10^{-5} *mbar of gas pressure and suppression electrode voltage (a) –2 kV, (b) –3 kV and (c) -4 kV.*

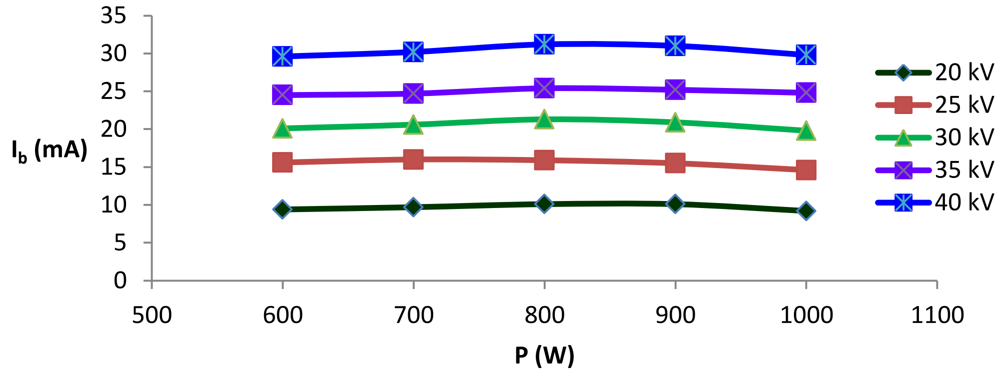

(a)

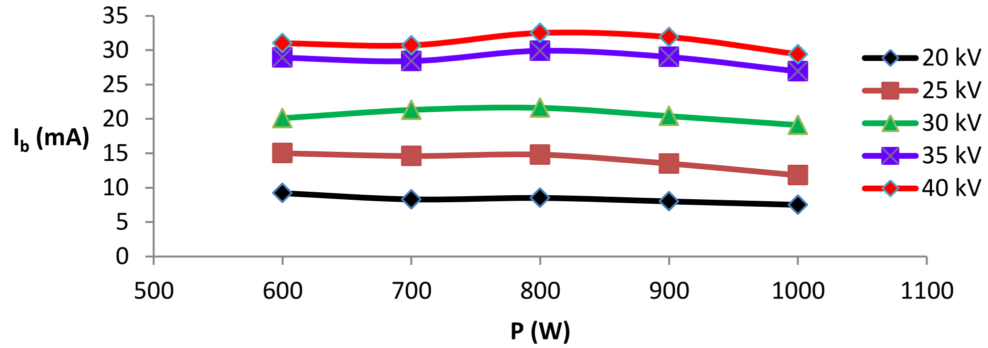

(b)

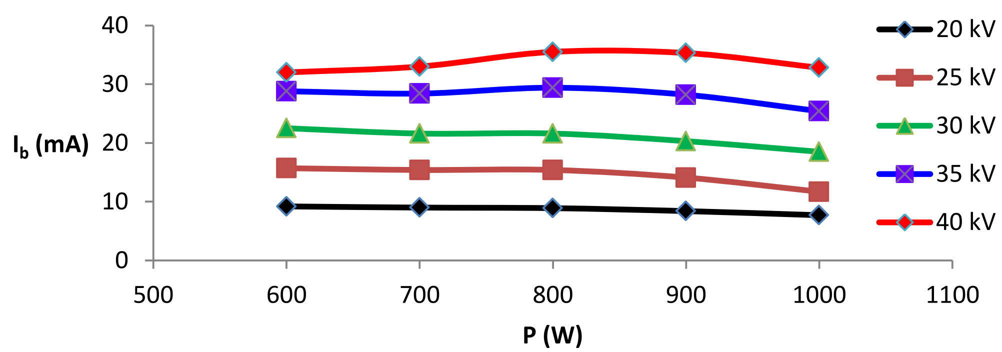

(c)

Figure 6.10 *Beam current versus microwave power for different values of extraction voltage at 1×10^{-5} mbar of gas pressure and suppression electrode voltage (a) –2 kV, (b) –3 kV and (c) -4 kV.*

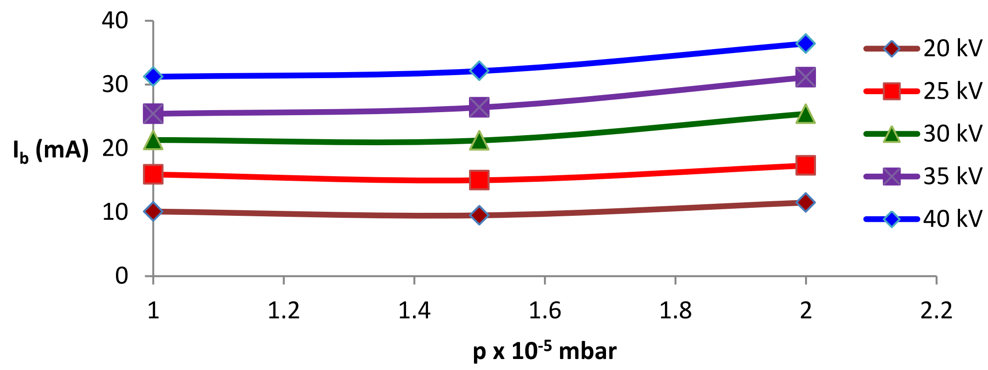

(a)

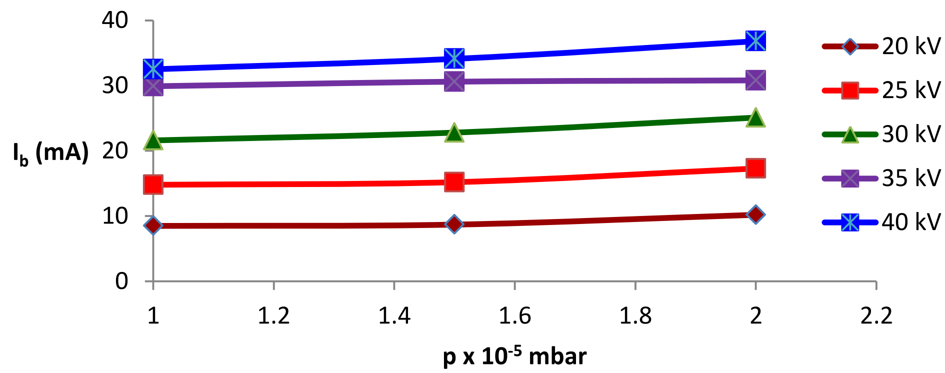

(b)

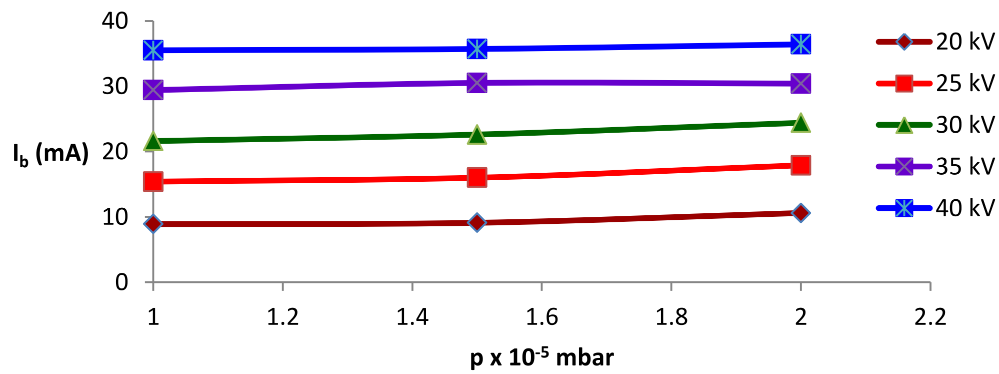

(c)

Figure 6.11 *Beam current versus residual gas pressure for different values of extraction voltage at 800 W of microwave power and suppression electrode voltage (a) –2 kV, (b) –3 kV and (c) -4 kV.*

current is more or less constant for pressure of $1 – 1.5\times10^{-5}$ mbar but increases at pressure 2×10^{-5} mbar. Similar features are seen from Figures 6.11 (b) and (c).

6.1.2.4 Pulsed mode operation of ion source

The pulsed mode operation of ion source is the starting operational requirement of LEHIPA. This is required to check the proper transport of ion beam through various accelerating structures and to reduce radiological problem due to beam loss. The ion source was operated in a pulse mode by generating pulsed plasma and extracting the ion beam. The magnetron was operated in a pulsed mode by the internal pulse generator and also by external pulse from function generator. The pulse repetition rate was varied from 1 Hz, 10 Hz and 100 Hz to CW. The ion beam current was not found stable for pulse duration below 1 ms. Figure 6.12 shows the waveform of pulse ion beam for microwave power of 1000 W, residual gas pressure of 2×10^{-5} mbar, extraction voltage of 25 kV and suppression voltage of -2 kV. The variation of pulsed beam current with microwave power is shown in Figure 6.13. It is seen from the Figure 6.13 that the beam current increases from 7 - 10 mA when the microwave power increases from 500 – 1000 W at residual gas pressure of 2×10^{-5} mbar and 25 kV extraction voltage.

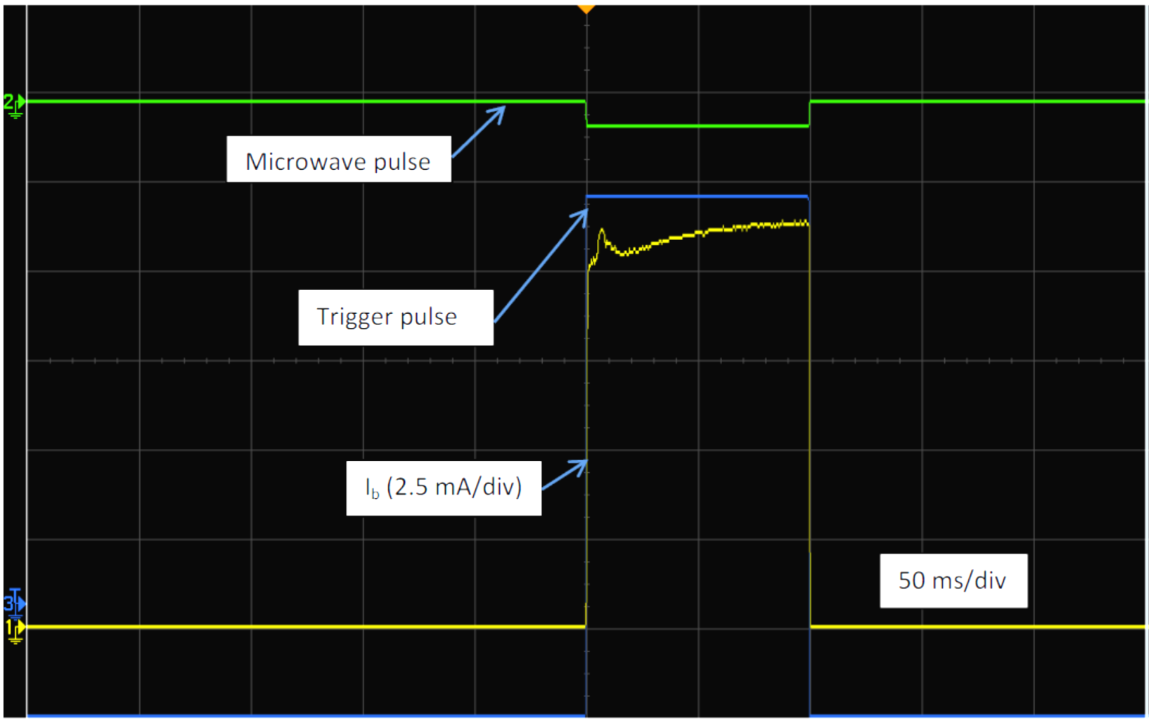

Figure 6.12 *Oscilloscope traces showing ion beam current, microwave pulse and trigger pulse for ion source operated in a pulsed mode.*

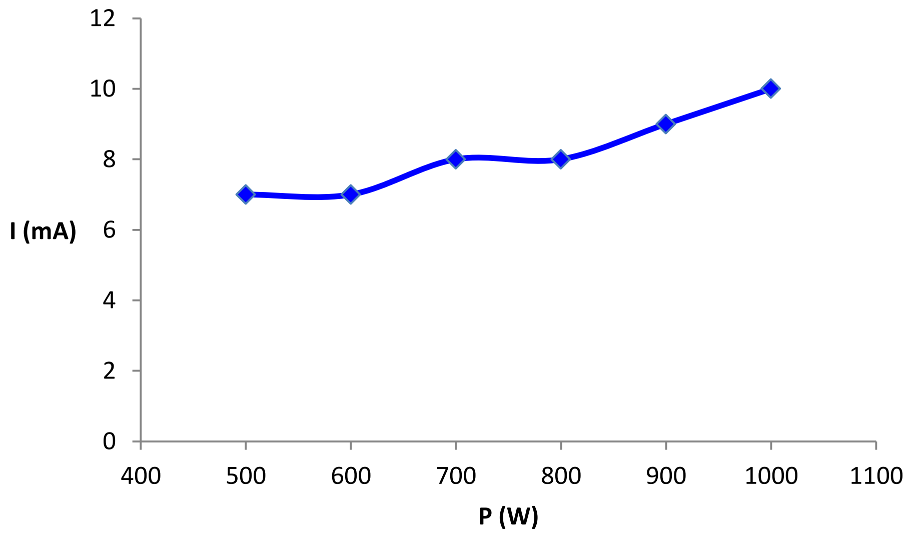

Figure 6.13 *Variation of pulsed beam current with microwave power.*

6.2 Low Energy Beam Transport Line for Emittance and Proton Fraction Measurement

A low energy beam transport line (LEBT) has been designed and developed for measuring two important beam parameters i.e., beam emittance and proton fraction [103]. The schematic of LEBT and the beam line components are shown in Figures 6.14 and 6.15.

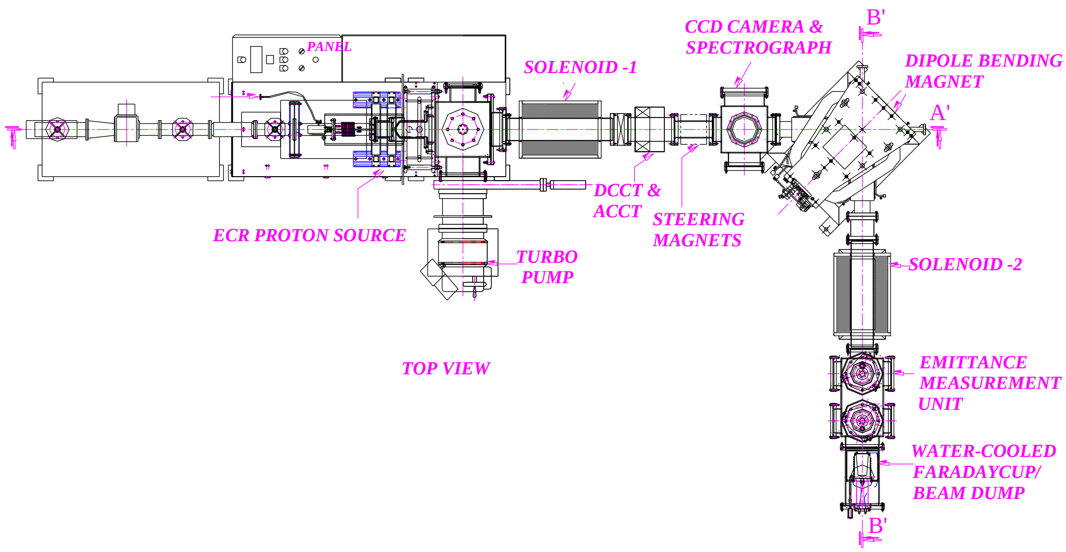

Figure 6.14 *Schematic of low energy beam transport line (LEBT).*

Figure 6.15 *Beam line components*

The purpose of LEBT is to transport and focus the ion beam from ion source to next accelerating structure or to application zone. The low energy beam transport line consists of two solenoid magnets and power supplies, two *X*-*Y* steering magnets and bipolar power supplies, an analyzing magnet and power supplies, turbo-molecular pump and controller, dry roughing pump, vacuum gauge heads and controllers and beam diagnostics i.e., emittance meter, DCCT, ACCT, CCD cameras and Faraday cup / beam dump. The beam optics of the beam line was studied using TRANSPORT, TRACE and GPT.

The beam optics calculations using TRANSPORT, the input beam parameters are x_i = 3.0 mm, x_i' = 34.4 mrad, y_i = 3.0 mm, y_i' = 34.4 mrad, BEAM ENERGY = 50 keV = 0.0096 GeV/c, DRIFT1 = 750 mm, SOLENOID1: B = 1.2 kG, L_{eff} = 500 mm, DRIFT2 = 1304 mm, BEND MAGNET: B = 1.054 kG, L_{eff} = 470 mm, DRIFT3 = 419 mm, SOLENOID2: B = 2.0 kG, L_{eff} = 500 mm and DRIFT4 = 200 mm. As the space charge compensation of 95% is reported [81] for residual gas pressure 2×10^{-5} mbar so the effective beam current of 1.5 mA is considered for 30 mA beam current. The beam envelope from TRANSPORT is shown in Figure 6.16.

The beam optics calculations using TRACE, the input beam parameters are EMIT0 = 24.9 π mm-mrad, α_x = -3.15, β_x = 0.375, α_y = -3.15, β_y = 0.375, BEAM ENERGY = 50 keV, I_b = 1.5 mA, DRIFT1 = 750 mm, SOLENOID1: B = 1.2 kG, L_{eff} = 500 mm, DRIFT2 = 1304 mm, BEND MAGNET: 90^0, DRIFT3 = 419 mm, SOLENOID2: B = 1.75 kG, L_{eff} = 500 mm and DRIFT4 = 200 mm. The beam is considered 95% space charge compensated. The beam envelope from TRACE is shown in Figure 6.17. The 3 D model of LEBT and beam envelope are shown in Figure 6.18 and the fields in solenoid magnets and analyzing magnet for the above mentioned beam parameters are shown in Figure 6.19.

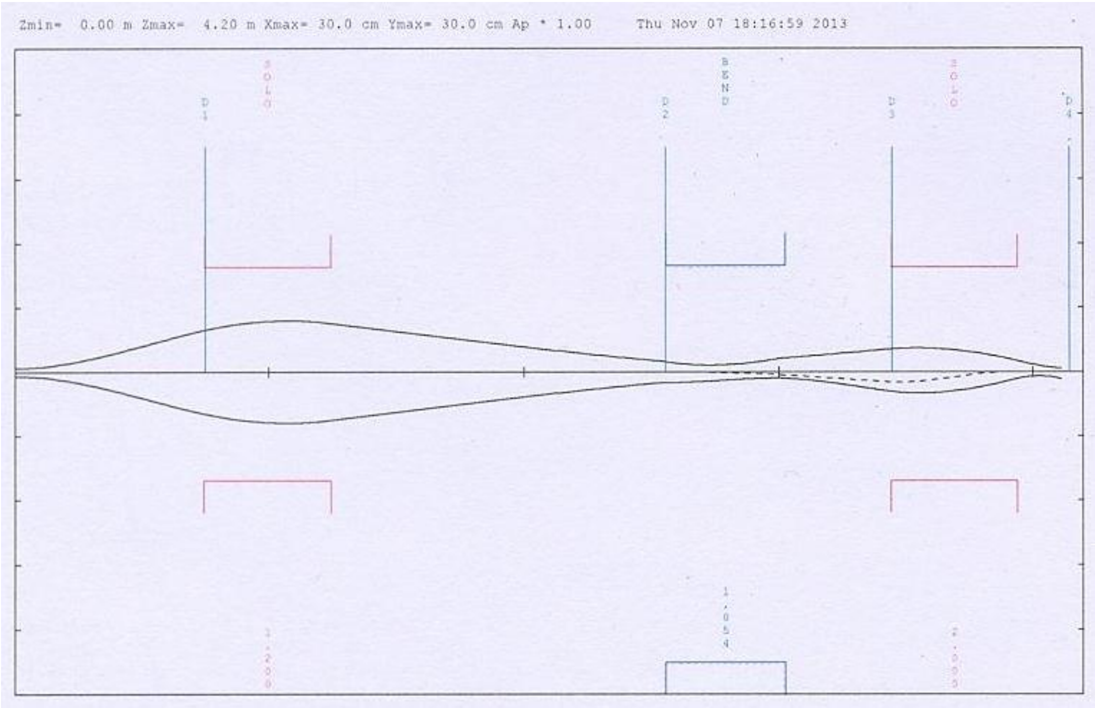

Figure 6.16 *Beam envelope in LEBT simulated using TRANSPORT*.

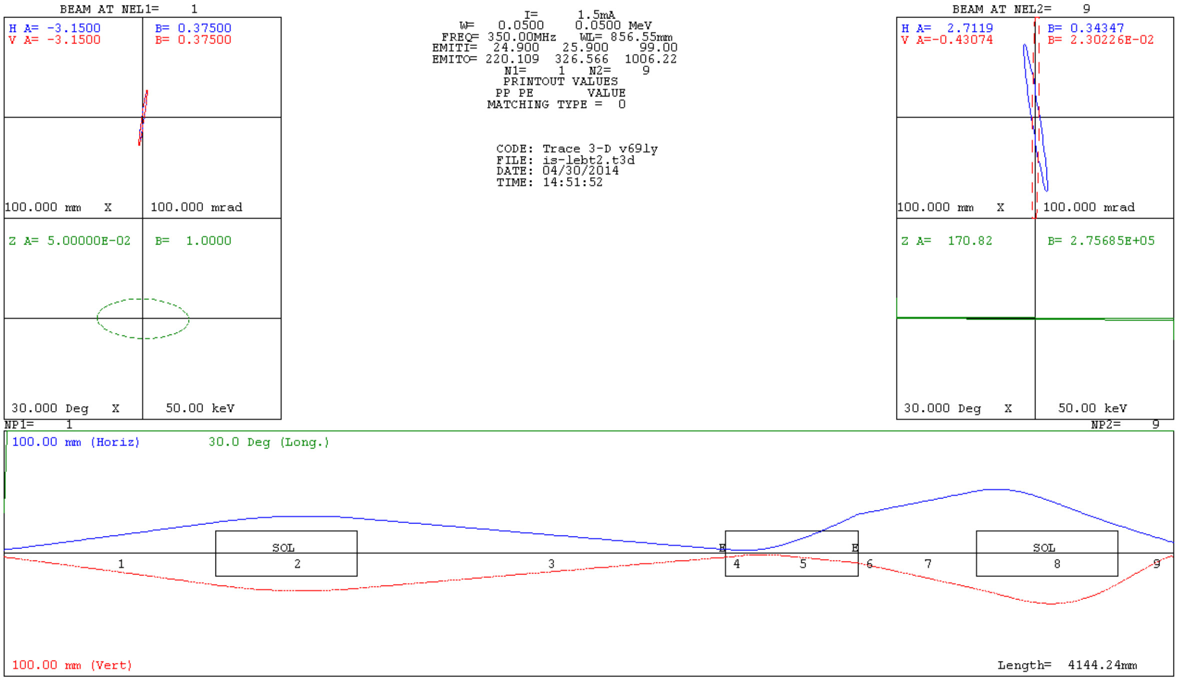

Figure 6.17 *Beam envelope in LEBT simulated using TRACE.*

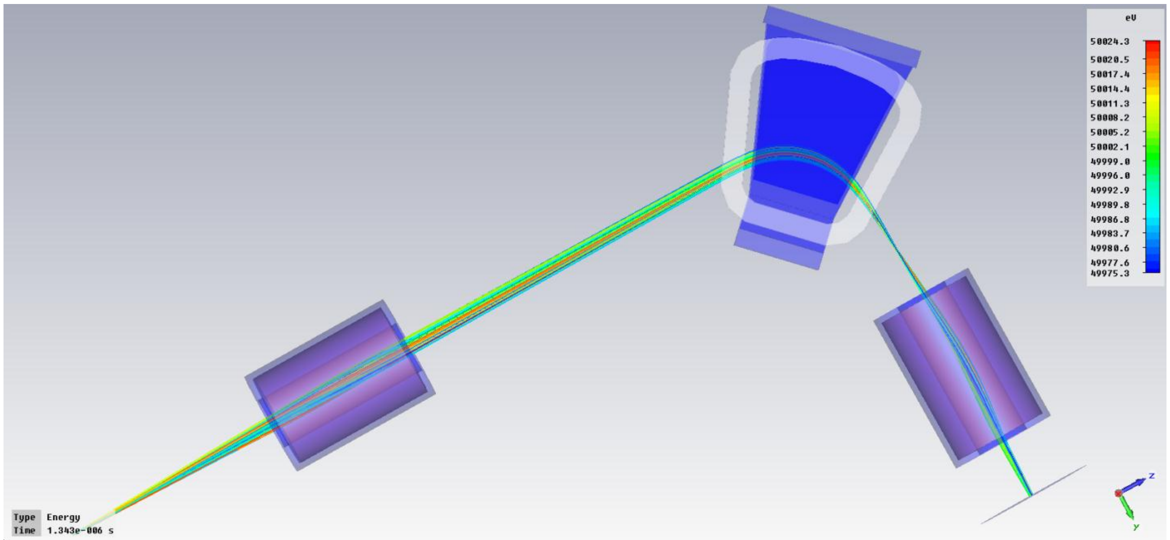

Figure 6.18 *3 D model and* beam *envelope in LEBT.*

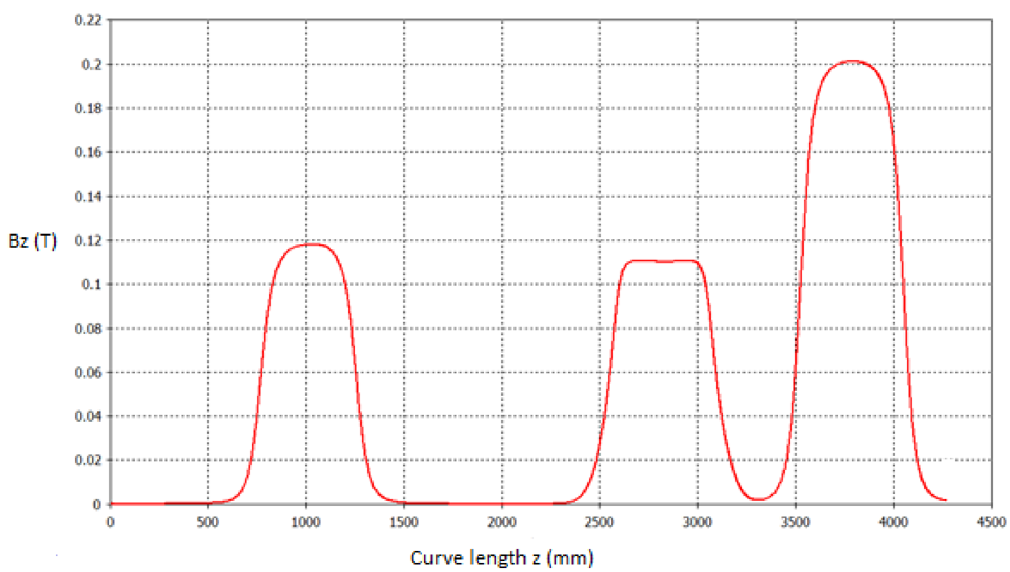

Figure 6.19 *Magnetic field values B versus curve length z in solenoid and bending magnet.*

.

The beam line was designed as per beam optics calculation. The beam line elements and beam diagnostics are described as follows:

6.2.1 Solenoid Focusing Magnets

Two solenoid magnets in LEBT were used to focus and transport the ion beam. The parameters of solenoid magnet are listed in Table 6.1.

Table: 6.1: *Parameters of solenoid focusing magnet*

Parameters	Designed values
Maximum field B (T)	0.35
Effective length (mm)	519
Aperture diameter (mm)	160
Outer diameter Yoke (mm)	360
Overall length of solenoid (mm)	560
Yoke material	St. 17
Coil type	Hollow conductor
Conductor dimensions (mm)	9×9 / ϕ 6
Number of turns N (turns)	400
Cooling type	Water cooling
Minimum pressure drop	3 bar
Total flow rate (lit/min)	8.6
Inlet temperature (^{0}C)	20
Maximum temperature rise (^{0}C)	22
Current I (A)	370
Voltage U (V)	40
Power P (kW)	14.8

For designing solenoid magnet, the 3D magneto-static calculation was carried out. The 3D model of solenoid magnet and field arrows is shown in Figure 6.20. The field contour is shown in Figure 6.21. The magnet has a slot in the return yoke for bringing cooling water and electrical interfaces to the coil. The coil is modeled as a cylinder with constant current density. The magnet model has been charged with a total of 354×400 = 141600 A-T and the central field is found to be 0.35 T. The magnetic length is 520 mm. Figure 6.22 shows the simulated field profile along the longitudinal axis. The simulated field homogeneity is 10^{-3} at y = 50 mm and magnetic length 500 mm. The fabricated solenoid magnet is shown in Figure 6.23. The measured field profile along the longitudinal axis and field calibration is shown in Figures 6.24 and 6.25. The measured effective magnetic length of the solenoid magnet is 500 mm.

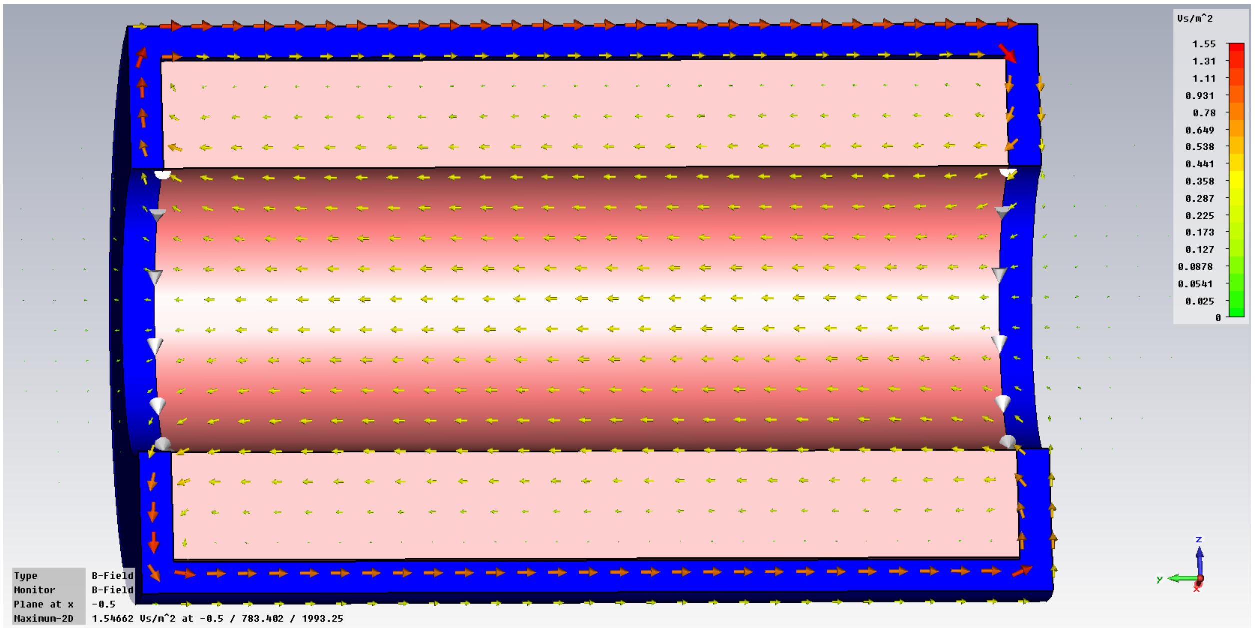

Figure 6.20 *Field arrows on the surface and inside the solenoid focusing magnet.*

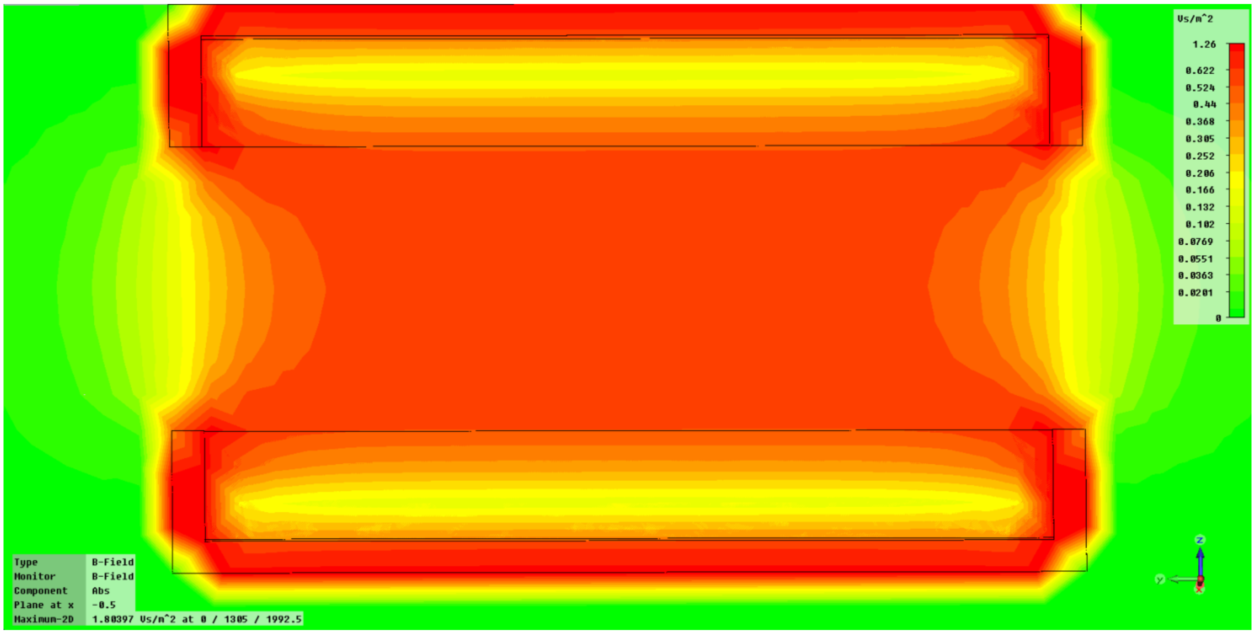

Figure 6.21 *Field contour of solenoid magnet.*

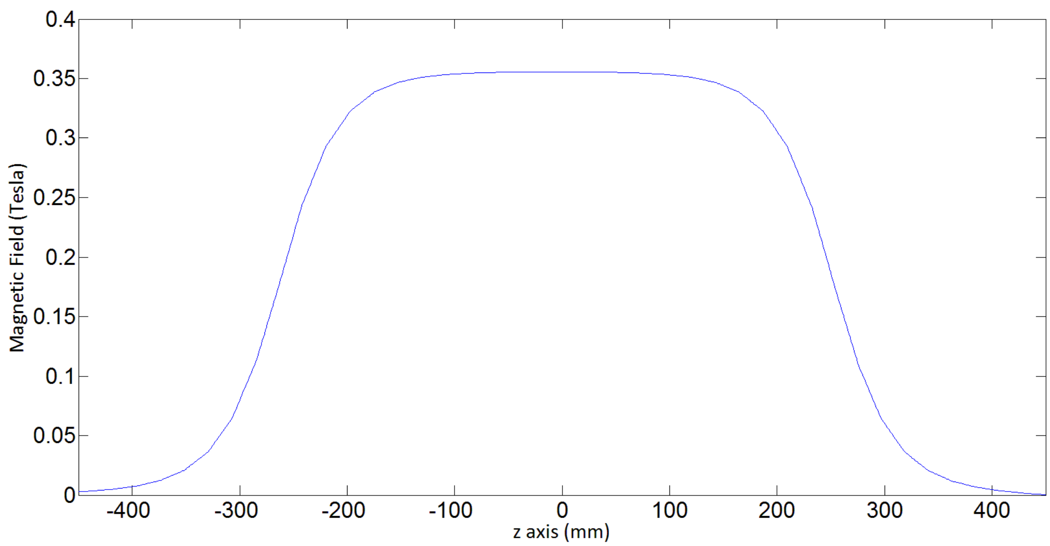

Figure 6.22 *Axial field of solenoid magnet.*

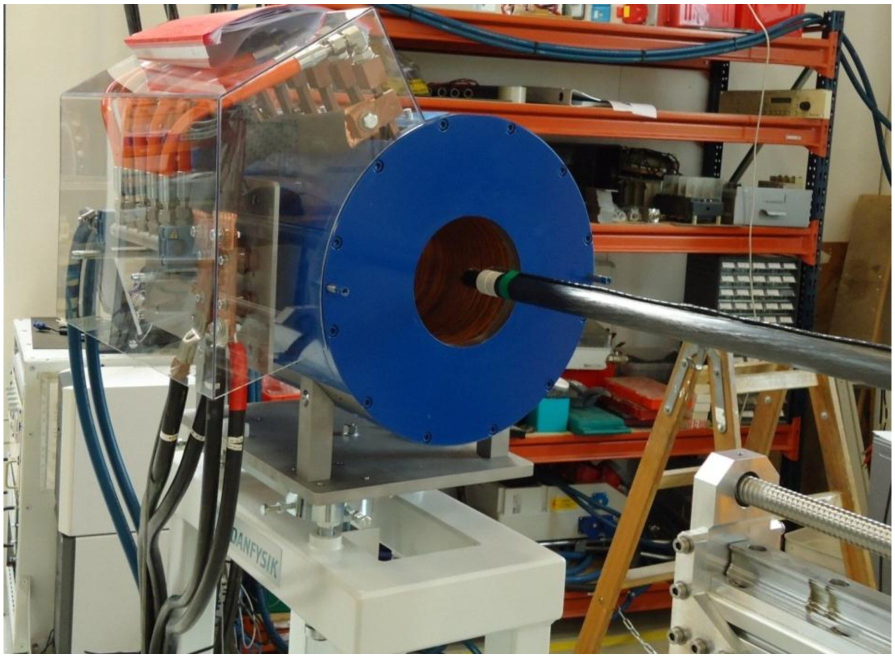

Figure 6.23 *Fabricated solenoid magnet under field measurement test using hall probe.*

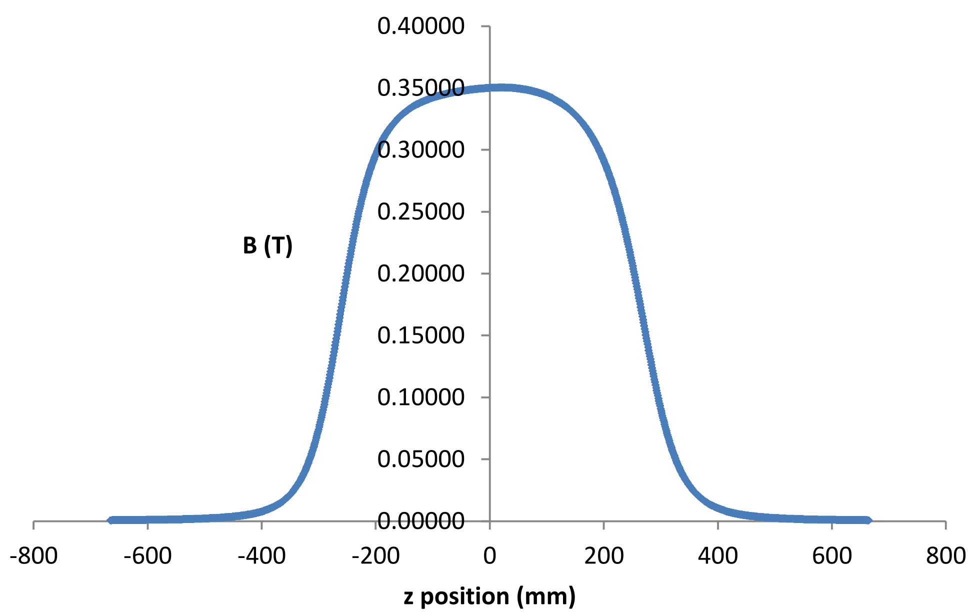

Figure 6.24 *Measured value of the axial field.*

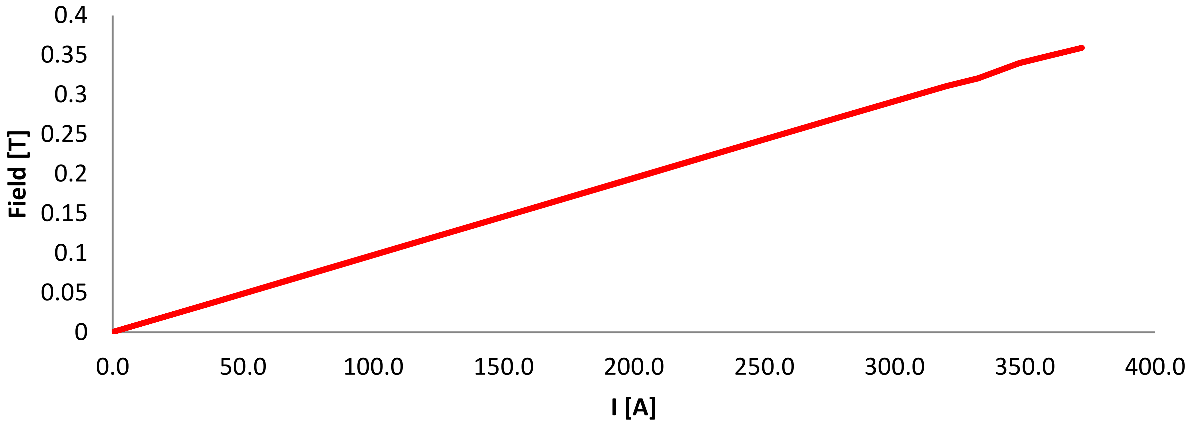

Figure 6.25 *Field calibration of solenoid magnet.*

6.2.2 Steering Magnets

The *X-Y* steering magnets was incorporated in the beam line to correct the trajectories of charge particle deviated from the central trajectories. The *X-Y* steering magnets were energized using bipolar power supplies. The fabricated steering magnet is shown in Figure 6.26. The parameters of steering magnet are listed in Table: 6.2.

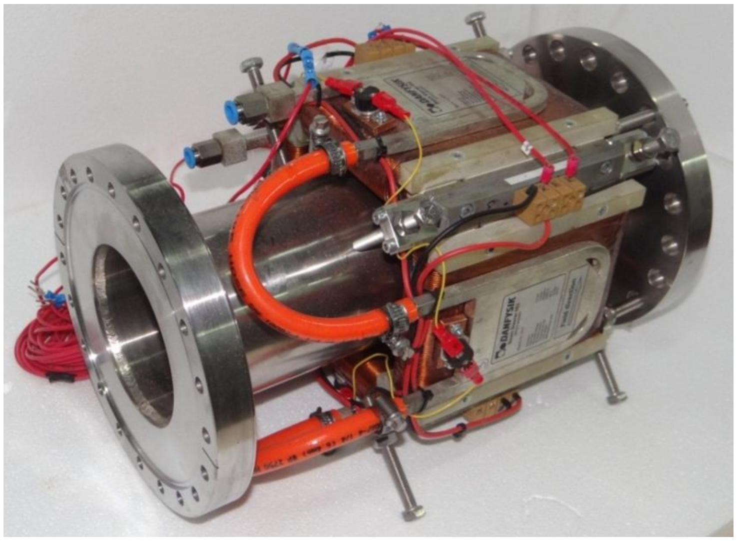

Figure 6.26 *The X-Y steering magnet mounted on beam tube*.

Table 6.2: *Parameters of X-Y steering magnets*

Parameters	Designed values
Maximum field (T)	0.18
Effective magnetic length (mm)	205
Maximum overall length (mm)	190
Field aperture diameter (mm)	110
Yoke material	St. 37
Coil Type	Solid conductor
Conductor dimensions (mm)	Φ 1.12
Number of turns per coil N	711
Cooling type	Indirect water cooling
Current I (A)	3
Voltage U (V)	30
Power P (W)	90
Total magnet weight W (kg)	20

6.2.3 Position and Profile Measurement Unit

In order to measure beam size, position and shape, the interceptive method using a water-cooled slit and a Faraday cup was designed and developed. The position and profile monitor consists of tantalum slit of 0.2 mm width and 80 mm length and is cooled by water passing through copper support bloc. The movement and position of the slit is remotely controlled using a stepper motor and controller.

6.2.4 Emittance Measurement Unit

Transverse emittance is one of the fundamental beam characteristics in any ion source and beam transport line. It is a measure of transverse trace space occupied by the beam. There are various methods of measuring beam emittance e.g. slit-slit, slit and collector, electric sweep, quadrupole scan, pepper pot etc. [104-114].

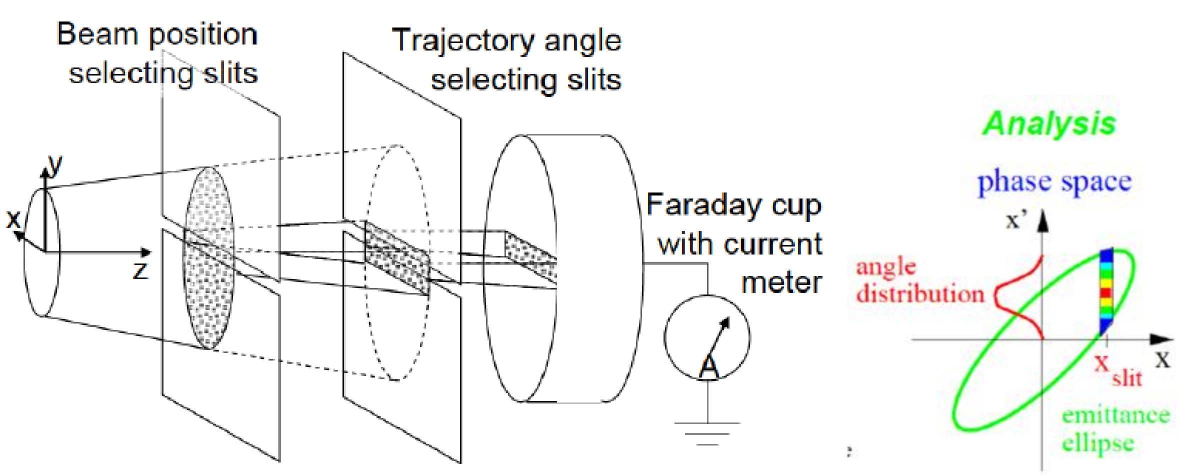

Figure 6.27 *Schematic of two-slit emittance measurement*.

The schematic of two-slit emittance meter is shown in Figure 6.27. In two slit method, a thin vertical upstream slit selects a small portion of the beam that is transmitted downstream. The slit position identifies the y, or vertical position of the beamlet, but all values of x and x' are allowed. The transmitted beam is measured using a slit and a collector. The slit positions, the transmitted current values, and the distance L separating the slit and the collector are used to generate the angular y' distribution of the beamlet. Repeating this process for different upstream slit positions produces y - y' density distribution that is used in the moment analysis to obtain the required rms beam emittances.

An Emittance Measurement Unit (EMU) was designed and developed to measure the transverse beam emittance as shown in Figure 6.28. It consists of two slits and a Faraday cup. The slits are separated by distance L= 300 mm. Both the slits are made of tantalum 0.2 mm wide aperture and 80 mm length and imbedded in a water-cooled copper block. The second slit has a Faraday cup attached to it. The movement of the slits are remotely controlled using stepper motors and controllers. The position of the slits are recorded using linear encoders. The Faraday cup current on the second slit is recorded on M/S Keithley 6485 and 2611 A current meter.

The first slit faces the full beam and cuts the beam. A small beamlet comes out of the first slit. For every position of the first slit, beamlet profile is scanned by the second slit. Suppose there are M positions of the first slit and for every M there are N positions of the second slit. So the matrix $M \times N$ is generated after one complete transverse scan of the beam. The matrix elements are the value of the Faraday cup currents.

The beam emittance is calculated from the stored matrix data as follows:

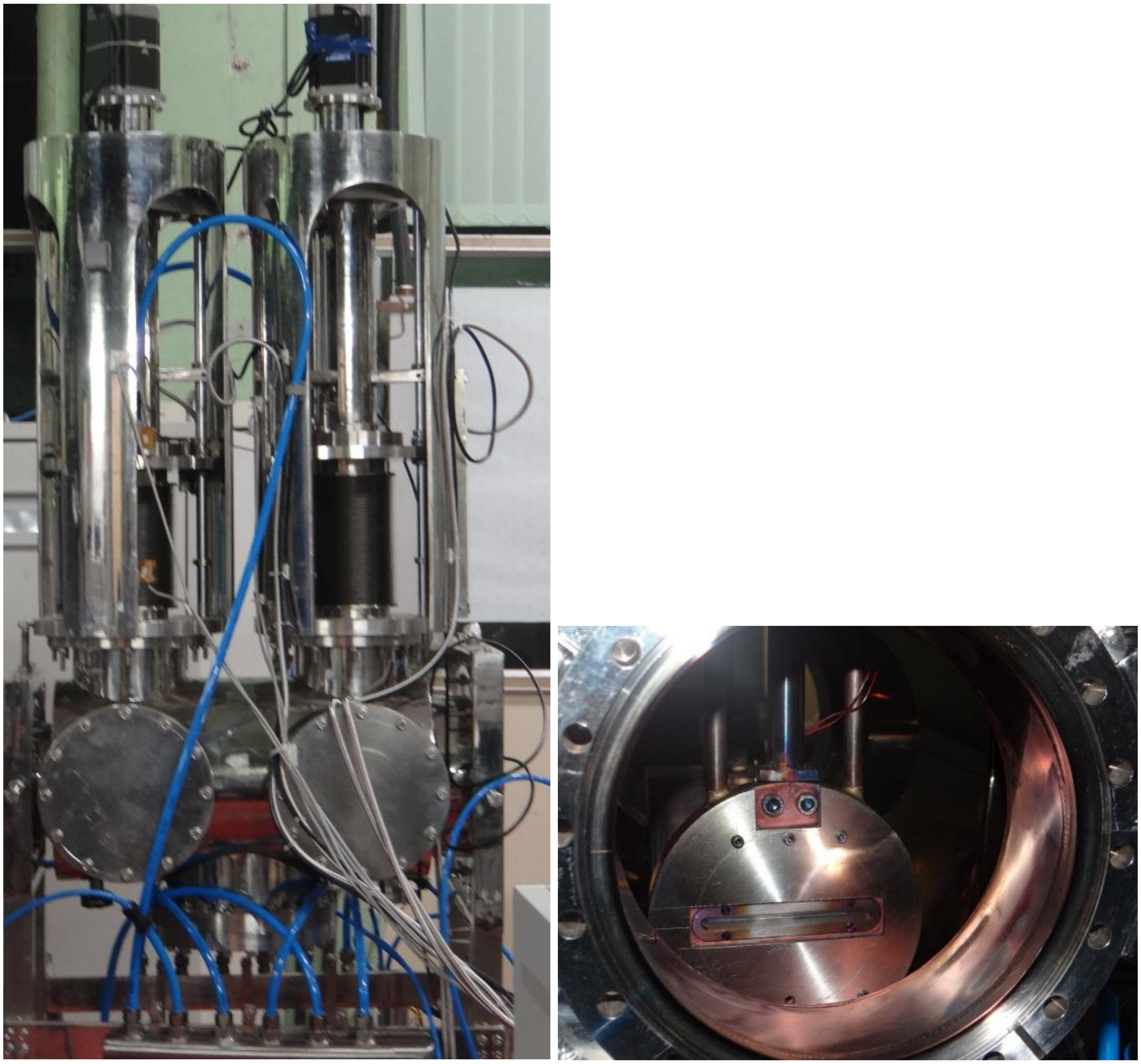

(a) (b)

Figure 6.28 *(a) Two slit emittance meter and (b) water-cooled slit of emittance meter.*

First the mean and mean square value of the position and divergence are estimated from the stored matrix data [Eqs. (6.1) - (6.3)],

$$\langle y\rangle = (1/I_{tot}) \sum [y_m I_m],\ \langle y'\rangle = (1/I_{tot}) \sum [y'_m I_m] \tag{6.1}$$

$$\langle y^2\rangle = (1/I_{tot}) \sum [(y_m - \langle y\rangle)^2 I_m],\ \langle y'^2\rangle = (1/I_{tot}) \sum [(y'_m - \langle y'\rangle)^2 I_m] \tag{6.2}$$

$$\text{and } \langle yy' \rangle = (1/I_{tot}) \sum [(y_m - \langle y \rangle)(y'_m - \langle y' \rangle) I_m] \quad (6.3)$$

where I_{tot} is the total beamlet current collected by the collector, I_m is the current collected at location y_m.

Then RMS emittance and RMS normalized emittance is calculated as

$$\varepsilon_{RMS} = [\langle y^2 \rangle \langle y'^2 \rangle - \langle yy' \rangle]^{1/2} \quad (6.5)$$

$$\varepsilon_{norm} = \beta\gamma\varepsilon_{RMS} \quad (6.6)$$

The phase space plots are made from the set $\{(y_m, y'_m)\}_m$.

The microcontroller was used in the instrumentation of the two slit emittance meter [115]. The sixteen bit microcontroller was chosen for this application. The schematic of instrumentation is shown in Figure 6.29. For providing precision motion of the slits, the stepper motor of 1.8º step size and a ball screw of 5 mm pitch mechanism are employed. Using the micro-step driver and the above mechanism, the precision motion of 5 micron are achieved for both the slits. The required slit step size from 5 micron to 5 mm can be set using this arrangement. The maximum stroke size of the slits is 150 mm. Two bipolar stepper motor of 50 kg.cm torque and 1.8º step angle are used for precision motion of the slits. Here, the stepper motors rotary motion is converted to linear motion. In motion conversion there are frictional losses, so to know the exact locations of the slits two linear incremental encoder of 5 micron resolutions are employed. For limiting the motion of the slits, two limit switches are installed. For every position of the first slit, profile scan of the beamlet are performed using the second slit. The settings to be provided for the full emittance scan are: a) stroke size and step size of first slit, b) stroke size and step size of second slit, c) start point of first slit, and d) start point of second slit.

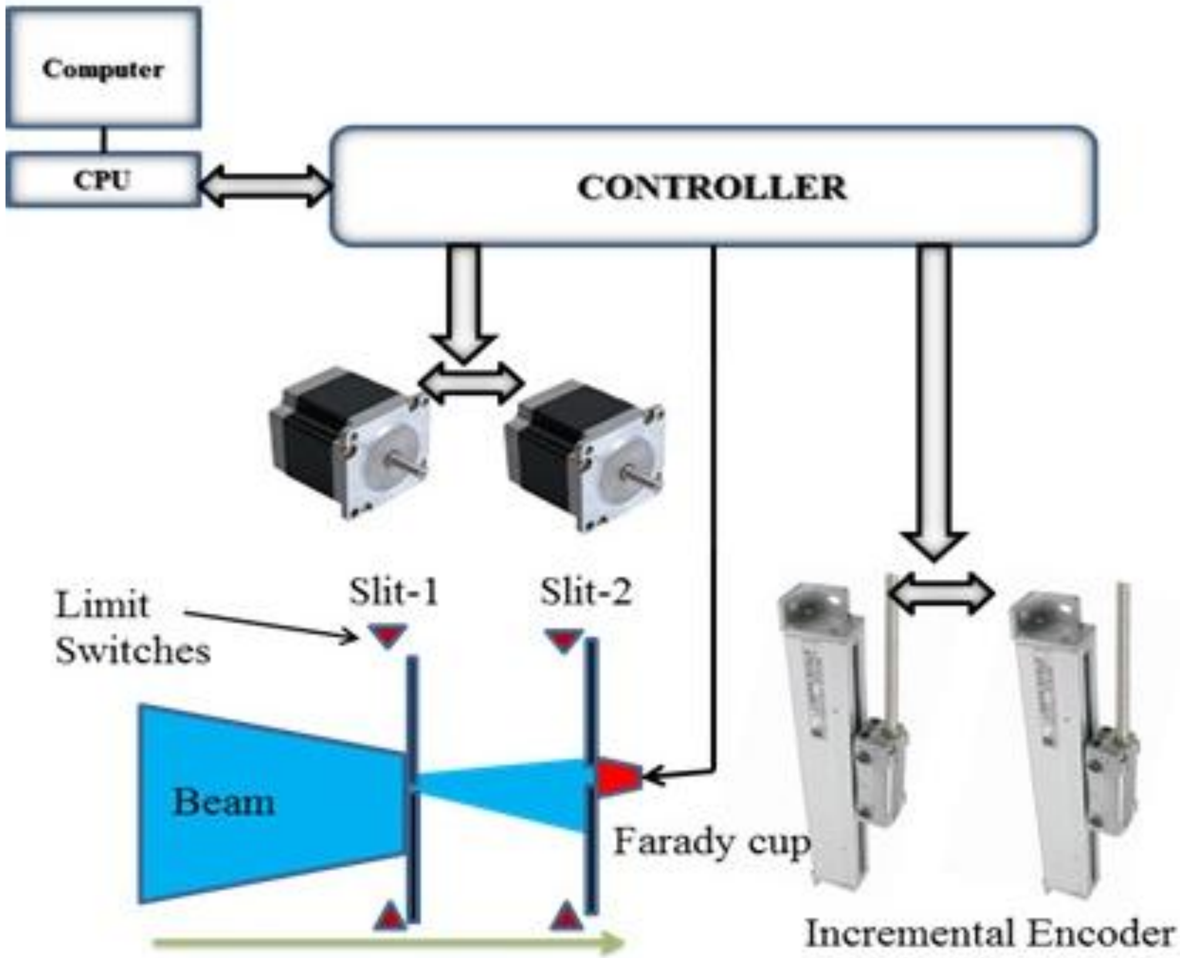

Figure 6.29 *Remote control and data acquisition of emittance meter.*

After finishing the emittance scan, $M \times N$ data points are generated and stored in PC in matrix form, where M and N are locations of the first and the second slit. From the stored data, the beam emittance is determined by computer program developed based on Eqs. (6.1 - 6.6) (Appendix III).

6.2.5 Magnetic Mass Analyzer

The species contained in the hydrogen ion beam are H^+, H_2^+, H_3^+ and impurities. It is important to know proton content in the ion beam for direct injection in RFQ accelerating structure. The proton fraction in the beam was measured using magnetic mass analyzer. The mass analyzing magnet has been designed and developed of the following parameter as shown in Table: 6.2. In the design of the analyzing magnet, the 3D magneto-static calculation was carried out. A 3 D model and field arrows of the analyzing magnet is shown in Figure 6.30. The magnet is modeled with a current of 22174 A-turns, which generates a central field of 0.26 T. The field profile along central axis of analyzing magnet is shown in Figure 6.31. The field homogeneity in the center of the magnet is shown in Figure 6.32 and is found to be within 4×10^{-4}. The fabricated magnet is shown in Figure 6.33. The field calibration is given in Figure 6.34. The measured field homogeneity is 3.3×10^{-4} mm over ± 40 mm. The measured effective length is 105.2 mm at field value of 0.23 T.

6.2.6 Faraday Cups

The Faraday cups are used for measuring total beam current. In Faraday cup, the accelerated particles are stopped inside the cup and the accumulated charge is converted into a corresponding current. Because all beam energy is accumulated in the cup, its physical appearance will vary with the beam energy and power involved. The design of the Faraday cup involves beam energy, beam power and power density, high frequency response for pulsed beam and secondary electron response. Target thickness must exceed range of the particles. Above 100W, cooling with low conductivity water is required. The internal geometry of the cup should distribute the power

Table 6.3: *Parameters of magnetic mass analyzer.*

Parameters	Designed values
Maximum field, B [T]	0.23
Bending radius, R_0 [mm]	300
Bending angle φ [degree]	90
Pole entrance and exit angle [degree]	31.8, 31.8
Pole gap d [mm]	110
Pole width W [mm]	386
Pole profile – entrance/exit	Approx. Rogowsky
Pole profile-sides	Sharp
Pole material	XC06
Yoke material	St. 37
Field homogeneity	1E-03
Conductor type	Hollow conductor
Impregnation system	DF 3C
Conductor dimensions [mm]	$7\times7/\ \phi4$
Number of turns per coil N	72
Total number of turns in magnet N_{tot}	144
Cooling type, Max. pressure drop (bar)	Water cooled, 2
Total flow rate (lit/min)	6
Current in the coil I [A]	154
Voltage complete magnet [V]	24
Power complete magnet [kW]	3.7

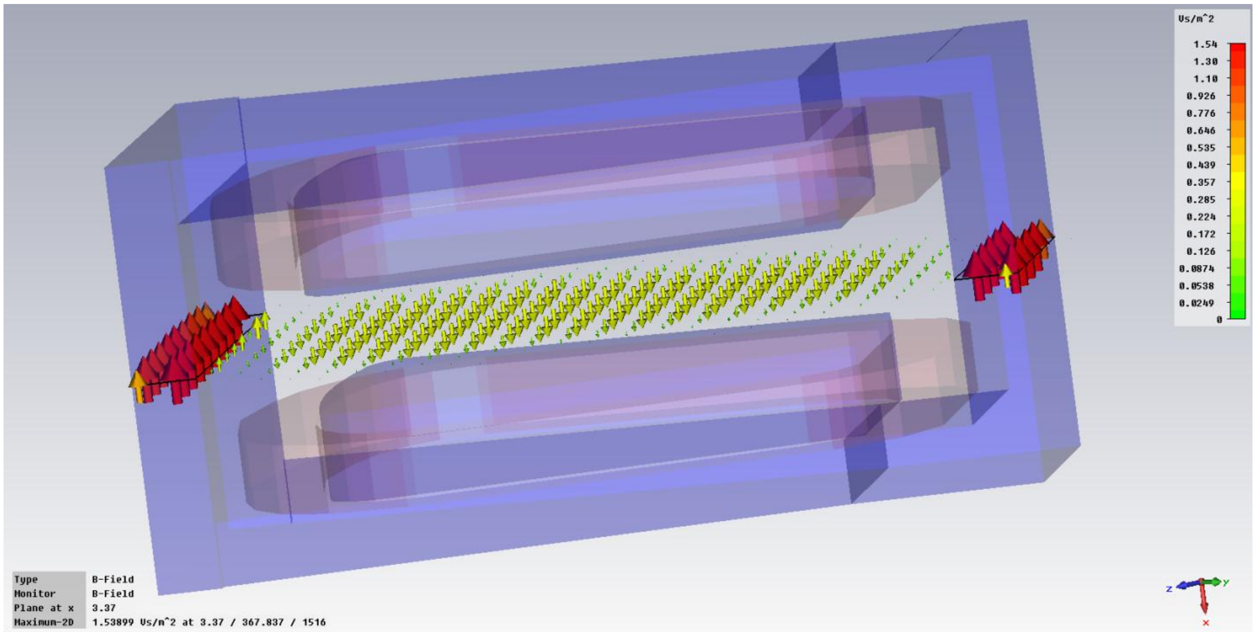

Figure 6.30 *3D model and field arrows of analyzing magnet.*

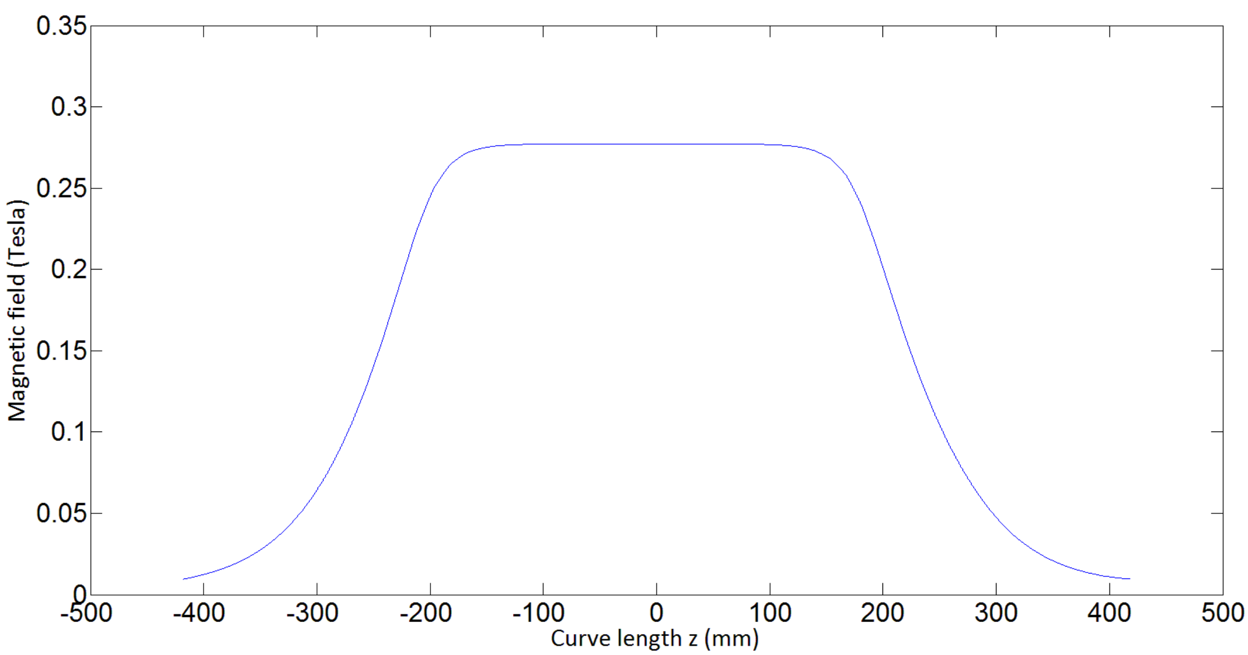

Figure 6.31 *Axial field in analyzing magnet.*

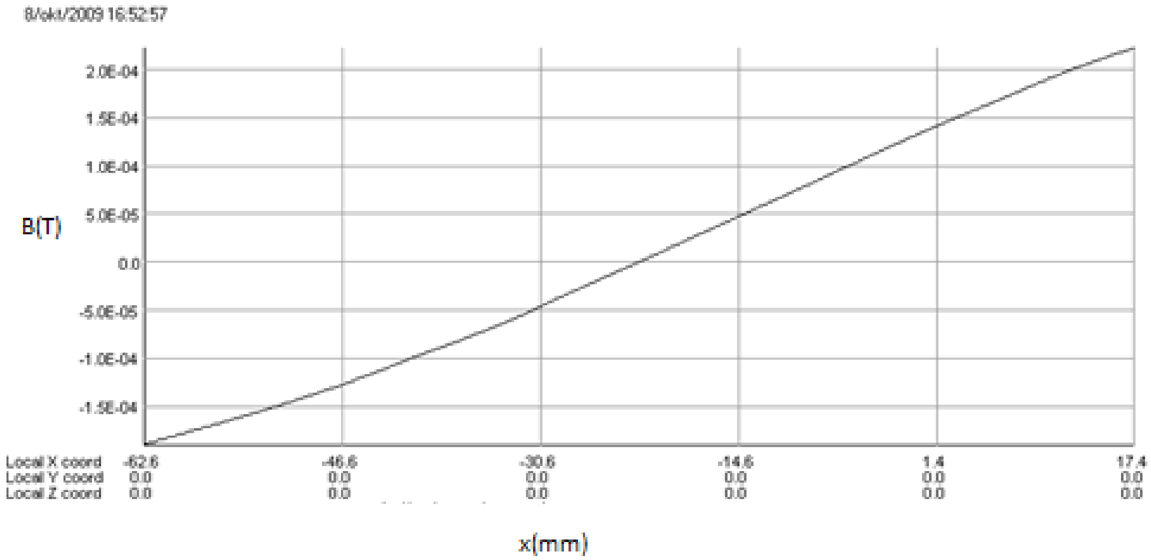

Figure 6.32 *Field homogeneity at the center of the magnet.*

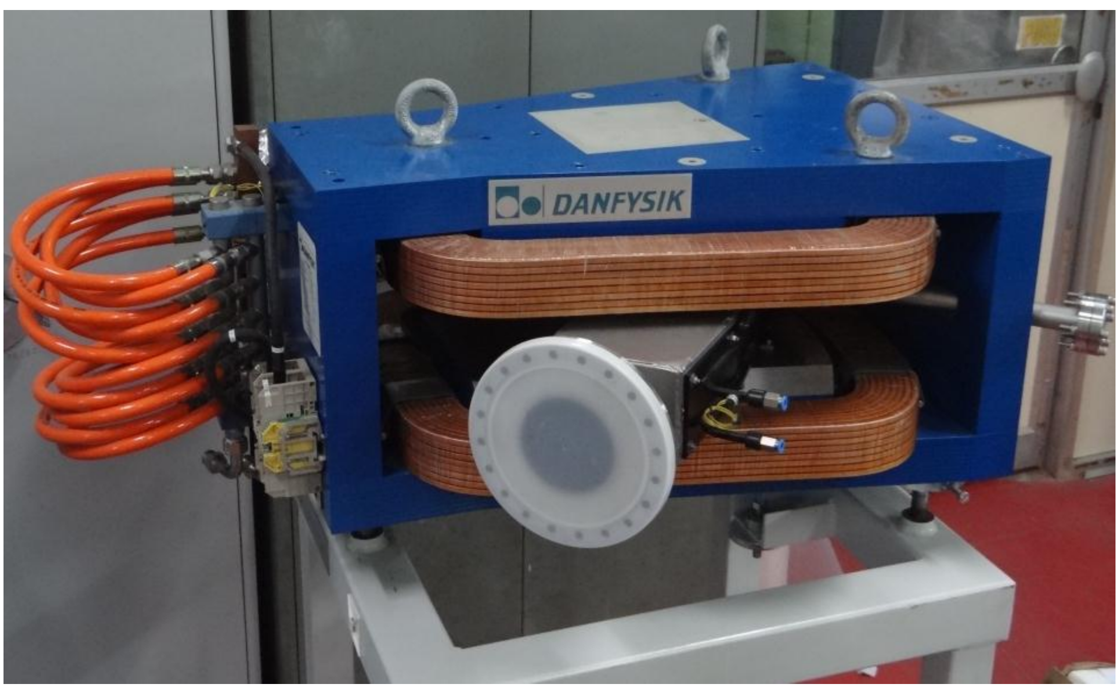

Figure 6.33 *Fabricated analyzing magnet*.

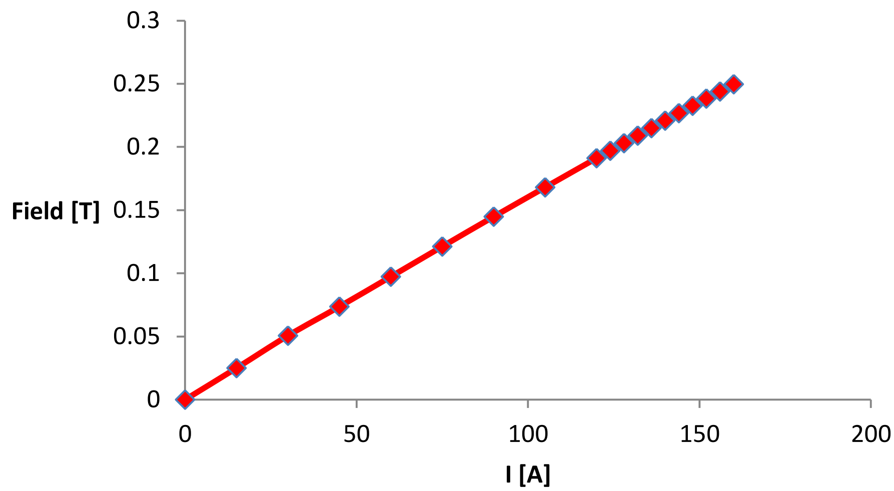

Figure 6.34 *Field calibration of analyzing magnet*.

over as large an area as practical. For pulsed beam, good high frequency performance entails good impedance matching. 50Ω constructions are common. For accurate measurements, secondary emission must be suppressed. This is done by making the target reentrant and introducing a bias of several hundred volts relative to the center conductor and/or introducing a dipole field of few hundred Gauss in the target region.

The shielded Faraday cups were designed and fabricated to measure the ion beam current in continuous wave and pulsed mode. The first type was fixed Faraday cup that also acts as beam dump. It was designed for beam power of 2 kW. It consists of water cooled copper block that absorbs the beam power and the beam current due to charge accumulation was recorded on a current meter. The electron suppression was achieved using bias plate kept at -100 to -300 V. The water circuits in the copper block were isolated from ground potential using ceramic water feedthroughs. The second type was a movable Faraday cup (MFC) that can be located at any point in radial direction. The movement of MFC was controlled using stepper motor and controller. The position of the Faraday cup was recorded using linear encoder.

and (b).

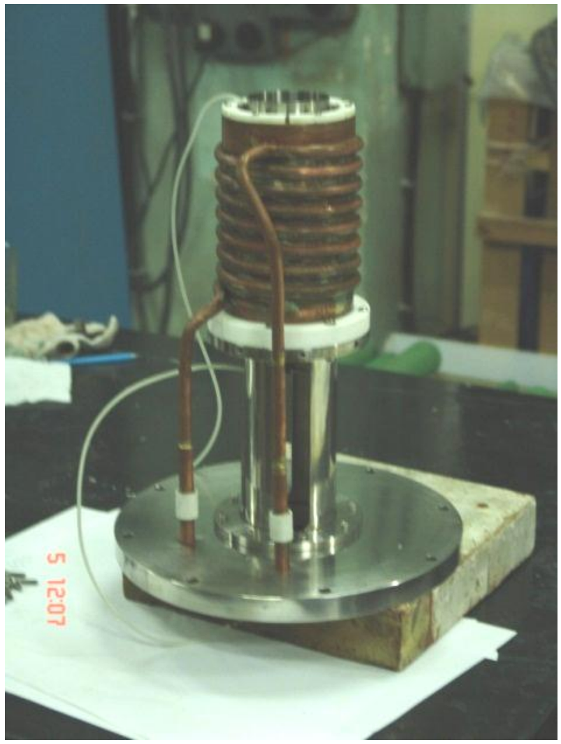

(a)

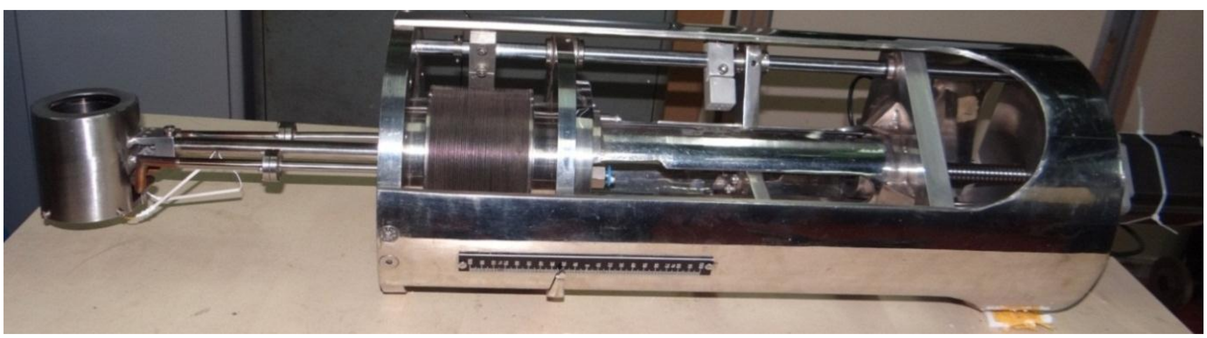

(b)

Figures 6.35 *(a) Fixed and (b) movable electron suppressed Faraday cups.*

The fabricated fixed and movable electron suppressed Faraday cups are shown in Figures 6.35 (a) and (b).

6.2.7 Direct Current and Alternative Current Transformer

For non-interceptive beam current measurements direct current transformer (DCCT) was used and the fluctuation in beam current and noise was measured using alternating current transformer (ACCT).

The DCCT, also known as zero flux current transformer, 2nd harmonic magnetic modulator and parametric current transformer measures the dc component of the beam current. DCCT consists of a high permeability torroidal magnetic core that surrounds the beam and couples to its magnetic field. In the absence of beam a magnetic modulator periodically derives the core into positive and negative saturation, and a sense winding produces a perfectly symmetrical positive and negative output voltage having no even harmonics. Magnetic field from the beam, or any other source that couples to the core, causes the core *B*-*H* loop to become slightly offset, resulting in generation of second harmonic in the sense winding. This signal is filtered, rectified, amplified and feedback to a third winding which just cancels the disturbing flux from the beam.

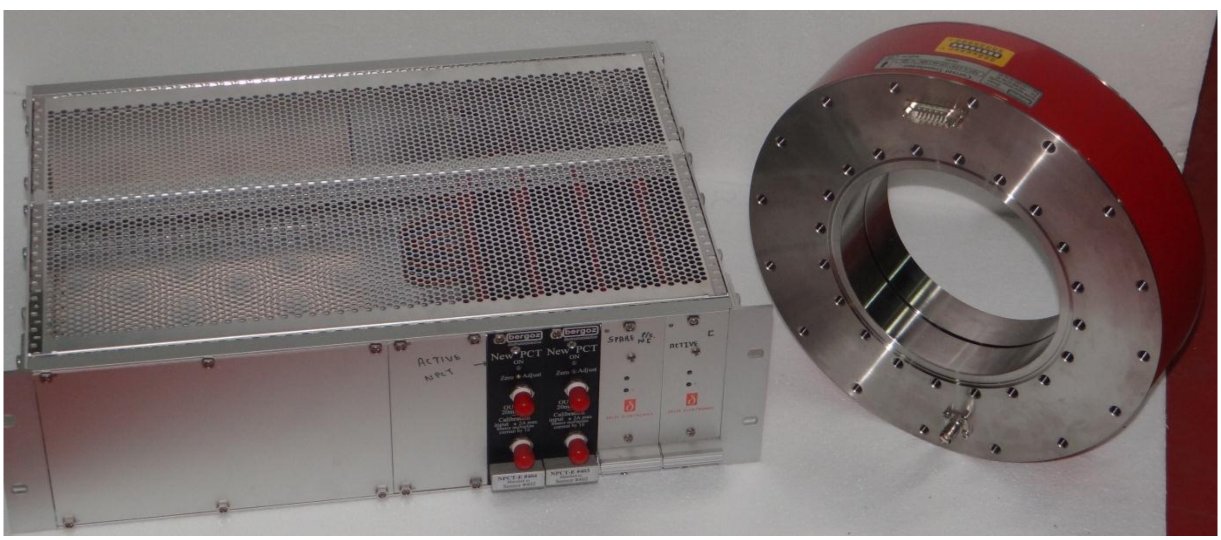

Figure 6.36 *Combined DCCT, ACCT and power supplies*.

A precision resistor in series with this bulking winding then produces a voltage proportional to beam current. Being a null measurement the linearity and accuracy of the method are high. The ACCT is specially designed to measure fluctuation in charged particle beams. It measures currents down to 1 mA_{ac}, with accuracy better than 1%. M/S Bergoz makes DCCT and ACCT are used and installed in the low energy beam transport line (Figure 6.36). Some of the typical parameters of DCCT are listed in Table: 6.4.

Table 6.4: *Parameters of DCCT.*

Parameters	Value
Frequency response	Dc to 100 kHz
Ranges	300 μA to 1 A
Resolution	0.5 μA (1s integration)
Dynamic range	$> 2 \times 10^7$
Absolute Accuracy	better than 0.05%
Linearity	better than 0.01%

6.3 Results and Discussions

The experiment was conducted to measure the beam emittance and proton fraction [116]. The beam emittance was measured at three locations, first after beam extraction, second after focusing the beam using one solenoid magnet and third after focusing the beam using one solenoid magnet and separating H^+ using an analyzing magnet.

6.3.1 Emittance measurement after beam extraction.

The ion beam emittance was measured at the ion source end after beam extraction. The schematic of emittance measurement is shown in Figure 6.37 and the actual set up in Figure 6.38. The intensity distribution of beamlet is shown in Figure 6.39 and the *y*-*y´* emittance plot is shown in Figure 6.40.

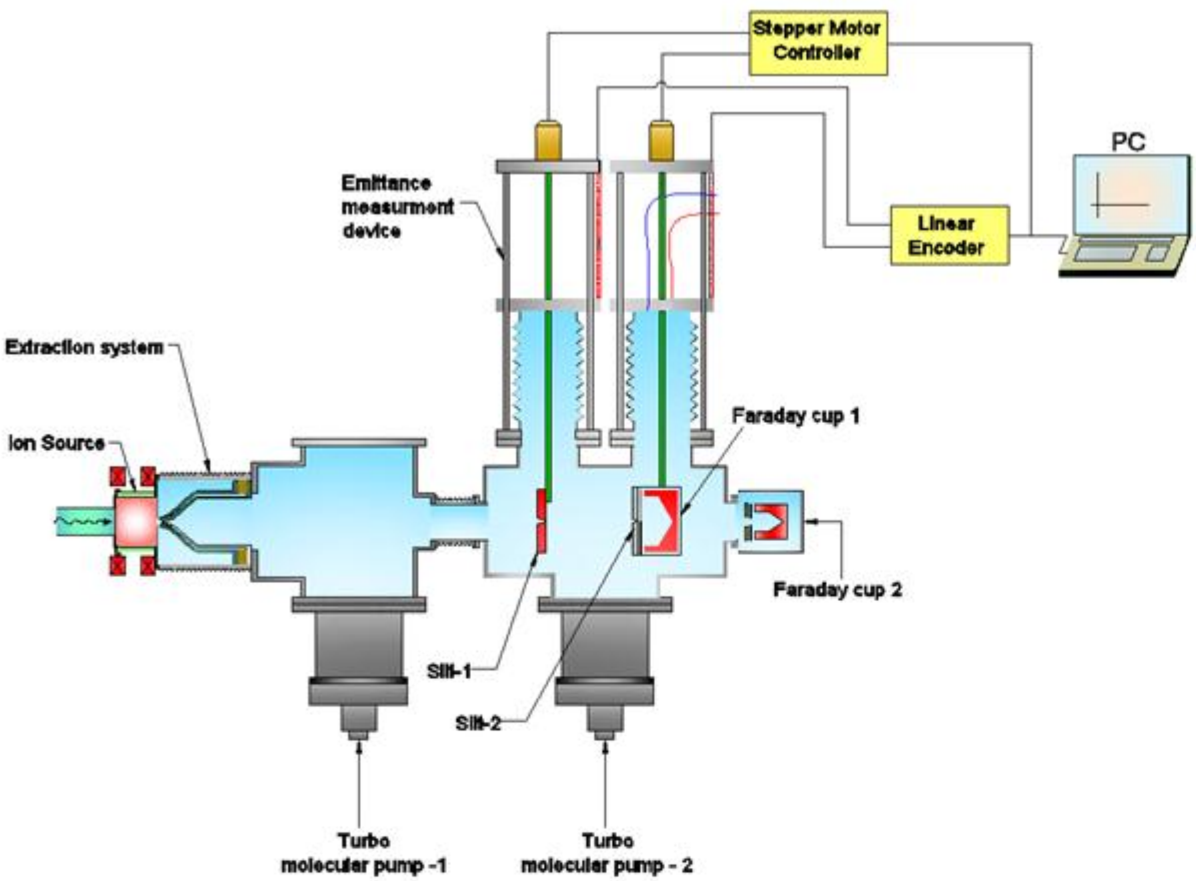

Figure 6.37 *Schematic of emittance measurement at ion source end.*

(b)

Figure 6.38 *Emittance measurement setup at ion source end*.

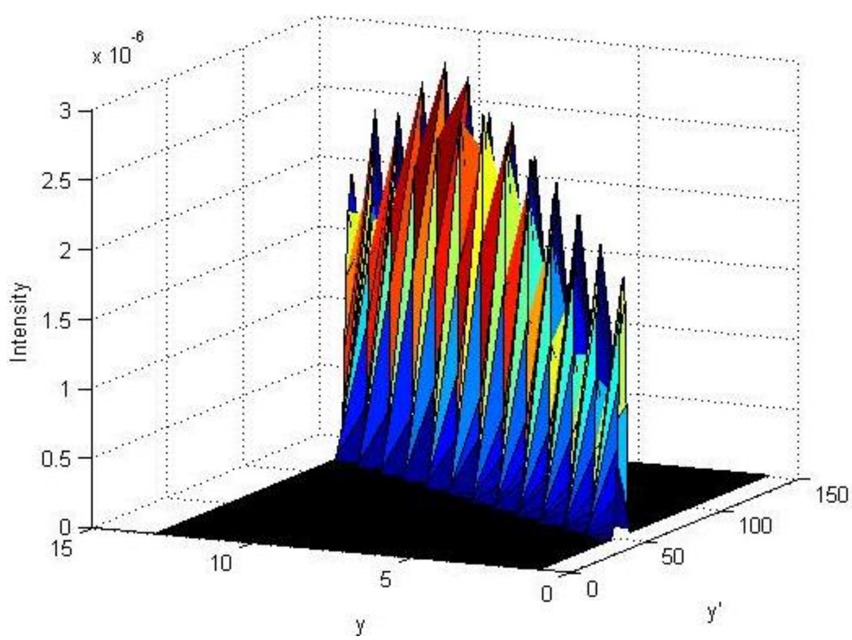

Figure 6.39 *Intensity of beamlet versus y and y'*

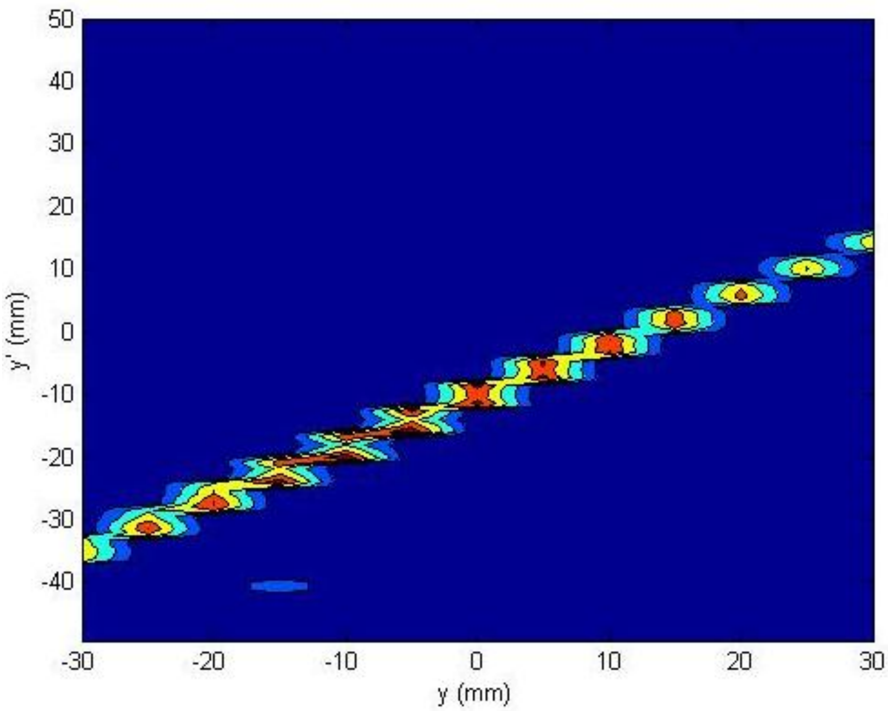

Figure 6.40 *Typical Emittance plot after extraction.*

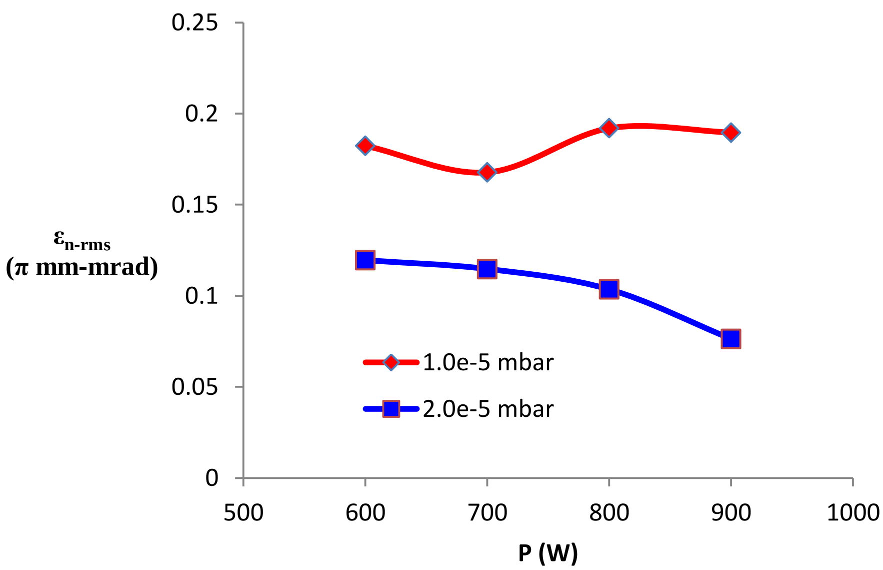

Figure 6.41 *Normalized rms beam emittance versus microwave power at 1.0 and 2.0×10^{-5} mbar of residual gas pressure at 25 kV extraction voltages and – 2 kV suppression voltages.*

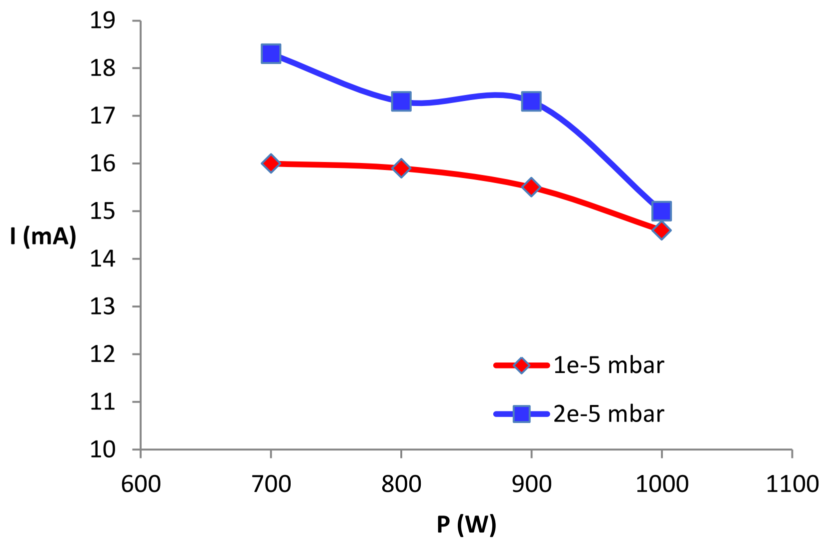

Figure 6.42 *Extracted beam current versus microwave power at 1.0 and 2.0×10^{-5} mbar of residual gas pressure at 25 kV extraction voltages and – 2 kV suppression voltages.*

The normalized rms beam emittance (including all species) is plotted versus microwave power for residual gas pressure of 1.0 and 2.0×10^{-5} mbar at 25 kV extraction voltages and -2 kV suppression voltages as shown in Figure 6.41. For residual gas pressure of 1×10^{-5} mbar, the rms normalized emittance is between 0.16 – 0.2 π mm-mrad and for pressure 2×10^{-5} mbar the rms normalized emittance is between 0.09 – 0.12 π mm-mrad. These emittance values are well within the design value.

From Figure 6.41 we can see that beam emittance/divergence has lower value when the pressure is 2×10^{-5} mbar, but the corresponding value of beam current from Figure 6.42 is higher, so it can be concluded that at high-currents the beam is more space charge compensated in presence of high gas pressure (2×10^{-5} mbar) into the beam line [42,117,118].

6.3.2 Emittance measurement after solenoid focusing

Next the emittance of the beam was measured after transporting and focusing the beam using one solenoid magnet. Before the emittance measurement the focusing of the hydrogen ion beam consisting of H^+, H_2^+ and H_3^+ was studied by simulation and in experiment. The focusing effect of solenoid magnet on H^+, H_2^+ and H_3^+ species is simulated using GPT code. The focusing effects are shown in Figures 6.43 – 6.45. In Figure 6.43, H^+ is focused while in H_2^+ and H_3^+ are under focused for the field value 1 kG. In Figure 6.44, H^+ is over focused, H_2^+ is focused and H_3^+ is under focused for the field value 1.4 kG. In Figure 6.45, H^+ and H_2^+ are over focused while H_3^+ is focused for the field value 1.7 kG.

The schematic and actual experimental setup of beam profile and emittance measurement is shown in Figure 6.46 (a) and (b). The beam focusing was performed in experiment by varying the beam size using one solenoid magnet and recording the beam profile by the profile monitor. The image of the focusing beam recorded on CCD camera is shown in Figure 6.47. The profile measurement with and without focusing is shown in Figure 6.48. In case of profile measurement only slit1 is used and the Faraday cup is attached to slit 1. The profile scan is obtained by moving the slit across the beam and recording the position and current signal on Faraday cup.

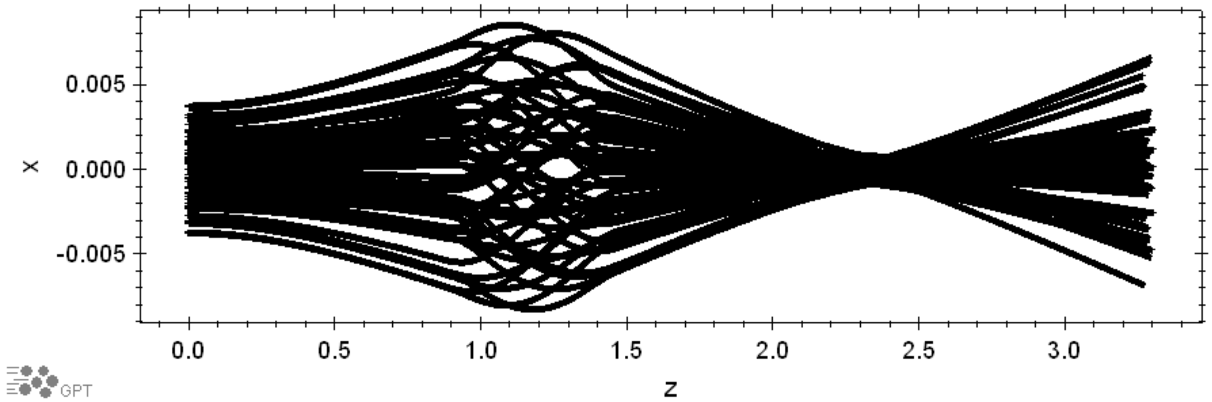

(a)

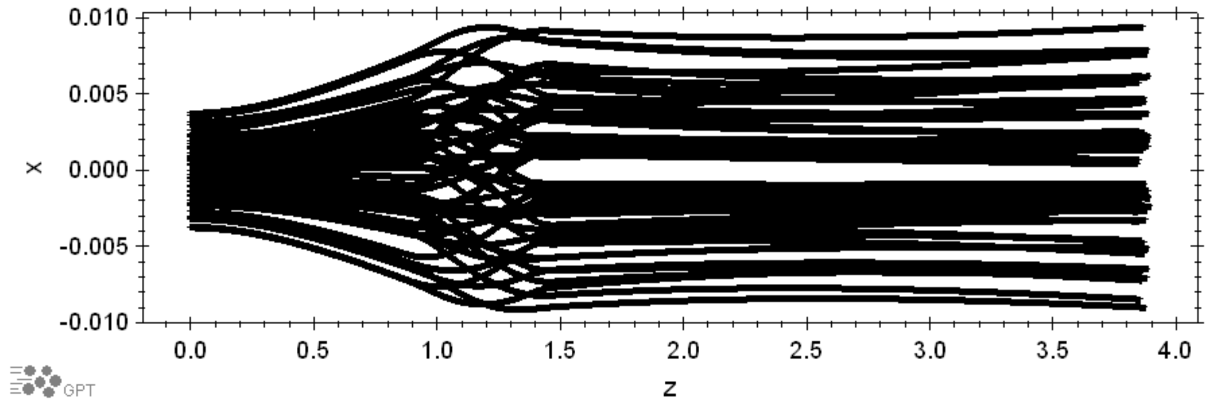

(b)

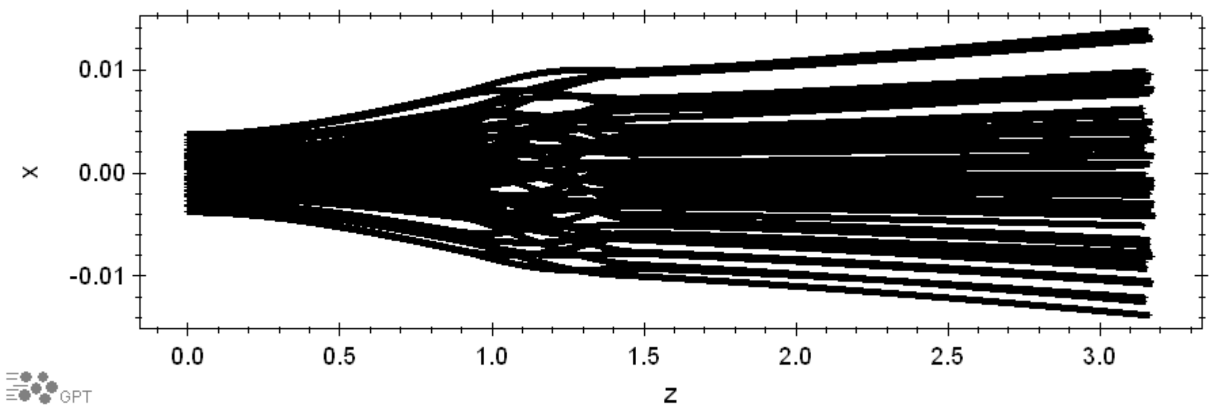

(c)

Figure 6.43 *Focusing effect of single solenoid magnet on (a)* H^+*, (b)* H_2^+ *and (c)* H_3^+ *for magnetic field* 1 *kG.*

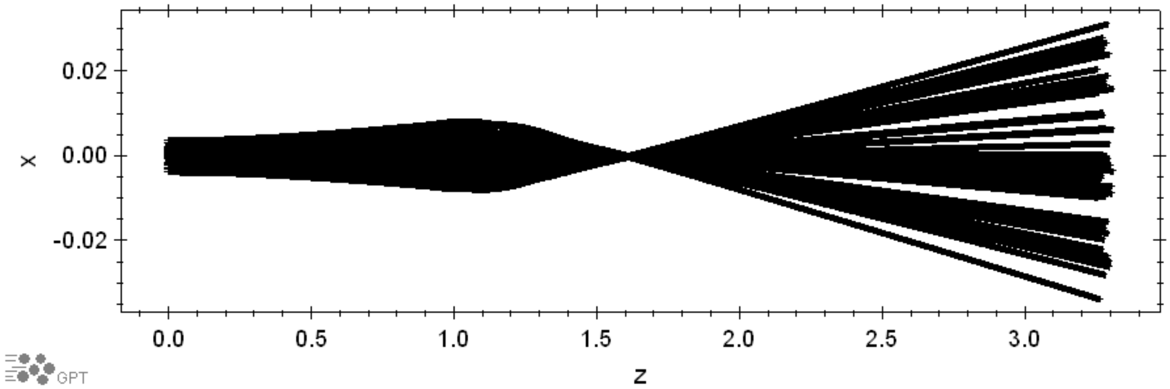

(a)

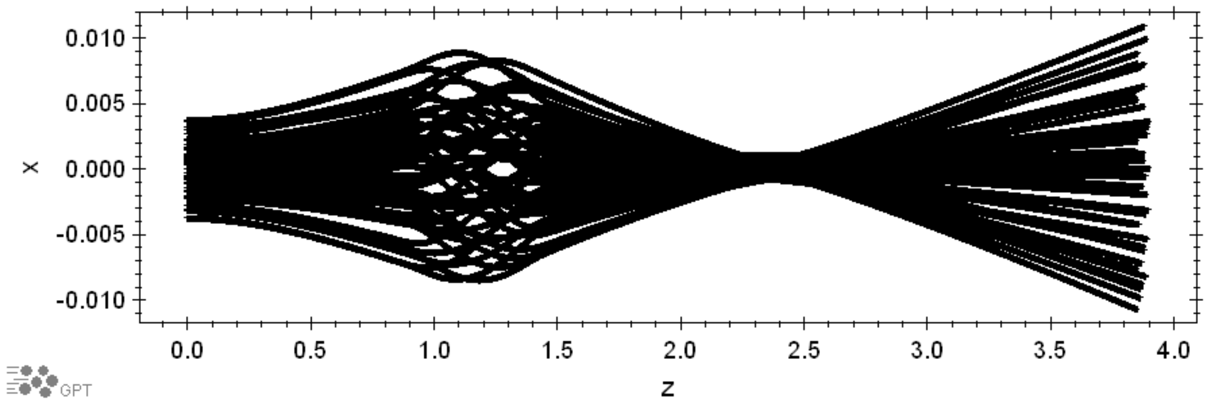

(b)

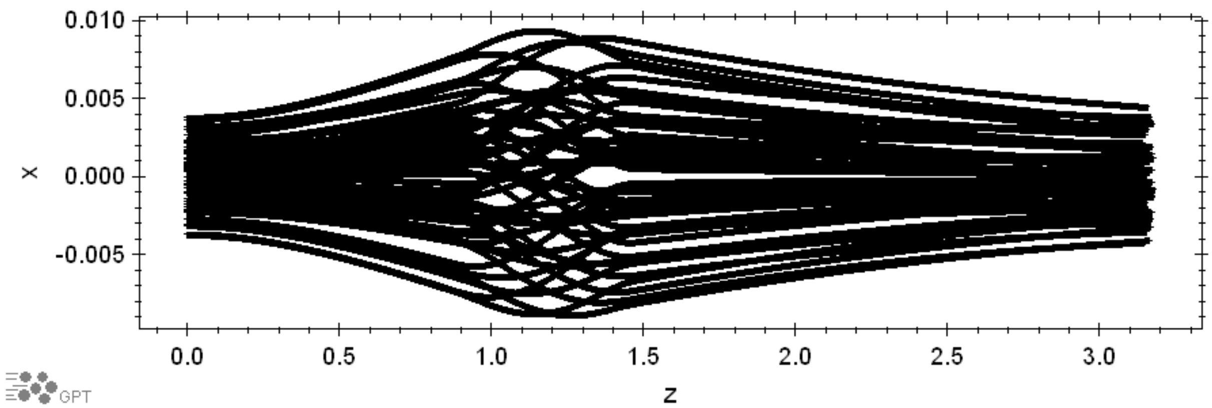

(c)

Figure 6.44 *Focusing effect of single solenoid magnet on (a)* H^+*, (b)* H_2^+ *and (c)* H_3^+ *for magnetic field* 1.4 *kG.*

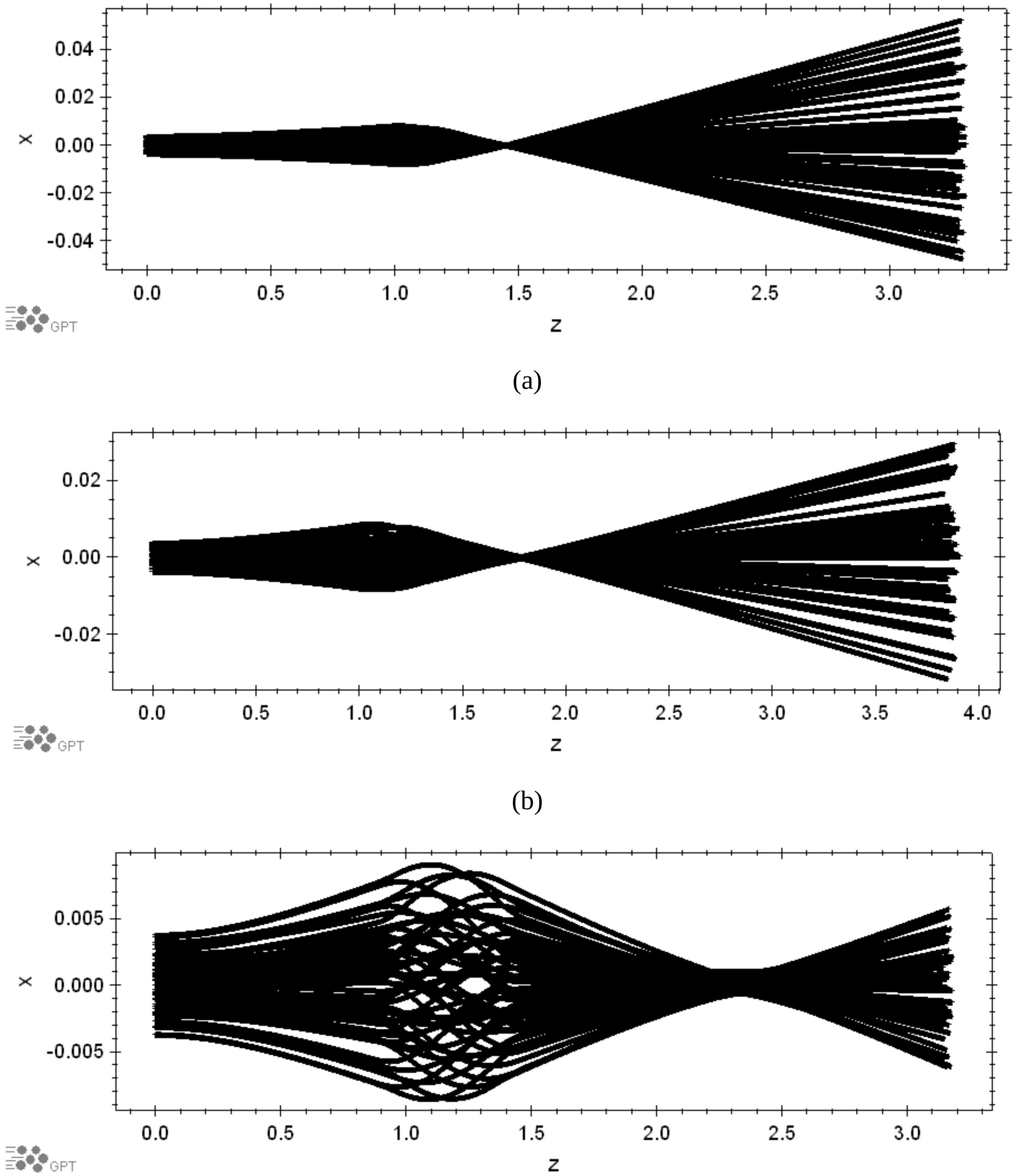

(a)

(b)

(c)

Figure 6.45 *Focusing effect of single solenoid magnet on (a)* H^+*, (b)* H_2^+ *and (c)* H_3^+ *for magnetic field* 1.7 *kG.*

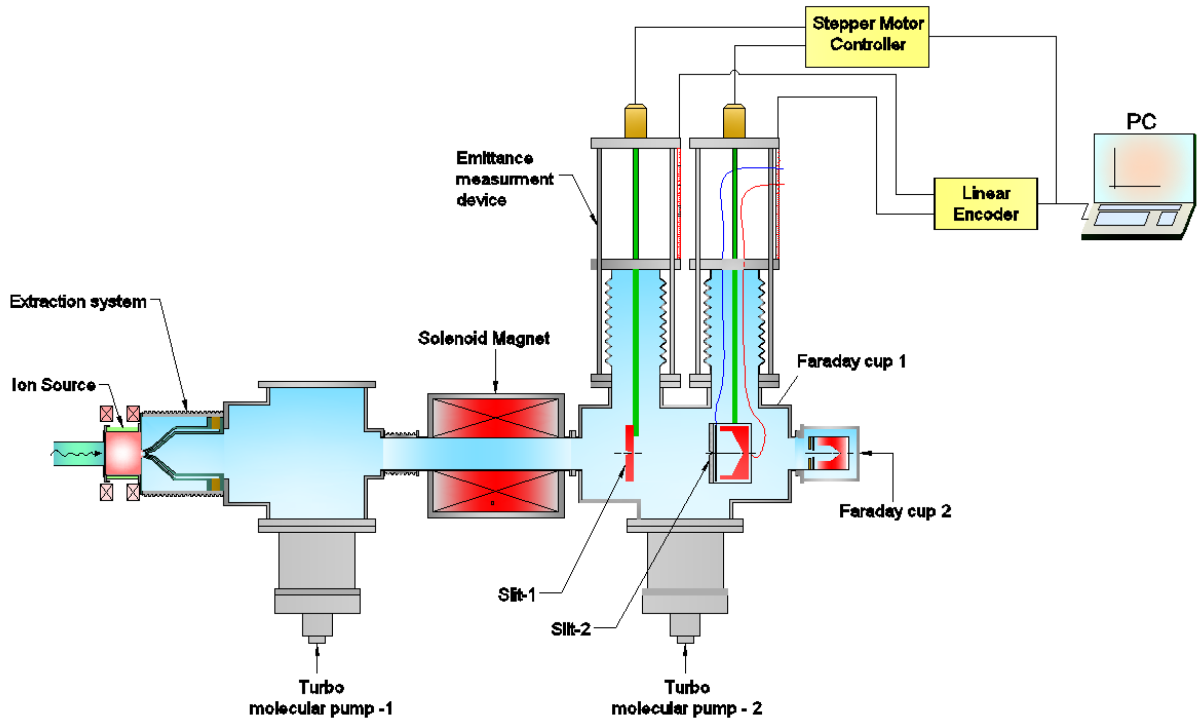

(a)

(b)

Figures 6.46 *(a) Schematic and (b) actual setup of beam profile and emittance measurement using one solenoid magnet.*

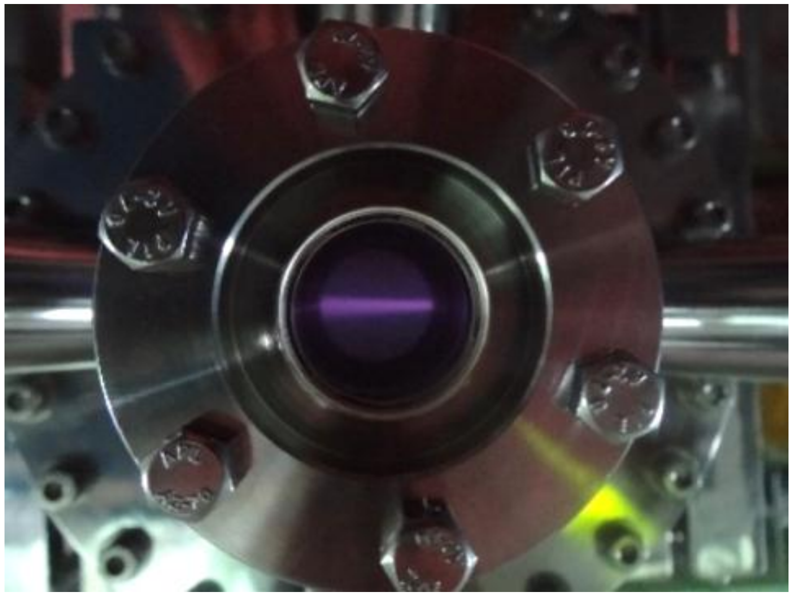

Figure 6.47 H^+ *focusing using one solenoid magnet for field value 1 kG.*

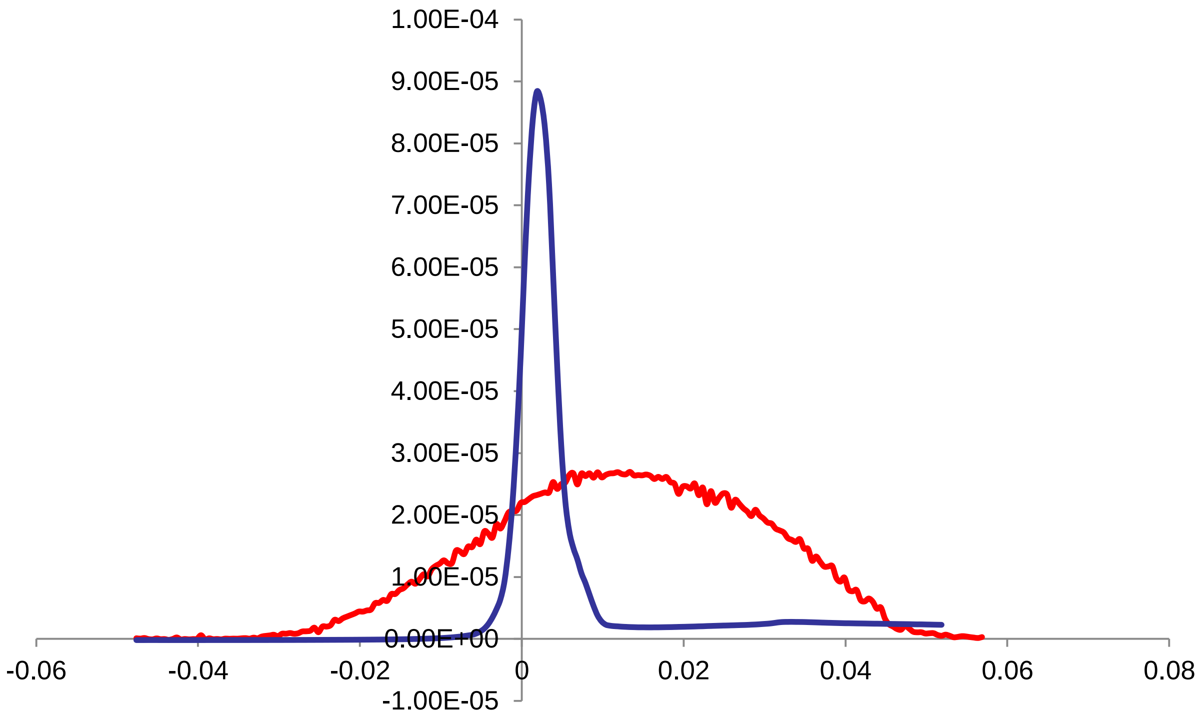

Figure 6.48 *Beam profile measured with and without solenoid focusing.*

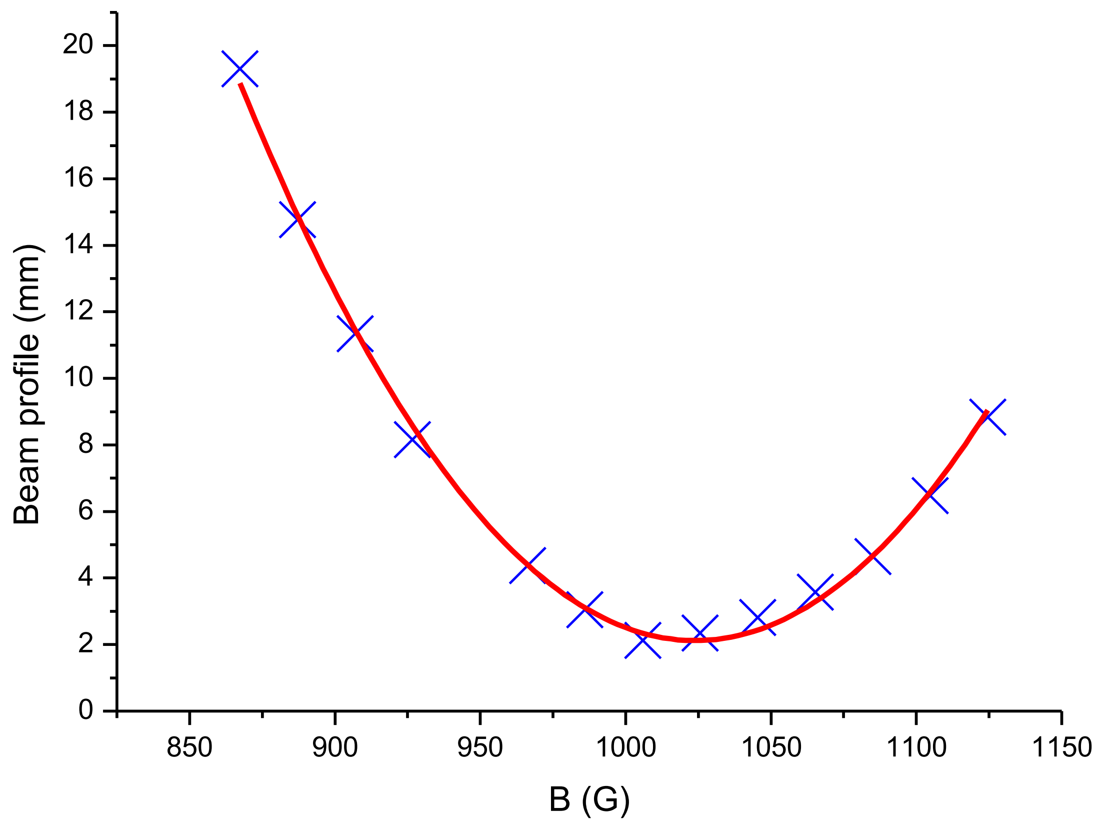

Figure 6.49 *Beam profile versus solenoid field.*

Figure 6.49 shows the plot of beam profile versus solenoid field. The beam profile diameter is minimum at ~ 1 kG field that corresponds to H^+.

After profile measurement, the beam emittance measurement was carried out using emittance meter. The plot of emittance after focusing is shown in Figure 6.50. The variation of beam emittance versus microwave power is shown in Figure 6.51 for residual gas pressure of 1 and 2×10^{-5} mbar and 25 kV extraction voltages and -2 kV suppressor voltages. The RMS normalized emittance of the beam (including all species) lies between 0.18 – 0.21 π mm-mrad for residual gas pressure 1×10^{-5} mbar and 0.15 – 0.18 π mm-mrad for residual gas pressure 2×10^{-5} mbar. The slight increase of beam emittance may be due to the aberration in solenoid focusing lens.

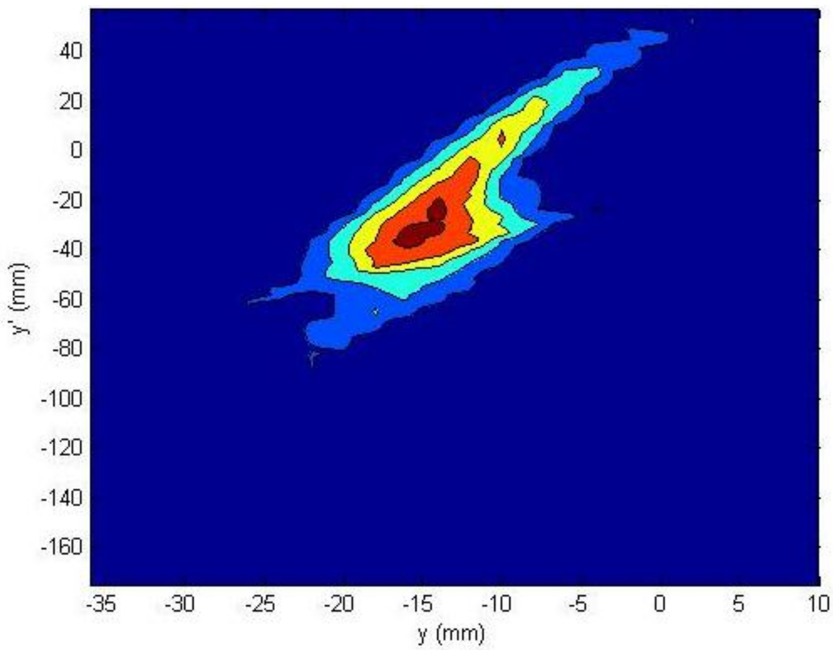

Figure 6.50 *Emittance plot after focusing using 1 kG field*.

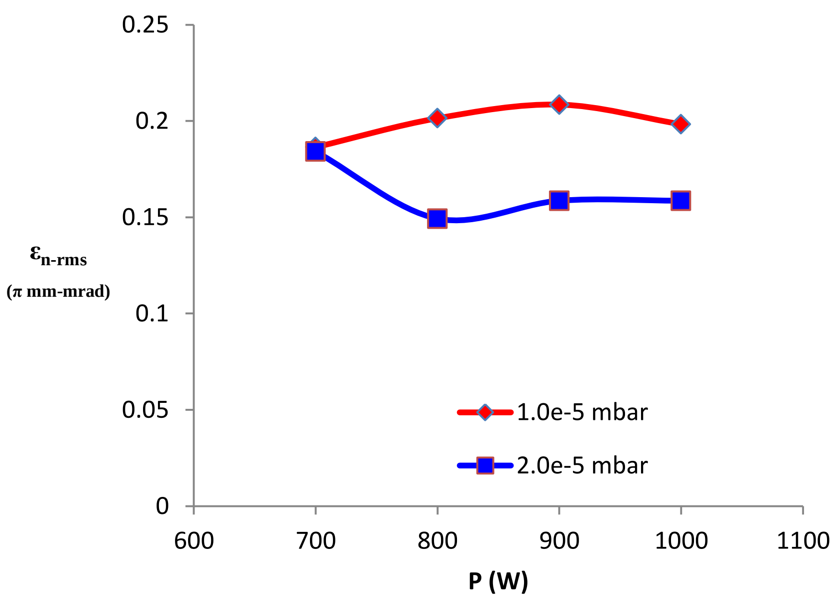

Figure 6.51 *RMS normalized beam emittance versus microwave power for 25 kV extraction voltage and -2 kV suppressor voltage.*

6.3.3 Emittance measurement after analyzing magnet

An analyzing magnet was installed in the low energy beam transport line after the solenoid magnet. The analyzing magnet separates the H^+ from higher molecular species H_2^+ and H_3^+. The setup of emittance measurement after analyzing magnet is shown in Figure 6.52. The emittance plot for H^+ is shown in Figure 6.53. The variation of proton beam emittance versus microwave power for residual gas pressures 1×10^{-5} mbar and 2×10^{-5} mbar is shown in Figure 6.54.

Figure 6.52 *Setup of emittance measurement after analyzing magnet*.

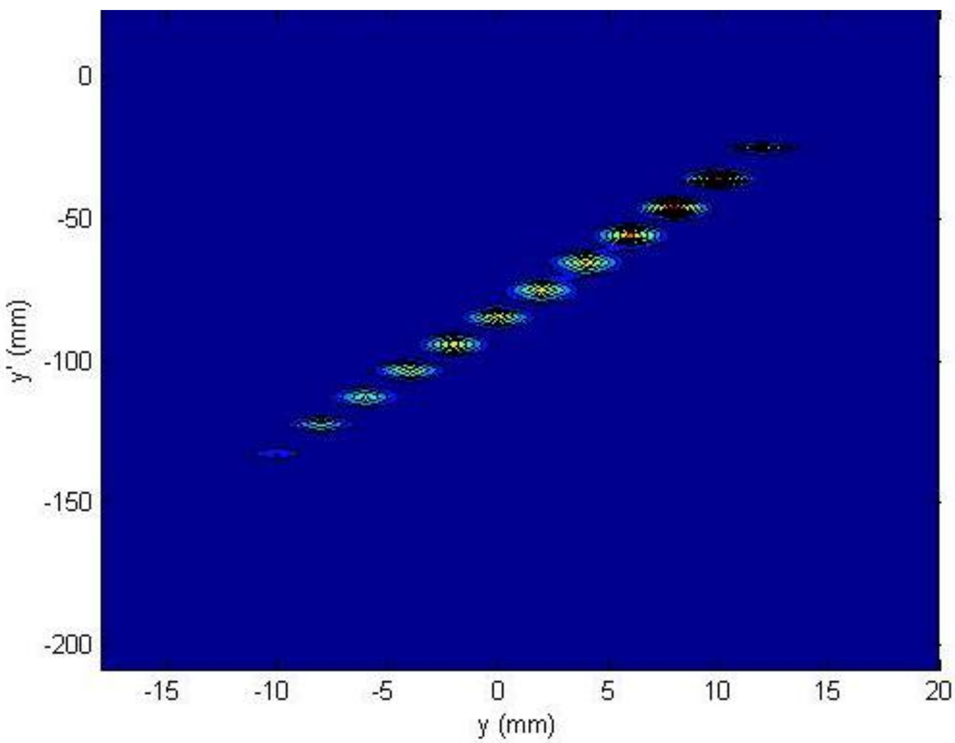

Figure 6.53 *Emittance plot of proton beam after solenoid magnet*.

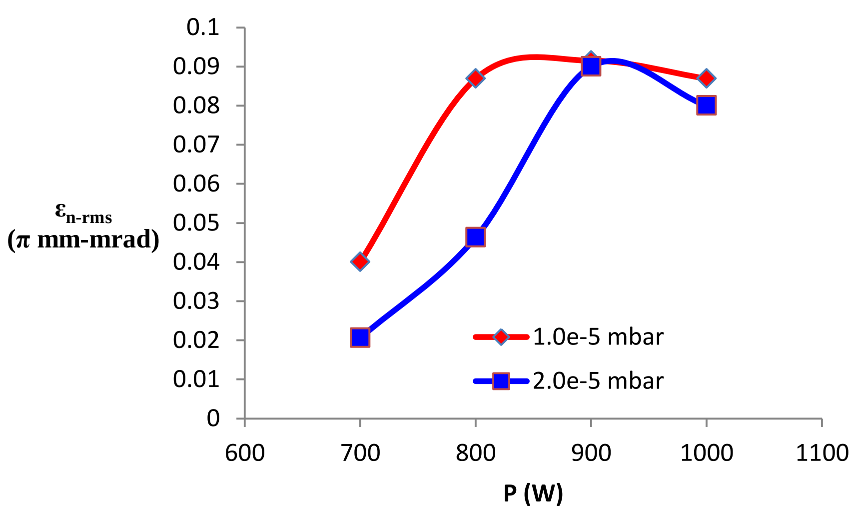

Figure 6.54 *RMS normalized proton beam emittance versus microwave power after analyzing magnet for 25 kV extraction voltages and -2 kV suppressor voltages.*

The proton beam emittance was measured after filtering the H_2^+ and H_3^+ components using analyzing magnet. For residual gas pressure of 1×10^{-5} mbar, the rms normalized emittance of proton beam lies between 0.04 – 0.09 π mm-mrad and for 2×10^{-5} mbar it lies between 0.02 - 0.09 π mm-mrad for 25 kV extraction voltages and -2 kV suppressor voltages.

6.3.4 Proton fraction measurement

The proton fraction of the beam was measured by scanning the magnetic field of the analyzing magnet and recording the current signal on Faraday cup [116]. A 0.2 mm width slit was incorporated in front of the Faraday cup for spatial resolution of three species H^+, H_2^+ and H_3^+. The schematic and actual setup of proton fraction measurement is shown in Figures 6.55 and 6.56.

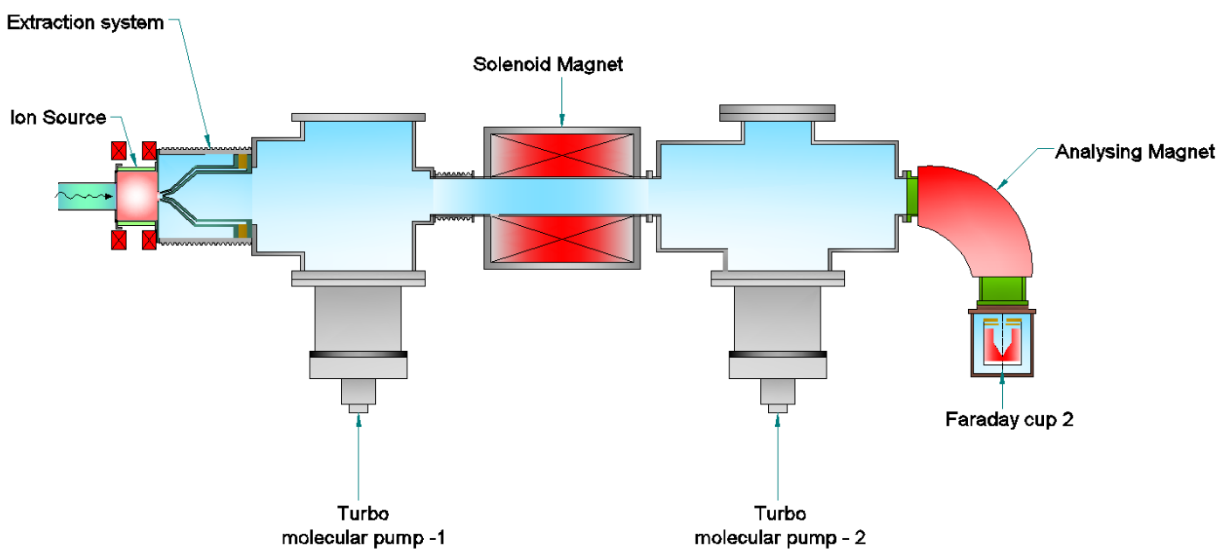

Figure 6.55 *Schematic of proton fraction measurement.*

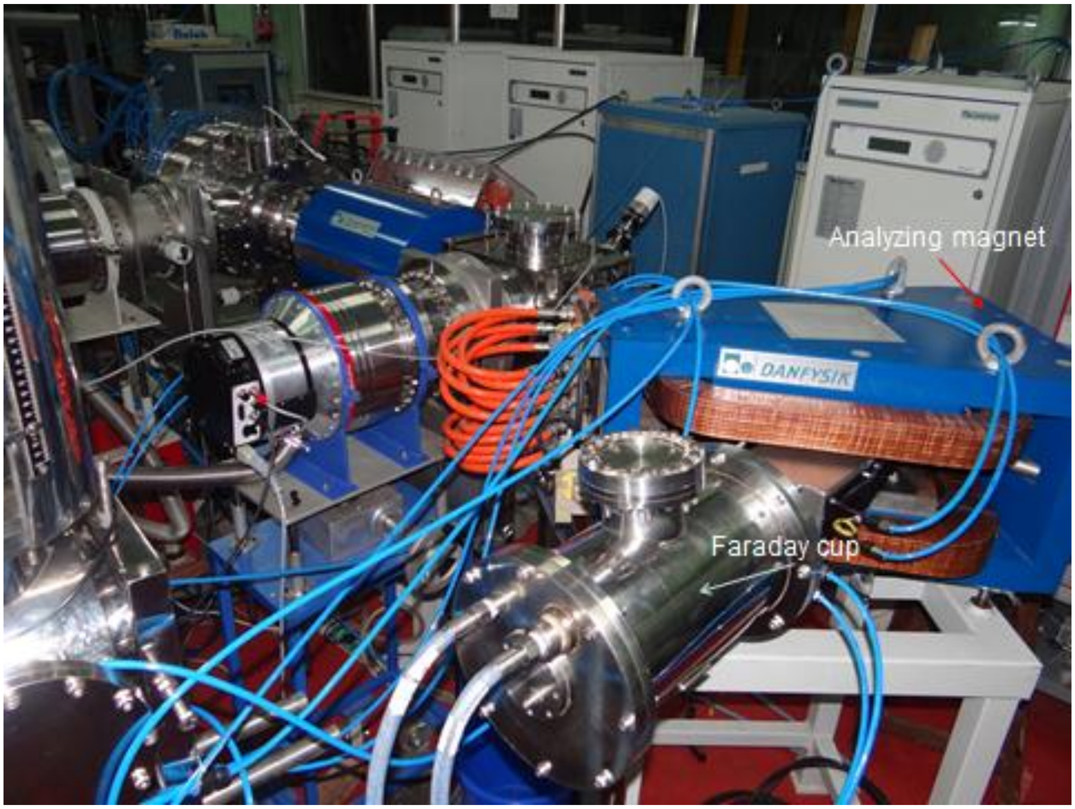

(b)

Figure 6.56 *Actual setup for proton fraction measurement.*

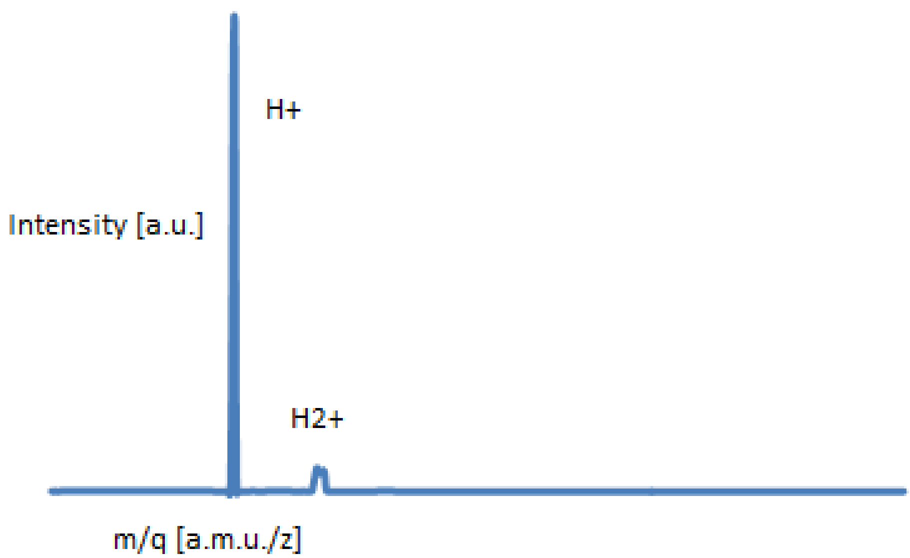

Figure 6.57 *Typical mass spectra of hydrogen ion beam.*

The mass spectrum of hydrogen ion beam is shown in Figure 6.57. The proton fraction has been calculated by means of these equations:

$$H^{+}\,\% = H^{+} / (H^{+} + H_2^{+} + H_3^{+}) \tag{6.1}$$

$$H_2^{+}\% = H_2^{+} / (H^{+} + H_2^{+} + H_3^{+}) \tag{6.2}$$

and

$$H_3^{+}\% = H^{+} / (H^{+} + H_2^{+} + H_3^{+}) \tag{6.3}$$

The variation of proton fraction versus microwave power is shown in Figure 6.58 for residual gas pressure of 2.0×10^{-5} mbar and 25 kV of extraction voltages and -2 kV of suppression voltages.

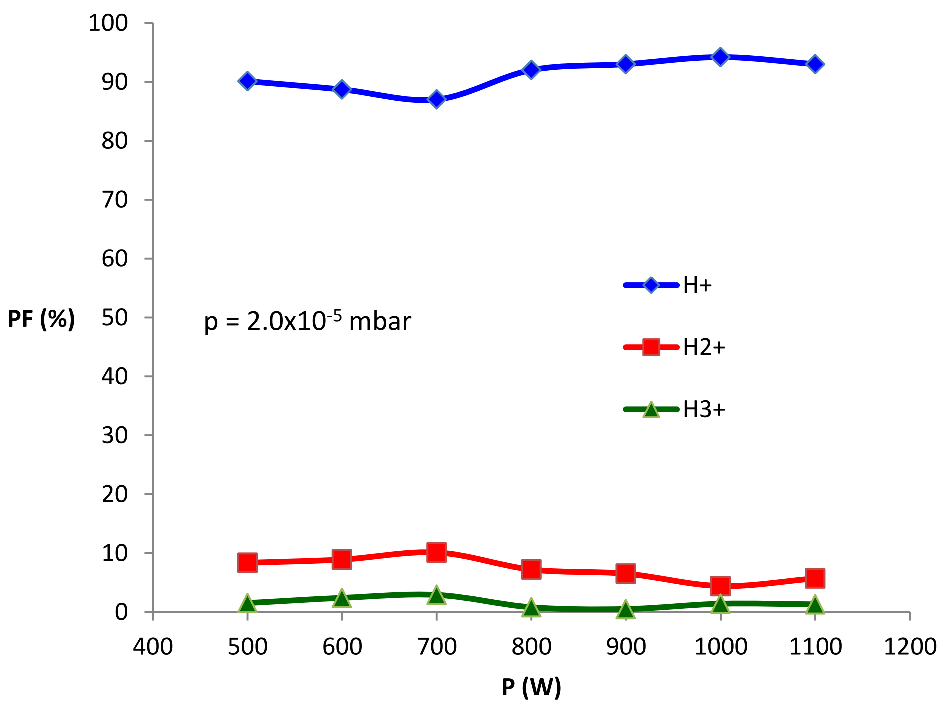

Figure 6.58 *Proton fraction versus microwave power for residual gas pressure of 2.0×10^{-5} mbar and 25 kV of extraction of extraction voltages and -2 kV of suppression voltages.*

The proton fraction measurement was performed by incorporating two Boron Nitride (BN) plates at two end of plasma chamber and enclosing the curved surface of plasma chamber with 1 mm thick Aluminum hollow cylinder. The proton fraction is found to be around 90% and is more or less constant for the microwave power range studied. The trends in Figure 6.58 can be understood as follows: a high proton fraction is generated by two step processes 1) $H_2 + e \rightarrow H + H + e$ and 2) $H + e \rightarrow H^+ + 2e$. In our ion source T_e ~ 4 - 14 eV, so the reaction rate coefficient for H^+ ions is larger than for generating H_2^+ ions [71]. Also by incorporating BN plates, the secondary electrons created by the impact of primary ions on BN plates result in dissociation of H_2^+ ions by the reaction $H_2^+ + e \rightarrow H^+ + H + e$. This two effects lead to very high H+ ions in the plasma chamber. For higher microwave power at fixed hydrogen gas flow, the electron temperature decreases slightly as shown in Figure 5.17 (b) (Here, the residual gas pressure of 2.0×10^{-5} mbar corresponds to 2.5×10^{-3} mbar in the plasma chamber). The cross-section for H_2^+ decreases slightly for lower electron temperature, so the proton fraction remains steady or slightly increases [71].

The variation of proton fraction versus neutral gas pressure is shown in Figure 6.59. The proton fraction slightly decreases from 90% to 89% for the residual gas pressure range studied. The proton fraction decreases with increasing pressure, as it has also observed in other works [15, 55, 120]: as the gas pressure increases, the electron temperature decreases (Figure 5.14 (b)) and the recombination processes play the dominant role.

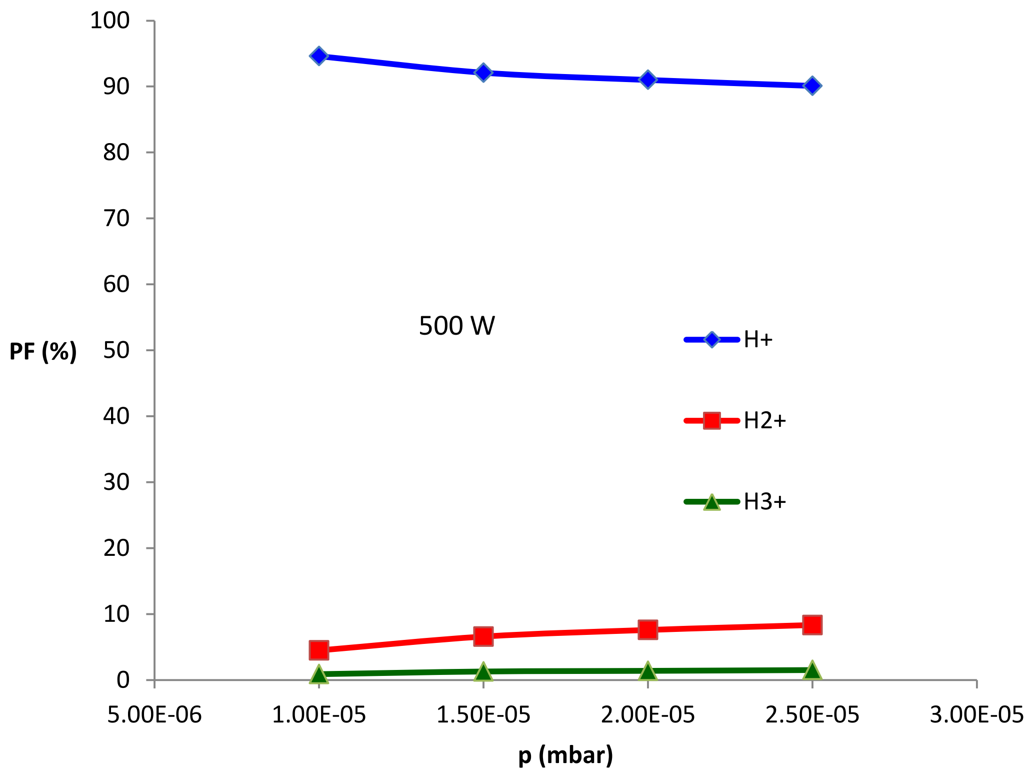

Figure 6.59 *Proton fraction versus residual gas pressure for 500 W microwave power and 25 kV of extraction of extraction voltages and -2 kV of suppression voltages.*

6.4 Summary

This chapter describes the studies on beam current, emittance and proton fraction measurement and the design and development of low energy beam transport line for these measurements. The ion beam was extracted from three electrode extraction geometry by biasing the plasma electrode and the suppressor electrode from +10 to +50 kV and -2 to -4 kV respectively. The maximum beam current extracted was 40 mA at beam energy 40 keV. The variations in the beam current as a function of extraction voltage, microwave power and gas pressure were studied. It was found that the beam current is governed by space charge limited current ($\propto V^{3/2}$) with the increase of extraction voltage. The beam current does not change significantly with the increase of microwave power and gas pressure. The ion source was also operated in pulsed mode and 10 mA, 100 ms beam current was extracted at 25 keV and its variation with microwave power was studied. A low energy beam transport line consisting of solenoid magnets, steering magnets and analyzing magnet was designed using 2 D and 3 D calculations. The beam line magnets were designed and fabricated. An emittance meter and Faraday cups were designed and developed to measure beam emittance and total beam current. The beam emittance was measured at three locations: 1) after beam extraction 2) after solenoid magnet and 3) after solenoid magnet and analyzing magnet. The measured value of beam emittance at these three locations was found to be $< 0.2\ \pi$ mm-mrad. The variation of beam emittance was studied as a function of microwave power. The proton fraction was measured using an analyzing magnet. The typical value of proton fraction is more than 90%. The variation of proton fraction with microwave power and gas pressure was studied.

Chapter 7

Control and Automation of ECR Proton Ion Source

In this chapter remote control and operation of the ion source is described. For reliable, stable and long-time operations of the ion source it is mandatory to monitor the forward and the reflected microwave power, chamber vacuum, solenoid coil power supply status, high voltage power supply status and the beam parameters. The control system of the ion source is a computer based control system where all the power supplies are operated remotely from computer. Graphic User Interface (GUI) is developed for the remote operation of the ion source. The control and automation of the ion source is developed in housed [121, 122].

For high beam availability from the ion source and to maximize beam-on time, rapid recovery from routine event, like ion source spark-down, is needed. Reliable recovery from routine event can be provided through computer based automated sequencing. For reliable operation, the data in the computer must be protected from being corrupted by the severe EMI transients produced during the spark down. Coupling between the high voltage power supplies (HVPS) and the computer control system is a primary cause of the disruption or damage to computers/logic that occasionally occurs during injector high voltage spark-down. The HVPS circuitry, the method of connecting to injector determines significant EMI coupling parameters such as stored energy, peak current, discharge frequency, di/dt and dV/dt.

The coupling between the spark in HVPS and the control system follows several paths, each with some coupling constant that primarily depends on the natural frequency of discharge circuit. Capacitive coupling from the HVPS' high dV/dt through the high impedance electric field is relatively easy to shield. Proper grounding of the metal enclosures surrounding the HVPS and of the shields on signal cables will eliminate almost all of the *dV/dt* driven interference. The only area of the injector system where this EMI source may dominate is unshielded cables or transducers if they are exposed to high voltage circuits. The effect of this, sometimes unavoidable, coupling can be minimized by shielding the exposed cables and transducers and/or shunting their stray capacitance with an RC low pass filter.

The most likely path of EMI into the control system is *di/dt* (Φ) coupling through the transient low impedance (magnetic) field. This low impedance field is much more difficult to shield. Coupling paths will exist through any mutual inductance between the HVPS discharge circuits and the control system. To control low impedance coupling, the best defense is the reduction of the inductance of all source and signal loops. This source of EMI may be suppressed on signal cables by installing isolators that break the low impedance loop formed by the signal cable conductors and thus convert the Φ induced voltage into a common mode voltage on the isolators. This defense is usually effective, but it can fail if the frequency and/or amplitude of the source of the EMI are extreme, thus driving noise current through the isolators. If the isolators are preceded by a passive low pass filter, the effect of extreme *di/dt* is mitigated.

Proper grounding will reduce the coupling of the spark induced transients into the data acquisition system. There are three grounding systems of particular interest: the AC power system, the HVPS system and the signal cable/data acquisition system. The thickness of the common construction materials used in electrical power distribution systems is much greater than skin depth at the transient frequencies. This fact allows the use of conduits and junction boxes for barrier shields and permit effective and transient current grounds to be easily made. A three phase shielded ultra-isolation transformer is employed to isolate the three phase ac power to the HVPS thereby limiting the coupling of spark transient to the AC power lines. Another shielded three-phase transformer provides three isolated single phase 230 V power sources for clean power to computer, oscilloscope, ADCs and vacuum control.

The HVPS is grounded for safety and the ion source is also grounded by the beam line. To avoid a large ground loop with high transient currents, the HVPS cable must be shielded and the shield must be grounded at both ends. This arrangement insures the HVPS transient discharge current (primarily) flows back long the cable shield since the coaxial cable shield is in “cutoff”. The concurrent advantage is that the inductance of the primary transient discharge loop, a major source of Φ coupling, is greatly minimized.

The local control panel provides control and monitoring of the ion source. The logic in the local control enforces proper operation of the ion source to provide equipment protection as outlined in the ion source standard operating procedure. The logic controls the order in which devices may be turned on when turning up the ion source. Logic is used to check the ion source status to determine if a controller device may be safely operated. The status consists of both discrete status and cooling water flow, and analog read-back/thresholds which determine whether or not the ion source is in a state that is proper for operations initiated by the operator or an automatic sequence. Control thresholds are available to the operator to modify as needed for running beam in varying conditions. For example, the HVPS thresholds are different when conditioning the ion source than when running.

ECR ion source is sub divided into five sections for remote control operations and monitoring, viz. microwave generator power supplies, solenoid coil power supplies, extractor electrodes high voltage power supplies, vacuum pump power supplies and monitoring of beam current, vacuum pressure and microwave power. Remote operation and control of all sections of the ECR ion source was done though computer. Control system architecture of the ion source is shown in Figure 7.1. The remote operations of all the five sections of the ion source were done using MOXA EDS208 industrial ethernet switch and two MOXA 5450I ethernet to 4 port serial converters. The converter is used to extend the serial port capability of the computer via ethernet switch. The remote operation of all the five sections of ECR ion source was done as follows: (i) *Microwave generator*: The 2 kW microwave generator (magnetron) was used to feed microwave power to plasma. Microwave generator was remotely accessed via serial RS232 link. For monitoring the microwave power, a dual channel RF power meter was used and accessed remotely via RS232 serial link. Both microwave generator and RF power meter assigned their dedicated serial port which is shown in Figure7.1. (ii) *Solenoid magnets power supplies*: For generating electron cyclotron resonance condition two solenoid coils were used that produces axial magnetic field of 875 G on plasma chamber.

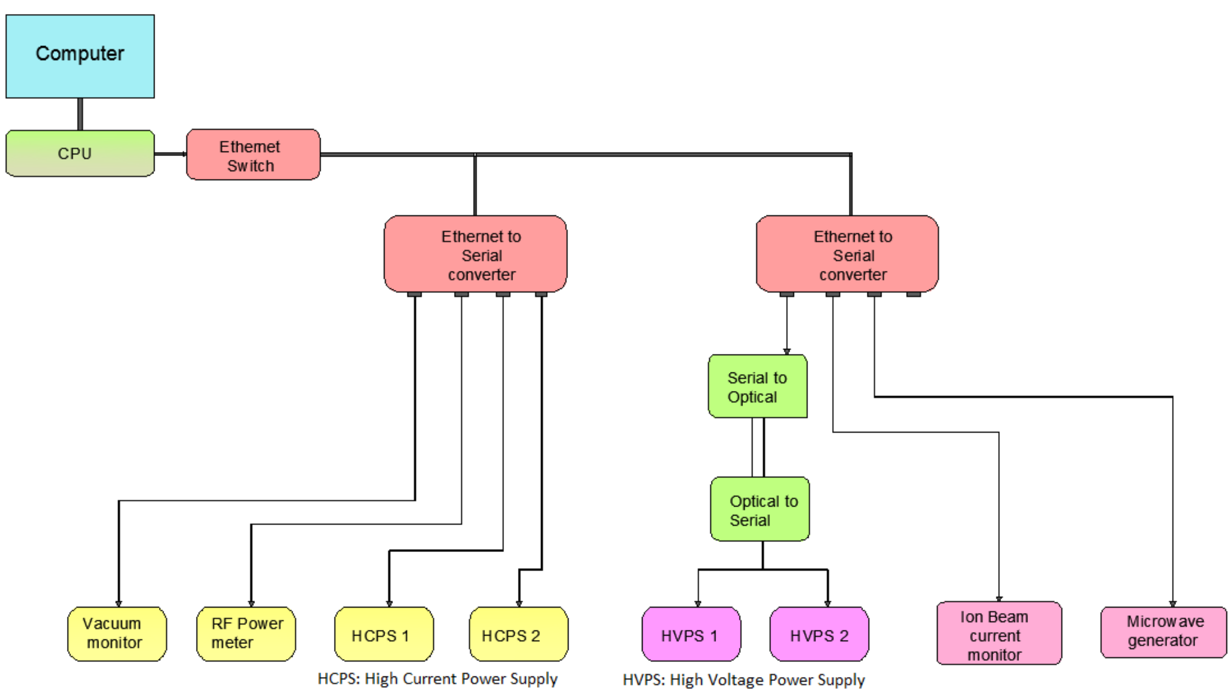

Figure7.1 *Block diagram of ECR ion source control architecture.*

The solenoid coils were energized using 800A, 10 V high current power supplies. Both the high current power supplies were remotely accessed via their dedicated comport. (iii) *High voltage power supplies*: Two high voltage power supplies of ratings 50 kV, 100 mA and -6 kV, 100 mA were used for ion beam extraction. The input powers of both the high voltage power supplies were provided by an ultra-isolation transformer to avoid ground loop problem. High voltage power supplies were remotely operated via 0 - 5 V analog input voltage that corresponds to 0 – 50 kV or 0 – (-6 kV) output voltage. Remote operation of HVPS was done using RS485 serial interface. Serial to optical conversion using MOXA TCF 142 was implemented to provide isolation to HVPS and computer. ADAM 4017+ was used to provide analog output 0 - 5 V to HVPS. For voltage read back of 0 – 5 V ADAM 4024 analog input module was used. The switching between remote and local mode was done using ADAM 4068 relay module.

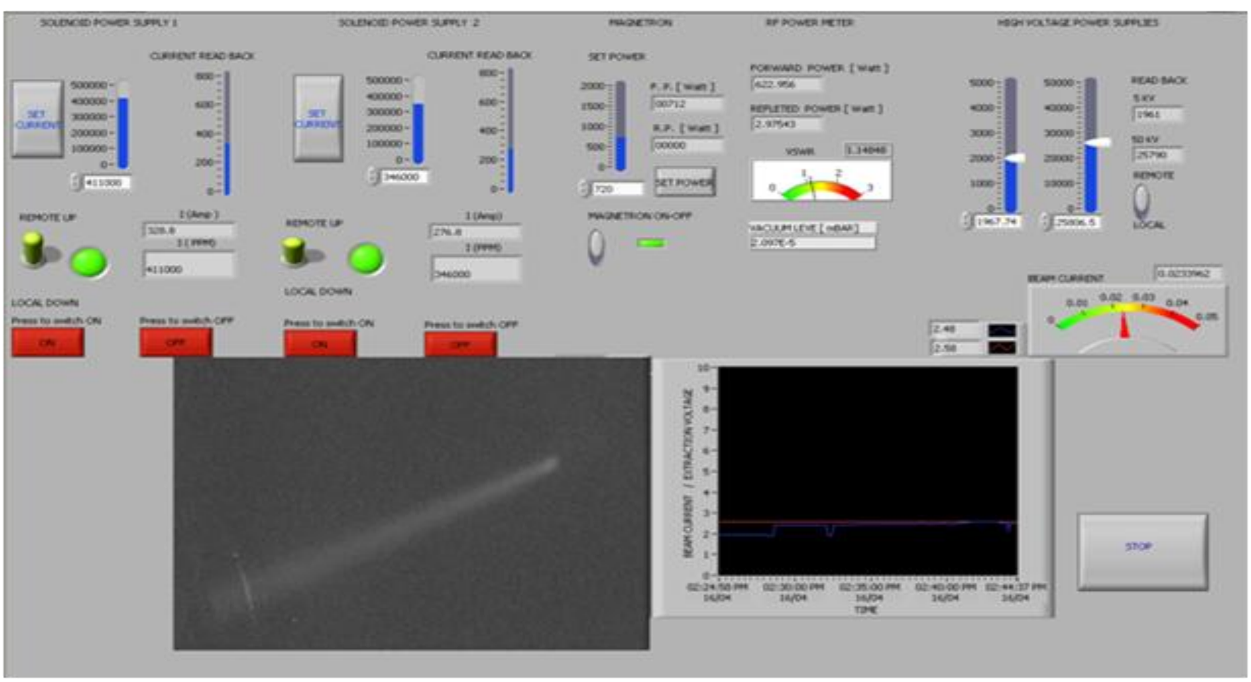

Figure7.2 *GUI of the ECR proton ion source.*

All these ADAM modules were controlled from single RS485 serial interface link. (iv) *Beam current and vacuum pressure monitoring:* The Faraday cup was used for measuring the ion beam current. The Faraday cup current was measured either on M/S Keithley current meter or across a 100 Ω shunt resistance. The voltage across the resistance was measured using ADAM 4024 analog input module. Vacuum gauges were used to monitor vacuum level and connected to vacuum gauge controller. Vacuum gauge controller was remotely accessed via serial RS232 link. The Graphical User Interference (GUI) of the ECR ion source was developed as shown in Figure 7.2.

Summary

This chapter describes the control and automation of ECR proton ion source. All the ion source components i.e., microwave generator and power supplies, solenoid coil power supplies, extractor electrodes high voltage power supplies, vacuum pump power supplies and monitoring of beam current, vacuum pressure and microwave power were remotely operated and monitored through PC. A GUI has been developed and used for this purpose.

Chapter 8

Conclusion and scope of future work

A high current Electron Cyclotron Resonance (ECR) proton ion source have been designed, fabricated, assembled, tested, characterized and commissioned for Low Energy high Intensity Proton Accelerator (LEHIPA) at CFB, BARC as shown in Figure 8.1. LEHIPA is under development and consists of H^+ ion source at 50 keV to be accelerated to 3 MeV by Radio Frequency Quadrupole (RFQ) and to 20 MeV by an Alvarez type Drift Tube Linac (DTL).

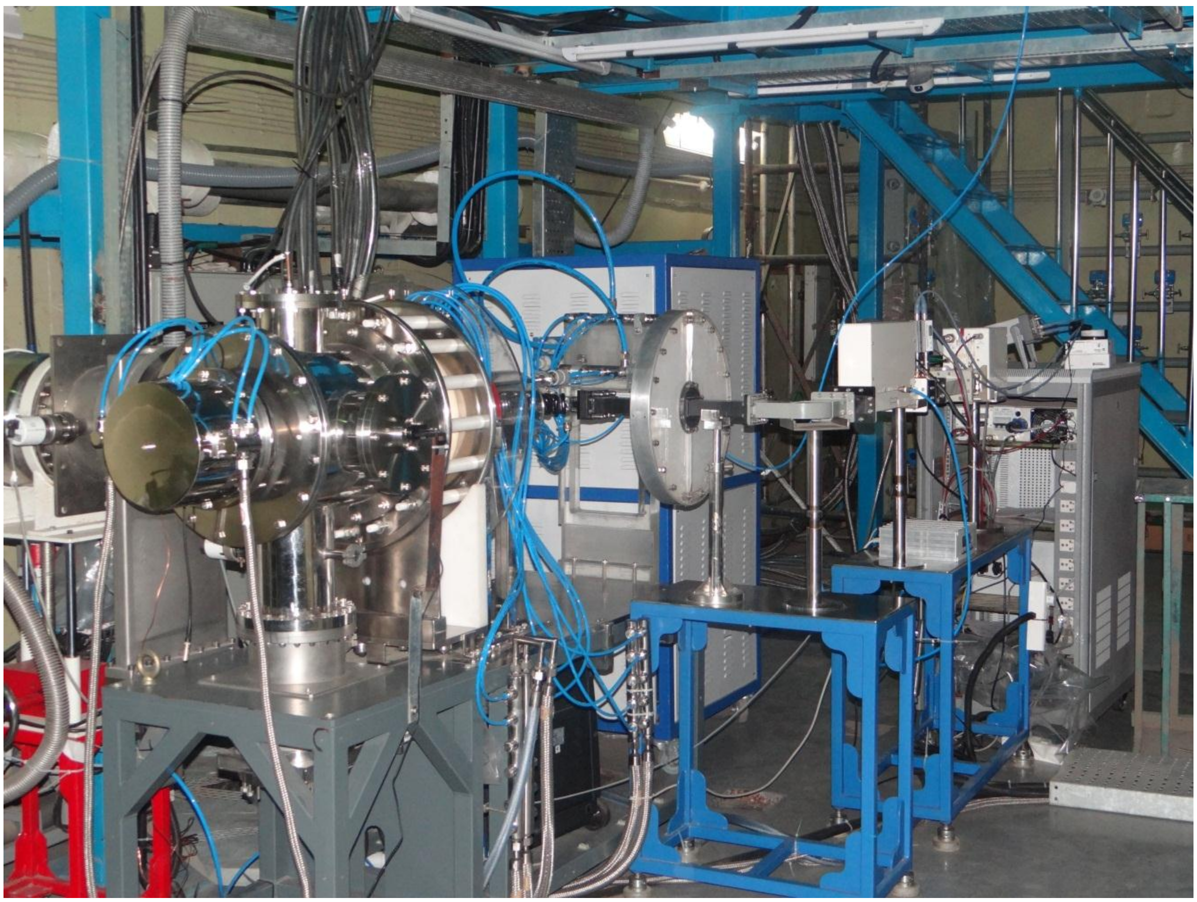

Figure8.1 *ECR proton ion source for LEHIPA commissioned at CFB, BARC.*

The key components of ECR proton ion source are microwave generator and transmission system, plasma chamber, vacuum system, solenoid coils and power supplies, beam extraction electrodes and power supplies, gas injection system, plasma diagnostics devices and beam measuring device.

The ion source and the subsystems that have been designed and developed are the following: microwave generator and transmission system, plasma chamber, solenoid coils for magnetic field, beam extraction system, vacuum system, gas injection system, beam and plasma measuring devices and Low Conductivity Process Water system (LCW). The microwave generator section consists of magnetron, circulator, dual directional coupler, four stub auto tuner, waveguide break and ridge waveguide. The microwave components were assembled on a test bench, terminated on a water-cooled matched load and tested up to full power label of 2 kW. The waveguide break, ridge waveguide and H-plane bend waveguide were designed and fabricated in house. The ridge waveguide and H-plane bend waveguide is operating under low pressure so it was designed to withstand vacuum pressure of 10^{-7} mbar. The ECR magnetic field of 875 G was generated using two solenoid coils and power supplies. The design of the solenoid coils was performed using magnetic field simulation software. The coils were fabricated using square hollow copper conductors of size 7 mm × 7 mm with 5 mm bore made of OFHC copper in pancake winding and vacuum impregnated in epoxy. The coils were tested by energizing each coil using 800A/10V highly stabilized power supplies. The field mapping was performed using Hall probe. The designed field values matches well with the measured ones. The water-cooled plasma chamber was designed and fabricated. The plasma chamber is 100 mm length and 90 mm diameter. For three- electrode ion source the plasma chamber is made of SS 304L and a water jacket is provided for cooling. For five-electrode ion source the plasma chamber is made from OFHC copper and the cooling circuit is provided by cavities on the outer walls.

The vacuum system of the ion source was designed to withstand a base pressure of 10^{-7} mbar. When the working gas was introduced it maintained a differential pressure of 10^{-3} mbar in plasma chamber and 10^{-5} mbar in extractor region. The vacuum was generated using turbo-molecular pump and dry roughing pump. The vacuum pressures in the ion source were monitored using penning/pirani combined gauge head and controllers and capacitance gauge head and controllers. The gas dosing system was designed to allow controlled working gas in the plasma chamber using precision leak valve and shut off valve that was floated at 50 kV and the gas reservoir and gas regulator that is at ground potential and isolated using polypropylene tube.

The Low Conductivity Process Water (LCW) system was designed to provide the cooling de-mineralized water to various subsystems of the ion source with the required flow rates. The parameters of water characteristics for the systems are: (1) conductivity < 1 μS/cm, (2) total dissolved solids < 1 ppm and (3) pH variation is within 6.8 – 7.2. The LCW system was used for cooling twenty components of the ion source and was designed for 65 kW heat removals, with pumping capacity 200 lit/min ($12m^3$/h). It comprises of makeup water system (demineralized water column) and self-circulation through ion exchange beds (resin column) for improving conductivity (polishing), recirculation pumps, SS-304 storage water tank, flexible tubing connections and instrumentation system.

The beam extractor system was designed to provide total beam current of 50 mA at beam energy 50 keV. The beam extraction system was optimized via electrode apertures, electrode gaps and electrode shapes to minimize beam size and divergence. The three and five electrode extraction was designed and fabricated for ion extraction. In three electrode ion source the electrodes were made of SS304L and for five electrodes from OFHC copper. The three and five electrode ion source was assembled in the test stand and vacuum tested. The high voltage test was performed under vacuum. Further tests and characterization are carried out with three electrode ion source only.

The ECR plasma generation, stabilization and characterization was performed before extracting the ion beam. Plasma discharge was initiated by first evacuating the plasma and extractor chamber to a base pressure 10^{-7} mbar. The hydrogen gas was introduced in the plasma chamber and maintained at pressure ~10^{-3} mbar. The magnetic field profile of 875 G at the entrance and exit of plasma chamber was established by energizing two solenoid coils. Microwave at 2.45 GHz and 400-1100 W power was fed in the plasma chamber. The discharge was stabilized by minimizing the reflected microwave power using four stub auto tuner and magnetic field. The reflected microwave power was found to be 1 to 2 % of forward microwave power for the pressure range studied. Plasma characterization was performed once the discharge was stabilized. An automated Langmuir probe and associated circuits were developed in housed to characterize ECR plasma. The current – voltage ($I – V$) characteristics of the probe were taken by sweeping the voltage on the probe from – 115 V to + 53 V. These data are recorded on the digital storage oscilloscope (DSO) and were transferred to the personal computer. The probe was inserted radially into the plasma so that the probe tip was located at the center of the plasma and at different radius to the outer edge of the plasma.

The pulsed plasma characterization was performed by operating the magnetron in a pulsed mode. The magnetron was operated at frequency of 2.45 GHz with 400 - 1000 W output power for μs to ms pulse duration and 1% to 99 % duty cycle.

The characterization of ECR plasma ion source was also performed. These results include measurements of ion density, electron temperature, plasma potential and electron energy distribution function. The measured value of plasma parameters are in the range, ion density:

5.6×10^{10} cm^{-3} to 3.8×10^{11} cm^{-3}, electron temperature: 4 eV - 14 eV and plasma potential: 20 V - 45 V. The following studies were performed on ECR plasma: 1) Dependence of reflected microwave power on forward microwave power for different neutral gas pressures, 2) Dependence of plasma electron density, plasma electron temperature and plasma potential on neutral gas pressure 3) Dependence of plasma electron density, plasma electron temperature and plasma potential on microwave power, and 4) Radial variation of plasma parameters for different microwave powers.

The characterization of the ion beam was performed in terms of total beam current, beam emittance and proton fraction. For ion beam extraction two high voltage power supplies were used 0 to +60 kV for plasma electrode and 0 to -6 kV for suppressor electrode. The plasma chamber was floated at extractor voltage. The solenoid coils were isolated from extractor voltage and kept at ground potential using Perspex insulator. The microwave section was also isolated from extractor voltage and kept at ground potential using DC waveguide break. The total ion beam current was measured using an electron suppressed Faraday cup developed in our laboratory. The total ion beam current of 42 mA (all species) was extracted at beam energy of 40 keV. But the long time operation of the ion source was hampered by (i) damage of microwave quartz window by bombardment of back streaming electrons and (ii) rise in cooling water temperature. These two problems were resolved by relocating the microwave window from the line of sight of back streaming electrons and by increasing the chill water flow in the heat exchanger. The ion beam was extracted when the plasma was stabilized and by applying bias of +10 to +50 kV on plasma electrode and -2 to -4 kV on suppressor electrode. The ion beam current was found stable for several hours of source operation. The following studies were performed when the beam was stable: 1) Dependence of beam current on extraction voltage 2)

Dependence of beam current on microwave power and 3) Dependence of beam current on residual gas pressure.

The ion source was operated in a pulsed mode by generating pulsed plasma and extracting the ion beam. The magnetron was operated in a pulsed mode by the internal pulse generator and also by external pulse from function generator. The pulse repetition rate was varied from 1 Hz, 10 Hz and 100 Hz to CW. The ion beam current was found not stable for pulse duration below 1 ms.

A low energy beam transport line (LEBT) has been designed and developed for measuring two important beam parameters i.e., beam emittance and proton fraction. The purpose of LEBT was to transport and focus the ion beam from ion source to the next accelerating structure. The low energy beam transport line consists of two solenoid magnets and power supplies, two x-y steering magnets and power supplies, an analyzing magnet and power supply, turbo-molecular pump and controller, dry roughing pump, vacuum gauge heads and controllers and beam diagnostics i.e., emittance meter, Direct Current Transformer, Alternative Current Transformer, CCD cameras and Faraday cups. The emittance meter and Faraday cups are designed and developed in our laboratory. The beam optics of the transport line was studied using standard software.

For measuring transverse beam emittance, an Emittance Measurement Unit (EMU) has been designed and developed in our laboratory. It consists of two slits and a Faraday cup. The slits are separated by distance 300 mm. Both the slits are made of tantalum 0.2 mm wide aperture and 80 mm length and installed on a water-cooled copper block. The second slit has a Faraday cup attached to it. The movements of the slits are remotely controlled using stepper motors and controllers. The positions of the slits are recorded using linear encoders. The Faraday cup current on the second slit is recorded on a current meter.

The ion beam emittance was measured at three locations (i) at the ion source end after beam extraction, (ii) after focusing the beam using one solenoid magnet. In this case before emittance measurement, the focusing of the hydrogen ion beam consisting of H^+, H_2^+ and H_3^+ is studied by simulation and in experiment by measuring the beam profile, and (iii) after focusing and separating H^+ using a solenoid magnet and an analyzing magnet. In these three cases variation of beam emittance with microwave power was studied. The value of beam rms normalized emittance ε_n measured for the above three cases falls in the range (i) 0.07 - 0.19 π mm-mrad (ii) 0.15 - 0.25 π mm-mrad and (iii) 0.02 - 0.11π mm-mrad respectively.

After ion beam emittance measurement, the proton fraction in the hydrogen ion beam was measured. The proton fraction of the beam was measured by sweeping the magnetic field of the analyzing magnet and recording the current signal on Faraday cup. A 0.2 mm width slit was incorporated in front of the Faraday cup for spatial resolution of three species H^+, H_2^+ and H_3^+. The proton fraction measured was > 90%. The variation of proton fraction with microwave power and residual gas pressure was studied.

The remote control and operation is an important aspect of the ion source as there are many parameters to control for smooth functioning of the ion source. For reliable, stable and long-time operations of the ion source it is mandatory to monitor the forward and the reflected microwave power, vacuum pressure, solenoid coil power supply status, high voltage power supply status and the beam parameters. The control system of the ion source is a computer based control system where all the power supplies are operated remotely from computer. Graphic User

Interface (GUI) of the ion source is developed for the operation of ion source. The control and automation of the ion source is developed in housed.

Scope of future work

The future work involves the testing and commissioning of five electrode ion source that has been fabricated and assembled. The beam and plasma characterization needs to be performed. The five electrode ion source has the advantage that the beam emittace can be minimized by varying the potential on the puller electrode. The emittance minimization also needs to be performed by space charge compensation of the ion beam in LEBT by introducing neutral gas in beam transport channel. The in depth studies of ECR plasma processes that results in high microwave power absorption and generation of high density plasma should be investigated. The theoretical model has be developed to explain how the plasma parameters i.e., electron density, electron temperature, electron and ion energy distribution function and plasma potential depends on magnetic field, gas pressure and microwave power so that it can be verified through experiment. The theoretical model could be based on hybrid Particle In Cell and Monte Carlo (PIC-MCC) simulation as the plasma processes are highly nonlinear. The model can be extended to incorporate neutral gas breakdown by microwave power to the formation of high density ECR plasma and high current ion beam extraction. For ion beam transport, the space charge compensation is an important aspect. Detailed theoretical and experimental studies needs to be conducted to know how the high current space-charged dominated beam is transported over long distances. The high current CW and pulsed beam diagnostics has to be developed for these investigations and some of them are: Allison meter and pepper pot for beam emittance, Wein filter for proton fraction, four grid analyser and electron beam probe for space-charge neutralization factor etc. In addition, the non-invasive diagnostic of residual gas fluorescence method has to be developed for proton fraction measurement.

APPENDIX I

The impedances of various sections of the double ridge waveguide are calculated as follows for $a_2/a_1 = 0.5$, $b_1/a_1 = 0.2356$, $2a_1 = 7.213$ cm, $2b_1 = 3.4$ cm:

In WR 284 section, $a_2/a_1 = 0.5$, $b_1/a_1 = 0.2356$, $2a_1 = 7.213$ cm and $2b_1 = 3.4$ cm. For $b_1/b_1 = 1$, the values of $\lambda_c'/\lambda_c = 1 = f_c/f_{c'}$, (from Figure 2 of reference [63]) where λ_c' and λ_c are the cutoff wavelengths of the waveguide with and without the ridge. In our case $\lambda_c = c/f_c = 3\times10^8/2.079\times10^9 = 0.1443$ m, $\lambda_g = \lambda/(1-(f_c/f))^{1/2} = 23.14$ cm and $\lambda_g/4 = 5.79$ cm.

The characteristic impedance at infinite frequency $Z_{0\infty}$ for the TE_{10} mode and cutoff wavelength of ridge waveguide λ_c for $b_1/a_1 = 0.136$ and 0.5 are available (Figs.2 and 3 of Ref.[89]). For b_1/a_1 not equal to 0.136 or 0.5, $Z_{0\infty}$ can still be determined very closely from Figures 2 and 3 of reference [63].

For the values of b_1/a_1 between zero and one third, $Z_{0\infty}$ is given by $[(b_1/a_1)/0.136]$ and for values between one third and two third, $Z_{0\infty}$ is given by $[(b_1/a_1)/0.5]$. In our case $b_1/a_1 = 0.2356$, so $Z_{0\infty}$ is given as $Z_{0\infty} = 80.5\times2\times[(b_1/a_1)/0.136] = 279\ \Omega$. The value of characteristics impedance Z_0 of rectangular waveguide is thus given as:

$$Z_0 = 377\,(b/a)\,[1/(1-f_c)^{1/2}] = 527\ \Omega. \quad (4.1)$$

The final $Z_{0f} = 527/1.57 = 336\ \Omega$.

In section I, $b_2/b_1 = 0.75$, $\lambda_c'/\lambda_c = f_c/f_{c'} = 1.11$ and $2b_2 = 2.55$ cm, $f_{c'} = 2.079/1.11 = 1.873$ GHz. $\lambda_g = 18.94$ and $\lambda_g/4 = 4.736$ cm. $Z_{0\infty} = 65\times2\times1.734 = 225.2\ \Omega$ and $Z_0 = Z_{0\infty}\times1.551 = 349.42\ \Omega$. So, $Z_{0f} = 349/1.57 = 222.6\ \Omega$.

In section II, b_3/b_1 = 0.6, $\lambda_c^{'}/\lambda_c = f_c/f_{c'}$ = 1.222 and 2b_3 = 2.04 cm, $f_{c'}$ = 1.701 GHz. λ_g = 17.03 and λ_g/4 = 4.25 cm. $Z_{0\infty}$ = 53×2×1.734 = 183.7 Ω and Z_0 = $Z_{0\infty}$×1.389 = 255.24 Ω. So, Z_{0f} = 255.24/1.57 = 162.57 Ω.

In section III, b_4/b_1 = 0.4, $\lambda_c^{'}/\lambda_c = f_c/f_{c'}$ = 1.45 and 2b_4 = 1.36 cm, $f_{c'}$ = 1.434 GHz. λ_g = 15.04 and λ_g/4 = 3.76 cm. $Z_{0\infty}$ = 37×2×1.734= 128.24 Ω and Z_0 = $Z_{0\infty}$×1.233 = 158.16 Ω. So, Z_{0f} = 158.16/1.57 = 100.74 Ω.

In section IV, b_5/b_1 = 0.22, $\lambda_c^{'}/\lambda_c = f_c/f_{c'}$ = 1.8636 and 2b_5 = 7.48 cm, $f_{c'}$ = 1.1156 GHz, λ_g/4 = 3.43 cm. $Z_{0\infty}$ = 22×2×1.734 = 76.25 Ω and Z_0 = 76.25×1.389 = 85.63 Ω. So, Z_{0f} = 85.63/1.57 = 54.5 Ω.

APPENDIX II

The first order estimate of pumping speed required to evacuate ion source with and without gas load is presented here. The ultimate base pressure in plasma chamber, extractor chamber and vacuum diagnostic chamber is first calculated as follows:

(i) Base pressure without gas load

For plasma chamber:

Total Stainless Steel surface area A_{ss}: 410 cm^2

Total viton surface area A_{vt} = 26.64 cm^2

Plasma chamber orifice: 8 mm

Conductance of the orifice C (for air): 5.84 lit/sec

Pump speed S_P: 2000 lit/sec

Effective pumping speed ($S_{eff} = 1/(1/S_P + 1/C)$): 5.84 lit/sec

Outgassing rate of Stainless Steel q_{ss}: 10^{-8} mbar-lit/s-cm^2

Outgassing rate of Viton q_{vt}: 10^{-7} mbar-lit/s-cm^2

Total throughput ($Q = q_{ss} A_{ss} + q_{vt} A_{vt}$): 6.7×10^{-6} mbar-lit/sec

Base pressure in plasma chamber (Q/ S_{eff}): 1.15×10^{-6} mbar

For extractor and vacuum diagnostic chamber:

Total Stainless Steel surface area A_{ss}: 26912 cm^2

Total Alumina Ceramic surface area A_{cer}: 1696 cm^2

Total viton surface area A_{vt} = 160 cm^2

Outgassing rate of Stainless Steel q_{ss}: 10^{-8} mbar-lit/s-cm^2, alumina q_{cer}: 5×10^{-8} mbar-lit/s-cm^2, Viton q_{vt}: 10^{-7} mbar-lit/s-cm^2.

Total throughput ($Q = q_{ss} A_{ss} + q_{cer} A_{cer} + q_{vt} A_{vt}$): 3.1×10^{-4} mbar-lit/sec

Base pressure in plasma chamber (Q/S_P): 3.26×10^{-7} mbar

(ii) With gas load and no hydrogen ionization

When the working gas is introduced, it appears as leak in the vacuum system. Then the pumping speed with gas load is calculated as follows:

Pressure to be maintained in the plasma chamber ($p_1 - p_2$): 10^{-3} mbar

Conductance of 8 mm aperture (for hydrogen) C: 22.16 lit/sec

Throughput required to maintain this pressure Q (= C ($p_1 - p_2$)): 0.022 mbar-lit/sec

This throughput is appeared as leak from the plasma chamber. Now to maintain a pressure of 10^{-5} mbar in the extractor chamber and diagnostic chamber with the gas load, the pumping capacity required is: $S = 0.022/10^{-5} = 2200$ lit/sec.

(iii) With hydrogen ionization

When the hydrogen gas is ionized, the typical gas ionization efficiency in ECR sources is η: 15 – 25%. Say for η: 20%, the throughput will become 0.0177 mbar-li/sec. Hence, the pumping capacity required is: S = 1700 lit/sec to maintain a pressure of 10^{-5} mbar in extractor chamber and diagnostic chamber.

APPENDIX III

The computer program for estimation of emittance is given as under:

```
% code to estimate rms Emittance
clc
n = 24;
nprime = 140;
clear x
clear new
clear xprime
clear I
for i = 1:n
    for j = 1:nprime
    x(i,j) = (10 -((i-1)*1));%%mm
    xprime(i,j) = (((25-(i-1)*1) - (j-1)*0.5)- x(i,j))/(0.3); %%mrad

    end
end
I = [enter stored I values];
for i = 1:n;
for j = 1:nprime
    if (I(i,j)< 0.0)
        I(i,j) = 0;
    end
end
```

```
end
max(I);
for i = 1:n;
for j = 1:nprime
if (I(i,j)< 0.01*(max(I)))
I(i,j) = 0;
end
end
end
Itotal = 0;
for i = 1:n
    for j = 1:nprime
        Itotal = Itotal + I(i,j);
    end
end

xc = 0;
for  i = 1:n
    for j = 1:nprime
        xc = xc + x(i,j)*I(i,j);
    end
end

xc = xc/Itotal;
xcprime = 0;
for i = 1:n
    for j = 1:nprime
        xcprime = xcprime + xprime(i,j)*I(i,j);
    end
end

xcprime = xcprime/Itotal;
avgxsqr = 0;
for i = 1:n
    for j = 1:nprime
        avgxsqr = avgxsqr + (x(i,j)-xc)^2*I(i,j);
    end
end

avgxsqr = avgxsqr/Itotal;
avgxpsqr = 0;
for j = 1:nprime
    for i = 1:n
        avgxpsqr = avgxpsqr + (xprime(i,j)-xcprime)^2*I(i,j);
    end
end

avgxpsqr = avgxpsqr/Itotal;
avgxxp = 0;
for i = 1:n
    for j = 1:nprime
        avgxxp = avgxxp + (x(i,j)-xc)*(xprime(i,j)-xcprime)*I(i,j);
    end
end

avgxxp = avgxxp/Itotal;
 clear B
```

```
clear G
BeamEnergy = 25 ; %%kV
B = ((2*BeamEnergy*10^3*1.6*10^-19/(1.6*10^-27))^0.5)/(3*10^8); %% beta of
the H ion beam
BH2 = ((2*BeamEnergy*10^3*1.6*10^-19/(2*1.6*10^-27))^0.5)/(3*10^8); %% beta
of the H2 ion beam
BH3 = ((2*BeamEnergy*10^3*1.6*10^-19/(3*1.6*10^-27))^0.5)/(3*10^8); %% beta
of the H3 ion beam
G = 1/((1-B^2)^0.5); %%gamma of the ion beam

epsilonrms = (avgxsqr*avgxpsqr - avgxxp^2)^0.5/pi;

epsilon_rms_normalised = epsilonrms*B*G, 'pi mm mrad'

alpha = -avgxxp/(epsilonrms*pi)

beta = avgxsqr/(epsilonrms*pi)

gamma = avgxpsqr/(epsilonrms*pi)

h = (beta + gamma)/2;
xc = 0;
yc = 0;
a = ((epsilonrms/2)^0.5)*((h + 1)^0.5 + (h - 1)^0.5);
b = ((epsilonrms/2)^0.5)*((h + 1)^0.5 - (h - 1)^0.5);
phi = 0.5*atan((2*alpha)/(gamma-beta));

%pdeellip(yc,xc,b,a,phi)
contourf(x,xprime,I)
%pde(0,0)
```

REFERENCES

1. S. S. Kapoor, Pramna J. Physics, **59**, 941 (2002).
2. P. Singh, SVLS Rao, R. Pande, T. Basak, S. Roy, M. Aslam, P. Jain, SCL Srivastava, Rajesh kumar, P. K. Nema, S. Kailas and V. C. Shani, Pramna J. Physics, **68**, 331 (2007).
3. P. Roychowdhury and D. P. Chakravarthy, Rev. Sci. Instrum. **80**, 123305 (2009).
4. SVLS Rao and P. Singh, Pramna J. Phys. **74**, 247 (2010).
5. R. Pande, S. Roy, SVLS Rao and P. Singh, Pramna J. Phys. **78**, 247 (2012).
6. F. Chen, '*Introduction to Plasma Physics and Controlled Fusion*', Plenum Press, New York, NY, 1984.
7. M. A. Lieberman and A. J. Lichtenberg, '*Principles of Plasma Discharges and Material Processing*' Wiley, New York, 1994.
8. R. Geller, '*Electron Cyclotron Resonance Ion Source and ECR Plasmas*', PA: Inst. Phys., Philadelphia, 1996.
9. I. G. Brown, '*The Physics and Technology of Ion Sources*', New York: Wiley, 2004.
10. N. A. Krall and A. W. Trivelpiece, *Principles of Plasma Physics,* CA: San Francisco Press, San Francisco, 1986.
11. V. L. Ginzburg, '*Propagation of Electromagnetic Waves in Plasmas*', Pergamon Press, Oxford, (1964).
12. G. Castro, '*Study of Innovative Plasma Heating Methods and Applications to High Current Ion Sources*', P_HD Thesis, Universita Degli Studi Di Catania, (2012).

13. T. A. Stix, '*Waves in plasma*', Springer-Verlag, New York (1992).

14. W. E. Greig, '*An Electron Cyclotron Resonance Toroidal Plasma System for thin Film Deposition*', Master Thesis, Texas Tech University (1995).

15. T. Taylor and J. S. C. Wills, Nucl. Inst. Meth. **A309**, 37, (1991).

16. P. Roychowdhury, H. Kewlani, L. Mishra, D. S. Patil and K. C. Mittal, Rev. Sci. Instrum. **84**, 073303 (2013).

17. N. Sakudo, Rev. Sci. Instrum. **71**, 1016 (2000).

18. G. Lisitano, R. Ellis, W. M. Hooke, and T. H. Stix, Rev. Sci. Instrum. **39**, 295 (1968).

19. G. Lisitano, M. Fontanesi, and E. S. Sindomi, Appl. Phys. Lett., **16**, 122 (1970).

20. G. Casto, D. Mascali, F. P. Romano, L. Celona, S. Gammino, D. Lanaia, R. Di Giugno, R. Miracoli, T. Serafino, F. Di Bartolo, N. Gambino, and G. Ciavola, Rev. Sci. Instrum. 83, 02B501 (2012).

21. C. D. Child, Phys. Rev. **32**, 492 (1911).

22. I. Langmuir and K. T. Compton, Rev. Mod. Phys. **3**, 251 (1931).

23. M. A. Leitner, D. C. Wutte, C. M. Lyneis, '*Design of the Extraction System of the Superconducting ECR Ion Source VENUS*', Proc. of the 2001 PAC, Chicago, June (2001).

24. Jack E Boers, Proceedings of the 1995 Particle Accelerator Conference, Dallas, Texas, 1-5 May 1995, p. 2312, IEEE Catalog Number 89CH2669-0.

25. R. Becker, W. R. Herrmannsfeldt, Rev. Sci. Instrum. **63**, 2756 (1992).

26. J. H. Billen and L. M. Young, Los Alamos National Laboratory Report No.: LA-UR-96-1834 (http://laacgl.lanl.gov/laacg).

27. http://www.cobham.com.

28. http://ansoft.com.

29. http://www.cst.com.

30. K. K. Brown and S. K. Howry, SLAC-91 (1970).

31. http://www.pulsar.nl.

32. C. Lejeune and J. Albert, '*Applied Charge Particle Optics*', A. Septier (Ed.). Part **13A**, Academic, 1980, New York.

33. J. S. Humphries, '*Charged Particle Beams*', John Weily & Sons, Inc., 1990.

34. F. J. Sacherer, IEEE Trans. Nucl. Sci. **NS-18**, 1105 (1971).

35. P. Lapostolle, IEEE Trans. Nucl. Sci. **NS-18**, 1101 (1971).

36. H. Wiedemann, '*Particle Accelerator Physics*', **Vol.1**, Springer-Verlag, Berlin (2007).

37. V. Toivanen, '*Studies of Electron Cyclotron Resonance Beam Formation, Transport and Quality*' P_HD Thesis, University of Jyvaskyla (2013).

38. M. G. Mazarakis, R. J. Barke, E. P. Colton, S. Fenster, J. S. Moenich, D. K. Nikfarjam, D. W. Price, N. Q. Sesol, J. M. Waston, IEEE Trans. Nucl. Sci. **NS-26**, 3042 (1979).

39. P. Spadtke, '*Beam Formation*', Proc. of CERN Accelerator School, Small Accelerators, **CERN 2006-012**, Zeegse, The Netherlands, p.71 (2005).

40. K. Schindl, '*Space Charge*', Proc. of CERN Accelerator School, Intermediate Level Accelerator Physics, **CERN 2006-002**, Zeuthen, Germany, p-305 (2003).

41. R. Gobin, P-Y. Beauvais, R. Ferdinand, P-A. Leroy, L. Celona, G. Ciavola, S. Gammino, Rev. Sci. Instrum. **70**, 2652 (1999).

42. P-Y. Beauvais, R. Ferdinand, R. Gobin, J. L. Lagneil, L. Celona, G. Ciavola, S. Gammino, Rev. Sci. Instrum. **71**, 1413 (2000).

43. R. Ferdinand, J. Sherman, R. Stevens, and T. Zaugg, '*Space Charge Neutralization Measurement of a 75-keV, 130 mA Hydrogen Ion Beam*', Proc. of the 1997 PAC, Vancouver, B.C., Canada, May (2007).

44. C. Rubbia, J. A. Rubio, S. Buono et al., '*Conceptual Design of a Fast Neutron Operated High-Power Energy Amplifier',* CERN/AT/95-94 (ET).

45. C. D. Bowman, E. D. Arthur, P. W. Lisowski, G. P. Lawrence, R. N. Jensen, J. L. Anderson, B. Blind, M. Cappiello, J. W. Davidson, et. al. Nucl. Inst. Meth. **A320**, 336 (1992).

46. P. Lisovsky, '*The ATP Project',* Proc. of PAC-97, p.3780 (1997).

47. H. V. Smith, Jr. and J. D. Schneider, '*Status Report on Low-Energy Demonstration Accelerator* (*LEDA*)', Proc. XX Int. Linac Conf., Monterey, USA, p.581 (2000).

48. Joseph Sherman, Andrew Avin, Lash Hansborough, David Hodgkins, Earl Mayer, J. David Schneider, H. Vernon Smith, Jr., Mathew Stettler, Ralph R. Stevens, jr., Michel Thuot and Thomas Zaugg, Robin, Ferdinand, Rev. Sci. Instrum. **71**, 830 (2000).

49. J-M. Lagneil, P-Y. Beauvais, D. Bogard, G. Bourdelle, G. Charruau, O. Delferriere, D. De Menezes, A. France, R. Ferdinard, Y. Gauthier, R. Gobin, F. Harrault, J-L. Janin, P-A. Leroy and I. Yao, Rev. Sci. Instrum. **71**, 830 (2000).

50. P-Y Beauvais, D. Bogard, R. Ferdinand, R. Gobin, J-M, Lagneil, M. Painchault, P. Ausset, U. Bothner, A. C. Mueller, N. Rouviere, and A. Thatchenko, '*Status Report on Scaley High Intensity Proton Injector Project*', Proc. EPAC 2000, Vienna, Austria, p.283 (2000).

51. A. Pisent, M. Comunian, A. Palmieri, G. V. Lamanna, D. Barni, '*TRASCO 100 MeV high Intensity Proton Linac*', Proc. XX Int. Linac Conf., Monterey, USA, p.857 (2000), See also http://trasco.lnl.infn.it/.

52. Y. Yamazaki, Y. Mori, M. Mizumoto, H. Yokomizo, '*High-intensity Proton Accelerator for the JAERI/KEK Joint Project*', Proc. of EPAC 2000, Vienna, Austria, p.286 (2000).

53. Y. S. Cho, H. J. Kwon, J. H. Jang, H. S. Kim, K. T. Seol, D. Y. Kim, Y. G. Song and I. S. Hong, Journal of the Korean Physical Society, **52**, 721 (2008).

54. T. Taylor and J. F. Mouris, Nucl. Inst. Meth. **A336**, 1, (1993).

55. J. Shermann, A. Arvin, L. Hansborough, D. Hodgkins, E. Meyer, J. D. Schneider, H. Vemon Smith Jr.,R. R. Stevens Jr., M. Thout, and T. Zaugg, Rev. Sci. Instrum. **69**, 1003 (1998).

56. J-M. Lagneil, P-Y. Beauvais, D. Bogard, G. Bourdelle, G. Charruau et al., Rev. Sci. Instrum. **71**, 830 (2000).

57. L. Celona, G. Ciavola, S. Gammino, R. Gobin and R. Ferdinand, Rev. Sci. Instrum. **71**, 771 (2000).

58. R. Hollinger, P. Beller, K. Volk, M. Weber, H. Klein, Rev. Sci. Instrum. **71**, 836 (2000).

59. Y. S. Cho, B. H. Choi, I. S. Hong, Y. S. Hwang, Rev. Sci. Instrum. **71**, 969 (2000)..

60. B. Chu, B. Tang, R. Ma, Q. Huang, Y. Ma, l. Chen, and W. Jiang, Rev. Sci. Instrum. **71**, 969 (2000).

61. S. Chandan, K. P. Dixit, V. Yadav, P. Roychowdhury, D. P. Chakravarthy, '*2.45 GHz, 2 kW (CW) Microwave Power Generator for ECR Ion Source*', Proc. of SIBTA 2007, BARC, Mumbai, p.380 (2007).

62. L. Celona, G. Ciavola and S. Gammino, Rev. Sci. Instrum. **69**, 1113 (1998).

63. S. B. Cohen, Proceedings of the IRE August issue, **35**, p.783 (1947).

64. M. Shimda, I. Watanabe and Y. Torii, Nucl. Instrum. Methods, **B 39**, 242 (1989).

65. O.A. Popov and H. Waldrom, J. Vac. Sci. Technol. **A7**, 914 (1989).

66. Y. H. Lee, J. E. Heidenreich and G. Fortuno, J. Vac. Sci. Technol. **A7**, 903 (1989).

67. D. A. Carl, D. W. Hess, and M. A. Lieberman, J. Vac. Sci. Technol. **A8**, 2924 (1990).

68. S. M. Gorbatkin, L. A. Berry, and J. B. Roberto, **A8**, 2893 (1990).

69. O. A. Popov, Surf. Coat. Technol. **36**, 917 (1988).

70. O. A. Popov, J. Vac. Sci. Technol. **A8**, 2909 (1990).

71. H. Zhang, '*Ion Sources*' Springer-Verlag, Berlin (1999).

72. J. R. Coupland, T. S. Green, D. P. Hammond and A. C. Riviere, Rev. Sci. Instrum. **44**, 1258 (1973).

73. P. Roychowdhury, P. Jain, K. P. Dixit, P. C. Saroj, S. R. Ghodke, S. Gharat, S. Chandan, V. Yadav, R. B. Chavan, S. R. Barje, Abhay Kumar, S. Guha, D. P. Chakravarthy and A. K. Ray, '*High Intensity ECR Ion Source Development for ADS*', Proc. of SIBTA 2007, BARC, Mumbai, p.206 (2007).

74. P. Roychowdhury, K. P. Dixit, S. R. Ghodke, P. C. Saroj, S. Chandan, S. Gharat, V. Yadav, R. B. Chavan and D. P. Chakravarthy, '*High Intensity ECR Ion Source Development for LEHIPA-ADS-Commissioning and Operational Experience*' Proc. of Indian Particle Accelerator Conference InPAC 2009, Paper No.226, February 10-13, 2009, RRCAT, Indore.

75. P. Roychowdhury and D. P. Chakravarthy, '*Simulation of Ion Beam Extraction from Single Aperture Triode Extraction Column*', Proc. of the International Symposium on Nuclear Physics, p.714, December 8-12, 2009, BARC, Mumbai.

76. P. Roychowdhury, S. R. Ghodke, D. P. Chakravarthy, Abhay Kumar, J. J. Roy and S. Guha, '*Five Electrode ECR Proton Source for LEHIPA*', Proc. of Indian Particle Accelerator Conference InPAC 2011, Paper No. 141, February 15-18, 2011, IUAC, Delhi.

77. P. C. Saroj, S. H. Gharat, S. Patade, P. Roychowdhury, K. V. Nagesh, D. P. Chakravarthy and A. K. Ray, '*Cooling System for High Current ECR Proton Source*' Proc. of SIBTA 2007, BARC, Mumbai, p.322 (2007).

78. W. Lochte-Holtgrevev, ed., '*Plasma Diagnostics*', Elsevier, New York, 1968.

79. R. Huddlestone, S. Leonard, ed. '*Plasma Diagnostic Technique*', Academic Press, San Diego, CA, 1965.

80. J. Swift, M. Schwar, '*Electrical Probes for Plasma Diagnostics*', Elsevier, New York, 1970.

81. I. H. Hutchinson, '*Principles of Plasma Diagnostics*', Cambridge University Press, New York, 2002.

82. H. Kewlani, P. Roychowdhury, L. Mishra, S. Gharat and K. C. Mittal, '*Design and Development of Langmuir Probe Circuit for Online Measurement of Plasma Parameters in ECR Ion Source*' Proc. of Indian Particle Accelerator Conference, InPAC-2013, 19-21 November, 2013 VECC, Kolkata. p. 308, Paper No.: ID-095.

83. P. Roychowdhury, H. Kewlani, L. Mishra, S. Grarat, D.S. Patil and D. P. Chakravarthy, '*Plasma Parameter Measurement in High Current ECR Ion Source*', Proc. 2nd International Workshop on Accelerator Driven Sub-Critical Systems & Thorium Utilization, BARC Mumbai, December 11-14, 2011, p.50.

84. J. Hopwood, D. K. Reinhard and J. Asmussen, J. Vac. Sci. Technol. **A 8**, 3103 (1990).

85. S. Cartier and R. Bosch, Rev. Sci. Instrum. **54**, 1789 (1983).

86. I. D. Sudit and C. C. Woods, Rev. Sci. Instrum. **64**, 2440 (1993).

87. G. Neumann, M. Kammeyer and B. Schneemann, Meas. Sci. Technol. **6**, 391 (1995).

88. A. Brockhaus, C. Borchardt and J. Engermann, Plasma Sources Sci. Technol. **3**, 539 (1994).

89. K. Hansen, T. Kinger, and A. Piel, Rev. Sci. Instrum. **65**, 2615 (1994).

90. F. Fujita and H. Yamazaki, Jan. J. Appl. Phys. **27**, 1477 (1998).

91. L. Kene'z, S. Biri, J. Karacsony and A. Valek, Nucl. Instrum. Methods **B187**, 249 (2002).

92. G. J. H. Brussaard, M. van der Steen, M. Carre`re, M. C. M. van de Sanden, and D. C. Schram, Phys. Rev. **E 54**, 1906 (1996).

93. J. G. Laframboise, J. Rubinstein, Phys. Fluids **19**, 1900 (1976).

94. J. Rubinstein, J. G. Laframboise, Phys. Fluids **21**, 1655 (1978).

95. H. Amemiya, H. Oyama and Y. Sakamoto, J. Phys. Soc. Jpn. **56**, 2401 (1987).

96. A. A. Azooz, Rev. Sci. Instrum. **79**, 103 (2008).

97. S. B. Singh, N. Chand and D. S. Patil, Vacuum **83**, 373 (2009).

98. R. Kar, S. A. Barve, S. B. Singh, D. N. Barve, N. Chand and D. S. Patil, Vacuum **85**, 151 (2010).

99. S. Kasthurirangan, A. N. Agnihotri, C. A. Desai and L. C. Trivedi, Rev. Sci. Instrum. 83, 073111 (2012).

100. O. A. Popov, J. Vac. Sci. Technol. **A 9**, 711 (1991).

101. H.S. Uhm and E. H. Choi, Phys. Fluids **B 5**, 1902 (1993).

102. P. Roychowdhury, L. Mishra, H. Kewlani, D. S. Patil and K. C. Mittal, Rev. Sci. Inst. **85**, 033303 (2014).

103. P. Roychowdhury, S. R. Ghodke, S. Gharat and D.P. Chakravarthy, '*Beam Line for Emittance and Specie Measurement in ECR Proton Source*', Proc. Indian Particle Accelerator Conference InPAC 2011, Paper No. 149, 15-18 February 2011, IUAC, Delhi.

104. D. C. Faircloth, S. Lawrie, A. P. Letchford, C. Gabor, P. Wise, M. Whitehead, T. Wood, M. Westall, D. Findlay, M. Perkins, P. J. Savage, D. A. Lee and J. K. Pozimski, Rev. Sci. Inst. **81**, 02A721 (2010).

105. A. Adonin, R. Hollinger, and P. Spadtke, Rev. Sci. Inst. **81**, 02A721 (2010).

106. M. Strohmeier, J. Y. Benitez, D. Leitner, C. M. Lynesis, D. S. Todd, and M. Bantel, Rev. Sci. Inst. **81**, 02B710 (2010).

107. D. Liakin, D. Seleznev, A. Orlov, R. Kuibeda, G. Kropachev, T. Kulevoy, Rev. Sci. Inst. **81**, 02B719 (2010).

108. B. X. Han, M. P. Stockli, R. F. Welton, T. R. Pennisi, S. N. Murry, M. Santanna and C. D. Long, Rev. Sci. Inst. **81**, 02B721 (2010).

109. Z. Yao, X. Tan, H. Du, B. Luo and Z. Liu, Rev. Sci. Inst. **79**, 073304 (2008).

110. M. P. Stockli, R. F. Welton, R. Keller and M. Leitner, Rev. Sci. Inst. **77**, 03B706 (2006).

111. Y. Higurashi, M. Kidera, M. Kase, T. Nakagawa, and Y. Yano, Rev. Sci. Inst. **75**, 1467 (2004).

112. R. Hollinger, K. Volk, and H. Klein, Rev. Sci. Inst. **73**, 1027 (2002).

113. S. Kondrashev, A. Barcikowski, B. Mustapha, P. N. Ostroumov and N. Vinogradov, Nucl. Instrum. Methods, A **606**, 296 (2009).

114. B. Tang, R. Ma, Y. Ma, L. Chen, Q. Huang, H. Liang, B. Chu and W. Jiang, Rev. Sci. Inst. **85**, 02A911 (2014).

115. H. Kewlani, P. Roychowdhury, L. Mishra, S. Gharat, S. Ghodke and K. C. Mittal, '*Design and Development of Instrumentation of Two Slit Emittance Meter for High Current ECR Ion Source*' Proc. of Indian Particle Accelerator Conference, InPAC-2013, 19-21 November, 2013 VECC, Kolkata. p. 564, Paper No.: ID-224.

116. P. Roychowdhury, L. Mishra, H. Kewlani, S. Grarat, D. S. Patil and K. C. Mittal, '*Development and Characterization of High Current Electron Cyclotron Resonance Proton Ion Source*' Proc. of Indian Particle Accelerator Conference, InPAC-2013, 19-21 November, 2013 VECC, Kolkata. p. 130, Paper No.: ITS-10.

117. P. Y. Beauvais, J. M. Lagneil, N. Pichoff, G. Haaoust and P. Chaix, '*Space-Charge Neutralization with a Low Energy Proton Beam*' Proc. of the XVIII International LINAC Conference, Geneva, Switzerland, 1996, page 202.

118. A. Benismail, R. Duperrier, D. Uriot and N. Pichoff, Phys Rev. ST Accel. Beams, **10**, 070101 (2007).

119. O. Waldmann and B. Ludewigt, Rev. Sci. Inst. **82**, 113505 (2011).

120. R. Miracoli, '*Characterization of Microwave Discharge Ion Source for High Proton Beam Production in CW and Pulsed Mode*' P$_H$D Thesis, Universita Degli Studi Di Catania (2010).

121. H. Kewlani, P. Roychowdhury, S. Grarat, L. Mishra, D. P. Chakravarthy and K. C. Mittal, '*Electron Cyclotron Resonance Ion Source Control System*', Proc. of Ninth International Workshop on Personal Computers held at VECC Kolkata December 4-7, 2012, p. 217, Paper No.: THPD43 (www.jacow.org).

122. V. Yadav, R. B. Chavan, K. P. Dixit, P. Roychowdhury, K. C. Mittal and D. P. Chakravarthy, '*Optically Isolated Remote Operation and Data Acquisition System for ECR Ion Source Developed for LEHIPA*', Proc. of Indian Particle Accelerator Conference InPAC 2011, 15-18 Feb. 2011, IUAC, Delhi, Paper No. 134.